The early Mesoproterozoic tectonic systems and IOCG mineralisation in the northern Gawler Craton

Jie Yu

Department of Earth Sciences
School of Physics, Chemistry and Earth Sciences

Thesis submitted in fulfilment of the requirements for the degree of
Doctor of Philosophy

July, 2023

Table of Contents

Table of Contents

Abstract

The Gawler Craton in southern Australia is renowned for the presence of its world-class iron oxide copper gold (IOCG) deposits, which formed at ca. 1595–1575 Ma, in association with voluminous Large Igneous Province (LIP) magmatism. These hydrothermal breccia deposits, including the supergiant Olympic Dam deposit, are dominated by hematite and formed in the upper crust. In the northern Olympic Cu-Au Province, a series of magnetite-dominated deposits/prospects associated with minor Cu-Au mineralisation are hosted in rocks that experienced multiple phases of high temperature metamorphism and deformation. These have long been considered to represent the deeper expression of the hematite-dominated IOCG systems.

Cairn Hill Fe (-Cu-Au) deposit, arguably the best example of a deeply eroded IOCG system in the Gawler Craton, is dominated by magnetite hosted in granulite facies rocks. New U-Pb zircon geochronology shows the magnetite-hornblende lodes at Cairn Hill were formed at ca. 1580 Ma at amphibolite facies conditions. The magnetite lodes are cross-cut by ca. 1515 Ma granitic dykes and then deformed by ca. 1490 Ma event at conditions of 4.6–5.3 kbar and 740–770 °C. However, Cu mineralisation at Cairn Hill occurs in brittle fractures, overprinting the 1490 Ma deformation and metamorphism. The spatial but not temporal association between magnetite and Cu has effectively overlain two distinct episodes of mineralisation to create a composite Fe-Cu deposit observed today. The age of the young Cu mineralisation is constrained by *in situ* apatite Lu-Hf geochronology. The granulite host-rock that predates Cu mineralisation yields apatite Lu-Hf ages of ca. 1490 Ma, while infiltration of Cu-bearing fluids resulted in recrystallisation of apatite, LREE mobilization and formation of secondary monazite at ca. 1460 Ma. The timing of Cu mineralisation coincides with the onset of Nuna fragmentation, representing a previously unrecognized mineralizing system in southern Australia that installed Cu in previously dehydrated crust during a long history of granulite-grade tectonic events. Detailed petrological and geochemical analyses of magnetite, apatite, and fluid inclusions are conducted to elucidate the genesis of iron and copper mineralisation at Cairn Hill. The early magnetite-apatite-hornblende assemblage may have been formed by magmatic fluids, similar to the deep, early magnetite-apatite at the deep and marginal parts of Olympic Dam. Ore-forming fluids responsible for Cu mineralisation are high-temperature, CO_2-rich and oxidized, which may have exsolved from intrusions.

The tectonic setting within which the Gawler Craton IOCG deposits and newly identified younger deposits/prospects is uncertain. During the time interval of IOCG mineralisation, Mabel Creek Ridge, in the northern Gawler Craton, is a granulite-facies domain recording early Mesoproterozoic metamorphism. New *P–T* pseudosection results and geochronology, coupled with the regional seismic and airborne magnetic data, reveal that Mabel Creek Ridge represents a record of early Mesoproterozoic extension in the Gawler Craton, during which thermally perturbed lower crustal rocks were exhumed within a gneiss dome. Early Mesoproterozoic extension took place within a complex geodynamic regime resulting from the interplay between final Nuna convergence along the margin of northeast Australia at ca. 1600 Ma, subduction to the southwest at ca. 1630–1610 Ma and plume-driven magmatism that resulted in the generation of voluminous felsic melts and associated IOCG mineralisation within the Gawler Craton-Curnamona Province system over the interval 1595–1575 Ma.

Thesis Declaration

I, Jie Yu, certify that this work contains no material which has been accepted for the award of any other degree or diploma in my name, in any university or other tertiary institution and, to the best of my knowledge and belief, contains no material previously published or written by another person, except where due reference has been made in the text. In addition, I certify that no part of this work will, in the future, be used in a submission in my name, for any other degree or diploma in any university or other tertiary institution without the prior approval of the University of Adelaide.

I acknowledge that copyright of published works contained within this thesis resides with the copyright holders of those works.

I also give permission for the digital version of my thesis to be made available on the internet, via the university's digital research repository, the library search and also through internet search engines, unless permission has been granted by the University to restrict access for a period of time.

I acknowledge the support I have received for my research through the provision of China Scholarship Council.

Jie Yu 20 July 2023

Acknowledgements

I am sincerely grateful to my supervisors, the most exceptional team in the world. Their vast knowledge, profound passion for geology, boundless patience with students, and unwavering dedication to scientific rigor have profoundly shaped me. I consider myself incredibly fortunate to have crossed paths with them, as they have not only guided me through my Ph.D. but have also imparted invaluable lessons that will shape my future academic career and life.

I would like to extend my heartfelt appreciation to my master's supervisor, Prof. Yan-Jing Chen of Peking University. Amidst the challenging circumstances of the COVID pandemic, he provided me with unwavering support and encouragement. I also would like to appreciate Stijn and Alex, whose groundbreaking advancements in apatite and garnet geochronology have greatly influenced the trajectory of my Ph.D. research. I am particularly indebted to Alex, who collected copious amounts of data during my time stranded in China, and also patiently imparts his profound understanding of the Lu-Hf secrets.

The Adelaide Microscopy team has been an unforeseen blessing in my academic journey. In contrast to my previous experiences, the team in Adelaide has been exceptionally knowledgeable and supportive. I am especially indebted to Ben, whose warmth and unwavering assistance have made my research immensely fruitful.

To the incredible individuals at the CERG tank—Dillon, Mitchell, Brad, Renee, Kiara, and Sam—I extend my heartfelt gratitude for acquainting me with Australia and the University of Adelaide. I vividly recall my first day in the office when they warmly welcomed me and even drew a map to show me their nearby hometown. Their kindness and camaraderie have made me feel at home in a distant continent. I would also like to express my gratitude to my later companions at the CERG tank—Sharmaine, Melissa, Alejandra, Ferdinand, and Tom—for their companionship during the challenging final stages of my Ph.D. journey.

I would like to acknowledge the China Scholarship Council for granting me the invaluable opportunity to pursue my studies abroad. I am deeply grateful to my parents for granting me the freedom and respect to embark on this journey, even though they may have no idea how far away it is from Shandong countryside to Adelaide. Lastly, I want to express my deepest gratitude to my love, Ms. Ninglu Zhang, a constant presence in the acknowledgments of my bachelor's and master's theses. You have been a beacon of light in my life, and I attribute much of my success to your unwavering support. I look forward to spending the rest of my days with you, cherishing every moment of our lives together.

Chapter 1

Introduction and thesis outline

1. Introduction to the Olympic Cu-Au Province

The discovery of the immense Olympic Dam Cu-U-Au deposit in the Gawler Craton, South Australia, established the association of iron-oxide-copper-gold (IOCG) as a distinct class of mineral deposits (Hitzman et al., 1992; Williams et al., 2005; Groves et al., 2010). In the Gawler Craton, the Olympic Dam deposit, together with the Prominent Hill and Carrapateena IOCG deposits, as well as numerous historic mines and prospects in the Moonta-Wallaroo district and Mount Woods Domain, constitute the Olympic Cu-Au Province (Fig. 1.1; Reeve et al., 1990; Oreskes and Einaudi et al., 1992; Belperio et al., 2007; Skirrow et al., 2007; Freeman and Tomkinson, 2010; Schlegel et al., 2018). The Olympic Cu-Au Province formed between ca. 1595–1575 Ma, in association with the voluminous Large Igneous Province (LIP) magmatism of the Gawler Range Volcanics and Hiltaba Suite granites (Bowden et al., 2017; Cherry et al., 2018; Courtney-Davies et al., 2020; McPhie et al., 2020; Jagodinski et al., 2023). The latter magmatism has been suggested to be driven by a mantle plume beneath a metasomatised subcontinental lithospheric mantle (SCLM) (Jagodinski et al., 2023; Wade et al., 2022). Cu mineralisation at Olympic Cu-Au Province has a significant contribution of mantle-derived material indicated by neodymium isotope studies (Johnson and McCulloch, 1995; Skirrow et al., 2018), and lithospheric-scale geophysical imaging reveals apparent crustal-scale metasomatic alteration connecting the upper mantle to the upper crustal IOCG mineralizing systems (Heinson et al., 2006; 2018). The lithospheric-scale geophysical imaging beneath the giant Olympic Dam deposit and peripheral Wirrda Well and Vulcan prospects may represent deep mineral systems or pathways of metalliferous fluids where conducting phases of graphite, sulfides, or magnetite are precipitated (Heinson et al., 2006, 2018; Hayward and Skirrow, 2010).

Exploring for and understanding the genesis of IOCG deposits is a topic of significant debate and ongoing research. The definition, classification, and genetic models of these deposits, as well as the role played by magmatic and non-magmatic fluids and the specific tectonic settings in which they form, remain areas of intense contention (e.g., Williams et al., 2005; Groves et al., 2010; Corriveau et al., 2016; Reich et al., 2016; Simon et al., 2018; Skirrow, 2022). Despite these controversies, IOCG deposits generally encompass two important groups based upon their predominant iron oxide species, namely magnetite-rich and hematite-rich endmembers (Williams, 2010; Barton, 2014; Skirrow, 2022). In the Olympic Cu-Au Province, Gawler Craton, most IOCG deposits are upper crustal hematite-dominated and breccia-hosted, including the Olympic Dam, Prominent Hill and Carrapateena deposits (Oreskes and Einaudi et al., 1992; Belperio et al., 2007; Schlegel et al., 2018). Fluid inclusion and oxygen isotope studies have revealed that ore-forming fluids responsible for the hematite-rich Cu-Au mineralisation at Olympic Dam and Prominent Hill deposits are generally between 200 and 400 ºC, formed by mixing of magmatic fluids with oxidized non-

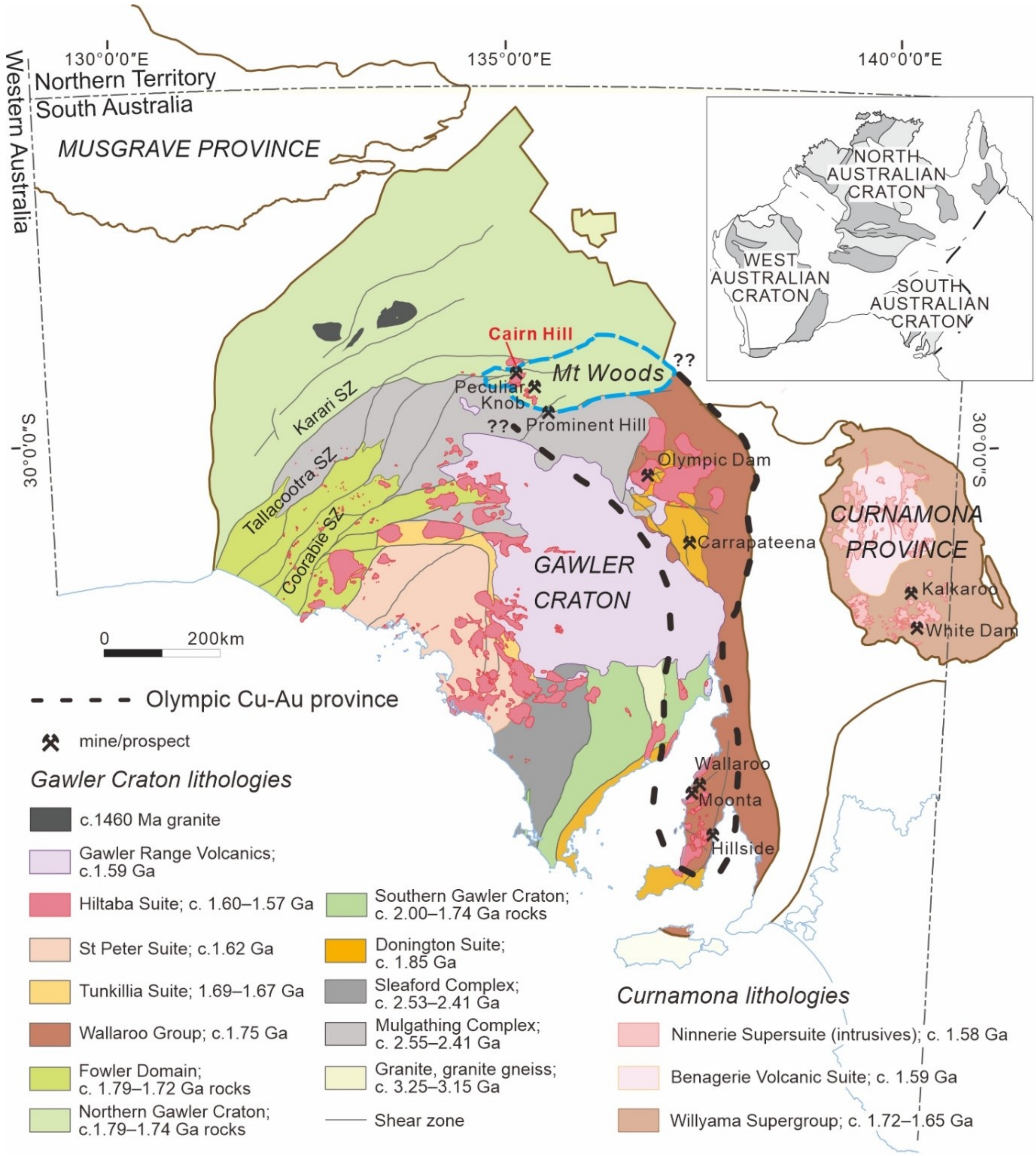

Figure 1.1 Simplified solid geology map of the Gawler Craton, showing the location of IOCG deposit in Olympic Cu-Au Province (after Reid et al., 2014).

magmatic basin brine or meteoric water (Oreskes and Einaudi, 1992; Bastrakov et al., 2007; Davidson et al., 2007; Schlegel et al., 2018). Surrounding these hematite-dominated Cu-Au deposits are a number of magnetite-dominated Cu-poor prospects or alteration zones that formed at higher temperatures (400–500 ºC) and are interpreted to represent the early and deeper mineralisation and alteration of the IOCG mineralizing systems (Oreskes and Einaudi, 1992; Bastrakov et al., 2007; Davidson et al., 2007). Recent drilling has revealed paragenetically early, deep magnetite-apatite mineralisation at depth and at the outer margins (e.g., Wirrda Well and Acropolis prospects) of the hematite-dominated Olympic Dam deposit (Ehrig et al., 2012;

Apukhtina et al., 2017; Verdugo-Ihl et al., 2020). This seems to support the genetic models that the earlier magnetite-rich mineralisation develops beneath the hematite-dominated IOCG systems (Hayward and Skirrow, 2010). However, no giant IOCG deposit/system are obliquely exhumed to the extent that they expose the mid-crust magnetite-rich alteration inferred from geophysical data to test the metallogenic models.

In the north of the currently defined Olympic Cu-Au Province is the poorly exposed Mount Woods Domain. The domain is comprised of amphibolite to granulite-facies rocks intruded by Hiltaba-equivalent granites and gabbros (Jagodinski et al., 2007; Morrissey et al., 2023). These are separated from the upper crustal rocks of the Olympic Domain by the Southern Overthrust. Deep exhumation in the Mount Woods Domain has exposed extensive tracts of mid-crust with magnetic-rich alteration containing Cu and Au, including the Cairn Hill Fe (-Cu-Au) deposit and Manxman and Joe's Dam prospects (Freeman and Tomkinson, 2010; Morrissey et al., 2023). These tracts of magnetite-rich Cu-Au alteration are hosted in amphibolite to granulite metamorphic grade rocks and have traditionally been considered to represent deeper parts of the mineralizing system that formed the world-class Olympic Dam and the associated large IOCG deposits (Hayward and Skirrow, 2010; Reid and Fabris, 2015; Skirrow, 2022). However, protoliths and metamorphic evolution of the host rocks, ore genesis and the time of mineralisation of these magnetite-dominated deposits/prospects in the Mount Woods Domain are poorly known, in contrast to the well-studied hematite-dominated IOCG deposits (Bowden et al., 2017; Cherry et al., 2018; Courtney-Davies et al., 2020; McPhie et al., 2020). These gaps have constrained our further understanding of IOCG mineralisation in the northern Olympic Cu-Au Province and IOCG metallogenic models in general. In addition, magmatism, alteration and mineralisation between 1560–1460 Ma in the Peake and Denison Domain, north-eastern Gawler Craton, present a number of correlations with the IOCG mineralisation in the Mount Isa Province, North Australian Craton (Bockmann et al., 2023), adding to the complexity of the IOCG mineralisation in the northern Gawler Craton.

2. Tectonic setting of the Gawler Craton

The Gawler Craton records a complex geological history from the Archean to the Mesoproterozoic (Fig. 1.1; Hand et al., 2007; Reid and Hand, 2012). Its basement comprises Mesoarchean gneisses in the southeastern Gawler Craton (3250–3150 Ma; Fraser et al., 2010) and two belts of 2555–2410 Ma volcanic, sedimentary, and magmatic rocks known as the Sleaford Complex in the southern Gawler Craton and the Mulgathing Complex in the central region of the craton (Daly and Fanning, 1993; Reid et al., 2014b). These rock packages were deformed and metamorphosed during the early Paleoproterozoic Sleafordian Orogeny (2470–2410 Ma; Hand et al., 2007; Reid and Hand, 2012; Halpin and Reid, 2016). The ca. 2000 Ma Miltalie Gneiss in the eastern part of the craton (Fig. 1.1) is interpreted to mark the onset of an extended period of rifting in the Gawler Craton (Payne et al., 2006; Hand et al., 2007). From ca. 2000 to 1730 Ma, a series of volcano-sedimentary and metasedimentary rocks were deposited across the Gawler Craton (Fanning et al., 1988, 2007; Oliver and Fanning, 1997; Payne et al., 2006; Jagodzinski et al., 2007; Howard et al., 2011b; Szpunar et al., 2011).

The craton-wide Kimban Orogeny (ca. 1730–1690 Ma) terminated widespread basin development and sedimentation, with activation of crustal-scale shear zones, granitic magmatism, widespread metamorphism, and localized basin development (Hand et al., 2007; Payne et al., 2008; Dutch et al., 2010; Reid et al., 2019a; Morrissey et al., 2023). Following the Kimban Orogeny, the Gawler Craton experienced dominantly magmatic events. The central and western Gawler Craton were intruded by the ca. 1690–1670 Ma Tunkillia Suite (Payne et al., 2010), with localized high to ultrahigh temperature metamorphism at ca. 1690–1665 Ma in the western Gawler Craton known as the Ooldean Event (Hand et al., 2007; Cutts et al., 2013). This was followed by the arc-related St Peter Suite in the southern Gawler Craton (ca. 1633–1608 Ma; Swain et al., 2008; Reid et al., 2019b) and high temperature magmas of the Gawler Range Volcanics (1595–1590 Ma) and coeval Hiltaba Suite granites (1595–1570 Ma) and associated mafic rocks (Daly, 1998; Wade et al., 2019; Jagozdinski et al., 2023). The ca. 1600–1540 Ma Kararan Orogeny was broadly coeval with magmatism and involved deformation and high thermal gradient metamorphism in the northern (e. g., Mabel Creek Ridge), western and southeastern Gawler Craton (Daly, 1998; Hand et al., 2007; Payne et al., 2008; Cutts et al., 2011; Forbes et al., 2011; Morrissey et al., 2013; Reid et al., 2019a; Bockmann et al., 2022). Migmatite with a ca. 1520 Ma metamorphic age is intersected in drill hole GOMA DH4 in the northern Gawler Craton (Reid et al., 2014a), and minor magmatism at ca. 1500 Ma has been identified in the southern Gawler Craton (Fanning et al., 2007; Jagodzinski et al., 2007). Localized ca. 1450 Ma A-type magmatism, high-temperature metamorphism, and shear zone reactivation occur in the northern Gawler Craton (Fraser and Lyons, 2006; Fraser et al., 2012; Morrissey et al., 2019). Thermochronology records regional cooling from mid-crustal temperatures between ca. 1460–1415 Ma across the northern Gawler Craton (Hall et al., 2018; Reid and Forster, 2021; Morrissey et al., 2023). Neoproterozoic and Phanerozoic sedimentary units overlie much of the stable craton (Preiss, 2000).

This thesis focuses on the tectonic setting of northern Gawler Craton during the early Mesoproterozoic, the recently proposed time interval of final assembly and breakup of the Nuna supercontinent (Cawood and Korsh, 2008; Payne et al., 2009; Pisarevsky et al., 2014; Morrissey et al., 2019; Kirscher et al., 2020). During this time interval (ca. 1.60–1.45 Ga), IOCG mineralisation in the eastern Gawler Craton was associated with extensive bimodal A-type magmatism and high temperature metamorphism (Hand et al., 2007). Mantle underplating or a mantle plume has been suggested as a crucial mechanism to create the high temperature magmatism in an anorogenic setting (Giles, 1988; Creaser, 1996). Recently, a switch from compression to extension in a backarc setting has been suggested for central and eastern Gawler Craton, evidenced by the compressional deformation recorded within the Hiltaba Suite and the flat-lying bimodal GRV (Giles et al., 2004; Betts and Giles, 2006; Wade et al., 2008; Hayward & Skirrow, 2010; Skirrow et al., 2018). In contrast to the central and eastern Gawler Craton, our knowledge of the tectonic setting of the extensively buried northern Gawler Craton is more limited, despite early Mesoproterozoic high-grade metamorphism being reported in Mount Woods Domain, Mabel Creek Ridge and Coober Pedy Ridge (Jagodzinski et al., 2007; Payne et al., 2008; Cutts et al., 2011; Forbes et al., 2011; Morrissey et al., 2023). Information on the tectonic development of the basement of northern Gawler Craton can only be derived from sparse mineral exploration drill holes and regional geophysical datasets, making it challenging to decipher the tectonic regimes of high-grade metamorphism and regional IOCG mineralisation.

Recently more evidence of younger A-type magmatism, metamorphism, alteration, and shear zone reactivation between ca. 1520 – 1450 Ma has been identified in the northern Gawler Craton (Reid et al., 2014a; Morrissey et al., 2019, 2023; Bockmann et al., 2023). The tectonic setting for these younger events and their importance to potential mineralisation is currently poorly understood. However, these events are similar to and broadly coeval with metamorphism, magmatism, deformation and hydrothermal mineralisation in the Mount Isa Province (Betts and Giles, 2006; Giles et al., 2006; Duncan et al., 2011; Cave et al., 2022; Bockmann et al., 2023). Considering the long-linked history between the North Australian Craton (NAC) and South Australian Craton (SAC) from the Archean to early Mesoproterozoic (Cawood and Korsh, 2008; Payne et al., 2009), the northern Gawler Craton has the potential to develop IOCG mineralisation similar to the Mount Isa Province (Bockmann et al., 2023) prior to separation during the rifting of the Nuna supercontinent (Morrissey et al., 2019). Therefore, a better understanding of these younger events and identification of younger mineralisation is crucial to compare and link the two important IOCG provinces in Eastern Proterozoic Australia.

3. Thesis outline

The aims of this thesis are to explore the early Mesoproterozoic tectonic architecture and IOCG mineralisation of the northern Gawler Craton, addressing the following questions:

1. Metamorphic history and crustal level of northern Olympic IOCG Province.
2. Geochronology and mineralisation history of IOCG systems in the northern Gawler Craton.
3. Ore genesis of arguably the best example of a deeply eroded IOCG system in the northern Gawler Craton, i.e., the Cairn Hill Fe (-Cu-Au) deposit.
4. Tectonic setting of northern Gawler Craton during early Mesoproterozoic.

The findings of this thesis allow the poorly understood deposits of the northern Gawler to be compared to the better-characterized upper crustal

IOCG systems in the Olympic Domain. The chapters of this thesis are briefly outlined below.

Chapter 2 investigates the protoliths and metamorphic history of the Cairn Hill deposit, constraining the ages of iron and copper mineralisation in the northern Olympic Cu-Au Province. Cairn Hill is the largest deposit in the northern Olympic Cu-Au Province and is of central importance to the concept that the northern Olympic Cu-Au Province represents deeper crustal levels of the much large hematite-dominated deposits elsewhere in the province. Chapter 2 presents zircon and monazite U–Pb ages and mineral equilibria forward modelling to demonstrate the Cairn Hill system consists of two distinct and temporally unrelated mineral systems separated by at least 100 Ma. Magnetite mineralisation formed no later than ca. 1580 Ma and experienced granulite-facies metamorphism and deformation at ca. 1490 Ma. Copper mineralisation at Cairn Hill occurred under brittle conditions and overprinted the ca. 1490 Ma ductile deformation and high-T metamorphism. Therefore, the spatial but not temporal association between Fe and Cu has effectively overlain two distinct mineral systems to create a composite IOCG deposit in the northern Olympic Cu-Au Province.

Chapter 3 investigates the timing of Cu mineralisation directly through detailed petrography and geochronology (in situ apatite Lu-Hf and in situmonazite and apatite U-Pb). The results of Chapter 2 highlight that Cu mineralisation is 100 Myr younger than Olymipc-equivalent IOCG mineralisation, and must post-dates high temperature metamorphism at ca. 1490 Ma. However, Chapter 2 does not directly constrain the timing of the mineralisation event. Many conventional dating methods in mineral deposits have low closure temperatures, such as sulfide Re-Os (ca. 500 °C; Lawley et al., 2013), hornblende ^{40}Ar-^{39}Ar (530 ± 40 °C; Harrison, 1982), biotite ^{40}Ar-^{39}Ar (310±40 °C; Harrison et al., 1985), and apatite U-Pb (~350–550 °C; Chew and Spikings, 2015), making it difficult to determine whether ages represent growth ages or cooling/resetting ages. To partially overcome this, Chapter 3 uses the thermally robust apatite Lu-Hf isotopic system (closure temperature ~650 °C; Glorie et al., 2023), in combination with texturally constrained in situ monazite U-Pb geochronology, aiming to directly constrain the timing of Cu mineralisation. The new geochronology data together with detailed petrography, demonstrate the veracity of the in-situ apatite Lu-Hf method for directly recording the timing of hydrothermal fluid activity and mineralisation. Cu mineralisation in the deeply exhumed northern Olympic Cu-Au Province occurred at ca. 1460 Ma, coeval with an inferred extension event elsewhere in the northern Gawler Craton.

Chapter 4 focuses on the genesis of the composite Cairn Hill deposit. Geochronological evidence in Chapters 2 and 3 identified two mineralisation events at Cairn Hill at ca. 1580 Ma and ca. 1460 Ma, but the genesis of its early iron and late copper mineralisation remains poorly understood. To elucidate the genesis of iron and copper mineralisation, detailed petrological and geochemical analyses of magnetite, apatite, and fluid inclusions have been undertaken.

Geochemistry of early-stage magnetite and apatite indicates the early magnetite-apatite-hornblende assemblage at Cairn Hill may have been formed by magmatic fluids, similar to the inferred deep, early magnetite-apatite at the deep and marginal parts of Olympic Dam (Ehrig et al., 2012; Apukhtina et al., 2017; Verdugo-Ihl et al., 2020). Ore-forming fluids responsible for Cu mineralisation are high-temperature, CO_2-rich and oxidized, which may be exsolved from intrusions. Since the Cairn Hill crustal volume would have been largely anhydrous by 1460 Ma due to the combined consequences of high-T metamorphism at ca. 1580 and 1490 Ma, the young ca. 1460 Ma Cu mineralisation may require the new addition of metals and fluids.

Chapter 5 investigates the metamorphic character of Mabel Creek Ridge and the tectonic evolution of the northern Gawler Craton. Mabel Creek Ridge is a granulite-facies domain that is known to record metamorphism coeval with the timing of IOCG mineralisation elsewhere in the Gawler Craton. It is investigated to provide context for the early Mesoproterozoic IOCG mineral systems in the northern Gawler Craton. Chapter 5 presents geochronology, *P–T* pseudosection modelling, and regional geophysical data to propose that Mabel Creek Ridge is an example of an early Mesoproterozoic (ca. 1600–1560 Ma) gneiss dome buried in the northern Gawler Craton. Seismic reflection data show Mabel Creek Ridge is flanked by divergent crustal-scale structures and contains sub-horizontal internal reflectors. Airborne magnetic data show the internal structure consists of regional-scale circular structural trends, suggesting that Mabel Creek Ridge has a regional-scale dome-like character. While gneiss domes can form in compressional settings (Searle and Lamont, 2020), they are mechanically more likely in extensional regimes (Teyssier and Whitney, 2002; Yin, 2004; Rey et al., 2011). The extensional tectonics may occur within a complex geodynamic regime resulting from the interplay between the final Nuna convergence along the margin of northeast Australia and subduction to the southwest at ca. 1600 Ma.

Chapter 6 contains a summary and discussion of the results and outcomes contained in this thesis. We also briefly discuss directions for future research to gain a comprehensive understanding of the young Cu mineralisation events in the northern Gawler Craton.

References

Apukhtina, O. B., Kamenetsky, V. S., Ehrig, K., Kamenetsky, M. B., Maas, R., Thompson, J., McPhie, J., Ciobanu, C. L., and Cook, N. J., 2017, Early, deep magnetite-fluorapatite mineralisation at the Olympic Dam Cu-U-Au-Ag deposit, South Australia*: Economic Geology, v. 112, no. 6, p. 1531-1542.

Barton, M. D., 2014, Iron Oxide(–Cu–Au–REE–P–Ag–U–Co) Systems, Treatise on Geochemistry, p. 515-541.

Bastrakov, E. N., Skirrow, R. G., and Didson, G. J., 2007, Fluid evolution and origins of iron oxide Cu-Au prospects in the Olympic Dam district, Gawler craton, south Australia: Economic Geology, v. 102, no. 8, p. 1415-1440.

Belperio, A., Flint, R., and Freeman, H., 2007, Prominent Hill: A Hematite-Dominated, Iron Oxide Copper-Gold System: Economic Geology, v. 102, no. 8, p. 1499-1510.

Betts, P. G., and Giles, D., 2006, The 1800–1100Ma tectonic evolution of Australia: Precambrian Research, v. 144, no. 1, p. 92-125.

Bockmann, M. J., Hand, M., Morrissey, L. J., Payne, J. L., Hasterok, D., Teale, G., and

Conor, C., 2022, Punctuated geochronology within a sustained high-temperature thermal regime in the southeastern Gawler Craton: Lithos, v. 430, p. 106860.

Bockmann, M. J., Payne, J. L., Hand, M., Morrissey, L. J., and Belperio, A. P., 2023, Linking the Gawler Craton and Mount Isa Province through hydrothermal systems in the Peake and Denison Domain, northeastern Gawler Craton: Geoscience Frontiers, p. 101596.

Bowden, B., Fraser, G., Davidson, G. J., Meffre, S., Skirrow, R., Bull, S., and Thompson, J., 2017, Age constraints on the hydrothermal history of the Prominent Hill iron oxide copper-gold deposit, South Australia: Mineralium Deposita, v. 52, no. 6, p. 863-881.

Cave, B., Perkins, W., and Lilly, R., 2022, Linking uplift and mineralisation at the Mount Novit Zn-Pb-Ag Deposit, Northern Australia: Evidence from geology, U–Pb geochronology and sphalerite geochemistry: Geoscience Frontiers, v. 13, no. 2, p. 101347.

Cawood, P. A., and Korsch, R., 2008, Assembling Australia: Proterozoic building of a continent: Precambrian Research, v. 166, no. 1-4, p. 1-35.

Cherry, A. R., Ehrig, K., Kamenetsky, V. S., McPhie, J., Crowley, J. L., and Kamenetsky, M. B., 2018, Precise geochronological constraints on the origin, setting and incorporation of ca. 1.59 Ga surficial facies into the Olympic Dam Breccia Complex, South Australia: Precambrian Research, v. 315, p. 162-178.

Chew, D. M., and Spikings, R. A., 2015, Geochronology and thermochronology using apatite: time and temperature, lower crust to surface: Elements, v. 11, no. 3, p. 189-194.

Corriveau, L., Montreuil, J. F., and Potter, E. G., 2016, Alteration Facies Linkages Among Iron Oxide Copper-Gold, Iron Oxide-Apatite, and Affiliated Deposits in the Great Bear Magmatic Zone, Northwest Territories, Canada*: Economic Geology, v. 111, no. 8, p. 2045-2072.

Courtney-Davies, L., Ciobanu, C. L., Tapster, S. R., Cook, N. J., Ehrig, K., Crowley, J. L., Verdugo-Ihl, M. R., Wade, B. P., and Condon, D. J., 2020, Opening the magmatic-hydrothermal window: high-precision U-Pb Geochronology Of The Mesoproterozoic Olympic Dam Cu-U-Au-Ag deposit, South Australia: Economic Geology, v. 115, no. 8, p. 1855-1870.

Creaser, R. A., 1996, Petrogenesis of a Mesoproterozoic quartz latite-granitoid suite from the Roxby Downs area, South Australia: Precambrian Research, v. 79, no. 3, p. 371-394.

Cutts, K. A., Kelsey, D. E., and Hand, M., 2013, Evidence for late Paleoproterozoic (ca 1690–1665Ma) high- to ultrahigh-temperature metamorphism in southern Australia: Implications for Proterozoic supercontinent models: Gondwana Research, v. 23, no. 2, p. 617-640.

Daly, S., 1998, Tectonic evolution and exploration potential of the Gawler Craton, South Australia: AGSO J. Aust. Geol. Geophys., v. 17, p. 145-168.

Daly, S., and Fanning, C., 1993, Archaean: Geological Survey of South Australia.

Davidson, G. J., Paterson, H., Meffre, S., and Berry, R. F., 2007, Characteristics and origin of the Oak Dam East breccia-hosted, iron oxide Cu-U-(Au) deposit: Olympic Dam region, Gawler craton, South Australia: Economic Geology, v. 102, no. 8, p. 1471-1498.

Duncan, R. J., Stein, H. J., Evans, K. A., Hitzman, M. W., Nelson, E. P., and Kirwin, D. J., 2011, A new geochronological framework for mineralisation and alteration in the Selwyn-Mount Dore corridor, Eastern fold belt, Mount Isa inlier, Australia: Genetic implications for iron oxide copper-gold deposits: Economic Geology, v. 106, no. 2, p. 169-192.

Dutch, R., Hand, M., and Kelsey, D., 2010, Unravelling the tectonothermal evolution of reworked Archean granulite facies metapelites using in situ geochronology: an example from the Gawler Craton, Australia: Journal of Metamorphic Geology, v. 28, no. 3, p. 293-316.

Ehrig, K., McPhie, J., and Kamenetsky, V., 2012, Geology and mineralogical zonation of the Olympic Dam iron oxide Cu-U-Au-Ag deposit, South Australia, *in* Hedenquist, J., Harris, M., and Camus, F., eds., Geology and genesis of major copper deposits and districts of the world: a tribute to Richard H. Sillitoe., Soc of Econ Geol Spec Pub, p. 16: 237–267.

Fanning, C., Flint, R., Parker, A., Ludwig, K., and Blissett, A., 1988, Refined Proterozoic evolution of the Gawler craton, South

Australia, through U-Pb zircon geochronology: Precambrian Research, v. 40, p. 363-386.

Fanning, C., Reid, A., and Teale, G., 2007, A geochronological framework for the Gawler Craton, South Australia: South Australia Geological Survey Bulletin, v. 55, no. 258.

Forbes, C. J., Giles, D., Hand, M., Betts, P. G., Suzuki, K., Chalmers, N., and Dutch, R., 2011, Using P–T paths to interpret the tectonothermal setting of prograde metamorphism: An example from the northeastern Gawler Craton, South Australia: Precambrian Research, v. 185, no. 1-2, p. 65-85.

Fraser, G., McAvaney, S., Neumann, N., Szpunar, M., and Reid, A., 2010, Discovery of early Mesoarchean crust in the eastern Gawler Craton, South Australia: Precambrian Research, v. 179, no. 1-4, p. 1-21.

Fraser, G., Reid, A., and Stern, R., 2012, Timing of deformation and exhumation across the Karari Shear Zone, north-western Gawler Craton, South Australia: Australian Journal of Earth Sciences, v. 59, no. 4, p. 547-570.

Fraser, G. L., and Lyons, P., 2006, Timing of Mesoproterozoic tectonic activity in the northwestern Gawler Craton constrained by 40Ar/39Ar geochronology: Precambrian Research, v. 151, no. 3-4, p. 160-184.

Freeman, H., and Tomkinson, M., 2010, Geological setting of iron oxide related mineralisation in the southern Mount Woods Domain, South Australia, Hydrothermal iron oxide copper-gold & related deposits: A global perspective, Volume 3, p. 171-190.

Giles, C. W., 1988, Petrogenesis of the Proterozoic Gawler Range Volcanics, South Australia: Precambrian Research, v. 40-41, p. 407-427.

Giles, D., Betts, P. G., and Lister, G. S., 2004, 1.8–1.5-Ga links between the North and South Australian Cratons and the Early–Middle Proterozoic configuration of Australia: Tectonophysics, v. 380, no. 1, p. 27-41.

Glorie, S., Hand, M., Mulder, J., Simpson, A., Emo Robert, B., Kamber, B., Fernie, N., Nixon, A., and Gilbert, S., 2023, Robust laser ablation Lu–Hf dating of apatite: an empirical evaluation: Geological Society, London, Special Publications, v. 537, no. 1, p. SP537-2022-2205.

Groves, D. I., Bierlein, F. P., Meinert, L. D., and Hitzman, M. W., 2010, Iron Oxide Copper-Gold (IOCG) Deposits through Earth History: Implications for Origin, Lithospheric Setting, and Distinction from Other Epigenetic Iron Oxide Deposits: Economic Geology, v. 105, no. 3, p. 641-654.

Hall, J. W., Glorie, S., Reid, A. J., Boone, S. C., Collins, A. S., and Gleadow, A., 2018, An apatite U–Pb thermal history map for the northern Gawler Craton, South Australia: Geoscience Frontiers, v. 9, no. 5, p. 1293-1308.

Halpin, J. A., and Reid, A. J., 2016, Earliest Paleoproterozoic high-grade metamorphism and orogenesis in the Gawler Craton, South Australia: The southern cousin in the Rae family?: Precambrian Research, v. 276, p. 123-144.

Hand, M., Reid, A., and Jagodzinski, L., 2007, Tectonic framework and evolution of the Gawler craton, southern Australia: Economic Geology, v. 102, no. 8, p. 1377-1395.

Harrison, T. M., 1982, Diffusion of 40Ar in hornblende: Contributions to Mineralogy and Petrology, v. 78, no. 3, p. 324-331.

Harrison, T. M., Duncan, I., and Mcdougall, I., 1985, Diffusion of 40Ar in biotite: temperature, pressure and compositional effects: Geochimica et Cosmochimica Acta, v. 49, no. 11, p. 2461-2468.

Hayward, N., and Skirrow, R., 2010, Geodynamic setting and controls on iron oxide Cu-Au (±U) ore in the Gawler Craton, South Australia: Hydrothermal iron oxide copper-gold and related deposits: A global perspective, v. 3, p. 105-131.

Heinson, G., Didana, Y., Soeffky, P., Thiel, S., and Wise, T., 2018, The crustal geophysical signature of a world-class magmatic mineral system: Scientific Reports, v. 8, no. 1, p. 10608.

Heinson, G. S., Direen, N. G., and Gill, R. M., 2006, Magnetotelluric evidence for a deep-crustal mineralizing system beneath the Olympic Dam iron oxide copper-gold deposit, southern Australia: Geology, v. 34, no. 7, p. 573-576.

Hitzman, M. W., Oreskes, N., and Einaudi, M. T., 1992, Geological characteristics and tectonic setting of Proterozoic iron oxide (Cu-U-Au-REE) deposits: Precambrian Research, v. 58, no. 1, p. 241-287.

Howard, K., Hand, M., Barovich, K., and Belousova, E., 2011a, Provenance of late Paleoproterozoic cover sequences in the central Gawler Craton: exploring stratigraphic correlations in eastern Proterozoic Australia using detrital zircon ages, Hf and Nd isotopic data: Australian Journal of Earth Sciences, v. 58, no. 5, p. 475-500.

Howard, K. E., Hand, M., Barovich, K. M., Payne, J. L., Cutts, K. A., and Belousova, E. A., 2011b, U–Pb zircon, zircon Hf and whole-rock Sm–Nd isotopic constraints on the evolution of Paleoproterozoic rocks in the northern Gawler Craton: Australian Journal of Earth Sciences, v. 58, no. 6, p. 615-638.

Jagodzinski, E., Reid, A., Chalmers, N., Swain, G., Frew, R., and Foudoulis, C., 2007, Compilation of SHRIMP U-Pb geochronological data for the Gawler Craton, South Australia, 2007: South Australian Department of Primary Industries and Resources.

Jagodzinski, E. A., Reid, A. J., Crowley, J. L., Wade, C. E., and Curtis, S., 2023, Precise zircon U-Pb dating of the Mesoproterozoic Gawler large igneous province, South Australia: Results in Geochemistry, v. 10, p. 100020.

Johnson, J. P., and McCulloch, M. T., 1995, Sources of mineralising fluids for the Olympic Dam deposit (South Australia) : Sm Nd isotopic constraints: Chemical Geology, v. 121, no. 1, p. 177-199.

Kirscher, U., Mitchell, R. N., Liu, Y., Nordsvan, A. R., Cox, G. M., Pisarevsky, S. A., Wang, C., Wu, L., Murphy, J. B., and Li, Z.-X., 2020, Paleomagnetic constraints on the duration of the Australia-Laurentia connection in the core of the Nuna supercontinent: Geology, v. 49, no. 2, p. 174-179.

Lawley, C., Selby, D., and Imber, J. J. E. G., 2013, Re-Os molybdenite, pyrite, and chalcopyrite geochronology, lupa goldfield, southwestern Tanzania: tracing metallogenic time scales at midcrustal shear zones hosting orogenic Au deposits, v. 108, no. 7, p. 1591-1613.

McPhie, J., Ehrig, K. J., Kamenetsky, M. B., Crowley, J. L., and Kamenetsky, V. S., 2020, Geology of the Acropolis prospect, South Australia, constrained by high-precision CA-TIMS ages: Australian Journal of Earth Sciences, v. 67, no. 5, p. 699-716.

Morrissey, L., Hand, M., Wade, B., and Szpunar, M., 2013, Early Mesoproterozoic metamorphism in the Barossa Complex, South Australia: links with the eastern margin of Proterozoic Australia: Australian Journal of Earth Sciences, v. 60, no. 8, p. 769-795.

Morrissey, L. J., Barovich, K. M., Hand, M., Howard, K. E., and Payne, J. L., 2019, Magmatism and metamorphism at ca. 1.45 Ga in the northern Gawler Craton: The Australian record of rifting within Nuna (Columbia): Geoscience Frontiers, p. 175-194.

Morrissey, L. J., Payne, J., Hand, M., Clark, C., and Janicki, M., 2023, One billion years of tectonism at the Paleoproterozoic interface of North and South Australia: Precambrian Research, p. under review.

Oliver, R., and Fanning, C., 1997, Australia and Antarctica: precise correlation of Palaeoproterozoic terrains.

Oreskes, N., and Einaudi, M. T., 1992, Origin of hydrothermal fluids at Olympic Dam Preliminary results from fluid inclusions and stable isotopes: Economic Geology, v. 87, p. 64-90.

Payne, J. L., Barovich, K. M., and Hand, M., 2006, Provenance of metasedimentary rocks in the northern Gawler Craton, Australia: Implications for Palaeoproterozoic reconstructions: Precambrian Research, v. 148, no. 3-4, p. 275-291.

Payne, J. L., Ferris, G., Barovich, K. M., and Hand, M., 2010, Pitfalls of classifying ancient magmatic suites with tectonic discrimination diagrams: An example from the Paleoproterozoic Tunkillia Suite, southern Australia: Precambrian Research, v. 177, no. 3-4, p. 227-240.

Payne, J. L., Hand, M., Barovich, K. M., Reid, A., and Evans, D. A. D., 2009, Correlations and reconstruction models for the 2500-1500 Ma evolution of the Mawson Continent: Geological Society, London, Special Publications, v. 323, no. 1, p. 319-355.

Payne, J. L., Hand, M., Barovich, K. M., and Wade, B. P., 2008, Temporal constraints on the timing of high-grade metamorphism in the northern Gawler Craton: implications for assembly of the Australian Proterozoic: Australian Journal of Earth Sciences, v. 55, no. 5, p. 623-640.

Pisarevsky, S. A., Elming, S.-Å., Pesonen, L. J., and Li, Z.-X., 2014, Mesoproterozoic paleogeography: Supercontinent and beyond: Precambrian Research, v. 244, p. 207-225.

Preiss, W., 2000, The Adelaide Geosyncline of South Australia and its significance in Neoproterozoic continental reconstruction: Precambrian Research, v. 100, no. 1-3, p. 21-63.

Reeve, J. S., Cross, K. C., Smith, R. N., and Oreskes, N., 1990, Olympic Dam copper-uranium-gold-silver deposit, *in* Hughes, F. E., ed., Geology of the mineral deposits of Australia and Papua New Guinea: Melbourne, Australasian Institute of Mining and Metallurgy Monograph 14, p. 1009–1035.

Reich, M., Simon, A. C., Deditius, A., Barra, F., Chryssoulis, S., Lagas, G., Tardani, D., Knipping, J., Bilenker, L., Sánchez-Alfaro, P., Roberts, M. P., and Munizaga, R., 2016, Trace element signature of pyrite from the Los Colorados iron oxide-apatite (IOA) deposit, Chile: A missing link between andean IOA and iron oxide copper-gold systems?: Economic Geology, v. 111, no. 3, p. 743-761.

Reid, A., and Fabris, A., 2015, Influence of Preexisting Low Metamorphic Grade Sedimentary successions on the distribution of iron oxide copper-gold mineralisation in the olympic Cu-Au province, Gawler Craton: Economic Geology, v. 110, p. 2147-2157.

Reid, A., and Forster, M., 2021, Mesoproterozoic thermal evolution of the northern Gawler Craton from 40Ar/39Ar geochronology: Precambrian Research, v. 358, p. 106180.

Reid, A. J., Halpin, J. A., and Dutch, R. A., 2019, Timing and style of high-temperature metamorphism across the Western Gawler Craton during the Paleo- to Mesoproterozoic: Australian Journal of Earth Sciences, v. 66, no. 8, p. 1085-1111.

Reid, A. J., and Hand, M., 2012, Mesoarchean to Mesoproterozoic evolution of the southern Gawler Craton, South Australia: Episodes, v. 35, no. 1, p. 216-225.

Reid, A. J., Jagodzinski, E. A., Armit, R. J., Dutch, R. A., Kirkland, C. L., Betts, P. G., and Schaefer, B. F., 2014a, U-Pb and Hf isotopic evidence for Neoarchean and Paleoproterozoic basement in the buried northern Gawler Craton, South Australia: Precambrian Research, v. 250, p. 127-142.

Reid, A. J., Jagodzinski, E. A., Fraser, G. L., and Pawley, M. J., 2014b, SHRIMP U–Pb zircon age constraints on the tectonics of the Neoarchean to early Paleoproterozoic transition within the Mulgathing Complex, Gawler Craton, South Australia: Precambrian Research, v. 250, p. 27-49.

Rey, P. F., Teyssier, C., Kruckenberg, S. C., and Whitney, D. L., 2011, Viscous collision in channel explains double domes in metamorphic core complexes: Geology, v. 39, no. 4, p. 387-390.

Schlegel, T. U., Wagner, T., Wälle, M., and Heinrich, C. A., 2018, Hematite Breccia-Hosted Iron Oxide Copper-Gold Deposits Require Magmatic Fluid Components Exposed to Atmospheric Oxidation: Evidence from Prominent Hill, Gawler Craton, South Australia: Economic Geology, v. 113, no. 3, p. 597-644.

Searle, M. P., and Lamont, T. N., 2020, Compressional metamorphic core complexes, low-angle normal faults and extensional fabrics in compressional tectonic settings: Geological Magazine, v. 157, no. 1, p. 101-118.

Simon, A. C., Knipping, J., Reich, M., Barra, F., Deditius, A. P., Bilenker, L., and Childress, T., 2018, Kiruna-type iron oxide-apatite (IOA) and iron oxide copper-gold (IOCG) deposits form by a combination of igneous and magmatic-hydrothermal processes: Evidence from the Chilean iron belt.

Skirrow, R. G., 2022, Iron oxide copper-gold (IOCG) deposits – A review (part 1): Settings, mineralogy, ore geochemistry and classification: Ore Geology Reviews, v. 140, p. 104569.

Skirrow, R. G., Bastrakov, E. N., Baroncii, K., Fraser, G. L., Creaser, R. A., Fanning, C. M., Raymond, O. L., and Davidson, G. J., 2007, Timing of iron oxide Cu-Au-(U) hydrothermal activity and Nd isotope constraints on metal sources in the Gawler craton, south Australia: Economic Geology, v. 102, no. 8, p. 1441-1470.

Skirrow, R. G., van der Wielen, S. E., Champion, D. C., Czarnota, K., and Thiel, S., 2018, Lithospheric Architecture and Mantle Metasomatism Linked to Iron Oxide Cu-Au Ore Formation: Multidisciplinary Evidence from the Olympic Dam Region, South Australia: Geochemistry, Geophysics, Geosystems, v. 19, no. 8, p. 2673-2705.

Swain, G., Barovich, K., Hand, M., Ferris, G., and Schwarz, M., 2008, Petrogenesis of the St Peter Suite, southern Australia: Arc magmatism and Proterozoic crustal growth of the South Australian Craton: Precambrian Research, v. 166, no. 1-4, p. 283-296.

Szpunar, M., Hand, M., Barovich, K., Jagodzinski, E., and Belousova, E., 2011, Isotopic and geochemical constraints on the Paleoproterozoic Hutchison Group, southern Australia: Implications for Paleoproterozoic continental reconstructions: Precambrian Research, v. 187, no. 1-2, p. 99-126.

Teyssier, C., and Whitney, D. L., 2002, Gneiss domes and orogeny: Geology, v. 30, no. 12, p. 1139-1142.

Verdugo-Ihl, M. R., Ciobanu, C. L., Cook, N. J., Ehrig, K. J., and Courtney-Davies, L., 2020, Defining early stages of IOCG systems: evidence from iron oxides in the outer shell of the Olympic Dam deposit, South Australia: Mineralium Deposita, v. 55, no. 3, p. 429-452.

Wade, C. E., Payne, J. L., Barovich, K. M., and Reid, A. J., 2019, Heterogeneity of the sub-continental lithospheric mantle and 'non-juvenile' mantle additions to a Proterozoic silicic large igneous province: Lithos, v. 340-341, p. 87-107.

Wade, C. E., Payne, J. L., Barovich, K., Gilbert, S., Wade, B. P., Crowley, J. L., Reid, A., and Jagodzinski, E. A., 2022, Zircon trace element geochemistry as an indicator of magma fertility in iron oxide copper-gold provinces: Economic Geology, v. 117, p. 703-718.

Williams, P., 2010, Classifying IOCG deposits, *in* Corriveau, L., and Mumin, H., eds., Exploring for Iron Oxide Copper-gold Deposits: Canada and Global Analogues. Geological Association of Canada, Short Course Notes, Volume 20, p. 3–21.

Williams, P. J., Barton, M. D., Johnson, D. A., Fontboté, L., De Haller, A., Mark, G., Oliver, N. H., and Marschik, R., 2005, Iron oxide copper-gold deposits: Geology, space-time distribution, and possible modes of origin: Economic Geology, p. 371-405.

Yin, A., 2004, Gneiss domes and gneiss dome systems: Geological Society of America Special Papers, v. 380, p. 1-14.

Chapter 2

The Fe-Cu disconnect: unravelling a composite IOCG deposit in the Olympic Fe-Cu-Au Province, Gawler Craton

Published in Economic Geology

https://doi.org/10.5382/econgeo.5037

Statement of Authorship

Title of Paper	The Fe-Cu disconnect: unravelling a composite IOCG deposit in the Olympic Fe-Cu-Au Province, Gawler Craton
Publication Status	☐ Published ☑ Accepted for Publication ☐ Submitted for Publication ☐ Unpublished and Unsubmitted work written in manuscript style
Publication Details	Yu, J., Morrissey, L., Hand, M., Payne, J., Chen, Y.J. 2023. The Fe-Cu disconnect: unravelling a composite IOCG deposit in the Olympic Fe-Cu-Au Province, Gawler Craton. Economic Gelogy, in press.

Principal Author

Name of Principal Author (Candidate)	Jie Yu		
Contribution to the Paper	Field work Data collection and modelling Manuscript writing		
Overall percentage (%)	70		
Certification:	This paper reports on original research I conducted during the period of my Higher Degree by Research candidature and is not subject to any obligations or contractual agreements with a third party that would constrain its inclusion in this thesis. I am the primary author of this paper.		
Signature		Date	04 April 2023

Co-Author Contributions

By signing the Statement of Authorship, each author certifies that:

i. the candidate's stated contribution to the publication is accurate (as detailed above);

ii. permission is granted for the candidate in include the publication in the thesis; and

iii. the sum of all co-author contributions is equal to 100% less the candidate's stated contribution.

Name of Co-Author	Laura Morrissey		
Contribution to the Paper	Field work Manuscript editing Ideas for manuscript		
Signature		Date	04 April 2023

Name of Co-Author	Martin Hand		
Contribution to the Paper	Manuscript editing Ideas for manuscript		
Signature		Date	04 April 2023

Name of Co-Author	Justin Payne		
Contribution to the Paper	Field work Manuscript editing Ideas for manuscript		
Signature		Date	04 April 2023

Name of Co-Author	Yan-Jing Chen		
Contribution to the Paper	Manuscript editing Ideas for manuscript Data collection		
Signature		Date	04 April 2023

Please cut and paste additional co-author panels here as required.

Abstract:

The northern Olympic Cu-Au Province, Gawler Craton, Australia, includes a series of magnetite-dominated deposits/prospects associated with minor Cu-Au mineralisation such as the 8.37 Mt Cairn Hill deposit. Cairn Hill has long been considered a deep, magnetite end-member of the IOCG family that is largely represented in the southern Olympic Province by the 1590 Ma hematite-dominated Olympic Dam, Carrapeteena and Prominent Hill deposits. In contrast to the southern district, the deposits in the northern Olympic Cu-Au Province are hosted in rocks that experienced multiple phases of high temperature metamorphism and deformation. New U-Pb zircon geochronology shows the magnetite-hornblende lodes at Cairn Hill were formed at ca. 1580 Ma at amphibolite facies conditions. The magnetite lodes are cross-cut by ca. 1515 Ma granitic dykes. A second high temperature event is recorded by U-Pb monazite geochronology at ca. 1490 Ma, and involved deformation and metamorphism along the Cairn Hill shear zone at conditions of 4.6–5.3 kbar and 740–770 °C. The 1490 Ma event reworked the iron lodes and 1515 Ma granitic dykes. However, Cu mineralisation at Cairn Hill occurs in brittle fractures and quartz-biotite veins, overprinting the 1490 Ma deformation and metamorphism. Despite a spatial association between magnetite and Cu, the long thermal history that affected magnetite mineralisation and the clear petrographic links between magnetite and high temperature granulite facies minerals contrasts with the late, low temperature hydrothermal Cu mineralisation and indicates the two are not paragenetically related. Therefore, the spatial but not temporal association between magnetite and Cu has effectively overlain two distinct episodes of mineralisation to create the Fe-Cu deposit observed today. Although this fits within the broad IOCG deposit family, exploration strategies for Cairn Hill-style composite deposits should be distinct from IOCG deposits with co-genetic Fe and Cu.

Keywords: Gawler Craton, Olympic IOCG, U-Pb geochronology, granulite, metamorphism

1. Introduction

The Gawler Craton, South Australia, contains an extensive record of Mesoproterozoic mineralisation in the central and eastern Gawler Craton. In the eastern Gawler Craton, the Olympic Cu-Au Province includes the Olympic Dam, Prominent Hill and Carrapateena iron oxide–copper–gold (IOCG) deposits, as well as numerous historic mines and prospects (Fig. 2.1; e.g., Reeve et al., 1990; Belperio et al., 2007; Skirrow et al., 2007; Reid and Fabris, 2015). Most of these deposits are hematite-dominated and commonly contain economic gold and usually sub-economic uranium and rare earth element mineralisation. The deposits formed between ca. 1595–1575 Ma, coeval with voluminous magmatism of the Hiltaba Suite and Gawler Range Volcanics (GRV) (e.g., Bowden et al., 2017; Cherry et al., 2018; Courtney-Davies et al.,

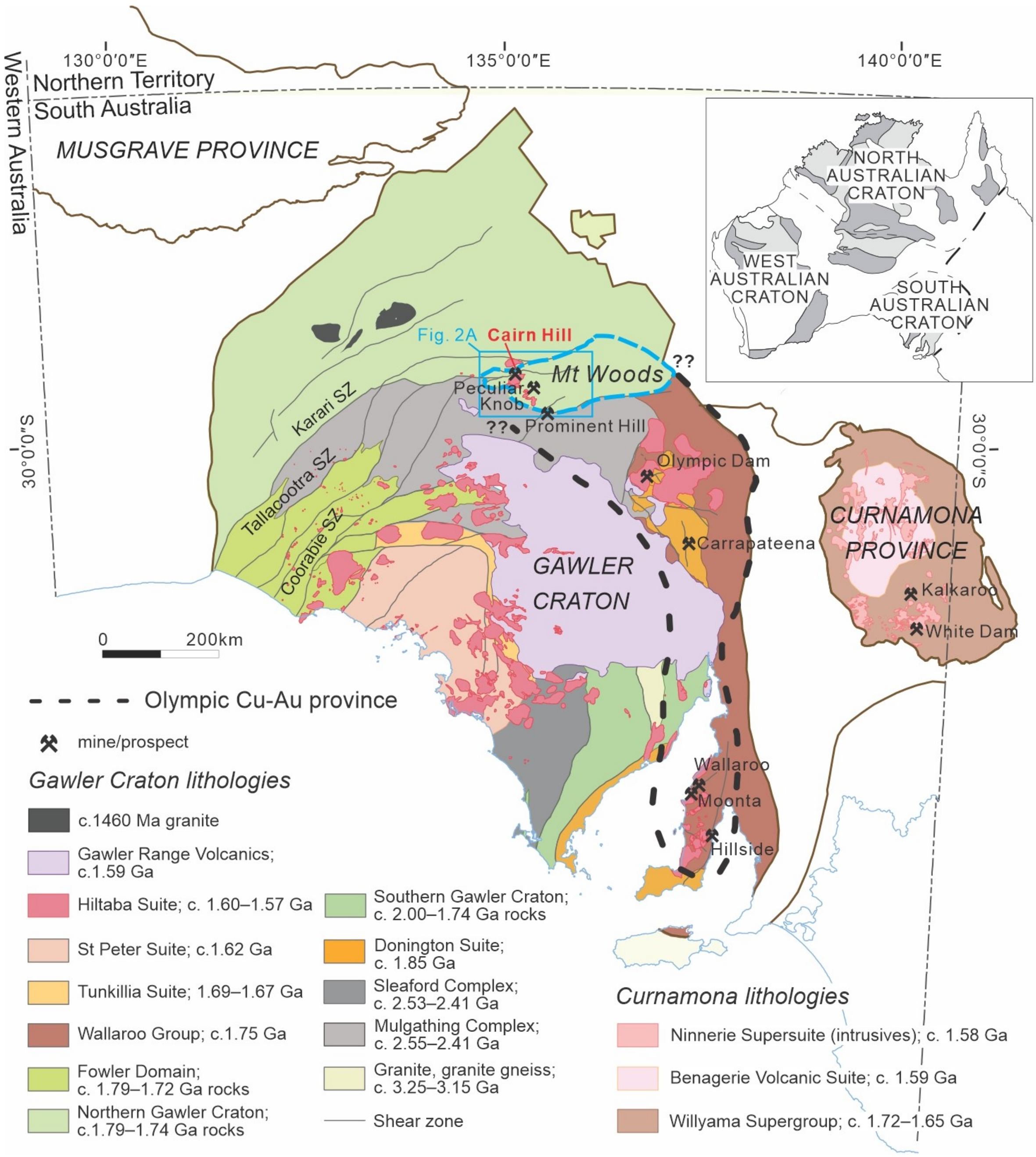

Figure 2.1 Simplified solid geology map of the Gawler Craton, showing the location of Mount Woods and Cairn Hill deposit (red) in the northern Olympic Cu-Au Province, with respect to other IOCG deposits (after Reid et al., 2014). The northern margin of the Olympic Domain is poorly constrained.

2020; McPhie et al., 2020). In the north of the currently defined Olympic Cu-Au Province is the poorly exposed Mount Woods Domain, which is a shear-bound domain comprising amphibolite to granulite-facies rocks intruded by Hiltaba-equivalent granites and gabbros (Jagodzinski et al., 2007; Morrissey et al., 2023). This region hosts the Cairn Hill Fe (-Cu-Au) deposit and numerous magnetite-dominated prospects such as Snaefell, Manxman, and Joe's Dam (Fig. 2.2A; Chalmers, 2007; Freeman and Tomkinson, 2010). The magnetite dominated Fe ± Cu deposits/prospects within the Mount Woods Domain differ from the hematite-dominated IOCG deposits located south of the Southern Overthrust, which represents the southern boundary of the Mount Woods Domain (Fig. 2.2A). These magnetite deposits/prospects are suggested to represent the deep expression of the Olympic IOCG system (Reid, 2019) without the subsequent upgrading by oxidizing, lower temperature fluids associated with the classic Olympic Dam hematite stage (Oreskes and Einaudi, 1992; Bastrakov et al., 2007). The age and petrogenesis of the magnetite-dominated deposits in the Mount Woods Domain is poorly known, in contrast to the well-defined mineralisation window for Olympic Dam and surrounding deposits (Cherry et al., 2018; Courtney-Davies et al., 2020; McPhie et al., 2020).

The Cairn Hill Fe (-Cu-Au) deposit is hosted in high-grade metamorphic rocks in the northernmost Olympic Cu-Au Province (Fig. 2.1). It was discovered in 2005 and has a current indicated resource of 3.77 Mt @ 47.8% Fe and inferred resource of 4.6 Mt @ 45.8% Fe (Cairn Hill Mine Mining Compliance Report 2021). The overall Cu grade is 0.03%, and Au grade is 0.005 g/t, making Cairn Hill a potential example of a magnetite-dominant IOCG deposit (Reid, 2019). Hitherto, there has been little constraint on the metamorphic history and timing of Fe ± Cu mineralisation in the deposit. This has limited our understanding of how it may fit into the regional IOCG framework. This study presents zircon and monazite LA-ICP-MS U-Pb geochronology, combined with detailed petrology and calculated metamorphic phase equilibria. The new data constrain the timing of metamorphism and mineralisation in the northern Olympic Cu-Au Province, and identify a new timeline for Cu mineralisation. The superposition of a younger Cu system on older iron mineralisation has created a composite IOCG deposit in the Gawler Craton, which has implications for exploration using a mineral systems approach (Wyborn et al., 1994; McCuaig et al., 2010; Skirrow et al., 2019).

2. Geological Setting

The Gawler Craton consists of an Archean to earliest Paleoproterozoic nucleus surrounded by Proterozoic orogenic belts (Fig. 2.1; Hand et al., 2007; Fraser et al., 2010). From ca. 2000 to 1730 Ma, a series of volcano-sedimentary and metasedimentary rocks were deposited across the Gawler Craton (Reid and Hand, 2012). Widespread sedimentation was succeeded by the Kimban Orogeny (ca. 1730–1690 Ma), which was associated with widespread metamorphism, magmatism, development of crustal-scale shear zones, and localized sedimentation (Hand et al., 2007; Payne et al., 2008, 2010; Howard et al., 2011). Following the Kimban Orogeny, the evolution of the Gawler Craton was dominated by magmatism, including the arc-related St Peter Suite in the southern Gawler Craton (ca. 1620 Ma; Reid et al., 2019), and the early Mesoproterozoic GRV (1594–1586 Ma) and coeval Hiltaba Suite granites (1600–1570 Ma; Jagozdinski et al., 2023). The Hiltaba–GRV magmatism is temporally and spatially associated with IOCG mineralisation in the Olympic Domain in the eastern Gawler Craton. Mineralisation has been precisely dated to 1594–1592 at Olympic Dam (Fig. 2.1; Cherry et al., 2018; Courtney-Davies et al., 2020) but most IOCG ore bodies have imprecise geochronological constraints (e.g., Skirrow et al., 2007; Bowden et al., 2017; McPhie et al 2020).

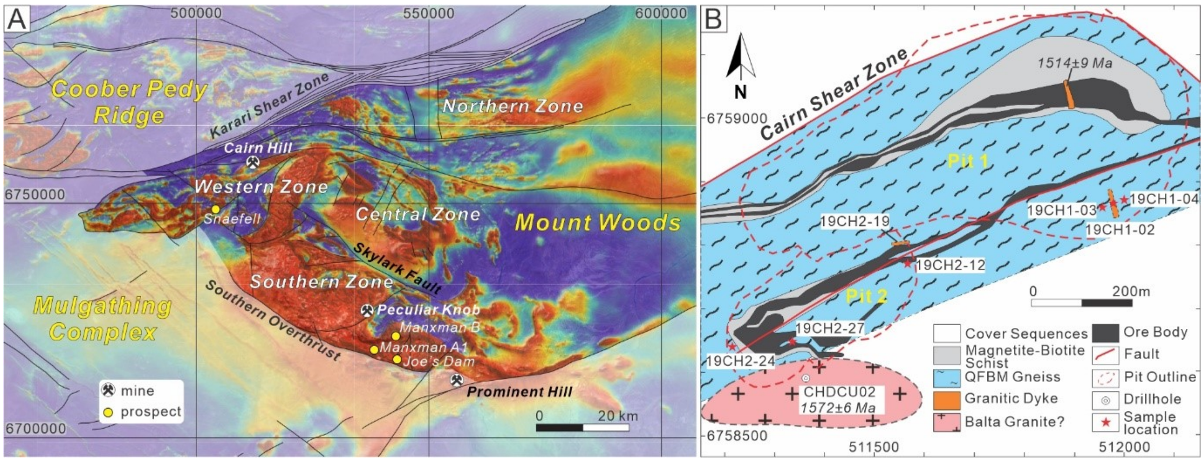

Fig. 2.2 (A) Total Magnetic Intensity (stacked reduced to pole and reduced to pole tilt) image of the Mount Woods Domain. TMI and shear zone interpretation from South Australian Resources Information Gateway (SARIG; https://map.sarig.sa.gov.au/). Geophysical zone interpretation after Morrissey et al. (2023); (B) Interpreted geology map of the Cairn Hill deposit (modified after Clark, 2014 and Jagodzinski and Reid, 2015).

The northern and southeastern Gawler Craton underwent widespread deformation and high-temperature metamorphism at ca. 1600–1540 Ma (Hand et al., 2007; Payne et al., 2008; Cutts et al., 2011; Bockmann et al., 2022). Subsequent events are limited to localized ca. 1520 Ma metamorphism in the northern Gawler Craton (Reid et al., 2014), minor magmatism at ca. 1500 Ma in the southern Gawler Craton (Jagodzinski et al., 2007) and localized ca. 1460 Ma magmatism, metamorphism, alteration and shear zone reactivation in the northern Gawler Craton (Fraser and Lyons, 2006; Fraser et al., 2012; Morrissey et al., 2019; Bockmann et al., 2023). Neoproterozoic and Phanerozoic sediments overlie much of the stable craton (Preiss, 2000).

The Mount Woods Domain is an aeromagnetically-defined region in the northern Gawler Craton that is bound to the north by the Karari Shear Zone and to the south by the Southern Overthrust (Fig. 2.1 and 2.2A). The Mount Woods Domain is divided into a series of subdomains (zones) separated by major shear zones (Fig. 2.2A). The oldest rocks in the region occur in the central zone and comprise metasedimentary rocks and garnet-bearing granite with protolith ages of ca. 2500–2400 Ma and ca. 1850 Ma (Tiddy et al., 2020; Morrissey et al., 2023). These units were deformed and metamorphosed at granulite facies conditions between ca. 1700–1670 Ma, coeval with felsic magmatism (Betts et al., 2003; Morrissey et al., 2023). In the southern zone, the Archean to Paleoproterozoic basement is overlain by metasedimentary rocks of the Skylark Metasediments and Coodnambana Metaconglomerate, which were deposited after ca. 1750 Ma (Jagodzinski et al., 2007; Tiddy et al., 2020; Morrissey et al., 2023). Felsic gneiss with a magmatic age of 1742 ± 27 Ma is identified in the southern zone (Fanning et al., 1988). Mafic and felsic intrusive rocks of the Balta Granite Suite (ca. 1595–1575 Ma) occur in the southern and western zones (Jagodzinski, 2005; Jagodzinski et al., 2007), and are equivalent to the Hiltaba Suite. The southern and western zones record amphibolite facies conditions coeval with the emplacement of the Balta Granite Suite

(Jagodzinski et al., 2007). Major shear zones and the westernmost Mount Woods Domain record upper amphibolite facies metamorphism and reworking at 1570–1550 Ma, with a further phase of shear zone activity along the northern margin at ca. 1480 Ma (Morrissey et al., 2023). Apatite U-Pb, biotite ^{40}Ar-^{39}Ar and biotite Rb-Sr ages range from ca. 1560 to 1390 Ma (Forbes et al., 2012; Fraser et al., 2012; Hall et al., 2018; Tiddy et al., 2020; Morrissey et al., 2023).

The Mount Woods Domain is adjacent to the highly mineralized Olympic Cu-Au Domain and hosts numerous Fe ± Cu deposits/prospects, including Cairn Hill, Peculiar Knob, Manxman, Joe's Dam, and Snaefell (Fig. 2.1 and 2.2A; Freeman and Tomkinson, 2010; Reid and Fabris, 2015). Among them, Cairn Hill, Manxman and Joe's Dam host low-grade copper-gold mineralisation associated with abundant magnetite alteration. The hematite breccia-hosted Prominent Hill deposit, despite often being included in the Mount Woods area, is located immediately south of the boundary fault Southern Overthrust and is hosted in low metamorphic grade rocks (Betts et al., 2003; Schlegel et al., 2018).

3. Deposit Geology

Cairn Hill, dominated by magnetite with minor Cu-Au, is a crucial Fe deposit on the northern boundary of the Olympic Cu-Au Province. It is located 55 km southeast of Coober Pedy (Fig. 2.1; Clark, 2014). It is located at the westernmost end of a prominent 15 km long, east-west trending, linear, aeromagnetic anomaly on the northwestern margin of the Olympic Cu-Au Province and sits within the Cairn Hill Shear Zone, interpreted to be a splay of the Karari Shear Zone (Fig. 2.1 and 2.2). Recent exploration shows that the Cu-Au mineralisation occurs only in the westernmost kilometer at Cairn Hill (Jagodzinski and Reid, 2015).

The predominant host rock at the mine site is a quartz-feldspar-biotite-magnetite gneiss (Fig. 2.3A–E). It has a foliation defined by biotite and magnetite, trending E–W coincident with the Cairn Hill Shear Zone (Fig. 2.2B). Rare garnet-bearing metasedimentary gneisses are observed in Pit 1 (19CH1-03, Fig. 2.3C). A quartzofeldspathic gneiss with a zircon U-Pb SHRIMP age of 1572 ± 6 Ma was intersected in drill hole south of Pit 2 (Fig. 2.2B; Jagodzinski and Reid, 2015). It is interpreted to be part of the Hiltaba-equivalent Balta Granite suite, and its boundary with the quartz-feldspar-biotite-magnetite gneiss remains unclear.

The iron mineralisation is predominantly comprised of two ~10 m wide, near-vertical, sub-parallel magnetite-apatite lodes (Fig. 2.2B, 2.3A). The Northern Lode is the thickest and focus of Pit 1, and the magnetite unit reaches a maximum width of 40 m at the eastern portion of Pit 1. It dips to the south and is pinched off to the east by a tight fold and sheared southern limb. The Southern Lode is sub-parallel to the Northern Lode and thickens to the west, hosting the magnetite resource of Pit 2. Both iron lodes are composed of coarse magnetite-apatite-hornblende (-albite) veins, with coarse-grained magnetite and apatite growing in the center, and alteration halos of hornblende and minor albite

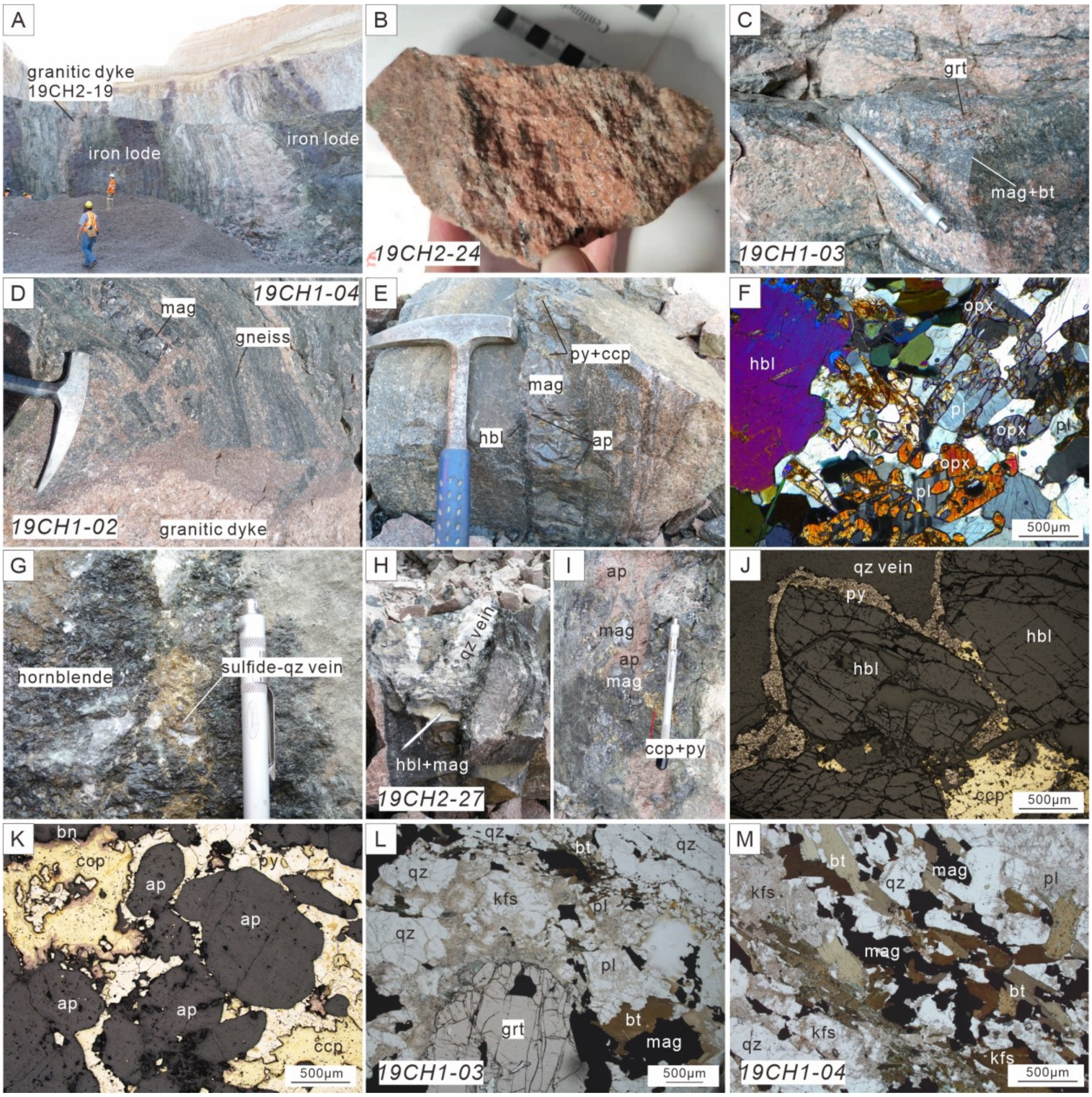

Fig. 2.3 Representative rock types from Cairn Hill used in this study. (A) Massive magnetite lodes in Cairn Hill Pit 2; (B) felsic gneiss 19CH2-24 from wall rock of Pit 2; (C) garnet-bearing metapelite 19CH1-03 in Pit 1; (D) granitic dyke (19CH1-02) crosscutting the magnetite-rich gneiss (19CH1-04); (E) typical occurrence of magnetite-apatite-hornblende band, parallel to the foliation of the gneiss; (F) hornblende metamorphosed to orthopyroxene-plagioclase, sample 19CH1-06, cross polarized light; (G) sulfide-quartz vein crosscutting hornblende; (H) sulfide-quartz vein infills in hornblende-magnetite band; (I) late copper mineralisation superimposed on the early magnetite-apatite-hornblende assemblage; (J) pyrite and chalcopyrite rims and encases hornblende, with void-filled quartz, sample 19CH2-27, reflected light; (K) sulfides infill the interval of early apatite, with bornite on the oxidized chalcopyrite, sample 19CH2-22, reflected light; (L) photomicrograph of garnet-bearing metapelite of sample 19CH1-03, plane polarized light; (M) photomicrograph of magnetite-rich gneiss 19CH1-04, plane polarized light. The mineral abbreviations used are those of Whitney and Evans (2010).

developing symmetrically on both flanks (Fig. 2.3A and E). Numerous cm- to dm-scale magnetite-apatite-hornblende (-albite) veins occur in the gneissic wall rock and share similar alteration, texture and orientation to the two major iron lodes (Fig. 2.3A and D). Hematite is rare at Cairn Hill and is commonly formed by the later oxidation of magnetite. Hornblende is locally metamorphosed to orthopyroxene-plagioclase (Fig. 2.3F) or orthopyroxene-clinopyroxene. A foliated granite dyke that crosscuts the northern magnetite lode yielded an interpreted magmatic age of 1514 ± 9 Ma (Fig. 2.2B; Jagodzinski and Reid, 2015), providing a lower age limit for magnetite mineralisation. The northern edge of the granite dyke is stretched into parallelism with the sheared host rocks, indicating ductile deformation after its emplacement.

Early magnetite-apatite alteration is overprinted by Cu (-Au) mineralisation. The chalcopyrite- pyrite (-pyrrhotite-bornite-sphalerite) assemblage occurs along intervals of brecciated magnetite-apatite or occurs as sulfide-quartz-biotite veins that crosscut the magnetite lodes and gneiss (Fig. 2.3G–K). Quartz veins appear to fill brittle fractures in the magnetite-apatite-hornblende (-albite) veins and the host gneiss. Pyrite and chalcopyrite rims and encases hornblende with textures consistent with void-fill synchronous with quartz crystallization. Hydrothermal alteration during the Cu mineralisation stage resulted in the formation of biotite, chlorite, siderite and calcite. Chlorite partially replaces the hydrothermal biotite and encloses the sulfides. Early transparent apatite was also altered during the infiltration of Cu-bearing fluids, forming pink apatite (Fig. 2.3I).

Hornblende $^{40}Ar/^{39}Ar$ (1492 ± 6 Ma), apatite U-Pb (1466 ± 5 Ma), and phlogopite $^{40}Ar/^{39}Ar$ (1462 ± 5 Ma) ages have been reported by Jagodzinski and Reid (2015), and these ages are all interpreted as cooling ages.

4. Samples and Results

4.1 Sample description and petrography

Three samples were analyzed for U-Pb zircon geochronology: 19CH2-24, 19CH2-27 and 19CH2-19 (Table 1). Sample 19CH2-24 is a medium- to coarse-grained gneiss that hosts magnetite mineralisation within Pit 2 (Fig. 2.3B). It contains K-feldspar, quartz, plagioclase and biotite and was interpreted to be an orthogneiss from field observations due to its homogenous nature in outcrop, but this interpretation is equivocal due to overprinting metamorphism and deformation. Sample 19CH2-27 is a hornblende selvage sampled from the edge of the coarse hornblende-magnetite vein (Fig. 2.3H). Sample 19CH2-19 is a medium-grained granitic dyke that cross-cuts mineralisation and a gneissic fabric but is also deformed and rotated into parallelism with a later shear foliation (Fig. 2.3A). It contains K-feldspar, quartz, and plagioclase with minor biotite and magnetite.

Five samples were selected for monazite U-Pb geochronology and all display evidence of at least one foliation (Table 1). Sample 19CH1-03 is granulite facies metasedimentary rock sampled from the south side of Pit 1 (Fig. 2.3C), close to sample 19CH1-04. The sample is mineralogically heterogeneous, with biotite and plagioclase-rich domains surrounding a garnet domain (Fig. 2.3L). The garnet domain contains a mineral assemblage of garnet, biotite, quartz, magnetite and ilmenite with minor K-feldspar and pinnitized cordierite. The garnet grains are up to 2–4 cm, and contain inclusions of biotite, quartz, magnetite and monazite. The biotite and plagioclase-rich

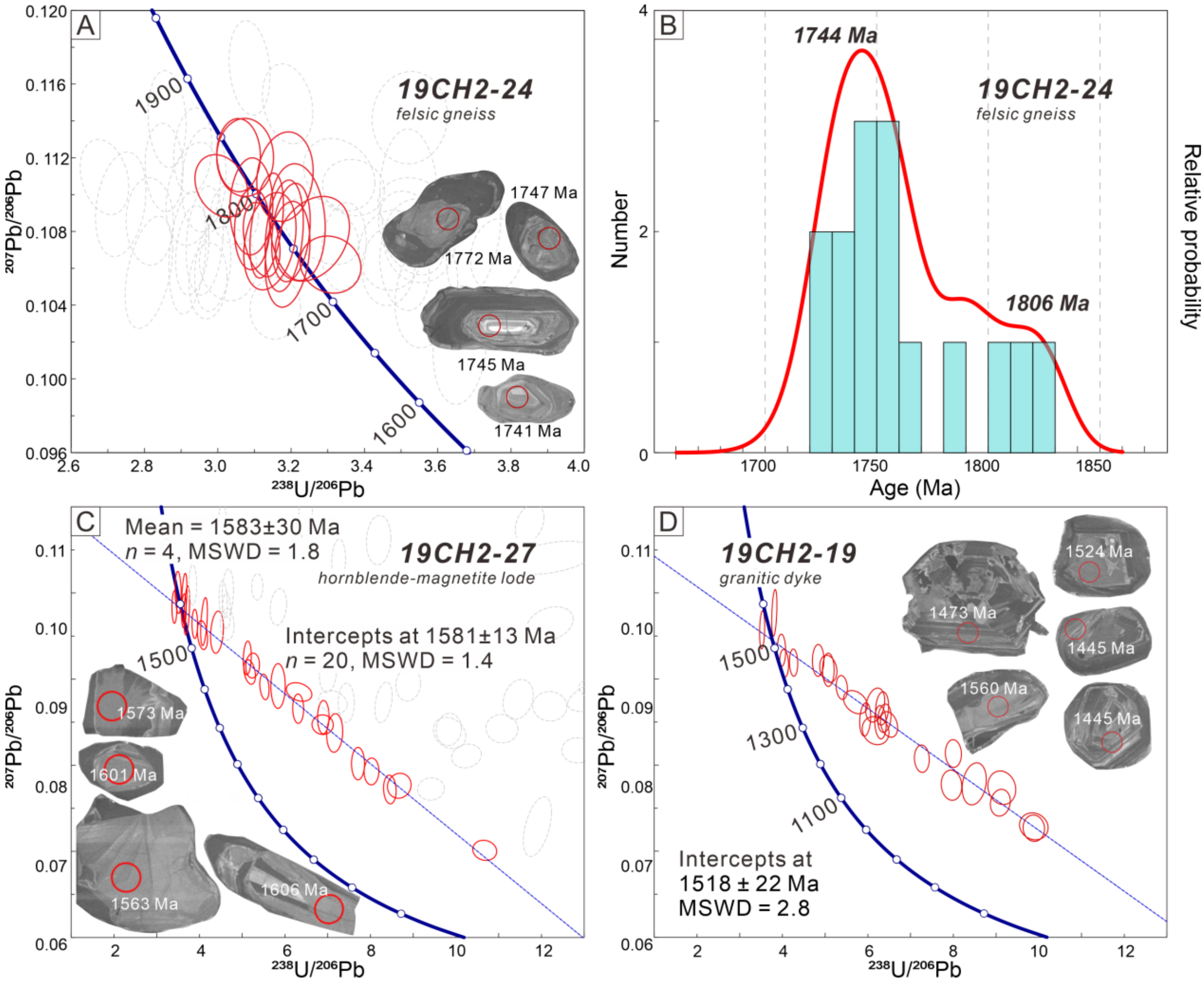

Fig. 2.4 Zircon geochronology results from Cairn Hill. (A and B) sample 19CH2-24, (C) sample 19CH2-27, and (D) sample 19CH2-19. Representative CL images of zircons analysed in this study depicting analysis locations (red circles) and corresponding $^{207}Pb/^{206}Pb$ age. Analyses not used for weighted mean age or errorchron calculations are shown as grey dashed circles on the concordia plots. The probability density plot in (B) is calculated using only concordant analyses.

domain is composed of biotite, quartz, K-feldspar, plagioclase, magnetite and ilmenite. It has a foliation defined by biotite and elongated magnetite, parallel to the gneissic fabric. Some biotite in this sample is altered to chlorite, and some feldspar is replaced by mica. This sample is modified by later shear deformation, with growth of fine-grained quartz, biotite and magnetite. Sample 19CH1-04 is a biotite-K-feldspar-plagioclase-quartz-magnetite-ilmenite gneiss (Fig. 2.3D and M) which is cross-cut by the granitic dyke represented by sample 19CH1-02 (Fig. 2.3D). Sample 19CH2-12 is a migmatitic gneiss with a similar mineral assemblage to 19CH1-04 and a 2–8 cm wide leucosome domain comprised of coarse-grained K-feldspar and quartz with minor biotite and magnetite. Detailed descriptions for all samples are provided in Supplementary materials.

4.2 Zircon and monazite U-Pb geochronology

The LA-ICP-MS U-Pb geochronology and trace element analyses were carried out at Adelaide Microscopy, the University of Adelaide,

Table 1 Summary of U-Pb geochronology samples.

Sample no.	Sample description	Zircon age ± 2σ (Ma)	Monazite age ± 2σ (Ma)	Age type	in situ /grain mount
Pit 2					
19CH2-24	qz-feldspar-bt-mag gneiss	ca. 1740		Magmatic/max. dep.	mount
19CH2-27	hbl-mag vein	1583 ± 30 1581 ± 13		Metamorphic	mount
19CH2-19	cross-cutting granitic dyke	1518 ± 22		Magmatic	mount
19CH2-12	qz-feldspar-bt-mag migmatitic gneiss		1587 ± 18 1494 ± 5	Metamorphic	in situ
Pit 1					
19CH1-03	Metasedimentary gneiss grt-qz-feldspar-crd-bt-mag gneiss		1620–1450 1489 ± 8	Metamorphic	in situ
19CH1-04	qz-feldspar-bt-mag gneiss		1568 ± 6 1487 ± 4	Metamorphic	in situ
19CH1-02	cross-cutting granitic dyke		1493 ± 6	Metamorphic	mount

Australia. The detailed methods and geochronology data are provided in Supplementary materials, Table A1 and A2. Sample 19CH2-24 yielded 50 viable analyses from zircon cores, of which 15 analyses are concordant (Fig. 2.4A). The 15 analyses do not form a single statistically valid age and instead yield dates of ca. 1830–1725 Ma, with a major peak at ca. 1740 Ma and a minor peak at ca. 1800 Ma (Fig. 2.4B). This range may indicate an igneous protolith that incorporated xenocrystic zircon from surrounding rocks, or that the protolith was a sedimentary rock. For the purposes of this study we assign an age of ca. 1740 Ma to the sample with the proviso that this may be an igneous protolith age or a maximum depositional age of the host rock to mineralisation. All analyses of dark rims on the zircon grains failed to produce usable signals.

Zircon grains separated from the hornblende selvage sample 19CH2-27 typically show a bright core overgrown by homogenous dark rims in CL images (Fig. 2.4C). The cores mostly show indistinct zoning that varies between sector, oscillatory or convolute zoning. Seventy-three analyses were made on 69 grains, with most analyses showing discordance related to a combination of Pb loss and common Pb. Only four analyses are concordant and these yield a statistically valid weighted mean $^{207}Pb/^{206}Pb$ age of 1583 ± 30 Ma (n = 4, MSWD = 1.8). Analyses with common Pb levels less than or equal to the concordant analyses (Fig. 2.4C) yield an errorchron with an upper intercept of 1581 ± 13 Ma (n = 20, MSWD = 1.4). The similarity in results indicates the age obtained from the concordant analyses is likely to be a valid age for the sample, and 1583 ± 30 Ma is thus taken to be the age of zircon cores within this sample.

In sample 19CH2-19, zircon grains are dark brown and 40–200 μm in length. In CL images, most grains display oscillatory zoned cores surrounded by dark, featureless rims (Fig. 2.4D). Rare oscillatory zoned cores contain a relict inner core with complex zoning that is too small to analyze. Seventy-two analyses were attempted on

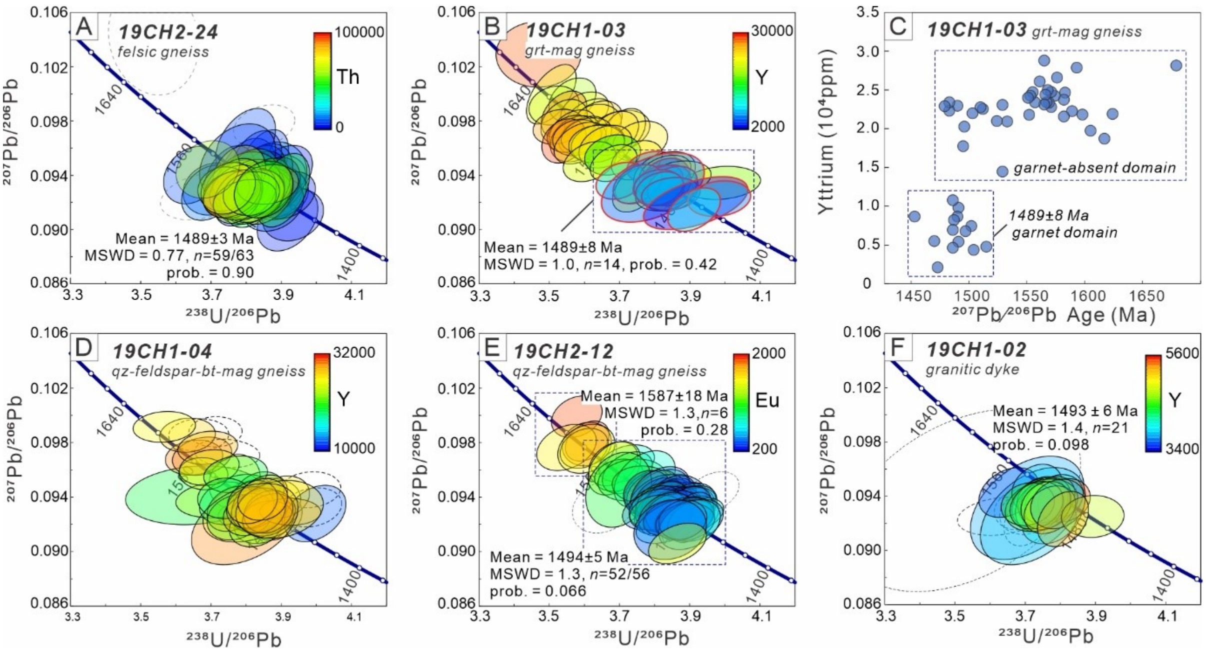

Fig. 2.5 Monazite geochronology data from Cairn Hill. Concordant ellipses are coloured for concentrations of elements of interest in each sample, with discordant analyses shown as dashed circles. (A) sample 19CH2-24, (B and C) sample 19CH1-03, with analyses from the garnet-bearing domain outlined in red within the dashed box, (D) sample 19CH1-04, (E) sample 19CH2-12, two age populations defined by variations in Eu content are highlighted by dashed boxes, (F) sample 19CH1-02.

the oscillatory zoned cores but only 25 were successful. These yield an upper intercept age of 1518 ± 22 Ma (n = 25, MSWD = 2.8). A single statistical population cannot be obtained without extensive culling of data, but the obtained errorchron age is sufficient for the purposes of this study.

Monazite from sample 19CH2-24 yield a weighted mean age of 1489 ± 3 Ma (n = 59, MSWD = 0.77) with an older discordant analysis at 1590 ± 20 Ma and one at 1692 ± 57 Ma (Fig. 2.5A). Samples 19CH1-03, 19CH1-04 and 19CH2-12 record a smear of concordant monazite dates from ca. 1620 Ma to ca. 1490 Ma and a range in monazite trace element compositions (Fig. 2.5 and Table A2). Sample 19CH1-03 contains two monazite groups that can be distinguished based on Y + HREE contents (Fig. 2.5B and C, Table A2). Monazite from the garnet-bearing domain has distinctly lower Y contents and defines a weighted mean age of 1489 ± 8 Ma (n = 14, MSWD = 1.0). Monazite from the garnet-absent domain contains higher Y contents and ranges in age from ca. 1620–1450 Ma, with one older concordant analysis at ca. 1679 Ma. In sample 19CH1-04 it is not possible to obtain discrete age populations based on monazite compositions, BSE images or microstructural location, however, two age populations of ca. 1580 Ma and ca. 1490 Ma are supported by the Unmix function within Isoplot 4.15 (Fig. 2.5D). Sample 19CH2-12 contains a population of monazite with high Eu concentrations that define a weighted mean age of 1587 ± 18 Ma (n = 6, MSWD = 1.3), whereas the remaining analyses yield a weighted mean age of 1494 ± 5 Ma (n = 52/56, MSWD = 1.3, Fig. 2.5E). Sample 19CH1-02 is a granitic dyke that cross-cuts the magnetite mineralisation and records a single monazite age population with a weighted mean age of 1493 ± 6 Ma (n = 21, MSWD = 1.4, Fig. 2.5F).

4.3 Phase pseudosection modeling

P–T pseudosection modeling was undertaken using GeoPS (Xiang and Connelly, 2021) with the activity models of White et al. (2014). GeoPS is a mineral equilibria forward modeling tool based on Gibbs energy minimization. The bulk composition for P–T modeling was determined by Bureau Veritas, Perth, by X-ray fluorescence spectrometry (Table A3). Oxidation state and H_2O content were determined based on mineral compositions and modal proportions of Fe^{3+} and hydrous minerals, respectively. The effect of varying oxidation state and H_2O content on the peak conditions were explored using T-X sections (Appendix Figure A1). Small variations in oxidation state and H_2O content do not significantly change the interpreted peak conditions.

Pelitic gneiss is rare at Cairn Hill and only the garnet-bearing sample 19CH1-03 contains a mineral assemblage that is able to provide significant constraints on P–T conditions of metamorphism. The sample contains a peak mineral assemblage of biotite, cordierite, garnet, ilmenite, K-feldspar, magnetite, plagioclase, quartz and melt. Garnet abundance within the sample is estimated to be 7–8 vol. %. Garnet modal abundance contours within the modeled stability field indicate peak P–T conditions of 4.6–5.3 kbar and 740–770 °C (Fig. 2.6).

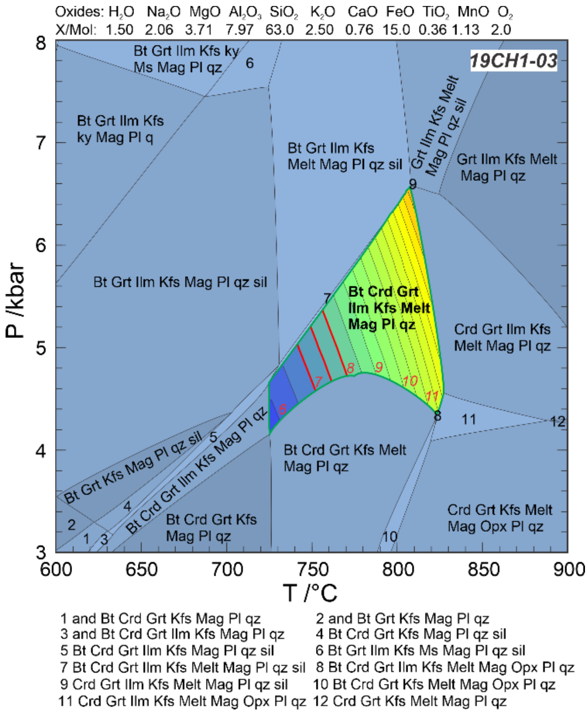

Fig. 2.6 Calculated P–T pseudosection for sample 19CH1-03, contoured for garnet abundance (vol. %). The red lines indicate the stability field (4.6–5.3 kbar, 740–770 °C) of the peak mineral assemblage (biotite, cordierite, garnet, ilmenite, K-feldspar, magnetite, plagioclase, quartz, melt).

5. Discussion

5.1 Age constraints on Cairn Hill protoliths

Concordant zircons from a sample of felsic gneiss (19CH2-24) range in age from ca. 1830–1725 Ma and broadly define a major peak at ca. 1740 and a minor peak at ca. 1800 Ma (Fig. 2.4A and B). This rock contains a strong gneissic foliation but is homogenous on the decimetre to meter-scale in the open-pit face, and was interpreted to have an igneous protolith. Felsic gneiss with a magmatic age of 1742 ± 27 Ma (Fanning et al., 1988) in the southern zone of the Mount Woods Domain may support an interpretation that the sample is a ca. 1740 Ma orthogneiss that also contains inheritance and some Pb loss during younger metamorphism.

However, the range in zircon dates obtained from the sample, combined with the recognition of rare domains of pelitic gneiss in Pit 1, raises the possibility that sample 19CH2-24 may have a metasedimentary protolith. Equivalent Fe-rich metasedimentary rocks with a detrital age peak at ca. 1750 Ma are widespread in the northern, eastern, and western Gawler Craton (Payne et al., 2006; Howard et al., 2011). Our interpretation is that the host rocks to Cairn Hill are likely to represent interlayered igneous and metasedimentary gneisses similar to those present in the Mount Woods and Nawa Domains (Jagodzinski et al., 2007; Howard et al., 2011). The presence of metasedimentary rocks within the confines of the mine has not been previously noted.

5.2 Magnetite mineralisation and high-grade metamorphism of Cairn Hill

The Gawler Craton hosts sedimentary iron formations that have been recrystallized and upgraded during metamorphism (e.g., Warramboo deposit; Morrissey et al., 2016). Within the Mount Woods area, neighboring prospects and drill holes contain magnetite mineralisation that is considered to be metamorphosed sedimentary iron formations (e.g., Snaefell prospect hosted by Skylark Metasediments) with some remobilization of iron observed (Chalmers, 2007). Meanwhile, recent drilling has revealed early, deep magnetite-apatite mineralisation at depth and at the outer margins (e.g., Wirrda Well and Acropolis prospects) of the hematite-dominated Olympic Dam deposit (Ehrig et al., 2012; Apukhtina et al., 2017; Verdugo-Ihl et al., 2020). The alteration minerals associated with the magnetite mineralisation at Cairn Hill, e.g., apatite, hornblende and albite, display similarities to a series of hydrothermal magnetite-dominated IOCG prospects (e.g., Joe's Dam and Manxman A1) in the southern Mount Woods Domain (Freeman and Tomkinson, 2010), and thus a hydrothermal origin for the magnetite is a simple explanation for Cairn Hill. Identification of the source of Fe mineralisation at Cairn Hill is complicated by the subsequent overprinting events, and is beyond the scope of this paper. However, we are able to place time constraints on the formation of the magnetite ore bodies. Zircon obtained from hornblende selvages to magnetite-apatite lodes constrain the magnetite mineralisation to no later than 1583 Ma, with this age either representing the mineralisation event itself or metamorphism of the ore bodies. The replacement of hornblende by orthopyroxene-plagioclase or orthopyroxene-clinopyroxene indicates the magnetite-apatite-hornblende lodes have subsequently been re-metamorphosed after this time.

Samples of the host felsic and metasedimentary gneisses contain geochronological evidence for events at ca. 1580 Ma and ca. 1490 Ma. Due to the superposition of the ca. 1490 Ma metamorphism (below), the P–T conditions associated with the ca. 1580 Ma event are difficult to estimate. However, based on the presence of the hornblende selvage, the growth of monazite and the crystallization of zircon in hornblende, the metamorphic conditions at 1580 Ma are conservatively estimated to be upper amphibolite facies. More regionally, amphibolite facies conditions are supported by a sillimanite-bearing metasedimentary rock in the southern Mount Woods Domain with metamorphic zircon rims yielding an age of 1595 ± 10 Ma (Jagodzinski et al., 2007).

Prior to this study, a 1514 Ma cross-cutting granitic dyke provided a minimum age constraint for Fe mineralisation at Cairn Hill (Jagodzinski and Reid, 2015), and this was inferred to also constrain Cu mineralisation. Similar granitic dykes analyzed in this study yield a zircon U-Pb age of 1518 ± 22 Ma (Fig. 2.4D) and a metamorphic monazite age of 1493 ± 6 Ma (Fig. 2.5F). All of these granitic dykes are wrapped into parallelism with the sheared host rock (Fig. 2.3A), consistent with ductile shear deformation occurring after granitic dyke intrusion. High-grade metamorphism at ca. 1490 Ma is further supported by sample 19CH1-03, which contains a population of ca. 1490 Ma monazite with low Y contents which is interpreted to have grown in equilibrium with garnet (Fig. 2.5B and C; Dumond et al., 2015). The ca. 1490 Ma metamorphic event is constrained to P–T conditions of 4.6–5.3 kbar and 740–770 °C and overprints the magnetite lodes.

5.3 A pseudo-IOCG mineral system in the Gawler Craton

Due to the presence of Cu mineralisation, Cairn Hill has been proposed as a magnetite-rich IOCG deposit (Skirrow et al., 2007; Reid and Fabris, 2015). However, the Cu-bearing sulfide–quartz veins show no signs of ductile deformation or metamorphism and instead have textures consistent with hydrothermal infill of open space fractures (Fig. 2.3G–K). This indicates the introduction of Cu under brittle conditions without subsequent deformation, which means the Cu mineralisation must post-date the ca. 1490 Ma high-grade metamorphism. Copper mineralisation therefore formed at least 100 Myr after the magnetite mineralisation and the two represent two independent mineralisation events.

In the Olympic Cu-Au Province, fluid inclusion studies reveal the temperature of the regional ore-forming fluids is < 500 °C for the magnetite stage and < 400 °C for the hematite-copper stage (Oreskes and Einaudi, 1992; Bastrakov et al., 2007; Davidson et al., 2007; Schlegel et al., 2018). Cairn Hill and much of the Mount Woods Domain was likely above the temperature window of Cu mineralisation seen elsewhere in the Olympic Cu-Au Province at ca. 1590 Ma. Therefore, if any IOCG-mineralisation did form in this region at 1590 Ma it is likely to have been at a higher crustal level that was subsequently eroded. Low-temperature chronometers suggest that regional cooling of the western Mount Woods Domain occurred between 1492 to 1390 Ma (Jagodzinski and Reid, 2015; Morrissey et al., 2023). At Cairn Hill, the cooling history is recorded by hornblende $^{40}Ar/^{39}Ar$, apatite U-Pb, and phlogopite $^{40}Ar/^{39}Ar$ ages of 1462–1492 Ma. Therefore, we suggest that it was not until after ca. 1490 Ma that the Cairn Hill area was exhumed to a depth and temperature suitable for the introduction of Cu-bearing fluids and precipitation of Cu ores, at least 100 Ma after the 1590 Ma IOCG event elsewhere in the IOCG province (Cherry et al., 2018; Courtney-Davies et al., 2020; McPhie et al., 2020). Although multiple post-1590 Ma hydrothermal events have been recognised previously in the Olympic Dam deposit (Cherry et al. 2017, 2018; Ehrig et al., 2021), these events are not proposed to have introduced new Cu (Cherry et al., 2017).

Skirrow (2022) outlines two end-members of the Cu-Au-Fe deposit family; deposits in which Cu and Fe are deposited from a single evolving system, and deposits in which Fe is pre-existing within the rock and Cu is deposited at a later date. Our new findings demonstrate Cairn Hill undoubtedly fits within the latter of these “IOCG” deposit types, but we suggest these should be considered distinct from the Olympic Cu-Au province. This is akin to the recommendations of Groves et al. (2010) who consider IOCG deposits sensu stricto (e.g. Olympic Dam) as a subgroup of iron oxide-associated deposits, with the broad group encompassing Cairn Hill. The post-1490 Ma Cu mineralisation requires a distinct Cu source to the ca. 1590 Ma IOCG deposits and is likely to have formed in a different over-arching tectonic regime. The pre-existing magnetite may act as a potential chemical trap site for superimposed oxidized copper-bearing fluids as opposed to genetically linked (Barton, 2014; Skirrow et al., 2019).

An important outcome of this study is the definition of a new Cu system in the Gawler Craton. We suggest that this system is unlikely to represent remobilization of pre-existing crustal Cu as the crustal column of Cairn Hill had undergone at least two amphibolite to granulite facies metamorphic events prior to the formation of Cu mineralisation. Both of these events reached sufficient P–T grades for the crust to have been dehydrated and any contained Cu and S is likely to have been mobilized out of the mid- to lower crust (e.g., Lee et al., 2012) well prior to the formation of the Cu mineralisation at Cairn Hill. Further research is required to identify the exact Cu source and subsequently determine the potential for economic Cu mineralisation forming at this time.

6. Conclusion

The Cairn Hill Fe (-Cu-Au) deposit records amphibolite-facies metamorphism at ca. 1580 Ma and upper amphibolite to granulite-facies (4.6–5.3 kbar, 740–770 °C) deformation along the Cairn Hill shear zone at ca. 1490 Ma. Magnetite mineralisation at Cairn Hill occurs no later than 1583 Ma, and was then metamorphosed and deformed at 1490 Ma. Copper mineralisation occurred under brittle conditions and overprinted the ductile deformation and high-T metamorphism at Cairn Hill. The recognition of the addition of Cu to the Cairn Hill deposit after ca. 1490 Ma provides a new timeline for mineralisation in the Gawler Craton. The spatial but not temporal association between magnetite and Cu has created a composite IOCG deposit signature in the northern Olympic Cu-Au province.

Acknowledgments

This project was supported by ARC Linkage Project LP160100578 (JLP and MH), the Mineral Exploration Cooperative Research Centre (MinEX CRC), and the China Scholarship Council. LJM is supported by an ARC DECRA Fellowship DE210101126. S. Gilbert and B. Wade are thanked for their technical support at

Adelaide Microscopy. K Faure is thanked for his assistance and discussions in the field. Constructive reviews from Dr. C. Wade and an anonymous reviewer are greatly appreciated.

References

Apukhtina, O. B., Kamenetsky, V. S., Ehrig, K., Kamenetsky, M. B., Maas, R., Thompson, J., McPhie, J., Ciobanu, C. L., and Cook, N. J., 2017, Early, deep magnetite-fluorapatite mineralisation at the Olympic Dam Cu-U-Au-Ag deposit, South Australia*: Economic Geology, v. 112, p. 1531-1542.

Barton, M. D., 2014, Iron Oxide(–Cu–Au–REE–P–Ag–U–Co) Systems, Treatise on Geochemistry, p. 515-541.

Bastrakov, E. N., Skirrow, R. G., and Davidson, G. J., 2007, Fluid Evolution and Origins of Iron Oxide Cu-Au Prospects in the Olympic Dam District, Gawler Craton, South Australia: Economic Geology, p. 1415-1440.

Belperio, A., Flint, R., and Freeman, H., 2007, Prominent Hill: A Hematite-Dominated, Iron Oxide Copper-Gold System: Economic Geology, v. 102, p. 1499-1510.

Betts, P. G., Valenta, R. K., and Finlay, J., 2003, Evolution of the Mount Woods Inlier, northern Gawler Craton, Southern Australia: an integrated structural and aeromagnetic analysis: Tectonophysics, v. 366, p. 83-111.

Bockmann, M. J., Hand, M., Morrissey, L. J., Payne, J. L., Hasterok, D., Teale, G., and Conor, C., 2022, Punctuated geochronology within a sustained high-temperature thermal regime in the southeastern Gawler Craton: Lithos, v. 430, p. 106860.

Bockmann, M. J., Payne, J. L., Hand, M., Morrissey, L. J., and Belperio, A. P., 2023, Linking the Gawler Craton and Mount Isa Province through hydrothermal systems in the Peake and Denison Domain, northeastern Gawler Craton: Geoscience Frontiers, p. 101596.

Bowden, B., Fraser, G., Davidson, G. J., Meffre, S., Skirrow, R., Bull, S., and Thompson, J., 2017, Age constraints on the hydrothermal history of the Prominent Hill iron oxide copper-gold deposit, South Australia: Mineralium Deposita, v. 52, p. 863-881.

Chalmers, N., 2007, The Mount Woods Domain: a geological review and discussion on mineralisation potential, Report Book 2007/7: South Australia.

Cherry, A. R., Kamenetsky, V. S., McPhie, J., Thompson, J. M., Ehrig, K., Meffre, S., Kamenetsky, M. B., and Krneta, S., 2018, Tectonothermal events in the Olympic IOCG Province constrained by apatite and REE-phosphate geochronology: Australian Journal of Earth Sciences, v. 65, p. 643-659.

Cherry, A. R., McPhie, J., Kamenetsky, V. S., Ehrig, K., Keeling, J. L., Kamenetsky, M. B., Meffre, S., and Apukhtina, O. B., 2017, Linking Olympic Dam and the Cariewerloo Basin: Was a sedimentary basin involved in formation of the world's largest uranium deposit?: Precambrian Research, v. 300, p. 168-180.

Clark, J. M., 2014, Defining the style of mineralisation at the Cairn Hill magnetite-sulphide deposit, Mount Woods Inlier, Gawler Craton, South Australia, The University of Adelaide.

Courtney-Davies, L., Ciobanu, C. L., Tapster, S. R., Cook, N. J., Ehrig, K., Crowley, J. L., Verdugo-Ihl, M. R., Wade, B. P., and Condon, D. J., 2020, Opening the magmatic-hydrothermal window: high-precision U-Pb Geochronology Of The Mesoproterozoic Olympic Dam Cu-U-Au-Ag deposit, South Australia: Economic Geology, v. 115, p. 1855-1870.

Cutts, K., Hand, M., and Kelsey, D. E., 2011, Evidence for early Mesoproterozoic (ca. 1590Ma) ultrahigh-temperature metamorphism in southern Australia: Lithos, v. 124, p. 1-16.

Davidson, G. J., Paterson, H., Meffre, S., and Berry, R. F., 2007, Characteristics and origin of the Oak Dam East breccia-hosted, iron oxide Cu-U-(Au) deposit: Olympic Dam region, Gawler craton, South Australia: Economic Geology, v. 102, p. 1471-1498.

Dumond, G., Goncalves, P., Williams, M. L., and Jercinovic, M. J., 2015, Monazite as a monitor of melting, garnet growth and feldspar recrystallization in continental lower crust: Journal of Metamorphic Geology, v. 33, p. 735-762.

Ehrig, K., Kamenetsky, V. S., McPhie, J., Macmillan, E., Thompson, J., Kamenetsky, M., and Maas, R., 2021, Staged formation of the supergiant Olympic Dam uranium deposit, Australia: Geology, v. 49, p. 1312-1316.

Ehrig, K., McPhie, J., and Kamenetsky, V., 2012, Geology and mineralogical zonation of the Olympic Dam iron oxide Cu-U-Au-Ag deposit, South Australia, *in* Hedenquist, J., Harris, M., and Camus, F., eds., Geology and genesis of major copper deposits and districts of the world: a tribute to Richard H. Sillitoe., Soc of Econ Geol Spec Pub, p. 16: 237–267.

Fanning, C., Flint, R., Parker, A., Ludwig, K., and Blissett, A., 1988, Refined Proterozoic evolution of the Gawler craton, South Australia, through U-Pb zircon geochronology: Precambrian Research, v. 40, p. 363-386.

Forbes, C. J., Giles, D., Jourdan, F., Sato, K., Omori, S., and Bunch, M., 2012, Cooling and exhumation history of the northeastern Gawler Craton, South Australia: Precambrian Research, v. 200-203, p. 209-238.

Fraser, G., McAvaney, S., Neumann, N., Szpunar, M., and Reid, A., 2010, Discovery of early Mesoarchean crust in the eastern Gawler Craton, South Australia: Precambrian Research, v. 179, p. 1-21.

Fraser, G., Reid, A., and Stern, R., 2012, Timing of deformation and exhumation across the Karari Shear Zone, north-western Gawler Craton, South Australia: Australian Journal of Earth Sciences, v. 59, p. 547-570.

Fraser, G. L., and Lyons, P., 2006, Timing of Mesoproterozoic tectonic activity in the northwestern Gawler Craton constrained by 40Ar/39Ar geochronology: Precambrian Research, v. 151, p. 160-184.

Freeman, H., and Tomkinson, M., 2010, Geological setting of iron oxide related mineralisation in the southern Mount Woods Domain, South Australia, Hydrothermal iron oxide copper-gold & related deposits: A global perspective, 3, p. 171-190.

Groves, D. I., Bierlein, F. P., Meinert, L. D., and Hitzman, M. W., 2010, Iron Oxide Copper-Gold (IOCG) Deposits through Earth History: Implications for Origin, Lithospheric Setting, and Distinction from Other Epigenetic Iron Oxide Deposits: Economic Geology, v. 105, p. 641-654.

Hall, J. W., Glorie, S., Reid, A. J., Boone, S. C., Collins, A. S., and Gleadow, A., 2018, An apatite U–Pb thermal history map for the northern Gawler Craton, South Australia: Geoscience Frontiers, v. 9, p. 1293-1308.

Hand, M., Reid, A., and Jagodzinski, L., 2007, Tectonic framework and evolution of the Gawler craton, southern Australia: Economic Geology, v. 102, p. 1377-1395.

Howard, K., Hand, M., Barovich, K., and Belousova, E., 2011, Provenance of late Paleoproterozoic cover sequences in the central Gawler Craton: exploring stratigraphic correlations in eastern Proterozoic Australia using detrital zircon ages, Hf and Nd isotopic data: Australian Journal of Earth Sciences, v. 58, p. 475-500.

Jagodzinski, E., 2005, Compilation of SHRIMP U-Pb geochronological data, Olympic Domain, Gawler Craton, South Australia, 2001-2003, Geoscience Australia, p. 197.

Jagodzinski, E., and Reid, A., 2015, PACE Geochronology: Results of collaborative geochronology projects 2013-2015, Government of South Australia. Department of the Premier and Cabinet. , p. Report Book, 2015/00003.

Jagodzinski, E., Reid, A., Chalmers, N., Swain, G., Frew, R., and Foudoulis, C., 2007, Compilation of SHRIMP U-Pb geochronological data for the Gawler Craton, South Australia, 2007, Report Book 2007/21, South Australian Department of Primary Industries and Resources.

Jagodzinski, E. A., Reid, A. J., Crowley, J. L., Wade, C. E., and Curtis, S., 2023, Precise zircon U-Pb dating of the Mesoproterozoic Gawler large igneous province, South Australia: Results in Geochemistry, v. 10, p. 100020.

Lee, C.-T. A., Luffi, P., Chin, E. J., Bouchet, R., Dasgupta, R., Morton, D. M., Le Roux, V., Yin, Q.-z., and Jin, D., 2012, Copper Systematics in Arc Magmas and Implications for Crust-Mantle Differentiation: Science, v. 336, p. 64-68.

McCuaig, T. C., Beresford, S., and Hronsky, J., 2010, Translating the mineral systems approach into an effective exploration targeting system: Ore Geology Reviews, v. 38, p. 128-138.

McPhie, J., Ehrig, K. J., Kamenetsky, M. B., Crowley, J. L., and Kamenetsky, V. S., 2020, Geology of the Acropolis prospect, South Australia, constrained by high-precision CA-TIMS ages: Australian Journal of Earth Sciences, v. 67, p. 699-716.

Morrissey, L. J., Barovich, K. M., Hand, M., Howard, K. E., and Payne, J. L., 2019, Magmatism and metamorphism at ca. 1.45 Ga in the northern Gawler Craton: The Australian record of rifting within Nuna (Columbia): Geoscience Frontiers, p. 175-194.

Morrissey, L. J., Hand, M., Lane, K., Kelsey, D. E., and Dutch, R. A., 2016, Upgrading iron-ore deposits by melt loss during granulite facies metamorphism: Ore Geology Reviews, v. 74, p. 101-121.

Morrissey, L. J., Payne, J., Hand, M., Clark, C., and Janicki, M., 2023, One billion years of tectonism at the Paleoproterozoic interface of North and South Australia: Precambrian Research, p. under review.

Oreskes, N., and Einaudi, M. T., 1992, Origin of hydrothermal fluids at Olympic Dam Preliminary results from fluid inclusions and stable isotopes: Economic Geology, v. 87, p. 64-90.

Payne, J. L., Barovich, K. M., and Hand, M., 2006, Provenance of metasedimentary rocks in the northern Gawler Craton, Australia: Implications for Palaeoproterozoic reconstructions: Precambrian Research, v. 148, p. 275-291.

Payne, J. L., Ferris, G., Barovich, K. M., and Hand, M., 2010, Pitfalls of classifying ancient magmatic suites with tectonic discrimination diagrams: An example from the Paleoproterozoic Tunkillia Suite, southern Australia: Precambrian Research, v. 177, p. 227-240.

Payne, J. L., Hand, M., Barovich, K. M., and Wade, B. P., 2008, Temporal constraints on the timing of high-grade metamorphism in the northern Gawler Craton: implications for assembly of the Australian Proterozoic: Australian Journal of Earth Sciences, v. 55, p. 623-640.

Preiss, W., 2000, The Adelaide Geosyncline of South Australia and its significance in Neoproterozoic continental reconstruction: Precambrian Research, v. 100, p. 21-63.

Reeve, J. S., Cross, K. C., Smith, R. N., and Oreskes, N., 1990, Olympic Dam copper-uranium-gold-silver deposit, *in* Hughes, F. E., ed., Geology of the mineral deposits of Australia and Papua New Guinea: Melbourne, Australasian Institute of Mining and Metallurgy Monograph 14, p. 1009–1035.

Reid, A., 2019, The Olympic Cu-Au Province, Gawler Craton: A Review of the Lithospheric Architecture, Geodynamic Setting, Alteration Systems, Cover Successions and Prospectivity: Minerals, v. 9, p. 371.

Reid, A., and Fabris, A., 2015, Influence of Preexisting Low Metamorphic Grade Sedimentary successions on the distribution of iron oxide copper-gold mineralisation in the olympic Cu-Au province, Gawler Craton: Economic Geology, v. 110, p. 2147-2157.

Reid, A. J., and Hand, M., 2012, Mesoarchean to Mesoproterozoic evolution of the southern Gawler Craton, South Australia: Episodes, v. 35, p. 216-225.

Reid, A. J., Jagodzinski, E. A., Fraser, G. L., and Pawley, M. J., 2014, SHRIMP U–Pb zircon age constraints on the tectonics of the Neoarchean to early Paleoproterozoic transition within the Mulgathing Complex, Gawler Craton, South Australia: Precambrian Research, v. 250, p. 27-49.

Reid, A. J., Pawley, M. J., Wade, C., Jagodzinski, E. A., Dutch, R. A., and Armstrong, R., 2019, Resolving tectonic settings of ancient magmatic suites using structural, geochemical and isotopic constraints: the example of the St Peter Suite, southern Australia: Australian Journal of Earth Sciences, v. 67, p. 31-58.

Schlegel, T. U., Wagner, T., Wälle, M., and Heinrich, C. A., 2018, Hematite Breccia-Hosted Iron Oxide Copper-Gold Deposits Require Magmatic Fluid Components Exposed to Atmospheric Oxidation: Evidence from Prominent Hill, Gawler Craton, South Australia: Economic Geology, v. 113, p. 597-644.

Skirrow, R. G., 2022, Iron oxide copper-gold (IOCG) deposits – A review (part 1): Settings, mineralogy, ore geochemistry and classification: Ore Geology Reviews, v. 140, p. 104569.

Skirrow, R. G., Bastrakov, E. N., Baroncii, K., Fraser, G. L., Creaser, R. A., Fanning, C. M., Raymond, O. L., and Davidson, G. J., 2007, Timing of iron oxide Cu-Au-(U) hydrothermal activity and Nd isotope constraints on metal sources in the Gawler craton, south Australia: Economic Geology, v. 102, p. 1441-1470.

Skirrow, R. G., Murr, J., Schofield, A., Huston, D. L., van der Wielen, S., Czarnota, K., Coghlan, R., Highet, L. M., Connolly, D., Doublier, M., and Duan, J., 2019, Mapping iron oxide Cu-Au (IOCG) mineral potential in Australia using a knowledge-driven mineral systems-based approach: Ore Geology Reviews, v. 113.

Tiddy, C. J., Betts, P. G., Neumann, M. R., Murphy, F. C., Stewart, J., Giles, D., Sawyer, M., Freeman, H., and Jourdan, F., 2020, Interpretation of a ca. 1600–1580 Ma metamorphic core complex in the northern Gawler Craton, Australia: Gondwana Research, v. 85, p. 263-290.

Verdugo-Ihl, M. R., Ciobanu, C. L., Cook, N. J., Ehrig, K. J., and Courtney-Davies, L., 2020, Defining early stages of IOCG systems: evidence from iron oxides in the outer shell of the Olympic Dam deposit, South Australia: Mineralium Deposita, v. 55, p. 429-452.

White, R. W., Powell, R., Holland, T. J. B., Johnson, T. E., and Green, E. C. R., 2014, New mineral activity–composition relations for thermodynamic calculations in metapelitic systems: Journal of Metamorphic Geology, v. 32, p. 261-286.

Whitney, D. L., and Evans, B. W., 2010, Abbreviations for names of rock-forming minerals: American Mineralogist, v. 95, p. 185-187.

Wyborn, L., Heinrich, C., and Jaques, A., 1994, Australian Proterozoic mineral systems: essential ingredients and mappable criteria: The AusIMM Annual Conference, 1994, p. 109-115.

Xiang, H., and Connolly, J. A. D., 2021, GeoPS: An interactive visual computing tool for thermodynamic modelling of phase equilibria: Journal of Metamorphic Geology, v. 40, p. 243-255.

Supplementary material

Tables A1–A3 that accompany this thesis chapter is available on Open Science Framework: https://osf.io/rcm7g/

Geochronology methods

LA-ICP-MS monazite U-Pb dating and trace element analyses were collected on an Agilent 8900 ICP-MS coupled with a RESOlution 193 nm excimer laser ablation system at Adelaide Microscopy, the University of Adelaide, Australia. Three samples were analyzed in grain mounts, and two samples were analyzed *in situ* to observe any trend between the age and textural location of the monazite analyses. For mount samples, monazites were separated by conventional heavy liquid and magnetic separation techniques and then handpicked under a binocular microscope. Representative monazite grains were mounted on adhesive tape and then polished to expose the centers of individual crystals. SEM imaging was conducted to reveal the internal structure of monazites and then identify sites for laser analyses. The ablation of monazite was performed with a spot size of 13–19 µm depending on the grain size, a frequency of 5 Hz, and laser energy of 4–5 J/cm^2. The total acquisition time for each analysis was 60 s, including 30 s of background measurement, followed by 30 s of laser ablation. Common lead was not corrected in the age calculations due to unresolvable interference of ^{204}Hg on the ^{204}Pb isotope peak. To compensate for this, mass 204 was monitored, and analyses were omitted if an appreciable common lead was observed. Mass bias, elemental fractionation and instrument drift were corrected using the monazite standard MAdel (TIMS normalization data: ^{207}Pb/^{206}Pb age = 492.01 ± 0.77 Ma, ^{206}Pb/^{238}U age = 517.9 ± 2.6 Ma and ^{207}Pb/^{235}U age = 513.13 ± 0.20 Ma; Payne et al., 2008) with standard bracketing every 10–12 unknown analyses. Data accuracy was monitored by analyses of in-house monazite standard 222 (^{206}Pb/^{238}U age 450.2 ± 3.4 Ma; Maidment, 2005) and Ambat (^{206}Pb/^{238}U age ca. 520 Ma). Throughout the course of this study standard 222 yielded a ^{206}Pb/^{238}U weighted mean age of 450 ± 1.2 (n = 38/40, MSWD = 1.05, prob = 0.39) and Ambat yielded a ^{206}Pb/^{238}U weighted mean age of 516 ± 1.5 (n = 29, MSWD = 0.84, prob. = 0.7). These values are within the expected external uncertainty of the LA-ICP-MS method of 1–2 % (Horstwood et al., 2016). Trace elements were processed using the glass NIST SRM 610. All monazite analyses were assumed to have 20 wt. % Ce.

Three samples from Cairn Hill were selected for zircon geochronology. Zircons were separated by conventional heavy liquid and magnetic separation techniques and then handpicked under a binocular microscope. Representative zircon grains were mounted on adhesive tape and then polished to expose the centers of individual crystals. Cathodoluminescence (CL) imaging was conducted to reveal the internal structure of zircons and help to identify the sites for the following laser analyses. LA-ICP-MS zircon U-Pb dating and trace element analyses follow the method of monazite U–Pb dating. The ablation of zircon was performed with a spot size of 29 µm, a frequency of 5 Hz, and laser energy of 2–3 J/cm^2. Mass bias, elemental fractionation and instrument drift were corrected using the zircon standard GJ-1 ($^{207}Pb/^{206}Pb$ = 607.7 ± 4.3 Ma, $^{206}Pb/^{238}U$ = 600.7 ± 1.1 Ma and $^{207}Pb/^{235}U$ = 602.0 ± 1.0; Jackson et al., 2004), with standard bracketing every 10–12 unknown analyses. Data accuracy was monitored by analyses of zircon standards 91500 ($^{207}Pb/^{206}Pb$ age = 1065 ± 0.3 Ma, $^{206}Pb/^{238}U$ age = 1062 ± 0.4 Ma and $^{207}Pb/^{235}U$ age = 1061 ± 0.3 Ma; Wiedenbeck et al., 1995) and Plesovice ($^{206}Pb/^{238}U$ = 337.13 ± 0.37 Ma; Slama et al., 2008). Throughout the course of this study 91500 yielded a $^{206}Pb/^{238}U$ weighted mean age of 1058 ± 3.3 (n = 22, MSWD = 0.56, prob. = 0.95) and Plesovice yielded a $^{206}Pb/^{238}U$ weighted mean age of 339 ± 0.85 (n = 22, MSWD = 0.96, prob. = 0.51). These values are within the expected external uncertainty of the LA-ICP-MS method of 1–2 % (Horstwood et al., 2016). Trace elements were processed using the glass NIST 610 as a standard. All zircon analyses were assumed to have 43.14 wt. % Zr.

Age calculation and trace element content of monazite and zircons were reduced using Iolite version 3.1 (Paton et al., 2011). Zircon geochronology and trace elements results are summarized in Appendix Table A1, and all monazite U-Pb geochronological and trace elements data are in Appendix Table A2. U-Pb data were plotted using Isoplot 4.15 (Ludwig, 2012). Only analyses within 2σ uncertainty of concordia are used for the weighted mean age calculation and unmixing calculations; discordant analyses are shown as dashed circles where they fall within the field of view. Uncertainties on weighted mean ages are quoted using 95% confidence. The concordia plots are color-scaled for the element of most interest for each sample.

Sample description and age results

Sample 19CH2-24

Sample 19CH2-24 is a felsic gneiss that represents the main host-rock for mineralisation. It is medium- to coarse-grained containing K-feldspar, quartz, plagioclase and biotite (Fig. 2.3B). Accessory minerals include magnetite, zircon, monazite and apatite. The gneissic foliation is parallel to the magnetite lodes. Differences in grain size can be seen in the different parts of the hand specimens, but there is no difference in mineralogy.

Zircon grains in sample 19CH2-24 are 60–200 μm in length with aspect ratios of 1:2 to 1:4. In CL images, grains commonly show a bright oscillatory zoned core overgrown by thin to thick rims with a low CL response (Fig. 2.4A). Rare grains are dark and homogeneous. Fifty analyses were collected from the oscillatory zoned cores, and of those 15 were concordant. Concordant analyses range in age from 1725 to 1830 Ma, and broadly define peaks at ca. 1800 Ma and ca. 1740 Ma (Fig. 2.4B). Zircons display steeply positive HREE slopes, positive Ce anomalies and negative Eu anomalies. Their Th/U ratios range from 0.16 to 1.14, with a low value of 0.014 for the oldest analysis (1826 ± 22 Ma). All analyses of the dark rims did not produce usable signals.

Monazites from sample 19CH2-24 are euhedral to subhedral grains and fragments ranging from 50 to 300 μm in length. Most monazite grains display complex patchy zoning.

In BSE images, rare grains show a bright core overgrown by dark porous rims, surrounded by thin bright outer rims. Sixty-three concordant analyses yield a weighted mean age of 1489 ± 3 Ma (*n* = 59/63, MSWD = 0.77; Fig. 2.5A) with one older discordant analysis at 1590 ± 20 Ma and one at 1692 ± 57 Ma. There is no difference in age between the different zones. The bright zones typically have higher Th contents than the dark zones, but there is no apparent difference in other elements.

Sample 19CH2-27

19CH2-27 is a hornblende selvage sample from the edge of the coarse hornblende–magnetite lode (Fig. 2.3G). The wall rock of the hornblende–magnetite lode is medium- to coarse-grained felsic gneiss, and later copper-quartz veins crosscuts the hornblende-magnetite layer. Abundant zircons are included in hornblende. Zircon grains are 60–200 µm in length with aspect ratios of 1:1 to 1:2 (Fig. 2.4C). In CL images, zircon grains typically show a bright core overgrown by homogenous dark rims. The bright cores are either oscillatory zoned or sector zoned. Seventy-three spots were analyzed from 69 grains, with most analyses showing discordance related to a combination of Pb loss and common Pb (Fig. 2.4C). Only four analyses are concordant and these yield a statistically valid weighted mean $^{207}Pb/^{206}Pb$ age of 1583 ± 30 Ma (*n* = 4, MSWD = 1.8). Analyses with common Pb levels less than or equal to the concordant analyses yield an errorchron with an upper intercept of 1581 ± 13 Ma (*n* = 20, MSWD = 1.4).

Sample 19CH2-19

19CH2-19 is a medium-grained granitic dyke on the edge of the southern magnetite lode, and is wrapped into parallelism with the gneiss (Fig. 2.3A). It contains K-feldspar, quartz, and plagioclase with minor biotite and magnetite. Zircon grains are dark brown and 40–200 µm in length. In CL images grains typically display oscillatory zoned cores surrounded by dark, featureless rims (Fig. 2.4D). Rare oscillatory zoned cores contain a relic inner core with complex zoning, which is too small to analyze. Seventy-two analyses were attempted on the oscillatory zoned cores but only 25 yielded meaningful time-resolved signals. Most of the grains are moderately to highly discordant, and define an errorchron with upper intercept age of 1518 ± 22 Ma (*n* = 25, MSWD = 2.8). Th/U ratios vary from 0.1–1.2 and there is a large range in U and Th contents (281–1317 ppm and 104.5–1243 ppm, respectively). All analyses show a weakly positive HREE slope, a positive Ce anomaly and negative Eu anomaly (Table A1).

Sample 19CH1-03

Sample 19CH1-03 is granulite facies metasedimentary rock sampled from the south side of Pit 1 (Fig. 2.3C), close to sample 19CH1-04. The sample is mineralogically heterogeneous, with biotite and plagioclase-rich domains surrounding a garnet domain. The garnet domain contains a mineral assemblage of garnet, biotite, quartz, magnetite and ilmenite with minor K-feldspar and cordierite. The garnet grains are up to 2–4 centimeters, and contain inclusions of biotite, quartz, magnetite and monazite. The biotite and plagioclase-rich domain is composed of biotite, quartz, K-feldspar, plagioclase, magnetite and ilmenite. It has foliation defined by biotite and elongated magnetite, parallel to the gneissic fabric. Some biotite in this sample is altered to chlorite, and some feldspar is replaced by mica. This sample is modified by later shear deformation, with growth of fine-grained quartz-biotite-magnetite along the shear.

Fifty-four analyses were collected from 16 monazite grains located in both garnet-bearing and garnet-absent domains. One analysis was excluded on the basis of discordance. One spot yields an old age of 1679 ± 42 Ma, with the remaining concordant analyses ranging in age from 1624–1453 Ma (Fig. 2.5B). Support for two age populations is given by the unmix function within Isoplot, which yields ages of 1577 ± 6 Ma and 1497 ± 6 Ma (relative misfit = 0.650). Two groups can also be distinguished based on Y (+HREE) concentrations (Fig. 2.5B and C). Fourteen analyses from the garnet-bearing domain contain distinctly lower Y contents, and yield a weighted mean $^{207}Pb/^{206}Pb$ age of 1489 ± 8 Ma (n = 14, MSWD = 1, prob. = 0.42). Monazite grains from the garnet-absent layers have higher Y contents and range in age from 1679–1479 Ma. Individual monazite grains in this domain may yield both young and old ages.

Sample 19CH1-04

Sample 19CH1-04 is a representative magnetite-bearing gneiss from Pit 1 (Fig. 2.3D). The mineralogy of the gneiss is dominantly biotite, magnetite, K-feldspar, plagioclase and quartz. Alternating biotite + magnetite-rich and biotite + magnetite-poor layers define the gneissic fabric, and biotite grains are oriented parallel to the layers. In the biotite + magnetite-rich layers, magnetite most commonly occurs either along biotite grain boundaries or as inclusions within biotite. The magnetite bands can be up to a few centimeters wide. Ilmenite occurs intergrown with magnetite, and minor apatite is observed locally. The biotite + magnetite-poor layers are mainly composed of medium- to coarse-grained K-feldspar, plagioclase and quartz.

Monazite grains are 30–160 µm in length and located throughout the sample. Most monazite grains are uniform in BSE brightness without zonation, whereas others display patchy zonation, forming bright zones at the edges or inside the grains. Forty-four analyses were collected from 21 grains mounted in epoxy resin. Five analyses were excluded from further interpretation on the basis of discordance (Fig. 2.5D). Concordant analyses range in age from 1605 to 1462 Ma. The unmix function in Isoplot yields ages of 1568 ± 6 Ma and 1487 ± 4 Ma (relative misfit = 0.428). Older ages typically come from dark cores/grains while the bright rims/grains yield younger ages.

Sample 19CH2-12

Sample 19CH2-12 is a migmatitic gneiss in Pit 2, with a similar mineral assemblage to 19CH1-04. The gneissic fabric is defined by alternating biotite-rich and biotite-poor layers. In the biotite-rich layers, both biotite and magnetite display strong foliation parallel to the gneissic fabric. Ilmenite occurs intergrown with magnetite. This sample contains a 2–8 cm leucosome domain comprising coarse-grained K-feldspar, plagioclase and quartz with minor biotite and magnetite. Abundant monazite grains ranging from 30 to 400 µm occur at the edge of the leucosome. The biotite-poor layers have the same mineral assemblage and texture as the leucosome.

Sixty-four analyses were collected from 30 monazite grains in the thin section, two of which were excluded on the basis of discordance (Fig. 2.5E). The remaining analyses range in age from 1620–1452 Ma, with most analyses clustering around 1500 Ma. There is a gradual decrease in the concentrations of Ca and Eu with age and a corresponding increase in Si (Table A2). The six oldest spots also have the highest Eu concentrations (Fig. 2.5E) and define a weighted mean $^{207}Pb/^{206}Pb$ age of 1587 ± 18 Ma (n = 6, MSWD = 1.3, prob. = 0.28). The remaining 56 analyses yield a weighted mean $^{207}Pb/^{206}Pb$ age of 1494 ± 5 Ma (n = 52/56, MSWD = 1.3, prob. = 0.066).

Sample 19CH1-02

19CH1-02 is from a medium- to coarse-grained granitic dyke crosscutting the magnetite gneiss (Fig. 2.3D). It is composed of K-feldspar, quartz, and plagioclase with minor biotite. Some plagioclase has been altered to clay minerals. Accessory minerals include zircon and monazite, where monazite grains (50–100 µm) tend to grow along the foliation defined by the biotite. Twenty-six analyses were collected from eight monazite grains mounted in epoxy resin. Four analyses were excluded on the basis of discordance, and additional analysis was excluded on the basis of a large uncertainty (Fig. 2.5F). The remaining analyses yield a weighted mean $^{207}Pb/^{206}Pb$ age of 1493 ± 6 Ma (n = 21, MSWD = 1.4, prob. = 0.098).

References

Paton, C., Hellstrom, J., Paul, B., Woodhead, J., and Hergt, J., 2011, Iolite: Freeware for the visualisation and processing of mass spectrometric data: Journal of Analytical Atomic Spectrometry, v. 26, p. 2508–2518.

Payne, J. L., Hand, M., Barovich, K. M., and Wade, B. P., 2008, Temporal constraints on the timing of high-grade metamorphism in the northern Gawler Craton: implications for assembly of the Australian Proterozoic: Australian Journal of Earth Sciences, v. 55, p. 623–640.

Maidment, D. W., 2005, Palaeozoic high-grade metamorphism within the Centralian Superbasin, Harts Range region, central Australia: Ph.D. thesis, Canberra, Australia, Australian National University, 433 p.

Horstwood, M. S. A., Košler, J., Gehrels, G., Jackson, S. E., McLean, N. M., Paton, C., Pearson, N. J., Sircombe, K., Sylvester, P., Vermeesch, P., Bowring, J. F., Condon, D. J., and Schoene, B., 2016, Community-Derived Standards for LA-ICP-MS U-(Th-)Pb Geochronology – Uncertainty Propagation, Age Interpretation and Data Reporting: Geostandards and Geoanalytical Research, v. 40, p. 311–332.

Jackson, S. E., Pearson, N. J., Griffin, W. L., and Belousova, E. A., 2004, The application of laser ablation-inductively coupled plasma-mass spectrometry to in situ U–Pb zircon geochronology: Chemical Geology, v. 211, p. 47–69.

Wiedenbeck, M., Alle, P., Corfu, F., Griffin, W., Meier, M., Oberli, F. v., Quadt, A. v., Roddick, J., and Spiegel, W., 1995, Three natural zircon standards for U-Th-Pb, Lu-Hf, trace element and REE analyses: Geostandards newsletter, v. 19, p. 1–23.

Sláma, J., Košler, J., Condon, D. J., Crowley, J. L., Gerdes, A., Hanchar, J. M., Horstwood, M. S. A., Morris, G. A., Nasdala, L., Norberg, N., Schaltegger, U., Schoene, B., Tubrett, M. N., and Whitehouse, M. J., 2008, Plešovice zircon — A new natural reference material for U–Pb and Hf isotopic microanalysis: Chemical Geology, v. 249, p. 1–35.

Ludwig, K., 2012, Isoplot 4.15: a geochronological toolkit for Microsoft Excel, Berkeley Geochronological Center.

Appendix Figure 1 *P–T* pseudosection modeling for Cairn Hill.

19CH1-03

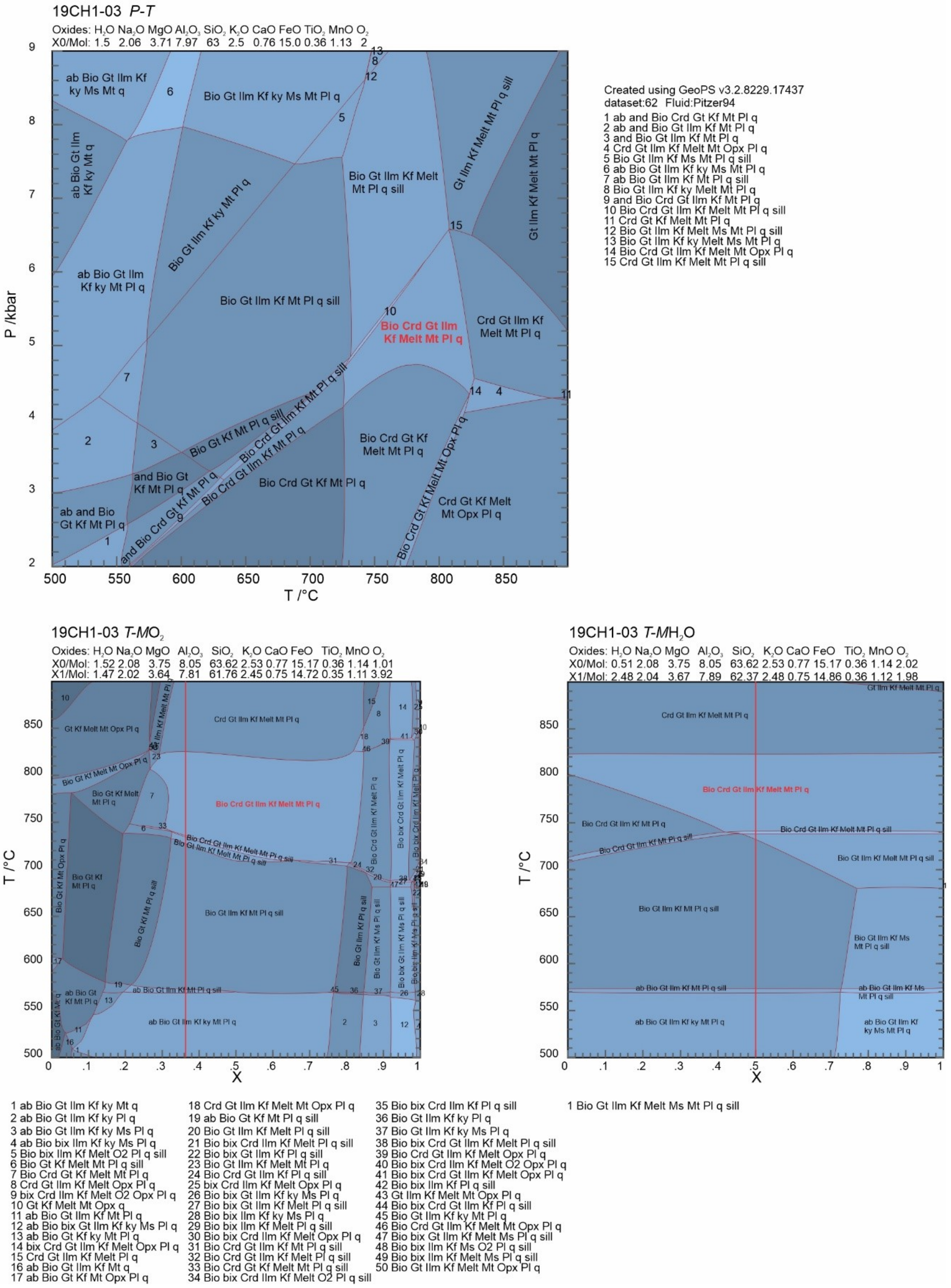

Chapter 3

Innovation in apatite geochronology opens new opportunity for copper systems in southern Australia

Statement of Authorship

Title of Paper	Uncovering the Cu system at the suspicious root of the Olympic Cu-Au Province, Gawler Craton: Direct evidence from in-situ Lu-Hf and U-Pb geochronology
Publication Status	☐ Published ☐ Accepted for Publication ☐ Submitted for Publication ☑ Unpublished and Unsubmitted work written in manuscript style
Publication Details	Yu, J., Hand, M., Payne, J., Morrissey, L., Simpson, A., Glorie, S., Chen, Y.J. 2023. Innovation in apatite geochronology opens new opportunity for copper systems in southern Australia.

Principal Author

Name of Principal Author (Candidate)	Jie Yu		
Contribution to the Paper	Field work Data collection and modelling Manuscript writing		
Overall percentage (%)	70		
Certification:	This paper reports on original research I conducted during the period of my Higher Degree by Research candidature and is not subject to any obligations or contractual agreements with a third party that would constrain its inclusion in this thesis. I am the primary author of this paper.		
Signature		Date	04 June 2023

Co-Author Contributions

By signing the Statement of Authorship, each author certifies that:

i. the candidate's stated contribution to the publication is accurate (as detailed above);

ii. permission is granted for the candidate in include the publication in the thesis; and

iii. the sum of all co-author contributions is equal to 100% less the candidate's stated contribution.

Name of Co-Author	Martin Hand		
Contribution to the Paper	Manuscript editing Ideas for manuscript		
Signature		Date	04 June 2023

Name of Co-Author	Justin Payne		
Contribution to the Paper	Field work Manuscript editing Ideas for manuscript		
Signature		Date	04 June 2023

Name of Co-Author	Laura Morrissey		
Contribution to the Paper	Field work Manuscript editing Ideas for manuscript		
Signature		Date	04 June 2023

Name of Co-Author	Alexander Simpson		
Contribution to the Paper	Data collection Manuscript editing		
Signature		Date	04 June 2023

Name of Co-Author	Stijn Glorie		
Contribution to the Paper	Manuscript editing		
Signature		Date	04 June 2023

Name of Co-Author	Yan-Jing Chen		
Contribution to the Paper	Manuscript editing Ideas for manuscript Data collection		
Signature		Date	04 June 2023

Please cut and paste additional co-author panels here as required.

Abstract

The Gawler Craton in southern Australia is renowned for the presence of its world-class iron oxide copper (IOCG) deposits which formed at 1590 Ma. These hydrothermal breccia deposits, including the giant Olympic Dam deposit, are dominated by hematite and formed in the upper crust. To the north, granulite facies magnetite-dominated rocks containing Cu mineralization have long been considered to represent the deeper expression of the IOCG system. However, in situ apatite Lu-Hf geochronology and age constraints from the granulite-grade wall rocks show the magnetite-hosted Cu mineralization is significantly younger and unrelated to the well-known Gawler Craton IOCG system. Apatite Lu-Hf ages from the granulite that predates Cu mineralization gives ages of 1490 Ma. Infiltration of Cu-bearing fluids resulted in recrystallisation of apatite, LREE mobilization and formation of secondary monazite. Lu-Hf ages for syn-mineralization apatite give 1460 Ma, consistent with ca. 1460 Ma U-Pb ages from secondary monazite. In contrast to the apatite in situ Lu-Hf ages, all apatite types produce a single U-Pb age of ca. 1460 Ma, demonstrating the ability of Lu-Hf to preserve a more complete history of apatite formation than U-Pb in high to medium temperature rock systems. The timing of mineralization coincides with the onset of Nuna fragmentation, representing a previously unrecognised mineralizing system in southern Australia that installed Cu in crust previously dehydrated during a long history of granulite-grade tectonic events. The recognition of this Cu system in rocks generally considered unprospective shows that continental breakup can rejuvenate metallic systems in otherwise unprospective crust.

1. Introduction

Obtaining robust dates for mineral deposits is necessary to identify the timing of their genesis and place them into a broader geodynamic framework (e.g., Selby et al., 2002; Gelcich et al., 2005; Li et al., 2017; Courtney-Davies et al., 2020; Manor et al., 2022). However, direct determination of the timing of mineralization is often challenging due to a lack of cogenetic minerals for conventional geochronology. Re-Os geochronology of sulfide phases is able to directly date mineralization but relies upon suitable phases being present and requires chemical digestion and chromatography methods prior to mass spectrometry (Stein et al., 2001). As a result, ore deposit geochronology commonly relies on proxies, such as bracketing mineralization by dating structurally controlled igneous rocks, if present, or dating regional alteration halos using U-Pb or Ar-Ar geochronology (Goldfarb et al., 2001; Sillitoe, 2010). Inferring the age of mineralization using the latter of these approaches runs the risk of obtaining the timing of earlier metamorphism or magmatism in the case of U-Pb geochronology on minerals such as zircon or monazite (Taylor et al., 2016), or cooling ages in the case of techniques such as mica Ar-Ar and apatite U-Pb geochronology (Selby et al., 2002; Harrison et al., 2009; Glorie et al., 2023).

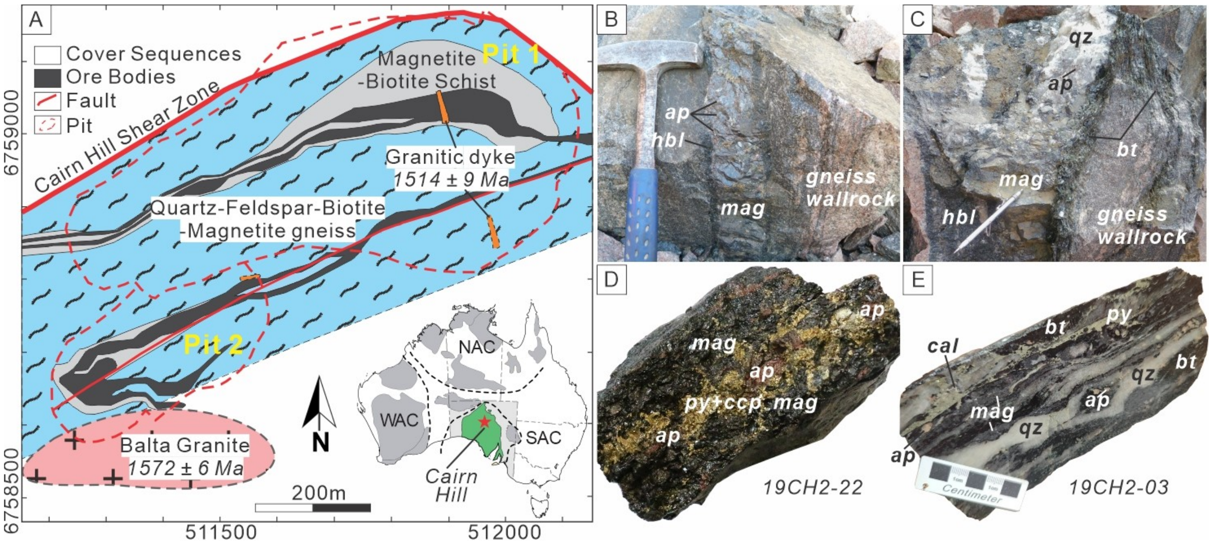

Fig. 3.1 (A) Location and geology map of the Cairn Hill deposit, adapted from Yu et al. (2023). (B) Representative iron ore hosted by gneiss, with hornblende flanking the magnetite and apatite lode. (C) Quartz-sulfide vein infills the magnetite lode, with minor hydrothermal apatite inside. (D) Late pyrite and chalcopyrite infill the brecciated magnetite and apatite (E) Quartz-sulfide-biotite-calcite vein, with recrystallization of magnetite and apatite.

Apatite [$Ca_5(PO_4)_3(F, Cl, OH)$] is a common calcium phosphate mineral in iron oxide copper-gold (IOCG) and iron oxide-apatite (IOA) deposits and has been proven to be a very useful U-Pb chronometer providing time constraints to mineralization, despite the moderate to significant amounts of non-radiogenic Pb (Groves et al., 2010; Stosch et al., 2011; Chew et al., 2014). However, IOCG and IOA deposits are primarily of the Precambrian age and may experience multiple hydrothermal and metamorphic overprinting (Williams et al., 2005; Groves et al., 2010; Li and Zhou, 2015; Ehrig et al., 2021; Campo-Rodríguez et al., 2022). The Lu-Hf system in apatite is more thermally robust than the apatite U-Pb system and can preserve growth ages at temperatures up to 650–730 °C (Barfod et al., 2005; Glorie et al., 2023), removing ambiguity as to whether apatite dates constrain the timing of mineralization as opposed to later thermal overprinting. While spatial resolution of conventional Lu-Hf dating is limited by the need for mineral dissolution and chemical separation of Hf from the HREEs (Barfod et al., 2005), the recent development of *in situ* Lu-Hf geochronology of apatite (Simpson et al., 2021; Glorie et al. 2023) provides an opportunity to test the utility of this isotope system for directly dating complex mineralization.

The Cairn Hill Fe-Cu deposit in the northern Olympic Cu-Au Province, Gawler Craton, South Australia, is an ideal location to demonstrate the utility of this method for constraining the age of mineralization (Fig. 3.1A; Yu et al., 2023). It has long been considered a deep, magnetite end-member of the IOCG family that is largely represented in the southern Olympic Province by the 1590 Ma hematite-dominated Olympic Dam, Carrapeteena and Prominent Hill deposits (Hayward and Skirrow, 2010; Reid and Fabris, 2015; Skirrow, 2022). Recently, Yu et al. (2023) revealed a composite IOCG deposit signature at Cairn Hill. Early Fe mineralization formed a magnetite-apatite-hornblende assemblage that was deformed at granulite facies conditions at 1490 Ma. Later Cu mineralization overprinted the magnetite assemblage and high-T metamorphism and was associated with the formation of a second generation of apatite with co-precipitated monazite. The presence of two texturally distinct generations of apatite creates a relatively unique opportunity to cross-reference the growth, resetting and recrystallization of apatite against U-Pb geochronology of monazite from metamorphic and mineralizing events within one deposit. We demonstrate that *in situ* apatite Lu-Hf dating can directly constrain the timing of mineralization and metamorphism in a complex deposit. Based on this, we identified a new Cu mineralization event in the extensively buried northern Gawler Craton.

2. Geological Setting

The Gawler Craton in southern Australia is one of the major components of Proterozoic Australia (Fig. 3.1A and S1; Hand et al., 2007). It consists of an Archean to earliest Paleoproterozoic nucleus surrounded by Palaeoproterozoic to early Mesoproterozoic basins and orogenic belts (Hand et al., 2007). Most notably, during the early Mesoproterozoic the 1595–1575 Ma Gawler Range Volcanics-Hiltaba Suite Large Igneous Province (Jagodzinski et al., 2023) was associated with extensive IOCG mineralization in the eastern Gawler Craton, including the world-class Olympic Dam deposit as well as other globally significant deposits, e.g., Prominent Hill and Carrapateena (Schlegel et al., 2018; Courtney-Davies et al., 2020). These large IOCG deposits formed in the upper crust (Reid and Fabris, 2015) and are preserved in comparatively strong crust bounded by younger orogenic belts that record high-temperature tectonism (Cutts et al., 2011; Morrissey et al., 2019, 2023; Bockmann et al., 2022; Yu et al., 2023). The northern and southeastern Gawler Craton underwent widespread deformation and high-temperature metamorphism at ca. 1600–1540 Ma, known as Kararan Orogeny (Hand et al., 2007; Payne et al., 2008; Cutts et al., 2011; Morrissey et al., 2019, 2022; Bockmann et al., 2022; Yu et al., 2023). Subsequent events are limited to localized ca. 1520 Ma metamorphism in the northern Gawler Craton (Reid et al., 2014) and minor magmatism at ca. 1500 Ma in the southern Gawler Craton (Jagodzinski et al., 2007). Along the Karari Shear Zone, high-temperature metamorphism at ca. 1490 Ma has been recently identified (Morrissey et al., 2023; Yu et al., 2023), followed by localized ca. 1460 Ma magmatism, metamorphism, and shear zone reactivation (Fraser et al., 2012; Morrissey et al., 2019).

The Cairn Hill deposit is located within the Cairn Hill Shear Zone in the northernmost Olympic Cu-Au Province and was previously considered a deeper expression of the large upper crustal IOCG deposits (Fig. S1; Reid and Fabris, 2015; Yu et al., 2023). The host rocks are dominated by quartz-feldspar-biotite-magnetite gneiss with a protolith age of ca. 1750 Ma (Fig. 3.1A). It has a foliation defined by biotite and magnetite, trending E–W coincident with the Cairn Hill Shear Zone. Iron mineralization predominantly comprises two sub-parallel magnetite-apatite-hornblende lodes within the shear fabric that formed prior to ca. 1580 Ma (Yu et al., 2023). Numerous cm- to dm-scale magnetite-apatite-hornblende (-albite) veins occur in the gneissic wall rock and share similar texture and orientation to the two major Fe lodes (Fig. 3.1B and 3.2A). Both magnetite-bearing lodes and veins are symmetrical, with magnetite and apatite growing in the center, and alteration halos of hornblende developing on both flanks. The hornblende surrounding the magnetite lodes has been locally replaced by orthopyroxene, plagioclase and clinopyroxene (Fig. 3.2B). The magnetite lodes are crosscut by ca. 1515 Ma granitic dykes that are wrapped into a shear fabric (Jogodzinski and Reid, 2015; Yu et al., 2023; Fig. 3.1A). Monazite from the gneissic wall rocks and the granitic dykes dominantly yields ages of ca. 1490 Ma, indicating the Cairn Hill deposit experienced granulite facies metamorphism and high-strain deformation at this time, and the conditions have been estimated to be 4.6–5.3 kbar, 740–770 °C (Yu et al., 2023).

The Fe mineralization and granulite facies gneissic fabrics are overprinted by Cu mineralization expressed by the formation of chalcopyrite + pyrite ± pyrrhotite ± bornite ± chalcocite ± sphalerite. The gangue minerals are dominated by quartz + biotite + chlorite ± carbonate ± siderite ± fluorite. Sulfides occur as infill along domains of brecciated magnetite-apatite or as sulfides + quartz ± biotite veins that crosscut the magnetite lodes and host gneiss (Fig. 3.1C–E, 3.2C). The Cu mineralization is proposed to be later than the ca. 1490 Ma high-grade metamorphism and deformation (Yu et al., 2023), but has not previously been dated directly. Low temperature thermochronometers including hornblende $^{40}Ar/^{39}Ar$, apatite U-Pb, and phlogopite $^{40}Ar/^{39}Ar$ ages range in age from ca. 1490–1460 Ma (Jagodzinski and Reid, 2015).

3. Methods

3.1 Apatite Lu-Hf geochronology

Representative samples of apatite were analyzed by *in-situ* Lu-Hf dating. Apatite samples were mounted and polished in 25 mm diameter epoxy disks. LA-ICP-MS Lu-Hf analyses were conducted at Adelaide Microscopy at the University of Adelaide. The analytical protocol followed the method of Simpson et al. (2021) and Glorie et al. (2022a, b), which is briefly introduced below. The Lu-Hf analyses were conducted using a RESOlution 193 nm excimer laser ablation system (Applied Spectra) with an S155 sample chamber (Laurin Technic) coupled to an Agilent 8900 ICP-MS/MS. A squid mixing device (Laurin Technic) was used to smooth the pulses of the laser. NH_3 was used as the reaction gas, supplied as a mixture of 10 % NH_3 in 90 % He. A flow rate of 3 mL/min (NH_3) was adopted to maximize the production of the +82 Hf reaction product ($Hf(NH)(NH_2)(NH_3)_3^+$) while maintaining sufficiently low Yb and Lu +82 (i.e., $REE(NH)(NH_2)(NH_3)_3^+$) for mass interference to be negligible. Laser spot diameters of 120 µm and high laser repetition rates of 10 Hz were used to increase sensitivity. The following isotopes (mass shifts included in brackets) were measured: ^{24}Mg, ^{27}Al, ^{43}Ca, $^{(89+85)}Y$, $^{(90+83)}Zr$, ^{172}Yb, ^{175}Lu, $^{(175+82)}Lu$, $^{(176+82)}Hf$, $^{(178+82)}Hf$. ^{175}Lu was monitored as a proxy for ^{176}Lu, and ^{178}Hf was monitored as a proxy for ^{177}Hf. Calculation of ^{176}Lu and ^{177}Hf

was performed assuming stable present-day $^{176}Lu/^{175}Lu$ and $^{177}Hf/^{178}Hf$ ratios, details of this correction can be found in Simpson et al. (2022).

LADR (Norris and Danyushevsky, 2018) was used to calculate background-subtracted ratios and correct instrument mass bias and drift for Lu-Hf ratios. NIST 610 glass was used as the primary reference material for Lu-Hf analysis (analyzed every 20–30 unknowns), using $^{176}Lu/^{177}Hf$ and $^{176}Hf/^{177}Hf$ composition of 0.1379 ± 0.005 and 0.282111 ± 0.000009, respectively, as determined by ID-MC-ICP-MS (Nebel et al., 2009). OD306 apatite (1597 ± 7 Ma; Thompson et al., 2016) was used to correct the matrix-induced fractionation. In-house reference apatites Bamble-1 (corrected Lu–Hf age: 1097 ± 5 Ma) and HR-1 (corrected Lu–Hf age: 343 ± 2 Ma) were monitored for accuracy checks and are in excellent agreement with previously published data (Glorie et al., 2022a, b). ISOPLOTR was used to calculate the inverse isochron and weighted mean ages (Vermeesch, 2018). The isochrons were anchored to an initial $^{177}Hf/^{176}Hf$ ratio of 3.55 ± 0.05, which covers the maximum variation in initial ratios on Earth (Simpson et al. 2021). The ^{176}Lu decay constant of 0.00001867 ± 0.00000008 Myr^{-1} (Söderlund et al., 2004) was used for all age calculations. Final reported uncertainties include the propagated uncertainty from the correction standard OD306.

3.2 Apatite U-Pb geochronology and trace elements

Apatite U–Pb isotopic data and trace elements were collected by LA–ICP–MS on an Agilent 8900 ICP-MS/MS coupled with a RESOlution 193 nm excimer laser ablation system at Adelaide Microscopy, following the analytical procedures and instrumental settings outlined in Glorie et al. (2017). Data reduction was carried out using the VisualAge_UcomPbine and X_Trace_Elements_IS data reduction software (DRS) in Iolite (Paton et al., 2011). Isoplot 4.15 (Ludwig, 2012) was used for U–Pb calculations. Regression lines in Tera-Wasserburg plots were all unanchored to allow age calculations without assumptions about the initial Pb isotopic composition. Madagascar apatite (MAD; ID-TIMS age of 473.5 ± 0.7 Ma; Thomson et al., 2012; Chew et al., 2014) was used as the primary reference material for apatite U–Pb age calculations, and NIST 610 glass was used as the primary standard for trace element concentration determinations. 401 and McClure apatite were used as secondary reference material to ensure data reliability (Schoene and Bowring, 2006; Thompson et al., 2016). We obtained a weighted mean $^{206}Pb/^{238}U$ age of 529.4 ± 4.6 Ma (n = 24, MSWD = 1.2) for 401 apatite and ^{207}Pb corrected weighted mean age of 524.6 ± 3.2 Ma (n = 24, MSWD = 0.92) for McClure apatite.

Elemental mapping was conducted for complexly zoned apatite grains using Cameca SX51 electron microprobe at Adelaide Microscopy with a beam current of 200 nA and an accelerating voltage of 15 kV.

3.3 Monazite U-Pb geochronology and trace elements

While monazite inclusions are common within and along the edges of altered apatite, most monazite grains are not large enough for

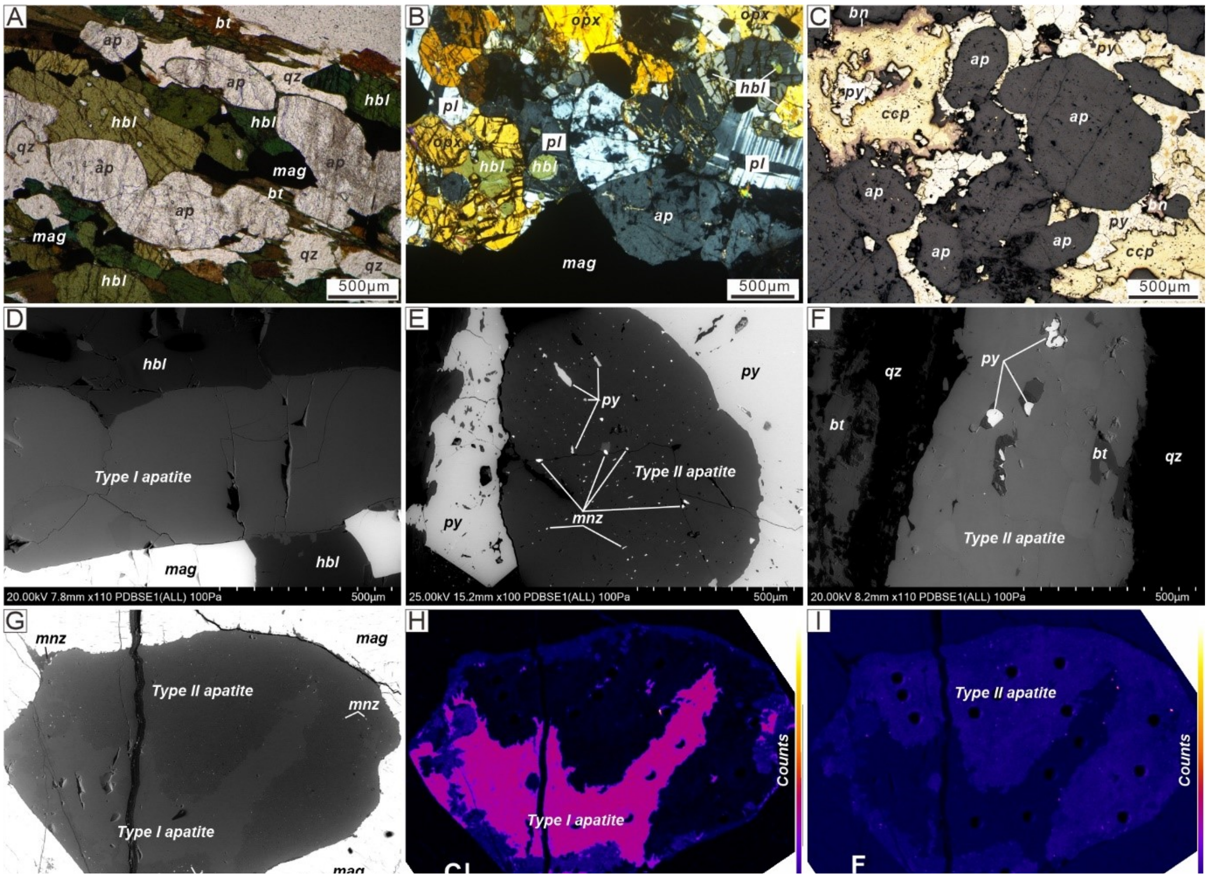

Fig. 3.2 (A) Magnetite + apatite + hornblende bands hosted in the gneiss. (B) Hornblende metamorphosed to orthopyroxene and plagioclase. (C) Sulfides infill the interval of early apatite, with bornite on the oxidized chalcopyrite. (D) BSE image of Type I apatite from the magnetite-apatite-hornblende lode. (E) BSE image of Type II apatite enclosed by pyrite containing inclusions of pyrite and monazite. (F) BSE image of Type II apatite containing inclusions of pyrite and biotite. (G-I) Type II apatite replacing Type I apatite, with development of abundant fine-grained monazite inclusions. Type I is Cl-rich while Type II is F-rich as shown by X-Ray mapping.

subsequent geochronology work. Detailed SEM imaging was conducted to identify monazite and reveal the relationship between monazite and apatite. Five samples contain monazite grains of sufficient sizes for dating. After checking the internal structure of the monazites, *in-situ* U-Pb dating and trace element analyses were synchronously conducted on an Agilent 8900 ICP-MS/MS coupled with a RESOlution 193 nm excimer laser ablation system. The ablation of monazite was performed with a spot size of 9–13 μm depending on the grain size, a frequency of 5 Hz, and laser energy of 4–5 J/cm^2. The total acquisition time for each analysis was 60 s, including 30 s of background measurement, followed by 30 s of laser ablation. Common lead was not corrected for in the age calculations due to unresolvable interference of ^{204}Hg on the ^{204}Pb isotope peak. Mass 204 was monitored during analysis to compensate for this, and analyses would be omitted if observed appreciable common lead. Age calculation and trace element content of monazite were reduced using Iolite (Paton et al., 2011). Mass bias, elemental fractionation and instrument drift were corrected using the monazite standard MAdel (TIMS normalization data: ^{207}Pb/^{206}Pb age = 492.01 ± 0.77 Ma, ^{206}Pb/^{238}U age = 517.9 ± 2.6 Ma and ^{207}Pb/^{235}U age = 513.13 ± 0.20 Ma; Payne et al., 2008). Data accuracy was monitored by analyses

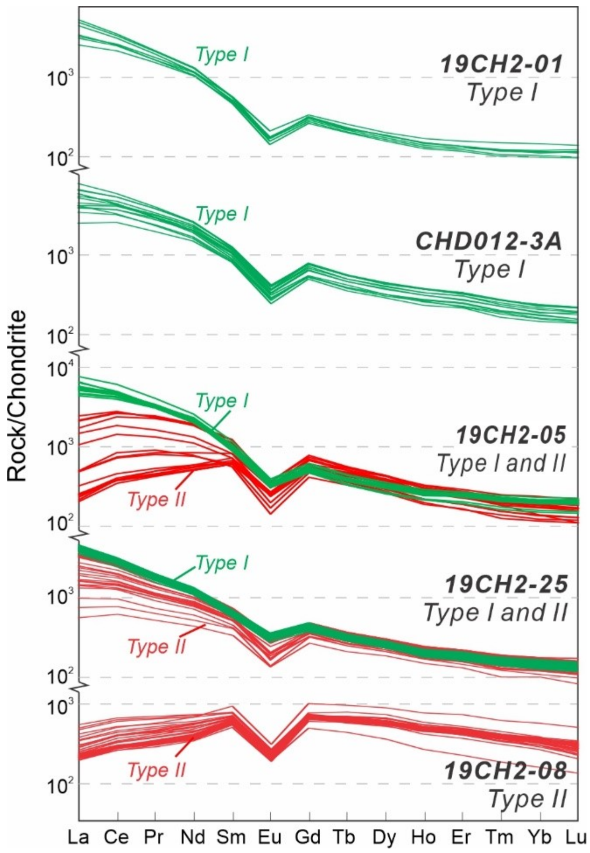

Fig. 3.3 REE patterns of two types of apatite.

of in-house monazite standard 222 ($^{206}Pb/^{238}U$ age 450.2 ± 3.4 Ma; Maidment, 2005) and Ambat ($^{206}Pb/^{238}U$ age ca. 520 Ma), and NIST 610 glass was used as the external standard for trace elements. The standard was analyzed every 20 unknown analyses. Throughout the course of this study standard 222 yielded a $^{206}Pb/^{238}U$ weighted mean age of 448.0 ± 1.4 (n = 26/28, MSWD = 1.3, prob = 0.14) and Ambat yielded a $^{206}Pb/^{238}U$ weighted mean age of 514.5 ± 2.6 (n = 27/28, MSWD = 3.6, prob. = 0). These values are within the expected external uncertainty of the LA-ICP-MS method of 1–2 % (Horstwood et al., 2016). All monazite analyses were assumed to have 20 wt. % Ce for the trace element contents calculation. Monazite U–Pb data were plotted using Isoplot 4.15 (Ludwig, 2012).

4. Results

4.1 Petrography of apatite and monazite

Apatite is the most common REE-bearing mineral at Cairn Hill. Two generations of apatite can be distinguished both petrographically and geochemically (Fig. 3.2). Type I apatite occurs in the magnetite-apatite-hornblende lodes/veins (Fig. 3.1B and 3.2A), is dominantly chlorapatite, colorless and euhedral, and ranges from 50 µm to 2 cm. Type I apatite appears homogeneous in back-scattered electron (BSE) images and contains few inclusions (Fig. 3.2D and G). It is enriched in LREE and depleted in HREE (Fig. 3.3). Type II apatite is fluorapatite, and pink to reddish in color (Fig. 3.1D, E and 3.2E–I). It replaces the type I apatite where Cu mineralization occurs and normally displays sharp contact with the relict type I apatite. In contrast to type I apatite, type II apatite displays a lower BSE response, has a porous texture and contains inclusions of pyrite, chalcopyrite and monazite. It is also variably depleted in LREE relative to type I apatite (Fig. 3.3).

Monazite is closely related to the development of type II apatite during the Cu mineralization and fluid-induced alteration and usually occurs as tiny inclusions in type II apatite and peripheral biotite (Fig. 3.4). Minor monazite is present as larger grains (> 100 µm) along the boundaries of apatite grains or in fractures within apatite. Monazite is cogenetic with chalcopyrite, pyrite, bornite, chalcocite, and allanite, locally forms coronas on chalcopyrite (Fig. 3.4I). The monazite grains display no zonation under high-resolution BSE imaging.

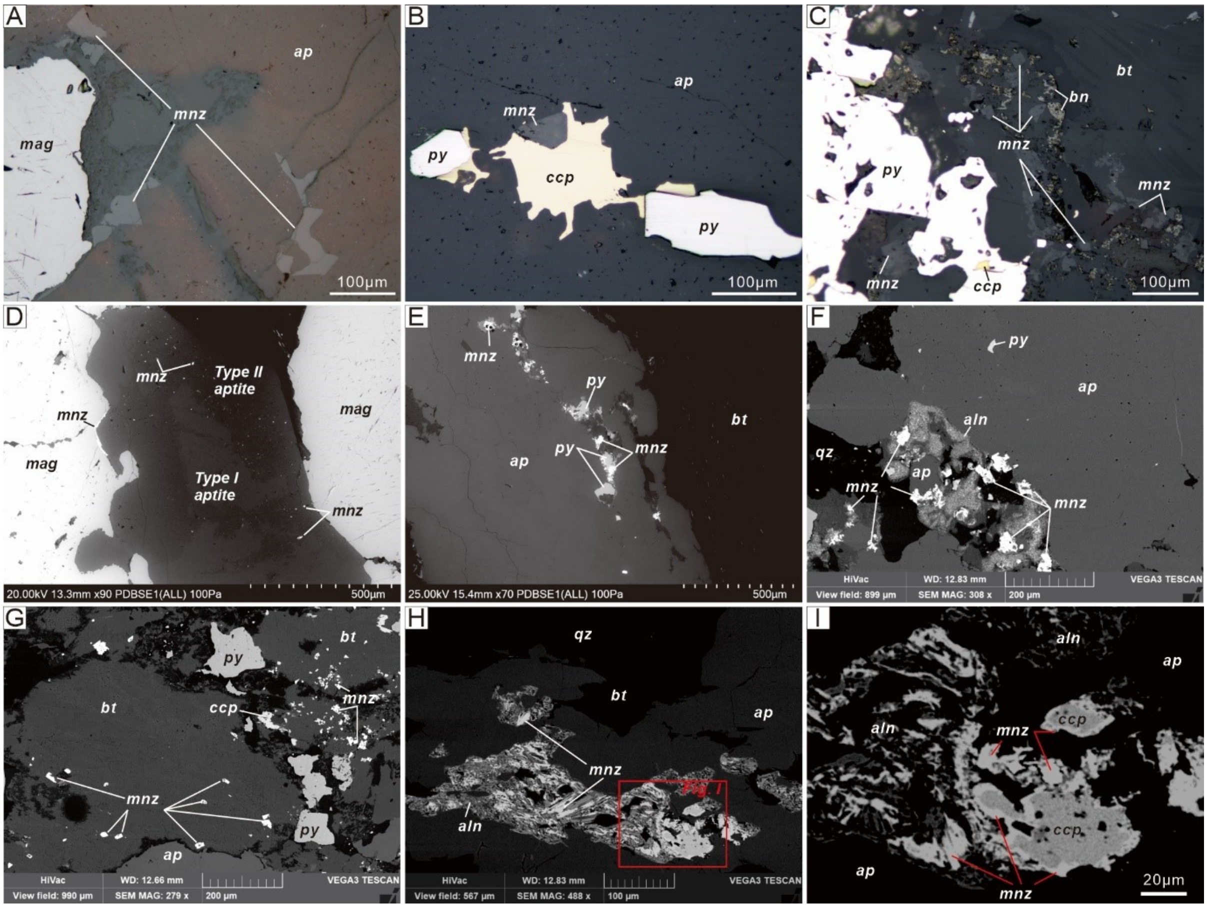

Fig. 3.4 (A) Reflected light image showing monazite located along grain boundaries and fractures of the Type II apatite. (B) RL image of euhedral monazite coexists with chalcopyrite and pyrite along a fissure in Type II apatite. (C) RL image of abundant monazite grains between domains of pyrite and biotite. (D) BSE image of monazite grains along the magnetite/apatite boundary or as inclusions in the Type II apatite. (E) Monazite and pyrite along apatite crystal gap. (F) Monazite and allanite on the edge of apatite and quartz. (G) Fine-grained monazite disseminated in the biotite in Cu ores. (H and I) Allanite, monazite and chalcopyrite along the altered apatite boundary, and monazite forms corona around the chalcopyrite.

Table 1 Summary of sample description and geochronology results

Sample	Mineral assemblage	Apatite type	Lu-Hf apatite age ± 2σ (Ma)	U-Pb apatite age ± 2σ (Ma)	U-Pb monazite age ± 2σ (Ma)
19CH2-01	mag+hbl+ap	I	1492 ± 22		
CHD012-3A	mag+hbl+bt+qz+ap	I	1490 ± 21		
19CH2-05	mag+py+ap	I	1495 ± 28		1461 ± 7
		II	1462 ± 25		
19CH2-25	mag+py+ccp+ap	I		1452 ± 11	1471 ± 30
		II	1462 ± 31	1440 ± 28	
19CH2-08	bt+ccp+py+cal+qz+ap	II	1461 ± 23	1456 ± 26	
19CH2-22	mag+py+ccp+ap	I+II			1468 ± 12
19CH2-03	mag+qz+bt+py+cpy+cal+ap	I+II			1455 ± 27
19CH2-07	bt+qz+ccp+py+bn+cc+ap	II			1467 ± 14

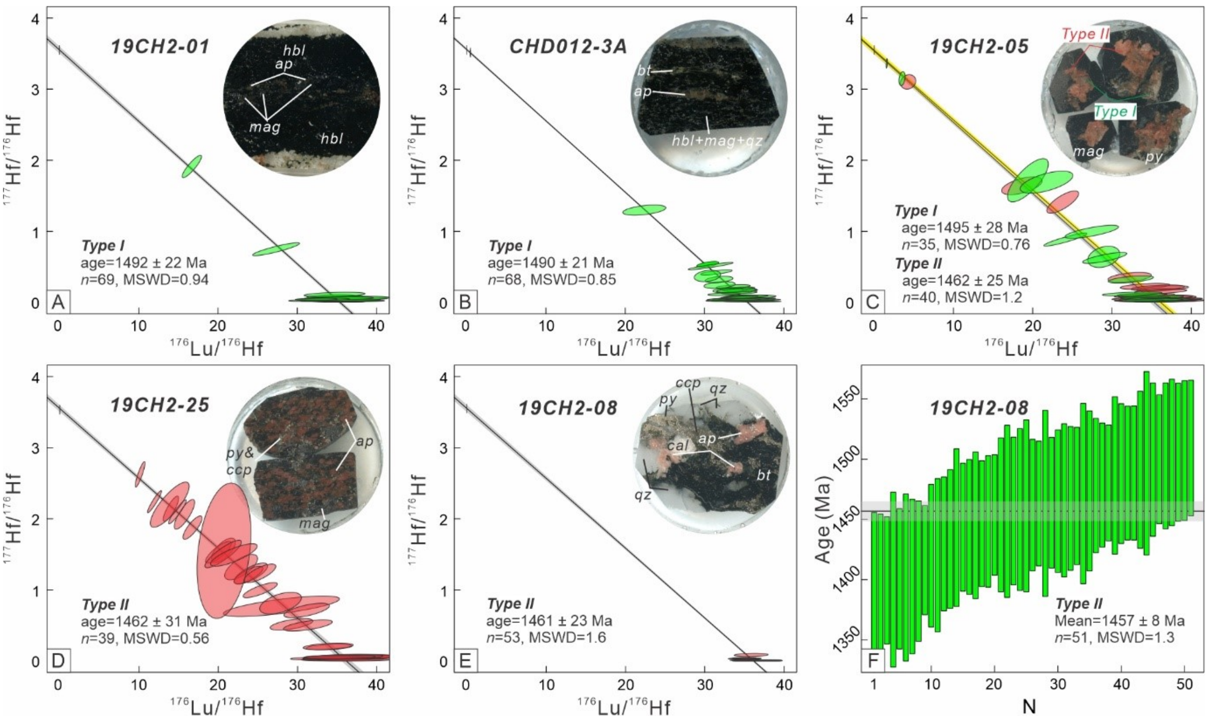

Fig. 3.5 (A–E) Apatite Lu-Hf inverse isochron ages for samples 19CH2-01, CHD012-3A, 19CH2-05, 19CH2-25 and 19CH2-08. (F) Weighted mean Lu-Hf age of sample 19CH2-08.

The multiple generations and petrographic relationships of apatite and monazite in samples from the Cairn Hill deposit provide a unique opportunity to constrain the timing of Cu mineralization and comment upon the robustness of the Lu-Hf system in apatite. Eight samples are used for further geochronology study, which include two samples of the magnetite-apatite-hornblende lode with no Cu overprint (19CH2-01 and CHD012-3A) and six samples of Cu-bearing ore (19CH2-05, -25, -08, -22, -03, and -07). A sample summary is provided in Table 1.

4.2 Apatite in-situ Lu-Hf geochronology

Samples 19CH2-01 and CHD012-3A only contain type I apatite and these samples define inverse isochron Lu-Hf dates of 1492 ± 22 Ma (n = 69, MSWD = 0.94) and 1490 ± 21 Ma (n = 68, MSWD = 0.85), respectively (Fig. 3.5A and B).

In sample 19CH2-05, type I apatite grains have been partly replaced by type II apatite with sharp contact boundaries (Fig. 3.2G–I). Type I apatite is enriched in LREE and yields an inverse isochron Lu-Hf date of 1495 ± 28 Ma (n = 35, MSWD = 0.76; Fig. 3.3 and 5C). Type II apatite displays varying degrees of LREE depletion, and yields an inverse isochron Lu-Hf date of 1462 ± 25 Ma (n = 40, MSWD = 1.2).

Sample 19CH2-25 contains type I and II apatite, distinguished by their different color, BSE brightness and REE patterns. Limited by the grain size, only type II apatite in sample 19CH2-25 is analyzed for Lu-Hf geochronology, and 39 spots define an inverse Lu-Hf isochron date of 1462 ± 31 Ma (MSWD = 0.56; Fig. 3.5D). Sample 19CH2-08 only contains type II apatite, characterized by LREE depletion (Fig. 3.3). It has negligible common Hf (^{176}Hf/^{177}Hf > 40) compared to samples 19CH2-05 and 19CH2-25,

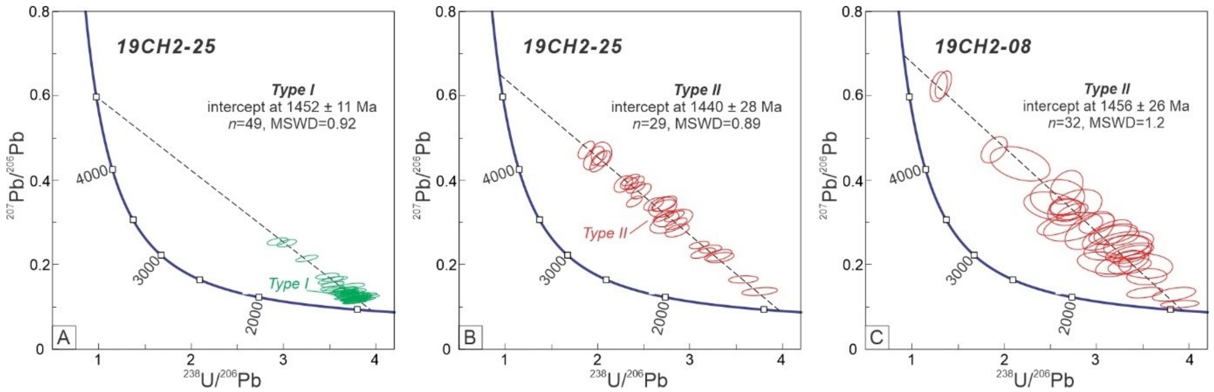

Fig. 3.6 Apatite U-Pb ages of samples 19CH2-25 and 19CH2-08.

and yields an inverse isochron Lu-Hf date of 1461 ± 23 Ma (n = 53, MSWD = 1.6; Fig. 3.5E). "Single spot ages" are calculated from ^{176}Hf/^{176}Lu ratios for sample 19CH2-08, and the corresponding single spot ages range from 1398 ± 60 Ma to 1511 ± 54 Ma and 51 spots define a weighted mean age of 1457 ± 8 Ma (MSWD = 1.3; Fig. 3.5F). All apatite Lu-Hf results are provided in Table S1.

4.3 Apatite U-Pb geochronology

Type I and II apatite from sample 19CH2-25 yielded similar U-Pb intercept dates of 1452 ± 11 Ma and 1440 ± 28 Ma, respectively. Type II apatite in sample 19CH2-08 yielded a U-Pb intercept date of 1456 ± 26 Ma. Type II apatite contains more initial Pb than type I apatite (Fig. 3.6 and Table S2).

4.4 Monazite U-Pb geochronology

Monazite U-Pb age data were obtained from five samples containing Type II apatite (Fig. 3.4). A total of 120 spots fall on the concordia curve (Fig. 3.7), 11 of which are analyzed by a 9 μm laser spot, and the rest are all analyzed by a 13 μm laser spot. The results are listed in Table S3 and only analyses within 2σ uncertainty of concordia are used for the weighted mean age calculation. From sample 19CH2-05, 60 analyses yield a weighted mean ^{207}Pb/^{206}Pb age of 1461 ± 7 Ma (MSWD = 0.45, prob. = 1.0) with Th contents of 1205–6780 ppm and U contents of 65–693 ppm. Twenty-seven analyses from 19CH2-22 yield a weighted mean ^{207}Pb/^{206}Pb date of 1468 ± 12 Ma (MSWD = 1.18, prob. = 0.24) with Th contents of 459–7445 ppm and U contents of 143–358 ppm. The three remaining samples, 19CH2-25, 19CH2-03, and 19CH2-07, have low volumes of monazite but yield weighted mean U-Pb dates of 1471 ± 30 Ma (n = 7, MSWD = 0.57), 1455 ± 7 Ma (n = 10, MSWD = 0.24) and 1467 ± 14 Ma (n = 16, MSWD = 0.48). Their Th contents vary from 964–11293 ppm, 44–3019 ppm and 21–8262 ppm, respectively, with U contents of 74–764 ppm, 107–438 ppm and 64–669 ppm, respectively. The REE pattern of all monazite is uniform with LREE enrichment, HREE depletion, and negative Eu anomalies (Table S3).

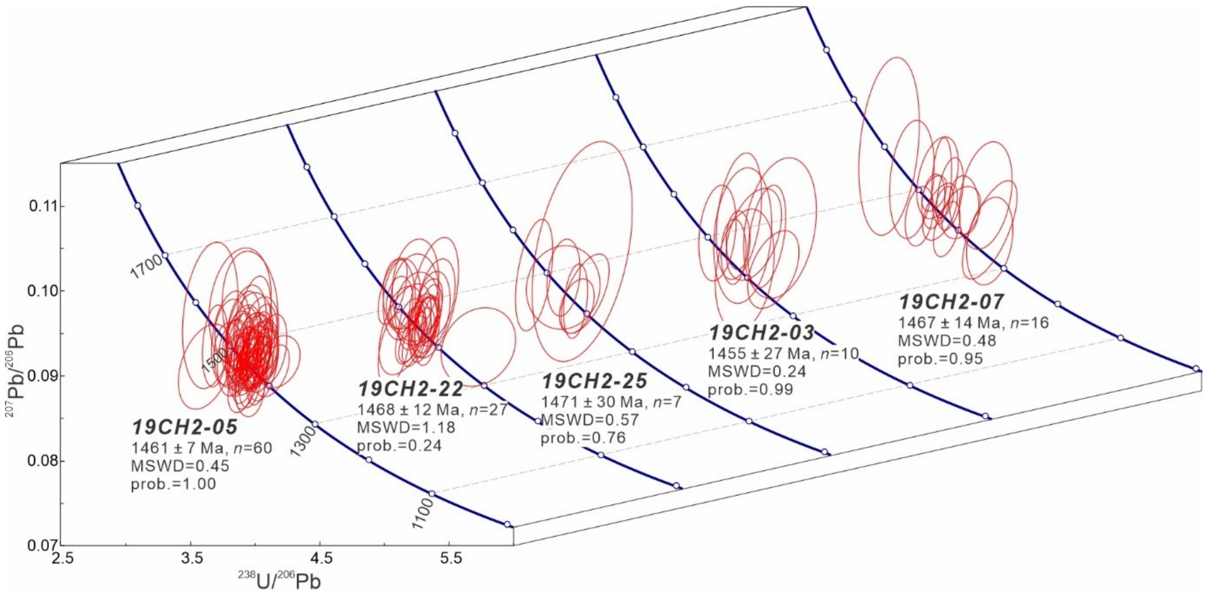

Fig. 3.7 Monazite U-Pb geochronology results.

5. Discussion

5.1 Direct and rapid dating of hydrothermal events using in-situ apatite Lu-Hf geochronology

Apatite is a common mineral associated with many forms of mineralization (Groves et al., 2010; Harlov, 2015; Mao et al., 2016). It could be highly susceptible to metasomatism/alteration via the coupled dissolution-reprecipitation (CDR) process (Putnis, 2009), which can be fingerprinted by mobility of trace elements, e.g., Mn, Sr, U, Th, S, F, Cl and REEs (Harlov et al., 2002; Bonyadi et al., 2011; Stosch et al., 2011; Harlov, 2015). The ability to determine apatite age with a thermally robust geochronometer can define undisturbed mineralization time, and the spatial resolution afforded by in-situ methods allows for a finer delineation of complex mineralization and overprinting.

Type I apatite is syngenetic with hornblende + magnetite mineralization that formed at ca. 1580 Ma, and experienced high-grade metamorphism and deformation at ca. 1490 Ma with the hornblende replaced by orthopyroxene + clinopyroxene or orthopyroxene + plagioclase (Fig. 3.2B; Yu et al., 2023). Conditions during this event have been estimated to be 4.6–5.3 kbar and 740–770 °C. Type I apatite yield consistent Lu-Hf ages of ca. 1490 Ma, coinciding with the monazite geochronology from host rocks, indicating the Lu-Hf system of Type I apatite has been reset by the ca. 1490 Ma high-grade metamorphism and deformation that overprinted the magnetite mineralization (Yu et al., 2023). Previous work has interpreted the closure temperature of Lu-Hf in apatite to be ~650–730 °C (Barfod et al., 2005; Glorie et al., 2023). This range is below the interpreted peak temperatures of the ca. 1490 Ma event and confirms that apatite Lu-Hf systematics are reset at these conditions. However, the retention of the ca. 1490 Ma age by Type I apatite demonstrates that it does not represent a cooling age and is not reset during the subsequent Cu mineralization event.

During the infiltration of Cu-bearing fluids into Fe-mineralized parts of the Cairn Hill Shear Zone, alteration and recrystallization of Type I apatite led to the development of Type II apatite. This fluid-facilitated process resulted in sharp boundaries between the recrystallized and pristine apatite rather than gradual self-diffusion profiles. This was accompanied by the removal of LREE from Type I apatite (Fig. 3.3) leading to the development of small amounts of monazite within LREE-depleted Type II apatite (Fig. 3.4). The mechanism of this coupled behavior has been well explained by a series of experiments under a wide range of PT conditions, where the formation of monazite/xenotime inclusions and rim grains is induced by pure H_2O, H_2O-CO_2 fluids, and aqueous solutions with KCl, H_2SO_4 and HCl (Harlov, 2015 and references therein). Monazite grains within Type II apatite from different samples from Cairn Hill yield consistent U-Pb ages of ca. 1460 Ma (Fig. 3.7). The 1460 Ma age is younger than the monazite ages in the deposit wall rock, which records ca. 1580 Ma and 1490 Ma high-grade metamorphism (Yu et al., 2023), but are in excellent agreement with the apatite Lu-Hf ages of ca. 1460 Ma obtained from Type II apatite (Fig. 3.5C–F). Previously, monazite inclusions and LREE depletion have been reported in apatite from natural ore deposits that have experienced complex hydrothermal overprinting (Torab and Lehmann, 2007; Harlov, 2015 and references therein). However, their complex overprinting histories are rarely precisely dated (Torab and Lehmann, 2007; Bonyadi et al., 2011; Li and Zhou, 2015), often because of (1) the small size and low Th and U contents of monazite inclusion, (2) inherited common Pb in apatite, and (3) modification of apatite U-Pb system by later thermal event. In addition, monazite generally contains more than 10^3–10^5 times the LREE content than apatite, and thus the fluid-induced alteration of apatite does not necessarily form monazite (Broom-Fendley et al., 2016). The utility of the *in-situ* apatite Lu-Hf method provides a simpler alternative for directly recording the timing of hydrothermal fluid activity and further allows us to correlate geochronology to the geochemical and isotopic characteristics of apatite.

Despite the overlapping uncertainties, the ca. 1460 Ma Lu-Hf ages for type II apatite are systematically younger than the ca. 1490 Ma Lu-Hf ages from type I apatite (Fig. 3.5). This age offset indicates the apatite *in-situ* Lu-Hf method approaches an age resolution of 2% during the Mesoproterozoic. Despite the large laser spot size (120 µm) of the *in-situ* Lu-Hf method, the two sets of ages extracted from complex apatite grains have shown the excellent spatial resolution of the method (Fig. 3.2G and 3.4D), which would be difficult for conventional solution Lu-Hf dating to match (Barfod et al., 2005). For apatite with higher Lu concentrations, a smaller laser spot size (e.g., 67 µm) could be used to achieve better spatial and temporal resolution.

In contrast to the distinct Lu-Hf apatite ages, the U-Pb system gives an age of ca. 1460 Ma for all the apatites (Fig. 3.6), irrespective of textural setting and geochemistry, and concurrent or slightly younger than the timing of fluid activity and mineralization defined by monazite U-Pb and

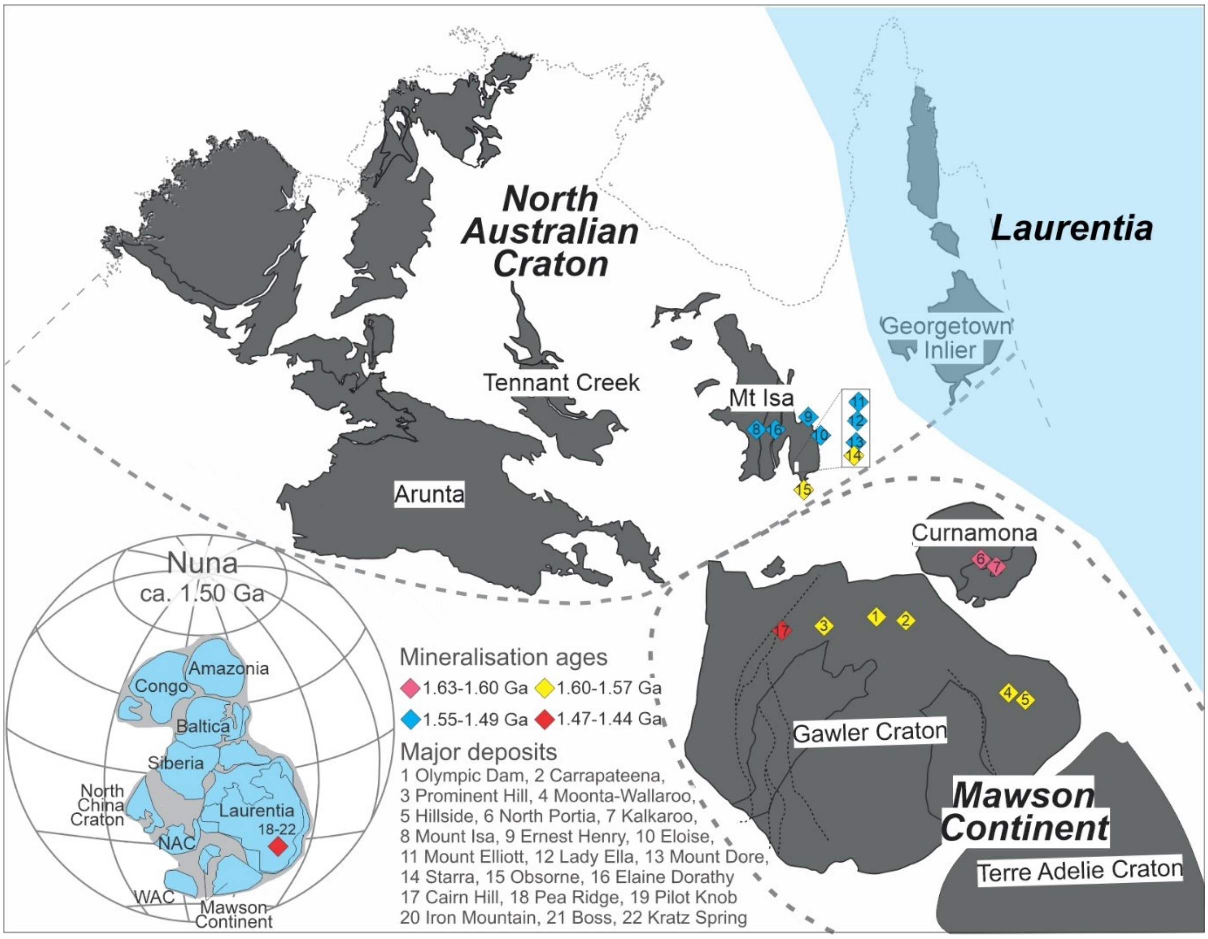

Fig. 3.8 Distribution of latest-Palaeoproterozoic to early-Mesoproterozoic deposits within the North Australian Craton (NAC) and South Australian Craton (SAC), modified after Kirscher et al. (2020) and Bockmann et al. (2023). The references for mineralization ages are in Day et al. (2016), Bockmann et al. (2023), and Sullivan et al. (2023).

apatite Lu-Hf ages. The ca. 30 Ma age difference between Lu-Hf and U–Pb in the type I apatite further highlights the Lu-Hf system in apatite can preserve a higher temperature history compared to U-Pb.

5.2 Young ca. 1460 Ma Cu mineralization in the Gawler Craton

The combination of pre-1580 Ma Fe-mineralization and post-1490 Ma Cu mineralization at Cairn Hill has created a composite IOCG mineral system signature in the northern Olympic IOCG province (Yu et al., 2023). The coupled apatite Lu-Hf ages and secondary monazite U-Pb ages indicate the age of Cu mineralization is ca. 1460 Ma. To the best of our knowledge, this is the first application of apatite in-situ Lu-Hf geochronology to determine the timing of mineralization. Our new result indicates the magnetite-hosted Cu-Au mineralization at Cairn Hill did not form at the same time as the giant 1590 Ma Olympic Dam IOCG deposit and the associated other large IOCG deposits in the eastern Gawler Craton (Courtney-Davies et al., 2020). Therefore, Cu mineralization in the deeply exhumed northern Olympic Cu-Au Province is not an expression of the deep roots of the globally significant upper crustal IOCG deposits in the eastern Gawler Craton as has generally been assumed (Hayward and Skirrow, 2010; Reid and Fabris, 2015; Skirrow, 2022).

The Gawler Craton (South Australian Craton) has a prolonged linked history to the North Australian Craton from the Archean to early Mesoproterozoic (Fig. 3.8; Cawood and Korsch, 2008; Payne et al., 2009), with subsequent rifting between 1.5 Ga and 1.35 Ga (Giles et al., 2004; Aitken et al., 2016; Morrissey et al., 2019). The northern Gawler Craton is thus a key region that connects the world-class Olympic IOCG province in the Gawler Craton and the Cloncurry IOCG province in the North Australian Craton (Hand et al., 2007; Duncan et al., 2011; Reid and Fabris, 2015; Bockmann et al., 2023 and references therein). The time window of the Olympic IOCG mineralization coincides with extensive magmatism between ca. 1600–1570 Ma (e.g., Gawler Range Volcanics and Hiltaba Suite granites; Jagozdinski et al., 2023). The Cloncurry IOCG province has IOCG deposits largely between 1550 Ma and 1490 Ma (Duncan et al., 2011), with the younger phase of mineralization ranging from 1515–1490 Ma related to the intrusion of A-type Williams-Naraku batholith (Betts et al., 2007; Duncan et al., 2011). The ca. 1460 Ma Cu mineralization in the extensively buried northern Gawler Craton is temporally and spatially distinct from the aforementioned IOCG provinces and may represent a continuation of the Cloncurry IOCG province or a previously unknown phase of Cu mineralization in southern Mesoproterozoic Australia.

The timing of Cu mineralization at Cairn Hill coincides with ca. 1460 Ma A-type magmatism in the northern Gawler Craton tied to the breakup of the Nuna supercontinent and the associated fragmentation of Mesoproterozoic Australia (Morrissey et al., 2019). In this case, mantle upwelling may introduce melt and metal to form young Cu systems in the dehydrated and refractory crust modified by multiple high-grade metamorphism (Reid and Hand, 2012; Yu et al., 2023). Lithospheric-scale shear zones that were active at this time (Fraser et al., 2012) are logical pathways for Cu introduction into the crust. Notably, the mineralized Cairn Hill Shear Zone is a lower-order splay from one of these major structures (Fig. 3.1A and S1). Similar lower-order splays elsewhere in the Gawler Craton may also be prospective for Cu mineralization, in the same way lower-order structures in orogenic Au systems are typically more prospective than the first-order lithospheric scale structures (Breeding and Ague, 2002; Groves et al., 2020). It is also worth noting that Cu mineralisation and A-type magmatism in the northern Gawler Craton occurred after the major magmatism-mineralization event throughout eastern Australia. However, on a global scale, they coincide with the A-type magmatism of granite-rhyolite province (ca. 1500–1440 Ma) and the IOA and IOCG deposits therein (e.g., Pea Ridge, Pilot Knob, Iron Mountain, Boss; ca. 1470–1440 Ma) in southern Laurentia (Fig. 3.8; Day et al., 2016 and references therein; Sullivan et al., 2023). Laurentia is commonly proposed to be contiguous with eastern Australia in Nuna supercontinent reconstructions (e.g., Payne et al., 2009; Kirscher et al., 2020), and develop widespread magmatism, high-T metamorphism, and deformation which are coeval with and stylistically similar to eastern Australia during ca. 1500–1400 Ma (Morrissey et al., 2019 and references therein). The recognition of ca. 1460 Ma IOCG and IOA mineralisation in the northern Gawler Craton and southern Laurentia may provide more evidence for their connection in Nuna reconstruction, or they may have developed in similar tectonic settings of rifting within the Nuna supercontinent or intracontinental extension (Groves et al., 2010). Importantly, the results of this study demonstrate the value of the in situ Lu-Hf geochronology of apatite as a tool for determining the age of mineralizing events allowing them to be placed in accurate geodynamic frameworks.

6. Conclusion

Cairn Hill Fe-Cu deposit develops two generations of apatite formed by two distinct mineralization events, separated by a phase of granulite facies metamorphism. Type I apatite within deformed magnetite lodes yields in-situ Lu-Hf ages of ca. 1490 Ma, consistent with granulite facies metamorphism. During the infiltration of Cu-bearing fluids, type I apatite was altered to type II apatite, with the removal of LREE and the development of secondary monazite. Type II apatite yields Lu-Hf ages of ca. 1460 Ma, consistent with ca. 1460 Ma U-Pb ages of monazite that formed during alteration of type I apatite. In contrast to the two apatite in situ Lu-Hf ages, all apatite types produce a single U-Pb age of ca. 1460 Ma, previously attributed to regional cooling. Our new data demonstrate the utility of the in-situ apatite Lu-Hf method for unraveling a complex mineral deposit with closely spaced metamorphism and mineralization events. The data identify a previously unknown Cu mineralization event in the Gawler Craton at ca. 1460 Ma, coinciding with the onset of Nuna fragmentation.

Acknowledgments

This project was supported by ARC Linkage Project LP160100578 (JP and MH), ARC Discovery Project DP220103037 (MH and SG), the Mineral Exploration Cooperative Research Centre (MinEX CRC) and the China Scholarship Council. LJM is supported by an ARC DECRA Fellowship DE210101126. SG is supported by an Australian Research Council Future Fellowship (FT210100906). K Faure is thanked for his assistance and discussions in the field. S Gilbert, B Wade, and A McFadden are thanked for their technical support at Adelaide Microscopy.

References

Aitken, A.R.A., Betts, P.G., Young, D.A., Blankenship, D.D., Roberts, J.L., Siegert, M.J., 2016. The Australo-Antarctic Columbia to Gondwana transition. Gondwana Research 29, 136-152.

Barfod, G.H., Krogstad, E.J., Frei, R., Albarède, F., 2005. Lu-Hf and PbSL geochronology of apatites from Proterozoic terranes: A first look at Lu-Hf isotopic closure in metamorphic apatite. Geochimica et Cosmochimica Acta 69, 1847-1859.

Betts, P.G., Giles, D., Schaefer, B.F., Mark, G., 2007. 1600–1500 Ma hotspot track in eastern Australia: implications for Mesoproterozoic continental reconstructions. Terra Nova 19, 496-501.

Bockmann, M.J., Hand, M., Morrissey, L.J., Payne, J.L., Hasterok, D., Teale, G., Conor, C., 2022. Punctuated geochronology within a sustained high-temperature thermal regime in the southeastern Gawler Craton. Lithos 430-431, 106860.

Bockmann, M.J., Payne, J.L., Hand, M., Morrissey, L.J., Belperio, A.P., 2023. Linking the Gawler Craton and Mount Isa Province through hydrothermal systems in the Peake and Denison Domain, northeastern Gawler Craton. Geoscience Frontiers, 101596.

Bonyadi, Z., Davidson, G.J., Mehrabi, B., Meffre, S., Ghazban, F., 2011. Significance of apatite REE depletion and monazite inclusions in the brecciated Se–Chahun iron oxide–apatite deposit, Bafq district, Iran: insights from paragenesis and geochemistry. Chemical Geology 281, 253-269.

Breeding, C.M., Ague, J.J., 2002. Slab-derived fluids and quartz-vein formation in an accretionary prism, Otago Schist, New Zealand. Geology 30, 499-502.

Broom-Fendley, S., Styles, M.T., Appleton, J.D., Gunn, G., Wall, F., 2016. Evidence for dissolution-reprecipitation of apatite and preferential LREE mobility in carbonatite-derived late-stage hydrothermal processes. American Mineralogist 101, 596-611.

Campo-Rodríguez, Y.T., Schutesky, M.E., de Oliveira, C.G., Whitehouse, M.J., 2022. Unveiling the polyphasic evolution of the Neoarchean IOCG Salobo deposit, Carajás Mineral Province, Brazil: Insights from magnetite trace elements and sulfur isotopes. Ore Geology Reviews 140, 104572.

Cawood, P.A., Korsch, R., 2008. Assembling Australia: Proterozoic building of a continent. Precambrian Research 166, 1-35.

Chew, D., Petrus, J., Kamber, B., 2014. U–Pb LA–ICPMS dating using accessory mineral standards with variable common Pb. Chemical Geology 363, 185-199.

Courtney-Davies, L., Ciobanu, C.L., Tapster, S.R., Cook, N.J., Ehrig, K., Crowley, J.L., Verdugo-Ihl, M.R., Wade, B.P., Condon, D.J., 2020. Opening the magmatic-hydrothermal window: high-precision U-Pb Geochronology Of The Mesoproterozoic Olympic Dam Cu-U-Au-Ag deposit, South Australia. Economic Geology 115, 1855-1870.

Cutts, K., Hand, M., Kelsey, D.E., 2011. Evidence for early Mesoproterozoic (ca. 1590Ma) ultrahigh-temperature metamorphism in southern Australia. Lithos 124, 1-16.

Day, W.C., Slack, J.F., Ayuso, R.A., Seeger, C.M., 2016. Regional Geologic and Petrologic Framework for Iron Oxide ± Apatite ± Rare Earth Element and Iron Oxide Copper-Gold Deposits of the Mesoproterozoic St. Francois Mountains Terrane, Southeast Missouri, USA. Economic Geology 111, 1825-1858.

Duncan, R.J., Stein, H.J., Evans, K.A., Hitzman, M.W., Nelson, E.P., Kirwin, D.J., 2011. A new geochronological framework for mineralization and alteration in the Selwyn-Mount Dore corridor, Eastern fold belt, Mount Isa inlier, Australia: Genetic implications for iron oxide copper-gold deposits. Economic Geology 106, 169-192.

Ehrig, K., Kamenetsky, V.S., McPhie, J., Macmillan, E., Thompson, J., Kamenetsky, M., Maas, R., 2021. Staged formation of the supergiant Olympic Dam uranium deposit, Australia. Geology 49, 1312-1316.

Fraser, G., Reid, A., Stern, R., 2012. Timing of deformation and exhumation across the Karari Shear Zone, north-western Gawler Craton, South Australia. Australian Journal of Earth Sciences 59, 547-570.

Gelcich, S., Davis, D.W., Spooner, E.T.C., 2005. Testing the apatite-magnetite geochronometer: U-Pb and 40Ar/39Ar geochronology of plutonic rocks, massive magnetite-apatite tabular bodies, and IOCG mineralization in Northern Chile. Geochimica et Cosmochimica Acta 69, 3367-3384.

Giles, D., Betts, P.G., Lister, G.S., 2004. 1.8–1.5-Ga links between the North and South Australian Cratons and the Early–Middle Proterozoic configuration of Australia. Tectonophysics 380, 27-41.

Glorie, S., Alexandrov, I., Nixon, A., Jepson, G., Gillespie, J., Jahn, B.-M., 2017. Thermal and exhumation history of Sakhalin Island (Russia) constrained by apatite U-Pb and fission track thermochronology. Journal of Asian Earth Sciences 143, 326-342.

Glorie, S., Burke, T., Hand, M., Simpson, A., Gilbert, S., Wade, B., 2022a. In situ Lu–Hf phosphate geochronology: Progress towards a new tool for space exploration. Geoscience Frontiers 13, 101375.

Glorie, S., Gillespie, J., Simpson, A., Gilbert, S., Khudoley, A., Priyatkina, N., Hand, M., Kirkland, Christopher L., 2022b. Detrital apatite Lu–Hf and U–Pb geochronology applied to the southwestern Siberian margin. Terra Nova 34, 201-209.

Glorie, S., Hand, M., Mulder, J., Simpson, A., Emo Robert, B., Kamber, B., Fernie, N., Nixon, A., Gilbert, S., 2023. Robust laser ablation Lu–Hf dating of apatite: an empirical evaluation. Geological Society, London, Special Publications 537, SP537-2022-2205.

Goldfarb, R.J., Groves, D.I., Gardoll, S., 2001. Orogenic gold and geologic time: a global synthesis. Ore Geology Reviews 18, 1-75.

Groves, D.I., Bierlein, F.P., Meinert, L.D., Hitzman, M.W., 2010. Iron Oxide Copper-Gold (IOCG) Deposits through Earth History: Implications for Origin, Lithospheric Setting, and Distinction from Other Epigenetic Iron Oxide Deposits. Economic Geology 105, 641-654.

Groves, D.I., Santosh, M., Zhang, L., 2020. A scale-integrated exploration model for orogenic gold deposits based on a mineral system approach. Geoscience Frontiers 11, 719-738.

Hand, M., Reid, A., Jagodzinski, L., 2007. Tectonic framework and evolution of the Gawler craton, southern Australia. Economic Geology 102, 1377-1395.

Harlov, D.E., 2015. Apatite: A Fingerprint for Metasomatic Processes. Elements 11, 171-176.

Harlov, D.E., Förster, H.-J.r., Nijland, T.G., 2002. Fluid-induced nucleation of (Y+ REE)-phosphate minerals within apatite: Nature and experiment. Part I. Chlorapatite. American Mineralogist 87, 245-261.

Harrison, T.M., Célérier, J., Aikman, A.B., Hermann, J., Heizler, M.T., 2009. Diffusion of ^{40}Ar in muscovite. Geochimica et Cosmochimica Acta 73, 1039-1051.

Hayward, N., Skirrow, R., 2010. Geodynamic setting and controls on iron oxide Cu-Au (±U) ore in the Gawler Craton, South Australia. Hydrothermal iron oxide copper-gold and related deposits: A global perspective 3, 105-131.

Horstwood, M.S.A., Košler, J., Gehrels, G., Jackson, S.E., McLean, N.M., Paton, C., Pearson, N.J., Sircombe, K., Sylvester, P., Vermeesch, P., Bowring, J.F., Condon, D.J., Schoene, B., 2016. Community-Derived Standards for LA-ICP-MS U-(Th-)Pb Geochronology – Uncertainty Propagation, Age Interpretation and Data Reporting. Geostandards and Geoanalytical Research 40, 311-332.

Jagodzinski, E., Reid, A., Chalmers, N., Swain, G., Frew, R., Foudoulis, C., 2007. Compilation of SHRIMP U-Pb geochronological data for the Gawler Craton, South Australia, 2007. South Australian Department of Primary Industries and Resources.

Jagodzinski, E., Reid, A., 2015. PACE Geochronology: Results of collaborative geochronology projects 2013-2015. Government of South Australia. Department of the Premier and Cabinet. , pp. Report Book, 2015/00003.

Jagodzinski, E.A., Reid, A.J., Crowley, J.L., Wade, C.E., Curtis, S., 2023. Precise zircon U-Pb dating of the Mesoproterozoic Gawler large igneous province, South Australia. Results in Geochemistry 10, 100020.

Kirscher, U., Mitchell, R.N., Liu, Y., Nordsvan, A.R., Cox, G.M., Pisarevsky, S.A., Wang, C., Wu, L., Murphy, J.B., Li, Z.-X., 2020. Paleomagnetic constraints on the duration of the Australia-Laurentia connection in the core of the Nuna supercontinent. Geology 49, 174-179.

Li, X., Zhou, M.-F., 2015. Multiple stages of hydrothermal REE remobilization recorded in fluorapatite in the Paleoproterozoic Yinachang Fe–Cu–(REE) deposit, Southwest China. Geochimica et Cosmochimica Acta 166, 53-73.

Li, Y., Selby, D., Condon, D., Tapster, S., 2017. Cyclic magmatic-hydrothermal evolution in porphyry systems: High-precision U-Pb and Re-Os geochronology constraints on the Tibetan Qulong porphyry Cu-Mo deposit. Economic Geology 112, 1419-1440.

Ludwig, K., 2012. Isoplot 4.15: a geochronological toolkit for Microsoft

Excel. Berkeley Geochronological Center.
Maidment, D.W., 2005. Palaeozoic high-grade metamorphism within the Centralian Superbasin, Harts Range region, central Australia. Australian National University.
Manor, M.J., Piercey, S.J., Wall, C.J., Denisová, N., 2022. High-Precision CA-ID-TIMS U-Pb Zircon Geochronology of Felsic Rocks in the Finlayson Lake VMS District, Yukon: Linking Paleozoic Basin-Scale Accumulation Rates to the Occurrence of Subseafloor Replacement-Style Mineralization. Economic Geology 117, 1173-1201.
Mao, M., Rukhlov, A.S., Rowins, S.M., Spence, J., Coogan, L.A., 2016. Apatite Trace Element Compositions: A Robust New Tool for Mineral Exploration*. Economic Geology 111, 1187-1222.
Morrissey, L.J., Barovich, K.M., Hand, M., Howard, K.E., Payne, J.L., 2019. Magmatism and metamorphism at ca. 1.45 Ga in the northern Gawler Craton: The Australian record of rifting within Nuna (Columbia). Geoscience Frontiers, 175-194.
Morrissey, L.J., Payne, J.L., Hand, M., Clark, C., Janicki, M., 2023. One billion years of tectonism at the Paleoproterozoic interface of North and South Australia. Precambrian Research 393, 107077.
Nebel, O., Morel, M.L., Vroon, P.Z., 2009. Isotope dilution determinations of Lu, Hf, Zr, Ta and W, and Hf isotope compositions of NIST SRM 610 and 612 glass wafers. Geostandards and Geoanalytical Research 33, 487-499.
Norris, A., Danyushevsky, L., 2018. Towards estimating the complete uncertainty budget of quantified results measured by LA-ICP-MS. Goldschmidt: Boston, MA, USA.
Paton, C., Hellstrom, J., Paul, B., Woodhead, J., Hergt, J., 2011. Iolite: Freeware for the visualisation and processing of mass spectrometric data. Journal of Analytical Atomic Spectrometry 26, 2508-2518.
Payne, J.L., Hand, M., Barovich, K.M., Reid, A., Evans, D.A.D., 2009. Correlations and reconstruction models for the 2500-1500 Ma evolution of the Mawson Continent. Geological Society, London, Special Publications 323, 319-355.
Payne, J.L., Hand, M., Barovich, K.M., Wade, B.P., 2008. Temporal constraints on the timing of high-grade metamorphism in the northern Gawler Craton: implications for assembly of the Australian Proterozoic. Australian Journal of Earth Sciences 55, 623-640.
Putnis, A., 2009. Mineral replacement reactions: Reviews of Mineralogy and Geochemistry, v. 70.
Reid, A., Fabris, A., 2015. Influence of Preexisting Low Metamorphic Grade Sedimentary successions on the distribution of iron oxide copper-gold mineralization in the olympic Cu-Au province, Gawler Craton. Economic Geology 110, 2147-2157.
Reid, A.J., Jagodzinski, E.A., Armit, R.J., Dutch, R.A., Kirkland, C.L., Betts, P.G., Schaefer, B.F., 2014. U-Pb and Hf isotopic evidence for Neoarchean and Paleoproterozoic basement in the buried northern Gawler Craton, South Australia. Precambrian Research 250, 127-142.
Schlegel, T.U., Wagner, T., Wälle, M., Heinrich, C.A., 2018. Hematite Breccia-Hosted Iron Oxide Copper-Gold Deposits Require Magmatic Fluid Components Exposed to Atmospheric Oxidation: Evidence from Prominent Hill, Gawler Craton, South Australia. Economic Geology 113, 597-644.
Schoene, B., Bowring, S.A., 2006. U–Pb systematics of the McClure Mountain syenite: thermochronological constraints on the age of the 40Ar/39Ar standard MMhb. Contributions to Mineralogy and Petrology 151, 615-630.
Selby, D., Creaser, R.A., Hart, C.J.R., Rombach, C.S., Thompson, J.F.H., Smith, M.T., Bakke, A.A., Goldfarb, R.J., 2002. Absolute timing of sulfide and gold mineralization: A comparison of Re-Os molybdenite and Ar-Ar mica methods from the Tintina Gold Belt, Alaska. Geology 30, 791-794.
Sillitoe, R.H., 2010. Porphyry Copper Systems. Economic Geology 105, 3-41.
Simpson, A., Gilbert, S., Tamblyn, R., Hand, M., Spandler, C., Gillespie, J., Nixon, A., Glorie, S., 2021. In-situ Lu Hf geochronology of garnet, apatite and xenotime by LA ICP MS/MS. Chemical Geology 577.

Simpson, A., Glorie, S., Hand, M., Spandler, C., Gilbert, S., Cave, B., 2022. In situ Lu–Hf geochronology of calcite. Geochronology 4, 353-372.

Skirrow, R.G., 2022. Iron oxide copper-gold (IOCG) deposits – A review (part 1): Settings, mineralogy, ore geochemistry and classification. Ore Geology Reviews 140, 104569.

Söderlund, U., Patchett, P.J., Vervoort, J.D., Isachsen, C.E., 2004. The 176Lu decay constant determined by Lu–Hf and U–Pb isotope systematics of Precambrian mafic intrusions. Earth and Planetary Science Letters 219, 311-324.

Stein, H.J., Markey, R.J., Morgan, J.W., Hannah, J.L., Scherstén, A., 2001. The remarkable Re–Os chronometer in molybdenite: how and why it works. Terra Nova 13, 479-486.

Stosch, H.-G., Romer, R.L., Daliran, F., Rhede, D., 2011. Uranium–lead ages of apatite from iron oxide ores of the Bafq District, East-Central Iran. Mineralium Deposita 46, 9-21.

Sullivan, B., Locmelis, M., Tunnell, B.N., Seeger, C., Moroni, M., Dare, S., Mathur, R., Schott, T., 2023. Genesis of the 1.45 Ga Kratz Spring Iron Oxide-Apatite Deposit Complex in Southeast Missouri, USA: Constraints from Oxide Mineral Chemistry. Economic Geology 118, 1149-1175.

Taylor, R.J.M., Kirkland, C.L., Clark, C., 2016. Accessories after the facts: Constraining the timing, duration and conditions of high-temperature metamorphic processes. Lithos 264, 239-257.

Thompson, J., Meffre, S., Maas, R., Kamenetsky, V., Kamenetsky, M., Goemann, K., Ehrig, K., Danyushevsky, L., 2016. Matrix effects in Pb/U measurements during LA-ICP-MS analysis of the mineral apatite. Journal of Analytical Atomic Spectrometry 31, 1206-1215.

Thomson, S.N., Gehrels, G.E., Ruiz, J., Buchwaldt, R., 2012. Routine low-damage apatite U-Pb dating using laser ablation–multicollector–ICPMS. Geochemistry, Geophysics, Geosystems 13.

Torab, F.M., Lehmann, B., 2007. Magnetite-apatite deposits of the Bafq district, Central Iran: apatite geochemistry and monazite geochronology. Mineralogical Magazine 71, 347-363.

Vermeesch, P., 2018. IsoplotR: A free and open toolbox for geochronology. Geoscience Frontiers 9, 1479-1493.

Williams, P.J., Barton, M.D., Johnson, D.A., Fontboté, L., De Haller, A., Mark, G., Oliver, N.H., Marschik, R., 2005. Iron oxide copper-gold deposits: Geology, space-time distribution, and possible modes of origin. Economic Geology, 371-405.

Yu, J., Morrissey, L., Hand, M., Payne, J.L., YanJing, C., 2023. The Fe-Cu disconnect: unravelling a composite IOCG deposit in the Olympic Fe-Cu-Au Province, Gawler Craton. Economic Geology, doi.org/10.5382/econgeo.5037.

Supplementary material

Tables S1–S3 that accompany this thesis chapter is available on Open Science Framework: https://osf.io/rcm7g/

Appendix Figures

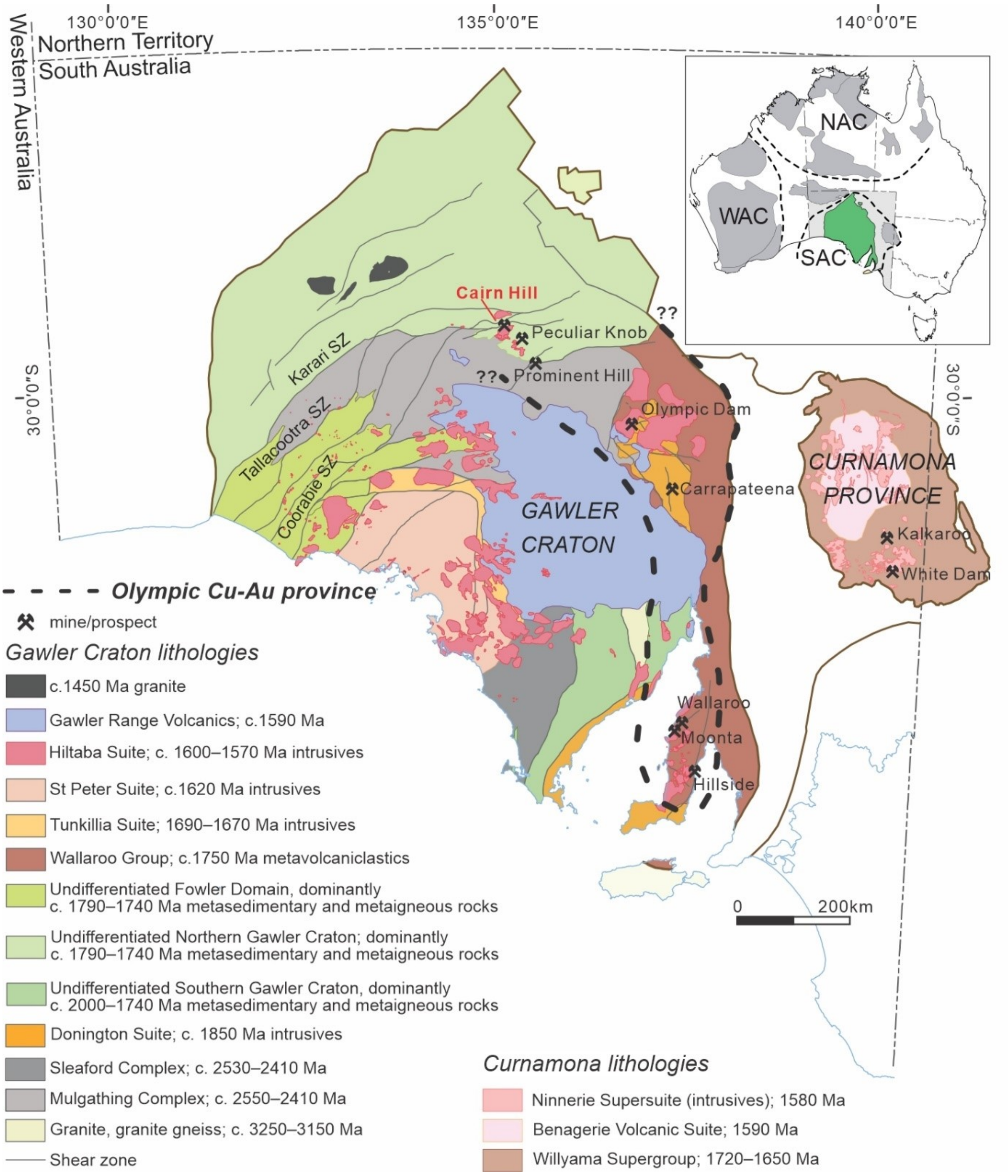

Fig.S1. Simplified solid geology map of the Gawler Craton (after Reid et al., 2014).

Chapter 4

The geochemistry of magnetite, apatite and fluid inclusions at Cairn Hill Fe-Cu-Au deposit: Insights into ore genesis of a composite IOCG system in the northern Gawler Craton

Statement of Authorship

Title of Paper	The geochemistry of magnetite, apatite and fluid inclusions at Cairn Hill Fe-Cu-Au deposit: Insights into ore genesis of a composite IOCG system in the northern Gawler Craton
Publication Status	☐ Published ☐ Accepted for Publication ☐ Submitted for Publication ☑ Unpublished and Unsubmitted work written in manuscript style
Publication Details	Yu, J., Hand, M., Payne, J., Morrissey, L., Chen, Y.J. 2023. The geochemistry of magnetite, apatite and fluid inclusions at Cairn Hill Fe-Cu-Au deposit: Insights into ore genesis of a composite IOCG system in the northern Gawler Craton

Principal Author

Name of Principal Author (Candidate)	Jie Yu		
Contribution to the Paper	Field work Data collection and modelling Manuscript writing		
Overall percentage (%)	70		
Certification:	This paper reports on original research I conducted during the period of my Higher Degree by Research candidature and is not subject to any obligations or contractual agreements with a third party that would constrain its inclusion in this thesis. I am the primary author of this paper.		
Signature		Date	24 July 2023

Co-Author Contributions

By signing the Statement of Authorship, each author certifies that:

i. the candidate's stated contribution to the publication is accurate (as detailed above);
ii. permission is granted for the candidate in include the publication in the thesis; and
iii. the sum of all co-author contributions is equal to 100% less the candidate's stated contribution.

Name of Co-Author	Martin Hand		
Contribution to the Paper	Manuscript editing Ideas for manuscript		
Signature		Date	24 July 2023

Name of Co-Author	Justin Payne		
Contribution to the Paper	Field work Manuscript editing Ideas for manuscript		
Signature		Date	24 July 2023

Name of Co-Author	Laura Morrissey		
Contribution to the Paper	Field work Manuscript editing Ideas for manuscript		
Signature		Date	24 July 2023

Name of Co-Author	Yan-Jing Chen		
Contribution to the Paper	Manuscript editing Ideas for manuscript Data collection		
Signature		Date	24 July 2023

Please cut and paste additional co-author panels here as required.

Abstract

Cairn Hill, in the northern Olympic Cu-Au Province, is a composite deposit recording two distinct mineralisation events ca. 100 Myr apart. An early magnetite-apatite assemblage that formed at ca. 1580 Ma is overprinted by late hydrothermal Cu mineralisation in brittle fractures that formed at ca. 1460 Ma. To elucidate the genesis of iron and copper mineralisation, we conducted detailed petrological and geochemical analyses of magnetite, apatite, and fluid inclusions. Different types of magnetite record varying concentrations of Al, Mn, Ti, V, and Mg, distinct from iron oxide apatite (IOA) or banded iron formation (BIF) deposits. Apatite associated with early magnetite shows different Cl and F contents, and was modified during the ca. 1460 Ma hydrothermal Cu mineralisation. The altered apatite has elevated F contents and decreasing Mn, REE, Na and Th. The changing abundance of redox-sensitive elements Fe and As indicate increasing fluid oxygen fugacity of ore-forming fluids, consistent with the variation of Fe-bearing solid phases in fluid inclusions. Ore-forming fluids responsible for Cu mineralisation are high-temperature, CO_2-rich and oxidized. They may have exsolved from hidden intrusions, undergone multiple fluid immiscibility and concentration, while preexisting magnetite acted as a chemical barrier and led to the precipitation of Cu at 325–470 °C. The early magnetite-apatite-hornblende assemblage may have been formed by magmatic fluids and were similar to the deep, early magnetite-apatite at the deep and marginal parts of Olympic Dam. Young ca. 1460 Ma Cu mineralisation is temporally closer to the Cloncurry IOCG deposits, and may have developed in an extensional setting and require mantle contribution.

Keywords: **Gawler Craton, composite IOCG, magnetite, apatite, fluid inclusion, geochemistry**

1. Introduction

Since the discovery of the immense Olympic Dam Cu-U-Au deposit in South Australia in 1975, the Olympic Domain in the eastern Gawler Craton has been the subject of intense mineral exploration for iron oxide Cu-Au (IOCG) deposits. The IOCG clan can be classified into hematite-rich and magnetite-rich endmembers on the basis of hematite or magnetite dominance and their different physico-chemical conditions of formation (Williams et al., 2005; Barton, 2014). Hematite-dominant IOCG deposits such as the giant Olympic Dam and Prominent Hill deposits in the eastern Gawler Craton are of the greatest economic interest and have consequently been the focus of the majority of the studies in the region (Hitzman et al., 1992; Oreskes and Einaudi, 1992; Belperio et al., 2007; Schlegel et al., 2018; Courtney-Davies et al., 2020). The northernmost Olympic IOCG Province is home to a number of magnetite-dominant Fe ± Cu deposits and prospects that have traditionally been considered to represent the deeper, magnetite-rich IOCG mineralizing system (Fig. 4.1; Freeman and

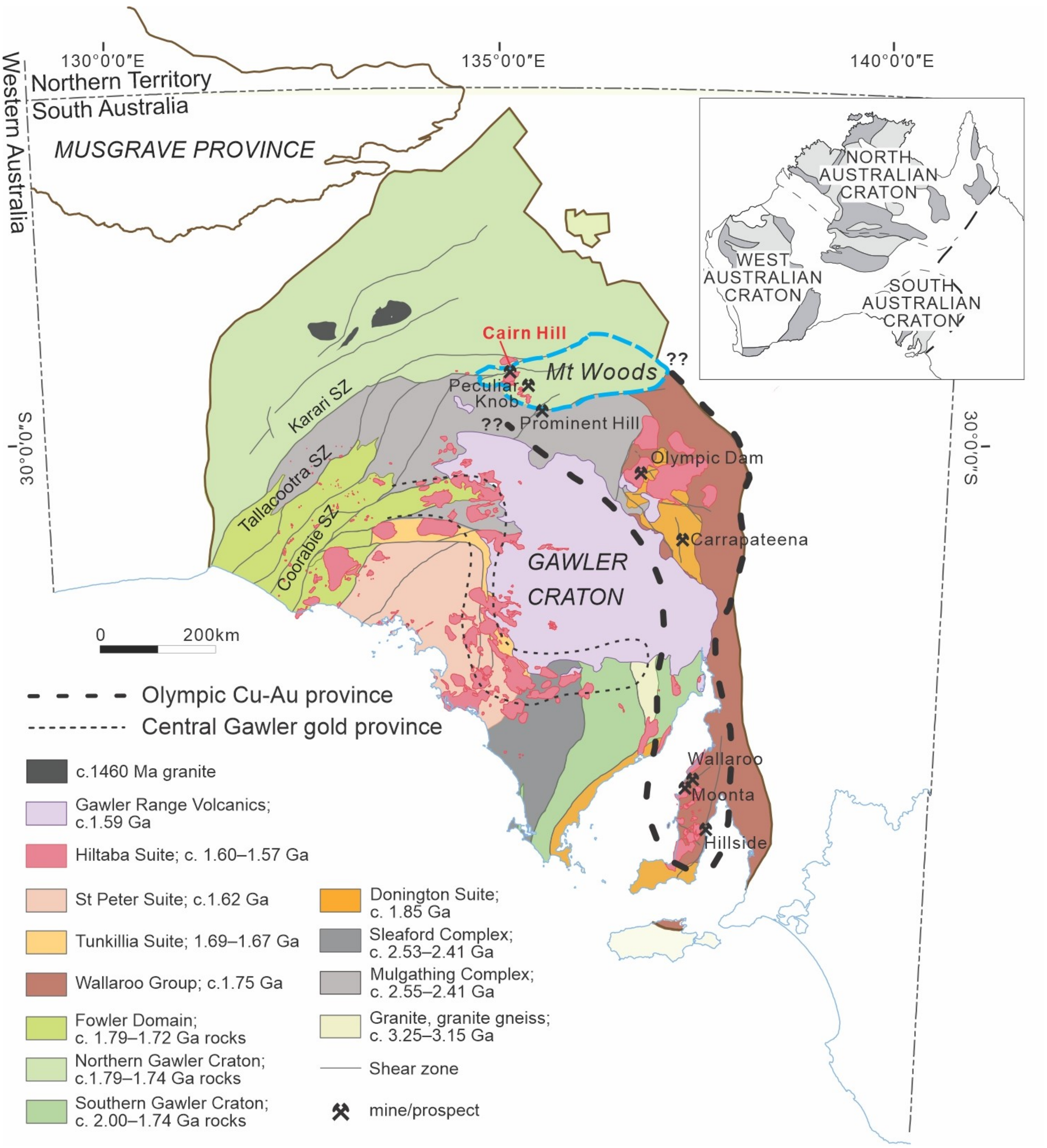

Fig.4.1 Simplified solid geology map of the Gawler Craton (after Reid et al., 2014b). The location of the Gawler Craton within Australia is shown in the inset.

Tomkinson, 2010; Reid and Fabris, 2015; Reid, 2019). However, recent zircon, monazite and apatite geochronology from the Cairn Hill deposit, the largest deposit in the northern Olympic Cu-Au Province, has recognized two distinct and temporally unrelated mineral systems separated by a phase of granulite facies metamorphism including early iron mineralisation prior to ca. 1580 Ma, metamorphism at ca. 1490 Ma and young Cu mineralisation at ca. 1460 Ma (Yu et al., 2023; Chapter 3), challenging the traditional exploration model.

Geochronological evidence has created a temporal framework for metamorphic and mineralisation events at Cairn Hill, but the genesis of its early iron and late copper mineralisation remains poorly understood. The origin of the ca. 1580 Ma magnetite-apatite assemblage is still uncertain, and it is unclear whether it represents the deeper expression of the hematite-dominant Olympic IOCG systems. Additionally, the nature of the ore-forming fluids and ore genesis for the ca. 1460 Ma Cu mineralisation remains enigmatic. The granulite-facies deformation and metamorphism that occurred at ca. 1490 Ma has obscured some of the original ore textures and intrusive relationships (Yu et al., 2023). These unanswered questions significantly impede our understanding of regional mineralisation and hinder future exploration efforts.

The Cairn Hill deposit contains abundant apatite and magnetite that can be linked to the different phases of mineralisation. In this manuscript, we present petrological and geochemical data on magnetite and apatite as well as petrology, microthermometry and compositional analyses of fluid inclusions associated with Cu mineralisation. On this basis, we discuss the ore genesis and the origin and evolution of fluids during the iron and copper mineralisation events at Cairn Hill. Specifically, we distinguish between a deeper Fe-P mineralisation contemporaneous with the Olympic IOCG deposits and younger hydrothermal Cu mineralisation potentially connected to the Cloncurry IOCG district.

2. Geological Setting

The Gawler Craton records a protracted history from the Archean to Mesoproterozoic (Fig. 4.1; see Hand et al., 2007; Fraser et al., 2010; Reid et al., 2014a). The central and eastern Gawler Craton host a diverse series of mineral deposits that formed in the Mesoproterozoic (Fig. 4.1; Fraser et al., 2007; Skirrow et al., 2007), including extensive iron-oxide copper-gold (IOCG) in the Olympic Domain in the eastern Gawler Craton (e.g., Olympic Dam, Prominent Hill and Carrapateena; Bowden et al., 2017; Courtney-Davies et al., 2020; McPhie et al., 2020) and a diverse series of gold, silver, and lead-zinc deposits in the central Gawler craton (Ferris and Schwarz, 2004; Fraser et al., 2007). These mineral provinces formed broadly coeval with a large igneous province comprising the Gawler Range Volcanics and Hiltaba Suite magmas, which formed between 1600–1570 Ma (Jagodzinski et al., 2023).

The Mount Woods Domain is a sparely outcropping, aeromagnetically-defined region of the northern Gawler Craton that is bound to the north by the extension of the Karari Shear Zone and to the south by the Southern Overthrust (Fig. 4.1, 4.2). It occupies the north of the highly mineralized Olympic Cu-Au Province and hosts numerous Fe ± Cu deposits and prospects, including Peculiar Knob, Cairn Hill, Manxman, Joes Dam, and Snaefell (Fig. 4.1, 4.2A; Freeman and Tomkinson, 2010; Jagodzinski and Reid, 2015). The basement of the Mount Woods Domain comprises unnamed metasedimentary and granitic protoliths with ages of ca. 2500–2450 Ma and orthogneiss, and migmatitic paragneiss of the Mount Woods Metamorphics that were deposited after ca. 1860 Ma (Tiddy et al., 2020; Morrissey et al., 2023). It is covered by the Skylark Metasediments, which comprise metapelitic and metapsammitic lithologies, minor banded iron formation, and calc-silicate deposited after ca. 1750 Ma (Jagodzinski et al., 2007; Morrissey et al., 2023). The southern and western Mount Woods Domain was intruded by mafic and felsic magmas of the ca. 1585 Ma Balta Granite Suite, equivalent to the Hiltaba Suite (Jagodinski, 2005). The Mount Woods Domain records multiple phases of deformation and metamorphism (Betts et al., 2003; Morrissey et al., 2023). The central and western Mount Woods Domain underwent granulite facies metamorphism between 1700–1670 Ma, approximately coeval with the Kimban Orogeny elsewhere in the Gawler Craton (Morrissey et al., 2023). South of the Skylark Fault, metamorphic zircon ages ranging from 1595 to 1575 Ma are reported from upper amphibolite facies rocks, broadly coeval with the intrusion of granite and gabbro in the Mount Woods Domain (ca. 1594–1584 Ma; Jagodzinski, 2005; Jagodzinski et al., 2007). Drill cores along or adjacent to the Skylark Fault and Southern Overthrust give monazite ages of ca. 1570–1550 Ma, interpreted to reflect deformation at amphibolite facies conditions (Morrissey et al., 2023). Localized metamorphism and deformation in the northern Mount Woods Domain occurred at ca. 1580 and 1490 Ma, including along the Cairn Hill Shear Zone (Morrissey et al., 2023; Yu et al., 2023a). Apatite U–Pb ages and biotite $^{40}Ar–^{39}Ar$ ages range from ca. 1560–1400 Ma (Forbes et al., 2012; Fraser et al., 2012; Hall et al., 2018; Tiddy et al., 2020), and biotite Rb-Sr ages range between ca. 1480–1380 Ma (Morrissey et al., 2023), broadly suggesting regional cooling after ca. 1450 Ma.

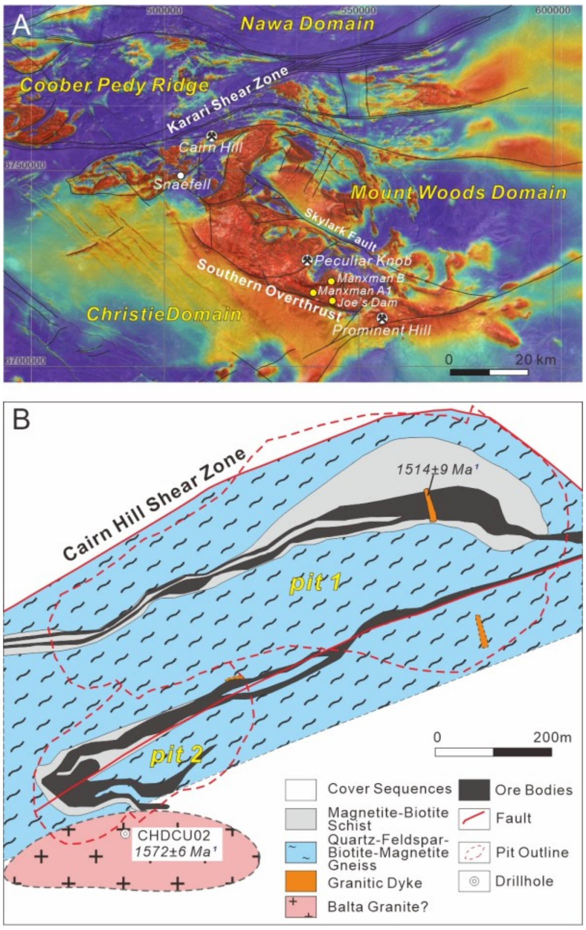

Fig. 4.2 (A) Total Magnetic Intensity image of the Mount Woods region (modified after Morrissey et al., 2023). TMI image and shear zone interpretation is from SARIG (https://map.sarig.sa.gov.au). (B) Interpreted geology map of the Cairn Hill deposit (modified after Clark, 2014, and Jagodzinski and Reid, 2015).

3. Ore deposit geology

Cairn Hill was discovered in 2005 and presently has an indicated resource of 37 Mt @ 28% Fe (including 3.77 Mt @ 47.8% Fe) and a target resource of 120 Mt @ 25–30% Fe (Cairn Hill Annual Compliance Report, 2020-2021). The Cairn Hill Fe (-Cu-Au) deposit is situated on the northwestern margin of the Mount Woods Domain. It is located at the westernmost end of a prominent 18 km long, east-west trending, linear, aeromagnetic anomaly on the northwestern margin of the Mount Woods Domain and south of a set of splays of the Karari Shear Zone (Fig.

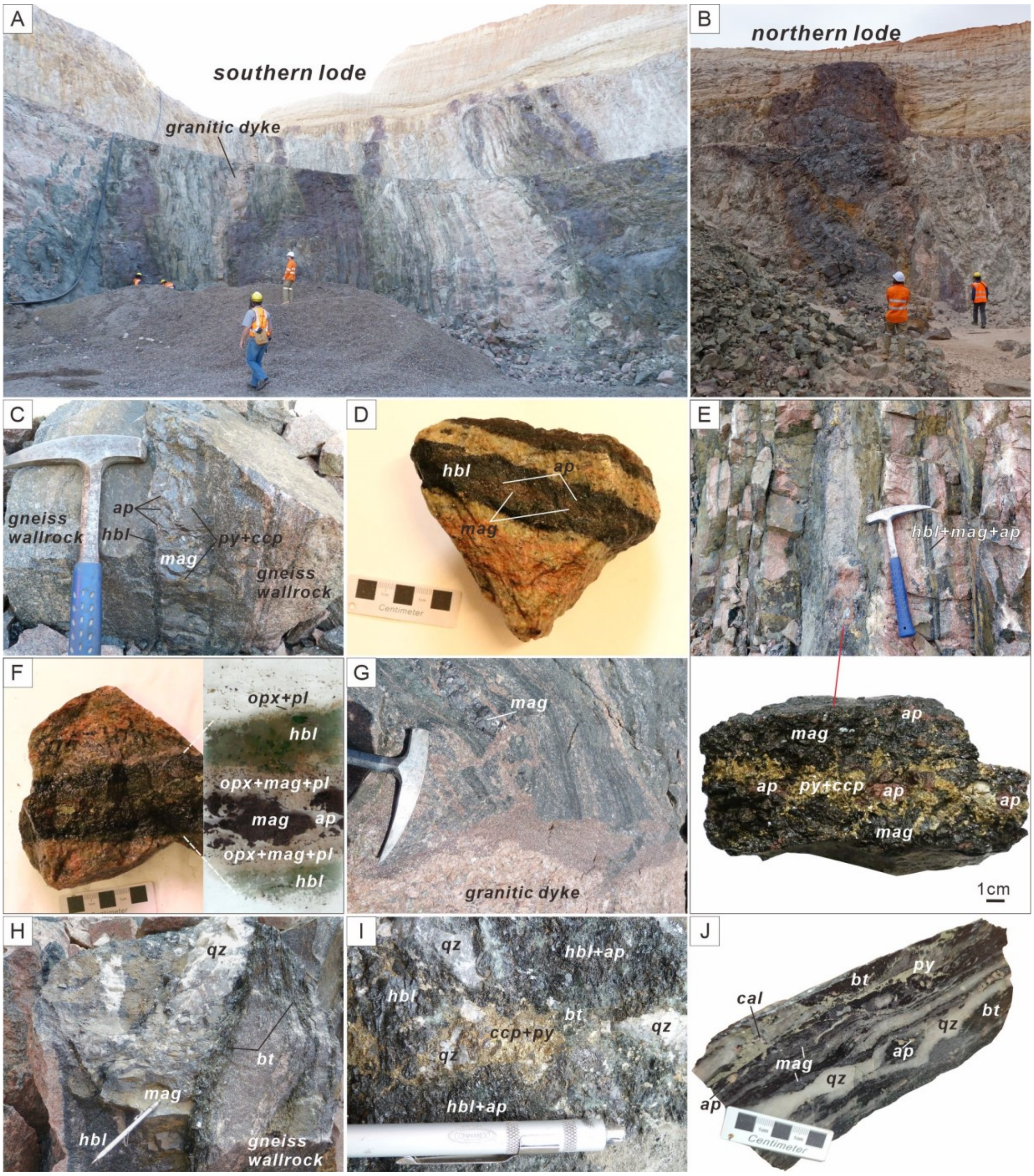

Fig. 4.3 Field occurrence of Cairn Hill. (A) Southern iron lode hosted by gneiss in pit 2, with granite dyke on the margin of the iron lode. (B) Northern iron lode hosted by gneiss in pit 1. (C) Representative symmetrical magnetite-apatite-hornblende vein, with massive magnetite developed in the middle and hornblende on both walls. Apatite is developed at the junction of magnetite and hornblende. (D) Representative hornblende-magnetite-apatite vein, with magnetite and apatite intermittently distributed in hornblende. (E) Abundant cm- to dm-scale magnetite-apatite-hornblende veins distributed in parallel in the gneiss wall rock, with late pyrite and chalcopyrite infilling the early magnetite. (F) Symmetrical magnetite + apatite + hornblende vein with hornblende metamorphosed to orthopyroxene + plagioclase. (G) Magnetite-bearing vein crosscut by granitic dyke. (H) Early magnetite + apatite + hornblende lode infilled by quartz vein, with biotite on edge. (I) Late chalcopyrite + pyrite + quartz + biotite infills the early magnetite + apatite + hornblende assemblage. (J) Quartz + chalcopyrite + pyrite + magnetite + biotite vein with relic apatite.

Mineral abbreviations after Whitney and Evans (2010).

4.2A). The intensity of the magnetic response escalates to the west, reaching its apex at the mining site. The overall Cu grade is 0.03%, and the Au grade is 0.005 g/t at Cairn Hill, making

Cairn Hill once regarded as example of magnetite-dominant IOCG mineralisation in the Gawler Craton (Reid and Fabris, 2015; Reid, 2019).

The Cairn Hill Fe (-Cu-Au) deposit is hosted by predominately quartz-feldspar-biotite-magnetite gneiss that locally contains garnet and cordierite (Fig. 4.2B and 4.3). This gneiss is interpreted to be interlayered igneous and metasedimentary rocks with protolith ages of ca. 1750 Ma (Yu et al., 2023), similar to those found in the Mount Woods and Nawa Domains (Jagodzinski et al., 2007; Howard et al., 2011a). The foliation defined by biotite and magnetite trends E-SW to W-NE coincident with the local shear zone. To the southwest of the mine is a pink-red, medium- to coarse-grained alkali-rich granite (Fig. 4.2B). A sample of migmatitic granitic gneiss from drill hole CHDCU02 yields a zircon U-Pb SHRIMP age of 1572 ± 6 Ma, suggesting the granite is part of the Hiltaba-equivalent Balta Granite suite (Jagodzinski and Reid, 2015).

The Cairn Hill deposit consists of two nearly parallel, sub-vertical magnetite-apatite-hornblende lodes, each about 10 meters wide (Fig. 4.2B). The thicker Northern Lode is the focus of Pit 1, and the magnetite unit there reaches a maximum width of 40 metres (Fig. 4.3B). The Southern Lode, which is sub-parallel to the Northern Lode, thickens towards the west (Fig. 4.3A). Numerous cm- to dm-scale magnetite-hornblende-apatite veins or bands occur in the wallrock, showing mineral assemblages and textures similar to those of the two major lodes (Fig. 4.3). The magnetite-rich veins are usually symmetrical, with coarse magnetite growing in the center, hornblende (sometimes with plagioclase or quartz) developing on both sides, and apatite generally distributed at the interface of magnetite and hornblende (Fig. 4.3C). Minor pyrite and chalcopyrite are present in the veins, but it is unclear whether they formed at the same time. Some veins are dominated by hornblende, with magnetite and apatite occurring

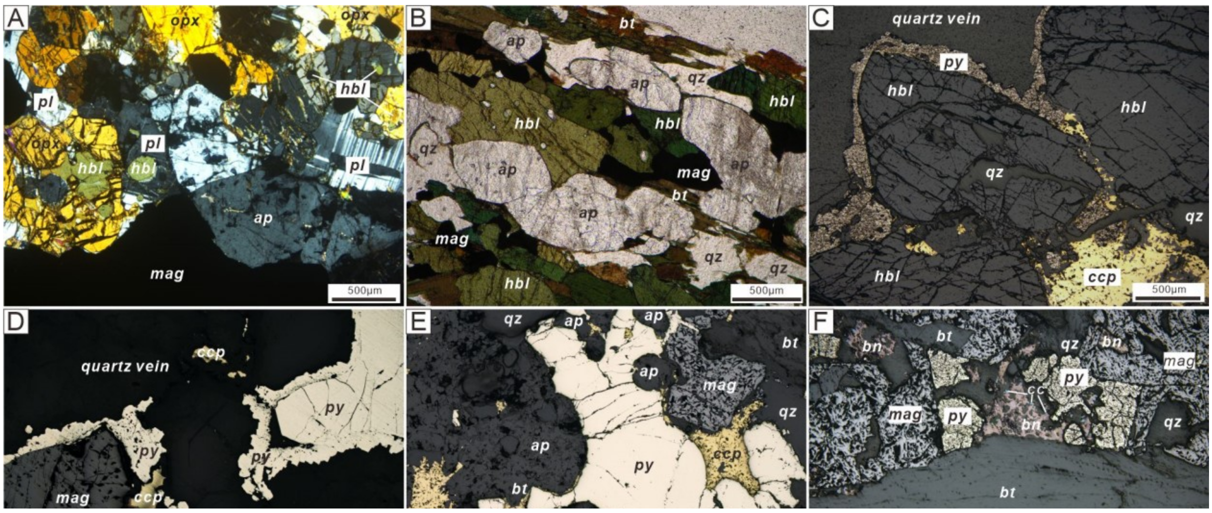

Fig. 4.4 Photomicrographs of representative samples at Cairn Hill. (A) Hornblende is locally metamorphosed to orthopyroxene + plagioclase. (B) Hornblende + magnetite + apatite vein from distal drill hole (CHDCU02), magnetite is intermittently distributed. (C&D) Early hornblende and magnetite are crosscut by quartz-sulfide veins. Sulfides precipitated on the surface of the magnetite and hornblende, which was subsequently infilled with quartz. (E) Pyrite and chalcopyrite crosscut or enclose the apatite and magnetite. (F) Magnetite + sulfides (py + ccp + bn + cc) in the biotite 'schist', Cu minerals are dominated by bornite and chalcocite.

discontinuously in the middle (Fig. 4.3D). Similar veins and bands are also visible in drill hole CHD012, located 1 kilometer east of the current open pits (Fig. 4.4B). Due to strong shear deformation, it is difficult to determine whether the magnetite-apatite-hornblende assemblage represents a hydrothermal vein, but the symmetrical vein texture suggests this possibility (Fig. 4.3C and F). Hornblende from coarse veins is often rich in zircon, which grows between hornblende crystals or is enclosed by them, and zircon is rare in the finer veins. Zircons separated from hornblende yielded a U-Pb age of 1583 ± 30 Ma, indicating that the magnetite-hornblende-apatite assemblage formed no later than 1583 Ma. Monazites from wall rocks yield a similar age population around 1580 Ma, suggesting that Cairn Hill underwent upper amphibolite facies metamorphism at ca. 1580 Ma (Yu et al., 2023).

The iron lodes are crosscut by foliated granitic dykes with zircon U-Pb ages of 1514 ± 9 Ma and 1518 ± 22 Ma (Fig. 4.3A and G; Reid et al., 2015; Yu et al., 2023). Both iron mineralisation and the granitic dykes were strongly modified by granulite facies metamorphism and deformation at ca. 1490 Ma, which reached conditions of 4.6–5.3 kbar and 740–770 °C (Yu et al., 2023). Hornblende in some veins/bands was metamorphosed to orthopyroxene + plagioclase or orthopyroxene + clinopyroxene (Fig. 4.3F and 4.4A). Apatite associated with magnetite commonly records Lu-Hf ages of ca. 1490 Ma, representing the resetting/recrystallization of the Lu-Hf isotopic system as a result of metamorphism and deformation (Chapter 3).

Copper mineralisation overprints the magnetite-apatite-hornblende assemblage and the high-grade metamorphism and deformation (Reid and Fabris, 2015; Reid, 2019; Yu et al., 2023). Ore minerals in the Cu stage include chalcopyrite + pyrite ± pyrrhotite ± bornite ± chalcocite ± sphalerite, and the gangue minerals are dominated by quartz + biotite + chlorite ± carbonate ± siderite ± fluorite. The sulfide + quartz + biotite assemblage infills the early magnetite + apatite + hornblende veins (Fig. 4.3E–I) or occurs in biotite-sulfide-quartz veins that crosscut the gneiss (Fig. 4.3J). The early magnetite-hornblende-apatite displays brittle deformation during the Cu mineralisation stage, usually being cracked and cataclastic, and encompassed or replaced by pyrite and chalcopyrite (Fig. 4.4C–E). Magnetite and apatite could also be mobilized and recrystallized along fractures or in the newly formed sulfide-quartz-biotite vein (Fig.4.3J and 4.4F). Bornite grows on the edge of chalcopyrite during later oxidation or occurs as the major Cu-bearing mineral in the biotite 'schist' on the edge of the magnetite lode (Fig. 4.2B, 4.3H and 4.4F). Siderite is observed in areas of intensive carbonatization. Hematite is only observed as a later oxidation product of magnetite (Fig. 4.5E). Alteration types mainly include biotitization, sericitization, chloritization, and carbonatization, where the early hornblende is replaced by biotite, sericite, and chlorite. Early apatite was modified during the infiltration of Cu-bearing fluids, forming recrystallized LREE-depleted pink apatite and secondary monazite (Chapter 3). In-situ Lu-Hf dating of the recrystallized apatite and U-Pb dating of the secondary monazite jointly constrain the Cu mineralisation time at ca. 1460 Ma (Chapter 3).

Table 1 Summary of magnetite and apatite samples

Ore stage	Magnetite type	Apatite type	Occurrence
Ca. 1580 Ma magnetite stage			
	Mag 1-M		massive iron lodes
	Mag 1-V	Type Ia	dm-scale symmetrical magnetite + hornblende + apatite veins
	Mag 2	Type Ib	cm-scale hornblende + apatite ± magnetite veins
Ca. 1460 Ma Cu stage			
	Mag 3	Type IIw, IIs and III	sulfide-biotite-quartz veins, ragged texture
	Mag 4		inclusion-free rims on earlier magnetite, or within the sulfide-biotite-quartz veins

4. Samples and methodology

4.1 Sample selection and preparation

EPMA and LA-ICP-MS were used to determine the major and trace elements of magnetite and apatite from a representative suite of samples taken from Cairn Hill (Table 1). Major elements and apatite Cl and F concentrations were determined by EPMA, while trace element concentrations were determined by LA-ICP-MS. Petrology of selected magnetite and apatite samples was first studied in thin/thick sections and epoxy mounts by transmitted/reflected light microscopy and by back-scattered electron (BSE) imaging. LA-ICP-MS analysis was performed on the EPMA spot or directly adjacent to it. All instrumentation employed for microanalytical work is housed at Adelaide Microscopy, the University of Adelaide, South Australia.

The quartz samples used for the fluid inclusion study were collected from the quartz-biotite-chalcopyrite-pyrite veins in Pit 2. Hydrothermal quartz is scarce in the early magnetite mineralisation, and fluid inclusions in apatite appear to be secondary in origin and are thus not analyzed. Twelve representative samples were further investigated by petrographic, microthermometric, and laser Raman microprobe methods at the Key Laboratory of Orogen and Crust Evolution, Peking University, China. The compositions of individual fluid inclusions were analyzed using LA-ICP-MS at the State Key Laboratory of Ore Deposit Geochemistry, IGCAS, China.

4.2 EPMA

Microprobe analyses were obtained on a CAMECA SX5 electron microprobe equipped with 5 wavelength-dispersive spectrometers. Analyses of apatite were conducted in a single-stage analytical protocol with a 5 µm beam diameter at an accelerating voltage of 10 kV and beam current of 15 nA. Fluorine was always measured on the first cycle because of potential F migration, and the beam condition used for apatite should not cause significant F migration. A constant accelerating voltage of 15 kV and a beam current of 20 nA were utilized during the magnetite analyses. Elemental mapping was conducted on the same SX5 microprobe with beam conditions of 200 nA and 20 kV. Wavelength dispersive x-ray (WDS) maps of Ca, P, Mn, F, Cl and Ce concentrations in the apatite crystals were obtained. Calibration and data reduction were conducted using 'Probe for EPMA' software (Donovan et al. 2016). The hydroxide (OH) content of apatite was calculated by mass balance using the quantitatively determined F and Cl concentrations and assuming the halogen site in apatite is occupied by $X_F + X_{Cl} + X_{OH} = 1$ (Hughes and Rakovan, 2015).

4.3 LA-ICP-MS

LA-ICP-MS trace element analyses of apatite and magnetite were conducted on an Agilent 7900x ICP-MS coupled with a New Wave UP-213 laser ablation system. Maximum sensitivity and low oxide interference production were achieved by daily optimization of the ICP-MS system. The ablation was performed with a frequency of 5 Hz and laser energy of 3.5 J/cm^2 using helium as the carrier gas. A spot size of 30 μm was utilized for apatite, and spot sizes of 30 or 60 μm were utilized for magnetite. The total acquisition time for each analysis was 70 s, including 30 s of background measurement, followed by 40 s of laser ablation. Mass bias, elemental fractionation and instrument drift were corrected using the reference materials GSD-1G (for magnetite) or NIST-610 (for apatite). The standards were analyzed every ten unknown analyses. The following isotopes were measured for apatite: ^{23}Na, ^{24}Mg, ^{29}Si, ^{31}P, ^{43}Ca, ^{47}Ti, ^{51}V, ^{53}Cr, ^{55}Mn, ^{57}Fe, ^{63}Cu, ^{66}Zn, ^{75}As, ^{88}Sr, ^{89}Y, ^{90}Zr, ^{137}Ba, ^{139}La, ^{140}Ce, ^{141}Pr, ^{146}Nd, ^{147}Sm, ^{153}Eu, ^{157}Gd, ^{159}Tb, ^{163}Dy, ^{165}Ho, ^{166}Er, ^{169}Tm, ^{172}Yb, ^{175}Lu, ^{178}Hf, ^{232}Th and ^{238}U. For magnetite, the following isotopes were measured: ^{23}Na, ^{24}Mg, ^{27}Al, ^{29}Si, ^{31}P, ^{39}K, ^{43}Ca, ^{47}Ti, ^{51}V, ^{53}Cr, ^{55}Mn, ^{57}Fe, ^{59}Co, ^{60}Ni, ^{63}Cu, ^{66}Zn, ^{69}Ga, ^{88}Sr, ^{89}Y, ^{90}Zr, ^{93}Nb, ^{98}Mo and ^{118}Sn, and only elements with detectable concentrations are reported. The Ca concentration obtained by EPMA for each individual apatite spot was used as an internal standard, and the average Ca content from the same sample was used in the data-reduction calculations when direct EMPA data were not available. Iron content determined by EMPA was employed as an internal standard for magnetite data calibration, and the average Fe content from the same sample was used in the data-reduction calculations when direct EMPA data were not available. Data handling and calculation of element concentrations were performed with the LADR software (Norris and Danyushevsky, 2018). During the data reduction, time-resolved signals were inspected and only inclusion-free signals were processed.

4.4 Microthermometry and Raman of fluid inclusions

Raman microanalysis of vapor and daughter mineral of individual fluid inclusions was performed on an RM-1000 laser Raman microprobe. The excitation wavelength was the 514.5 nm line of an Ar^+ ion laser operating at 25 mW. The spectra were recorded with a counting time of 3 s and ranged from 200 to 4000 cm^{-1}, with one accumulation, and the spectral resolution was ± 1 cm^{-1}. Wavenumber calibration was carried out using an internal silicon standard and was performed as an automated procedure using the software of Wire version 4.2.

Microthermometry was carried out on a Linkam THMSG600 Heating-Freezing System attached to an Olympus BX53M microscope. Thermocouples were calibrated at -56.6 °C, 0.0 °C, and +374.1 °C using synthetic fluid inclusions supplied by FLUID INC. The heating/freezing rate is generally 0.2–10 °C/min but reduced to 0.2 to 2 °C/min near the phase transition. The precision of temperature measurements is ± 0.5 °C to ± 2 °C in the range of -120 to -60 °C, ± 0.2 °C in the range of -60 °C to + 100 °C, and ± 2 °C for temperatures above + 100 °C. Fluid inclusion data were acquired only on fluid inclusion assemblages to avoid accidental deviations.

The salinity and density for H_2O-NaCl inclusions were calculated using the program HokieFlincs_H_2O-NaCl (Steele-MacInnis et al., 2012). The salinities of two-phase L-V inclusions (W-type) were determined from corresponding ice-melting temperatures (Tm_{ice}) using the method of Bodnar (1993), and the salinities of halite-bearing hypersaline inclusions (SH-type) were determined from halite dissolution temperatures (Tm_S) using the algorithm of Sterner et al. (1988). Trapping pressures of SH-type inclusions are estimated using the empirical equation proposed by Becker et al. (2008). Salinities of CO2-bearing inclusions were estimated using the equations of Collins (1979). Densities and pressures for individual CO2-bearing inclusions were calculated by the program FLINCOR of Brown (1989) with the equations of Brown and Lamb (1989).

4.5 LA-ICP-MS analyses of individual fluid inclusions

Compositions of individual fluid inclusions were analyzed using LA-ICP-MS following the procedure described in Lan et al. (2017, 2018). The analytical facility consists of an Agilent 7900 ICP-MS coupled with a GeoLas Pro 193-nm ArF excimer laser. Samples were placed into an 8 cm^3 cell and ablated with laser energy of 10 J/cm^2 and a frequency of 6 Hz. After measuring a gas blank for ~30 s, the laser was turned on. Both stepwise and straight ablation methods were used to drill the target fluid inclusions depending on their depth. The laser beam diameters were adjusted between 16 and 44 μm (depending on the size of the fluid inclusions) for each analysis to ensure complete ablation of the fluid inclusion while minimizing the explosion of the quartz. During the analysis, less than 60 % of ablations of inclusions were successful. NIST SRM-610 was used as the external standard and analyzed every ten fluid inclusions analyses. Calibration and signal integration of the LA-ICP-MS data were performed using the SILLS program (Guillong et al., 2008). The first section of the signals was from the host mineral, and these signals were used for mineral matrix correction of the fluid inclusions. Once the fluid inclusions were opened, the mixed fluid inclusion and host mineral signals typically lasted 5 to 15 s. For data reduction, the internal standards used for correcting host mineral contributions to the ablation signals were Si for quartz. Weight percent NaCl equivalent concentrations of fluid inclusions obtained from microthermometry were used as internal standards (Heinrich et al., 2003). The method of

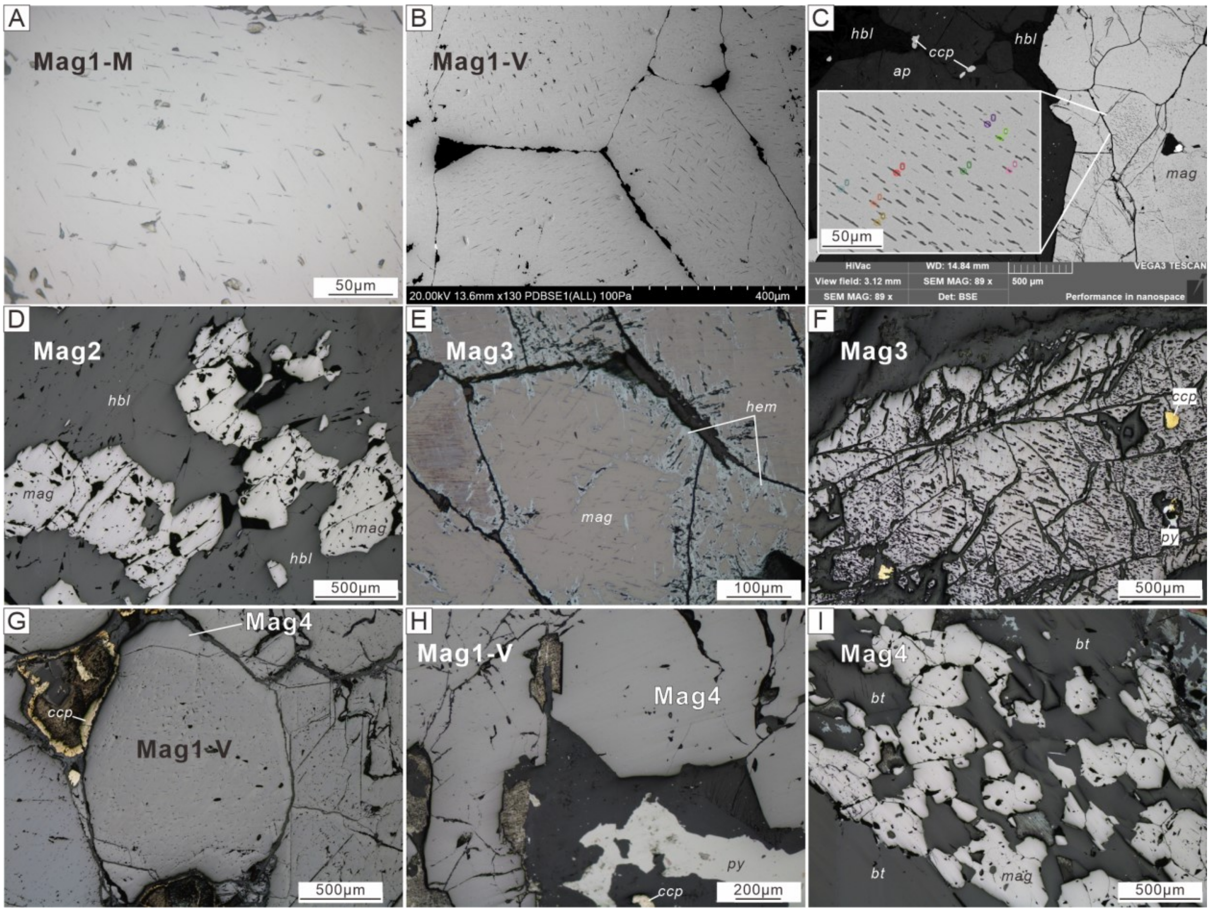

Fig. 4.5 Photomicrographs of different magnetite types from Cairn Hill. (A) Mag1-M magnetite with exsolution texture from massive iron lodes. (B) Mag1-V magnetite with exsolution texture from cm- to dm-scale magnetite-hornblende-apatite veins. (C) Al, Mg-bearing silicate exsolution unevenly distributed in Mag1-V magnetite. (D) Mag2 magnetite intermittently distributed in hornblende. (E) Magnetite is partly oxidized to hematite along boundary and fracture. (F) Mag3 relic magnetite hosted in biotite-quartz-sulfide veins. (G and H) Mag1-V is recrystallized to clean Mag4 magnetite on the rim. (I) Mag4 magnetite in biotite-quartz-sulfide veins.

charge balancing to the NaCl equivalent (Allan et al., 2005) was used to correct for salinity contributions from other chloride salts (e.g., Ca, K, Mn, Fe, Zn, Sr, and Pb) to the freezing point depression-derived estimate. The corrected Na concentrations transformed the relative element concentrations into absolute values.

As a result of decrepitation in obtaining the precise salinity of individual inclusion for LA-ICP-MS analysis, approximately one-third of the SH-type inclusions adopted the average salinity of the corresponding fluid assemblage as internal standards. This approach may have increased uncertainty by < 5 %.

5. Results

5.1 Magnetite petrology and chemistry

There are five types of magnetite in the iron ore bodies from Cairn Hill, identified here as Mag1-M, Mag1-V, Mag2, 3, and 4 (Table 1). Mag1-M magnetite is volumetrically dominant (>90 %) and was sampled from the two massive iron lodes (Fig. 4.3A and B). Mag1-M magnetite exhibits exsolution lamellae of Mg, Al, and Fe-bearing silicates aligned along magnetite crystallographic planes (Fig. 4.5A). The silicate lamellae are typically < 2 μm wide, ~30 μm long and uniformly distributed. Mag1-V magnetite is associated with hornblende and apatite crystals in veins several centimetres in width (Fig. 4.3C). Some grains show recrystallization textures characterized by aggregates of magnetite grains exhibiting a mosaic texture with ~120° triple junctions (Fig. 4.5B). Mag 1-V contains similar exsolution and mosaic textures to the Mag1-M magnetite from the massive iron lodes, however, in some Mag1-V magnetite grains the exsolution texture is not uniformly distributed (Fig. 4.5C). Mag2 magnetite also comes from veins of hornblende + apatite + magnetite, where hornblende is volume-dominant and magnetite and apatite less abundant (Fig. 4.3D and 4.5D). The Mag2 grains do not contain exsolution or mosaic textures. Mag3 magnetite comes from the sulfide-biotite-quartz veins and exhibits a ragged texture, with local development of hematite along magnetite grain boundaries and within fractures (Fig. 4.5E). Mag 3 contains similar exsolution textures to Mag 1, but the exsolved Mg, Al, and Fe-bearing silicates have been altered to biotite and chlorite (Fig. 4.5F). Mag3 magnetite is interpreted to be modified Mag1-M or Mag1-V magnetite. Mag4 is closely related to sulfide mineralisation. It does not contain exsolution textures but rarely contains inclusions of pyrite, quartz or biotite. Mag 4 occurs as inclusion-free rims on earlier magnetite or as distinct grains within the sulfide-biotite-quartz veins (Fig. 4.5G–I).

Major and trace element compositions for magnetite from all samples are presented in Appendix Table A1 and A2. All magnetite analyses on EPMA (n = 96) have measured Fe concentrations ranging from 69.0–71.9 wt.% and most analyses have detectable Ti, Si, Mg, Al, Mn and Cr concentrations. EPMA analyses of exsolution lamellae yield higher Mg, Al, Si and Mn contents indicating that they are Mg, Al, Fe, Mn-bearing silicates (n = 38), although the exact mineralogy cannot be determined as the microprobe beam spot (5 μm) is larger than the width of the lamellae (< 2 μm) (Table A1). LA-ICP-MS analyses of different magnetite types from Cairn Hill yielded distinctly different geochemical characteristics (n = 227). In particular, the differences are most pronounced for elements such as Al, Mn, Ti, V, and Mg (Fig. 4.6). Mag1-M magnetite from the massive iron lodes yields the highest Mg, Al, Ti and Mn concentrations of 832–1997 ppm, 4485–8927 ppm, 1841–3983 ppm and 1414–1974 ppm, respectively. Compared to Mag1-M, Mag1-V magnetite has lower concentrations of Mg, Al, Ti and Mn, raging 39–1677 ppm, 1560–7116 ppm, 400–1922 ppm and 157–1053 ppm, respectively (Fig. 4.6). Mag2 magnetite does not contain exsolution lamellae; in line with this, it contains less Mg (38–311 ppm), Al (828–2366 ppm) and Mn (250–677 ppm) compared to Mag 1 with exsolution textures. Mag2 has roughly the same Ti content (409–1456 ppm) as Mag1-V, but it has a higher V content of 100–306 ppm. Among all magnetite types, hydrothermal magnetite Mag4 has the lowest concentrations of Mg (30.6–239 ppm), Al (926–2196 ppm), Ti (98–336 ppm) and Mn (11–362 ppm). Relic magnetite modified by hydrothermal fluids, i.e., Mag3, exhibits a geochemical signature between magnetite from the iron bodies and hydrothermal magnetite.

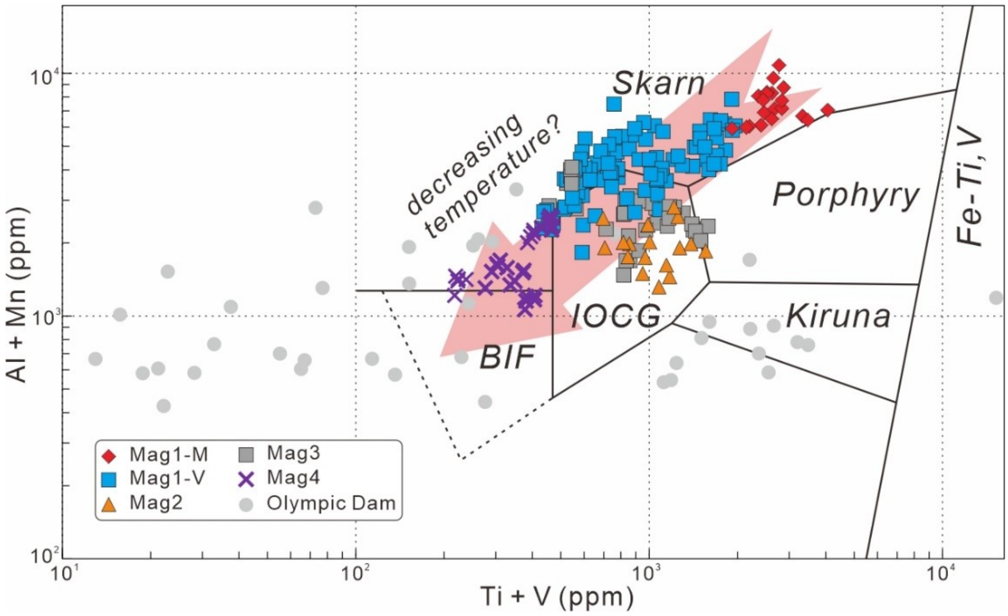

Fig. 4.6 [Al+Mn] vs. [Ti+V] discrimination diagram after Nadoll et al. (2014) for all magnetite types.

In Figure 4.6, the [Al + Mn] and [Ti + V] concentrations in magnetite from Cairn Hill are plotted in the discriminant diagram of Nadoll et al. (2014). Each generation of magnetite plots as a relatively distinct grouping, with the exception of Mag2 and Mag3 which display overlapping chemical characteristics. Mag1-M, fromthe massive iron lodes, and Mag1-V, from centimetre-wide iron veins, appear to show a decreasing trend in Al + Mn and Ti + V, if Mag1-M is taken to have formed first in the paragenesis. Mag4 represents a continuation of this trend. Mag2 and Mag3 plot at higher Ti + V values for equivalent Al + Mn values in the other groups.

5.2 Apatite petrology and chemistry

Apatite is the most common REE-bearing mineral at Cairn Hill. Previously, Chapter 3 distinguished two types of apatite, including the Type I clear apatite associated with early magnetite mineralisation and Type II pink-reddish apatite associated with sulfide mineralisation and hydrothermal alteration. In this contribution, we have further subdivided the apatite types and named them Type Ia, Type Ib, Type IIw, Type IIs and Type III (Fig. 4.7). Their specific characteristics are as follows:

Type Ia apatite is hosted by the iron ores, associated with Mag1-M and Mag1-V magnetite. It is typically euhedral to subhedral in shape. Type Ia apatite is transparent, unaltered, homogeneous, and bright in back-scattered electron (BSE) imaging, without porosity or monazite inclusions. It is commonly altered to Type IIw apatite during the Cu mineralisation superimposition (Fig. 4.7A–C). Type IIw apatite has a pink to reddish color and forms along grain boundaries and brittle fractures of Type Ia apatite. Type IIw apatite is darker in BSE imaging (Fig. 4.7C), overprints the bright Type Ia apatite cores or completely replaces Type Ia apatite. The dark Type IIw apatite displays sharp contacts with Type Ia apatite and exhibits porosity and sulfide and monazite inclusions.

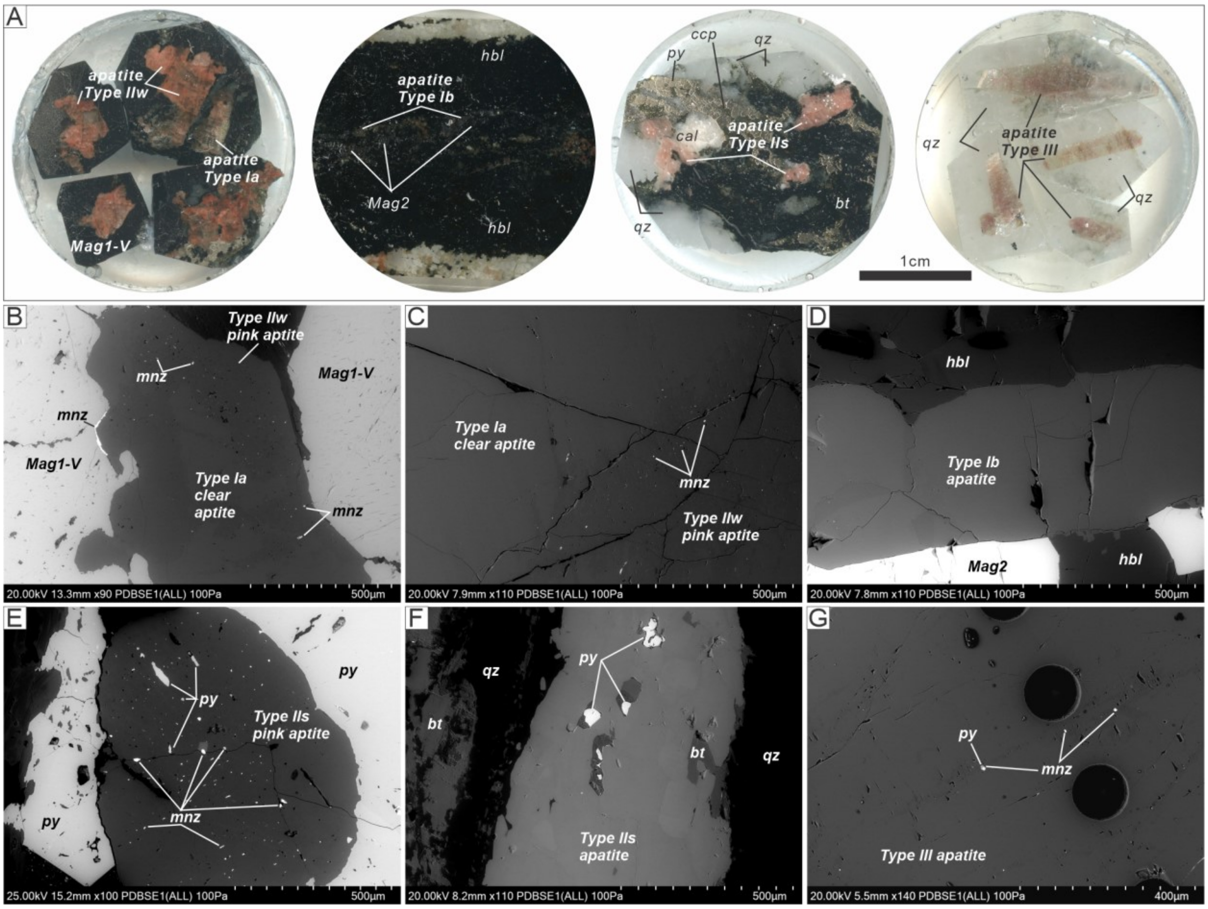

Fig. 4.7 (A) Mount samples for different apatite types. (B & C) Type Ia apatite associated with Mag1-V magnetite is altered to Type IIw apatite, with porosity and monazite inclusion inside. (D) Type Ib apatite distributed in hornblende. (E) Type IIs apatite enclosed by pyrite, with abundant pyrite and monazite inclusions. (F) Type IIs apatite in quartz-sulfide-biotite veins, its surface is clean without porosity or inclusions. (G) Type III apatite in quart vein, with minor pyrite and monazite inclusions developing along microfractures.

Type Ib apatite is associated with Mag2 magnetite in veins of hornblende + apatite + magnetite, where hornblende is volume-dominant. These apatite grains are colorless, transparent, and euhedral. Single apatite grain size ranges from 50 μm to centimeters. In BSE imagery, the Type Ib apatite is uniform in color and has a clean surface with no pores or monazite inclusions, similar to that of Type Ia (Fig. 4.7D).

Type IIs apatite is euhedral to subhedral, hosted in the biotite-sulfide-quartz ores (Fig. 4.3J and 4.7A). It is homogeneously pink without relict clear apatite cores and contains various amounts of pyrite, biotite, monazite, and/or quartz inclusions. The relationship between apatite, biotite and sulfides indicates that the (re)crystallization of Type IIs apatite is simultaneous with Cu mineralisation (Fig. 4.7E and F). In BSE imagery, this kind of apatite is uniform in color and has a clean surface.

Type III hydrothermal apatite is sampled from the coarse sulfide-quartz veins, euhedral and ranging from 50 μm to centimetres in size (Fig. 4.7A). Type III apatite is colorless and transparent and is locally altered to pink along fractures. In BSE imagery, the vast majority of the grainsare uniform in color and have clean surfaces. Minor pyrite and monazite inclusions are identified

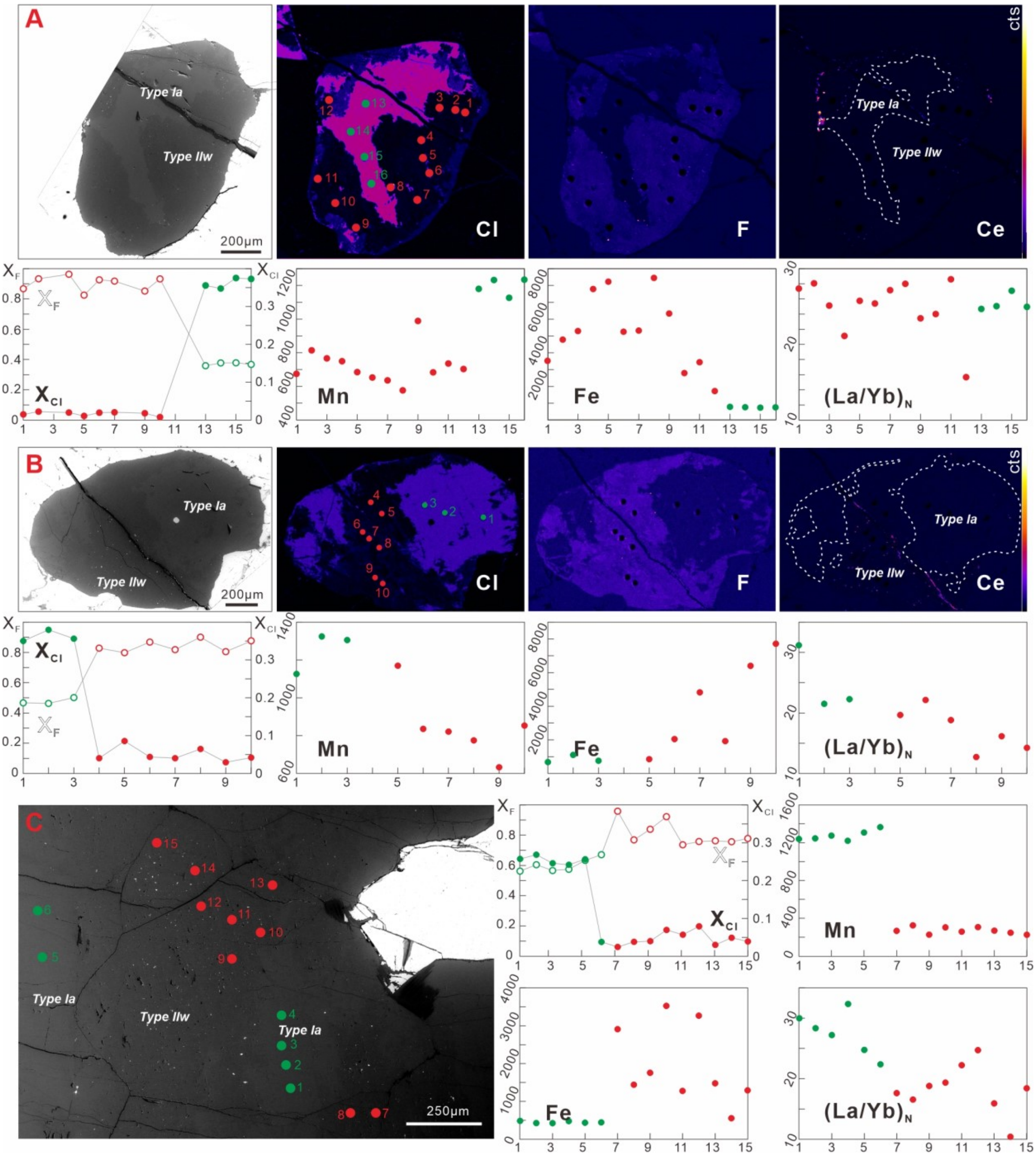

Fig. 4.8 BSE images, X-Ray mapping of Cl, F, and OH, and spot compositions, for representative apatite grains that have undergone hydrothermal alteration.

along fractures and are associated with narrow zones of porosity development (Fig. 4.7G).

A total of 60 apatite grains were analysed in samples collected from the open pits and drill hole CHD012 on the east of current open pits. The compositional results determined by EPMA (n = 351) and LA-ICP-MS (n = 367) are presented in Table A3 and A4.

Electron microprobe WDS maps of Cl, F, and Ce reveal strong chemical zonation of apatite grains and complex textures (Fig. 4.8). Fluorine and Cl are inversely coupled, with Cl-rich domains restricted to unaltered transparent Type Ia apatite and F-rich domains related to the altered pink type II apatite. The interface between the Cl-rich and F-rich domains is sharp and

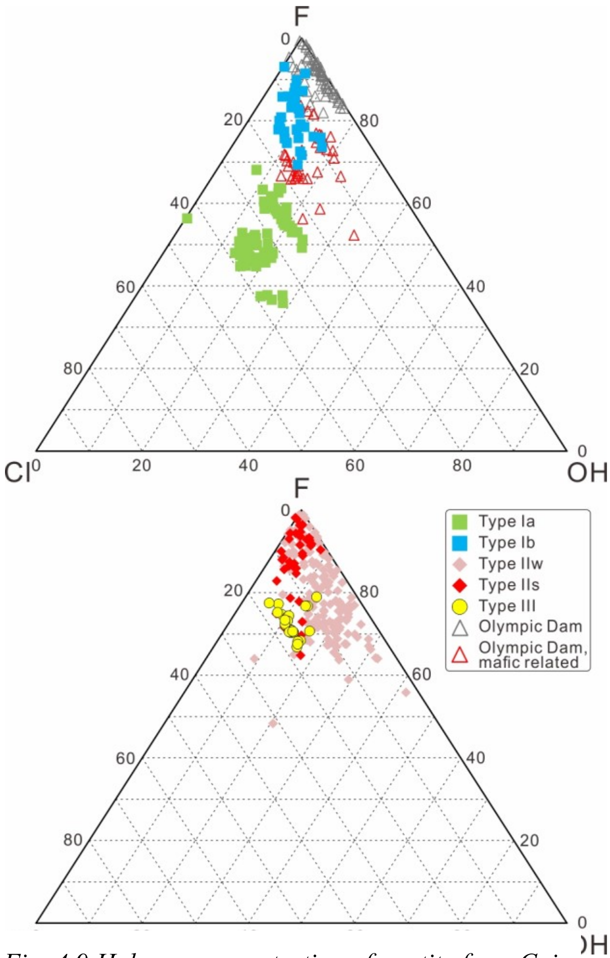

Fig. 4.9 Halogen concentration of apatite from Cairn Hill and Olympic Dam determined by EPMA. Data for Olympic Dam from Krneta et al. (2016).

consistent with the boundaries between the bright and dark zones in BSE imagery. Ce maps shows numerous monazite inclusions within the BSE-dark zones, which are spatially related to the F-rich domains, indicating the redistribution of REE during the hydrothermal alteration.

Type Ia apatite has the highest X_{Cl} (0.22–0.44) and lowest X_F (0.35–0.65) values, while Type Ib clear apatite from finer-grained hornblende-magnetite-apatite veins has relatively lower X_{Cl} (0.04–0.16) and higher X_F (0.69–0.93) values (Fig. 4.9). Compared to the unaltered Type Ia apatite, the weakly altered Type IIw apatite has lower X_{Cl} (0.001–0.31) and higher X_F (0.48–1.08) values, while the strongly altered Type IIs apatite is mainly F-apatite, with X_{Cl} and X_F values of 0.01–0.18 and 0.65–1.0, respectively. Type III hydrothermal apatite has a narrow range of X_{Cl}, X_F and X_{OH} values of 0.08–0.17, 0.67–0.79 and 0.05–0.16, respectively. The replacement of Cl-rich apatite by F-rich apatite is supported by spot analyses from single apatite grain (Fig. 4.8).

A summary of trace element data for the different types of apatite is presented in Fig. 4.10. Type Ia apatite is characterized by an enrichment of LREE and high $(La/Yb)_N$ ratios. It also has the highest Mn (605–1723 ppm) and Na (217–926 ppm) concentrations among all apatite analyzed. Type Ib apatite has a similar REE pattern and $(La/Yb)_N$ ratios to Type Ia apatite but lower Mn and Na concentrations of 503–771 ppm and 26–631 ppm, respectively.

The bulk of Type II apatite contains lower LREE, Mn, Th, and Na concentrations than Type I apatite. This pattern can be demonstrated by the overall apatite analysis (Fig. 4.10) and by the different zones of individual apatite grains (Fig. 4.8). Spot analyses from single grains with complex BSE and halogen zonation show the alteration of Cl-apatite by F-rich apatite is generally accompanied by depletion of Mn and LREE and introduction of Fe.

Some Type IIw apatite shows LREE depletion compared to Type I apatite, while Type IIs apatite consistently exhibits LREE depletion ($(La/Yb)_N$ ratios of 1–8) and the lowest Th contents (0.2–6 ppm). Type IIw apatite and Type IIs apatite are also distinguished by their different Fe, As, and Lu contents. Type IIw apatite has higher Fe contents (70–19000 ppm, mean of 3424

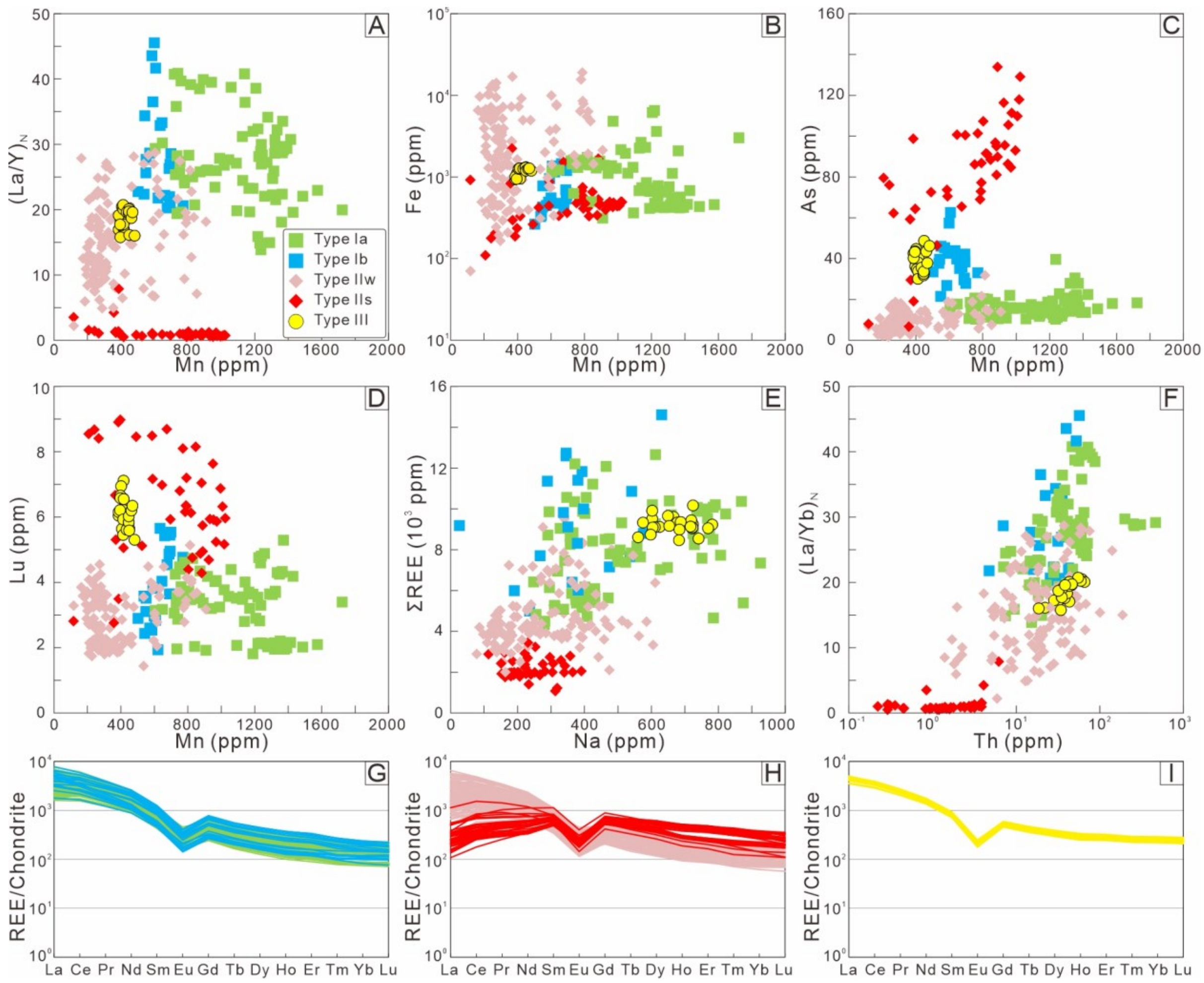

Fig. 4.10 Trace element compositions of different types of apatite at Cairn Hill. (A) $(La/Yb)_N$ vs. Mn. (B) Fe vs. Mn. (C) As vs. Mn. (D) Lu vs. Mn. (E) REE vs. Na. (F) $(La/Yb)_N$ vs. Th. (G) REE patterns for Type Ia and Ib apatites. (H) REE patterns for Type IIw and IIs apatites. (I) REE patterns for Type III apatite.

ppm) than the unaltered clear apatite Type Ia (313–10212, average 1298 ppm) and Type Ib (264–1454, average 714 ppm), while Type IIs apatite has overall lower Fe contents (110–2232 ppm, average 562 ppm). Type IIw apatite has the lowest As contents (2–32 ppm), while Type IIs has the highest As contents of all analyses (7–134 ppm). Lu contents of Type IIw apatite do not differ from that of the unaltered apatite (i.e., Type Ia and Type Ib), but Type IIs apatite has significantly higher Lu contents of 2.8–9.0 ppm with a mean of 6.3 ppm.

Type III apatite has a similar REE pattern to Type Ia and Ib apatite; however, it is distinguished from Type Ia and Ib apatite by its low Mn contents (386–482 ppm), and from Type IIw apatite by its higher ΣREE and Na content (560–782 ppm) and from Type IIs by higher ΣREE, LREE and Th contents (18.6–65.6 ppm).

5.3 Fluid inclusion petrology

Fluid Inclusion petrographic and microthermometric studies focused on fluid inclusion assemblages (FIA), i.e., a group of inclusions trapped synchronously, representing a true fluid inclusion assemblage. FIA were selected for study if they are trapped along the same primary growth zone in quartz, or along the

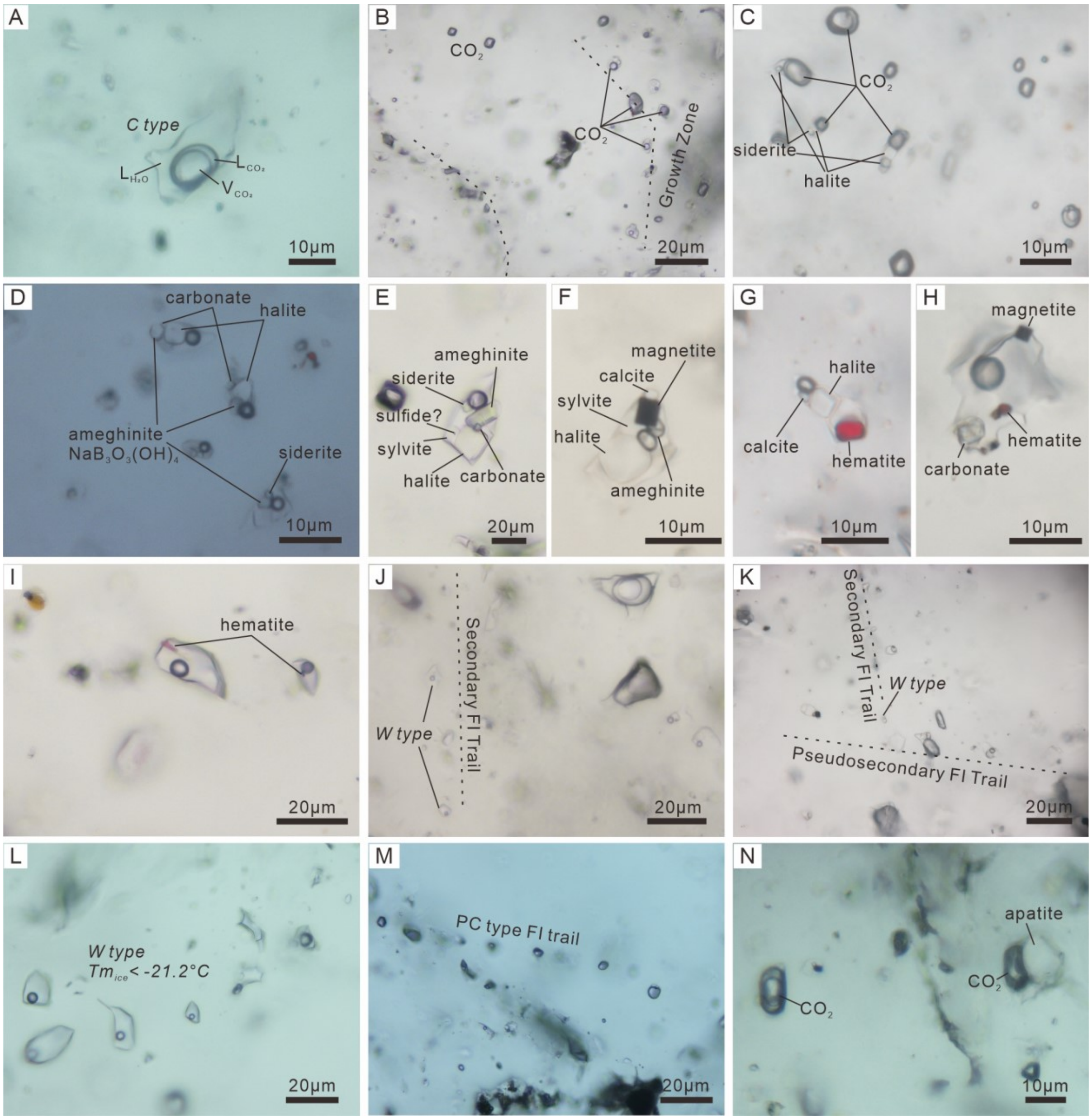

Fig. 4.11 Photographs of representative fluid inclusions. (A) C-type inclusion with "double eyelid". (B) The assemblage of PC, C and S type inclusions along the growth zone of quartz. (C) Coexisting PC and S type inclusions, halite and siderite daughter minerals are present in the CO_2-rich fluids. (D–G) Various halite-bearing SH-type inclusions. Multiple daughter minerals include halite, sylvite, ameghinite, siderite, calcite, magnetite, hematite, sulfide, and unknown carbonate. (H) SN-type inclusions with the solid phase of magnetite, hematite and carbonate, no halite is present in the inclusions. (I) SN-type inclusions with hematite as the only solid phase. (J & K) W-type inclusions form secondary trails. (L) W-type inclusions with Tm_{ice} lower than -21.2 °C. (M) PC-type inclusions form trails crosscut the quartz crystal. (N) Apatite is occasionally captured as a solid phase in the CO_2-rich inclusions.

same healed fracture, and visually contain identical phase ratios, similar shapes, and similar daughter minerals. Single fluid inclusions that occur as isolated inclusions are excluded in this study.

Fluid inclusions types are subdivided based on their compositions, phases (L-V-S) present at room temperature, and phase transitions observed during heating and cooling. They were also classified for primary, pseudo-secondary, and secondary inclusions using the criteria defined by

Roedder (1984). Five main types of inclusions have been identified from the study of polished fluid inclusion sections, designated as C-, PC-, SH-, SN-, and W-types, respectively.

C-type inclusions consist of two (liquid H_2O + CO_2-rich supercritical fluid) or three phases (liquid H_2O + liquid CO_2 + vapor CO_2) at room temperature, with carbonic phases (liquid CO_2+vapor CO_2) occupying 25 – 95% of total volume (Fig. 4.11A and J). They are generally 6 to 30 μm in diameter and have rounded isometric, elliptic, or negative crystal shapes. Minor C-type inclusions have carbonic phases less than 50 % of total volume, while carbonic phases occupy more than 60 % in the majority of C-type inclusions. Most C-type inclusions occur in growth zones or form trails in quartz grains and are regarded as primary. Apatite is observed in some C-type inclusions (Fig. 4.11N), and these inclusions are classified as SN-types. C-type inclusions commonly coexist with PC-type and SH-type inclusions and form fluid inclusion assemblages together (Fig. 4.11B, C, and J).

PC-type inclusions are pure CO_2 inclusions containing liquid CO_2 or liquid CO_2 + vapor CO_2 at room temperature and are usually closely associated with C-type inclusions (Fig. 4.11B, C, J, and K). PC-type inclusions are generally 8 to 40 μm in diameter and rounded isometric or negative crystal shape. PC-type inclusions are abundant and account for > 80% of the carbonic inclusions, typically as primary or pseudo-secondary.

SH-type inclusions generally occur as primary inclusions, with or without a CO_2 phase, and coexist with C-type and PC-type inclusions (Fig. 4.11B–D). SN-type inclusions typically form secondary trails, together with W-type inclusions, which crosscut entire quartz crystals (Fig. 4.11H–K). SH and SN-type inclusions are solid- or daughter mineral-bearing, distinguished by halite presence or absence. SH-type inclusions contain halite, irrespective of whether they have other kinds of daughter minerals (Fig. 4.11C–G), while SN-type inclusions contain no halite but contain opaque or transparent solid minerals that do not melt during heating (Fig. 4.11H, I and N), e.g., magnetite, hematite, and carbonate. SH-type inclusions typically contain various daughter minerals besides halite, and individual inclusions can contain up to 6 daughter crystals (Fig. 4.11 E). Daughter crystals include halite, sylvite, calcite, siderite, ameghinite [$NaB_3O_3(OH)_4$], magnetite, hematite, and an unindentified sulfide based on the melting behavior during heating and/or laser Raman analysis. It is worth noting that siderite and hematite do not occur together in the same inclusion (Fig. 4.13C–I).

W-type inclusions show two visible phases at room temperature, i.e., liquid H_2O and vapor H_2O, and occur as irregular-shaped to rounded, 4 to 25 μm in size (Fig. 4.11K and L). In general, the vapors have filling degrees of 5 to 20 vol. %. Most W-type inclusions occur as secondary trails along with healed fractures and generally coexist with SN-type inclusions.

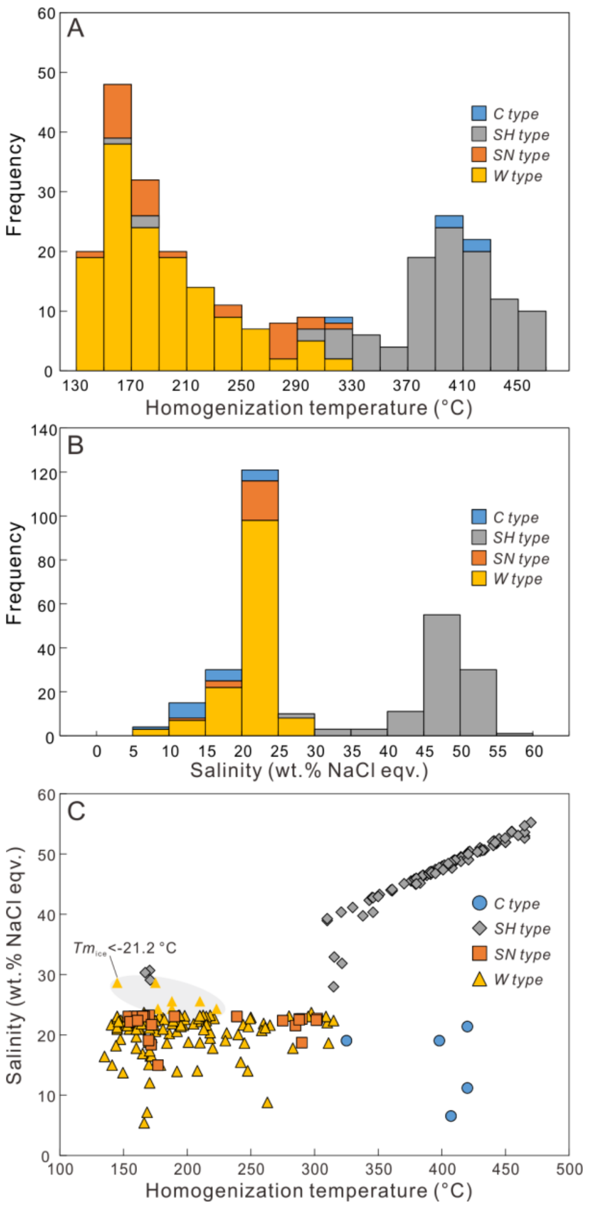

Fig. 4.12 (A) Histogram of fluid inclusion homogenization temperatures. (B) Histogram of fluid inclusion salinities. (C) Plot of salinity vs. homogenization temperature for different fluid inclusions at Cairn Hill.

5.4 Microthermometry and pressure estimation

A total number of 342 inclusions from Cairn Hill were analyzed by microthermometry, and the results are presented in Table A5 and summarized in Table 2 and Fig. 4.12. It is challenging to get accurate total homogenization temperature for some inclusions, especially the C-type and SH-type inclusions, as they tend to decrepitate at the temperature of 260–420 °C before total homogenization. The decrepitation behavior indicates the high capture pressure of these inclusions.

C-type inclusions display the melting of CO_2 solid at temperatures between -58.4 °C and -56.8 °C, indicating the gas phase is mainly CO_2, consistent with the laser Raman spectroscopic analysis. Melting of CO_2 clathrate occurs at temperatures between -9.7 °C and 6.5 °C, corresponding to a salinity range of 6.5 to 21.4 wt. % NaCl equiv. (Fig. 4.12B). The wide range of CO_2 clathrate melting temperature and salinity is consistent with the coexisting pure carbonic and halite-bearing inclusions. The CO_2 phase is partially homogenized to vapor, and the partial homogenization temperature is uniform in every fluid inclusion assemblage ranging from 26.0 to 31.0 °C. Only five inclusions achieve total homogenization at 325–420 °C (Fig. 4.12A) and then decrepitate subsequently, while the rest of C-type inclusions decrepitate at 260–420 °C prior to total homogenization. However, the importance of this kind of inclusion should not be underestimated as they indicate high capture pressure.

PC-type inclusions contain only liquid CO_2 or liquid CO_2 + vapor CO_2 at room temperature, but a vapor bubble occurs during cooling runs. These inclusions yield melting temperatures for solid CO_2 from -58.4 °C to -56.9 °C. The homogenization temperatures of CO_2 to the vapor phase vary from 22.0 °C to 30.3 °C, corresponding to densities of 0.21–0.36 g/cm^3 (Table 2). There is no difference between primary and pseudo-secondary PC-type inclusions.

Table 2 Microthermometric data for different types of inclusions.

Fluid inclusion	Tm_{CO2} (°C)	Tm_{clath} (°C)	Th_{CO2} (°C)	Tm_{ice} (°C)	Tm_S (°C)	Th_{L-V} (°C)	Th_{total} (°C)	Salinity (wt.%)	Dentisty (g/cm³)	Note
C type	-58.4 to -56.8	-9.7 to 6.5	26.0 – 31.0			325–420	325–420	6.5–21.4	0.32–0.77	CO_2 volume ranges from 25% to 95%; Many inclusions decrepitate during heating
PC type	-58.4 to -56.9		22.0 – 30.3						0.21–0.36	All homogenized to vapor
SH type	-58.4 to -56.9	-9.6 – 8.0	23.0 – 30.8		100–470	150–470	167–470	28.0–55.2	0.98–1.31	Sylvite melts at 55–190 °C
SN type	-57.1 to -56.8	-9.6	27.5 – 29.5	*-21.3 to -11*		150–326	150–326	*15.0–23.2*	-	Salinities are minimum estimation.
W type				-30.0 to -3.3		135–315	135–315	5.4–23.2	0.86–1.14	Tm_{ice} below -21.2 °C indicates the presence of Ca and K

When present, the CO_2 phase in SH-type inclusions yields melting temperatures for solid CO_2 of -57.3 to -57.1 °C. The CO_2 phase is partially homogenized to vapor with partial homogenization temperatures ranging from 23 to 30.8 °C. Most SH-type inclusions show consistent microthermometric behavior, i.e., halite dissolution after vapor bubble disappearance while halite dissolutes before vapor disappearance in 8 inclusions (Table A5). The liquid-vapor homogenization by vapor bubble disappearance is observed at 150–470 °C. The halite dissolution for SH-type inclusions occurs at 100 °C to 470 °C, corresponding to salinities from 28.0 to 55.2 wt.% NaCl equiv. (Fig. 4.12), and densities of 0.88–1.31 g/cm³. Besides halite, sylvite could also dissolve during heating, and seven inclusions experienced sylvite dissolution at 55–190 °C. The melting of other daughter minerals (both transparent and opaque) is not observed during heating, and thus the salinity estimation here is the minimum value of the actual salinity of the ore-forming fluids.

Since the insolubility of daughter minerals in SN-type inclusions, we can only get liquid-vapor homogenization data for the SN subtype inclusions, and the salinities estimation based on the freezing point is not reliable. Ice-melting temperatures range from -21.3 to -11.0 °C. Liquid–vapor homogenization in these inclusions occurs at temperatures between 150 °C and 326 °C (Fig. 4.12A). The salinities estimation is 15.0–23.2 wt. % NaCl equiv. (Fig. 4.12B), and these values could only provide a lower limit of the actual salinity.

The majority of W-type inclusions are secondary, and they have ice-melting temperatures from -21.2 to -3.3 °C and total homogenization temperatures ranging from 135 to 315 °C. Some inclusions yield ice-melting temperatures from -30.0 °C to -21.3 °C (Fig. 4.11L and 4.12C), lower than that of the NaCl-H_2O system, indicating that the inclusions with low ice-melting temperatures could be Ca- or K-bearing.

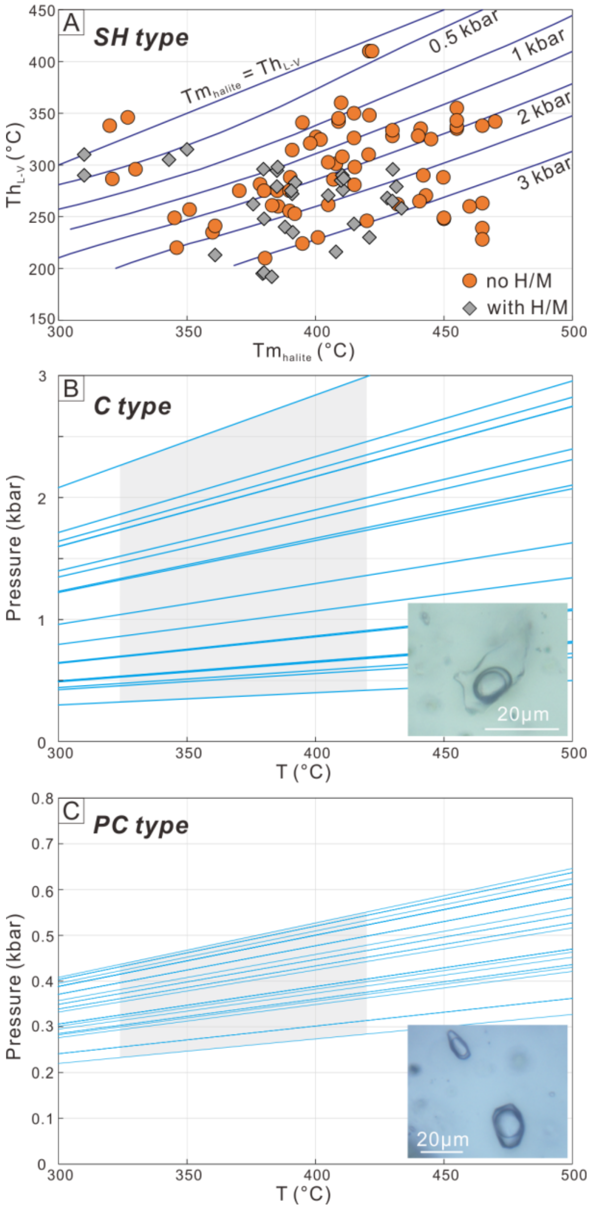

Fig. 4.13 The estimated capture pressure of SH, C, and PC-type inclusions.

Trapping pressure can be estimated only when the exact trapping temperature is known, or fluid inclusions are trapped during phase separation (Roedder and Bodnar, 1980; Brown and Hagemann, 1995). Pressure estimation has been done for C-type, PC-type, and SH-type inclusion, which are assumed to form by the unmixing of primary ore-forming fluids at 325–420 °C. For carbonic inclusions, the pressure estimation is mainly based on the CO_2 phase homogenization style and temperature and the volume percent of the CO_2 phase (Brown and Lamb, 1989), and thus we can still get pressure estimation at a specific temperature from the isocapacity curves even the carbonic inclusions decrepitate prior to total homogenization. Halite dissolution temperature and vapor bubble disappearance temperature are plotted in Fig. 4.13A to estimate the trapping pressures of SH-type inclusions using the empirical equation proposed by Becker et al. (2008). The estimated pressure for SH-type inclusions is 0.5–3 kbar, representing the range of hydrostatic and lithostatic pressure. The calculated pressure for C-type inclusions ranges from 0.4–3 kbar (Fig. 4.13B; Brown and Lamb, 1989), consistent with the SH-type inclusions and representing the range of hydrostatic and lithostatic pressure. PC-type inclusions yield homogeneous and stable trapping pressure, and their maximum values represent the minimum estimation of hydrostatic pressure ranging from 0.4–0.55 kbar at the temperature of 325–420 °C (Fig. 4.13C)..

5.5 Compositions of fluid inclusions

LA-ICP-MS analytical results for 94 individual inclusions are summarized in Fig. 4.14, and all data are presented in Table A6 with detection limits. Analysis for C-type inclusions failed to yield any meaningful data due to the decrepitation. PC-type inclusions are not analyzed as the trace element content of pure CO_2 inclusions usually is very low, and almost no valid data can be obtained. SN inclusions are also not analyzed because they lack reliable salinity data and have various solid phases that may be captured occasionally.

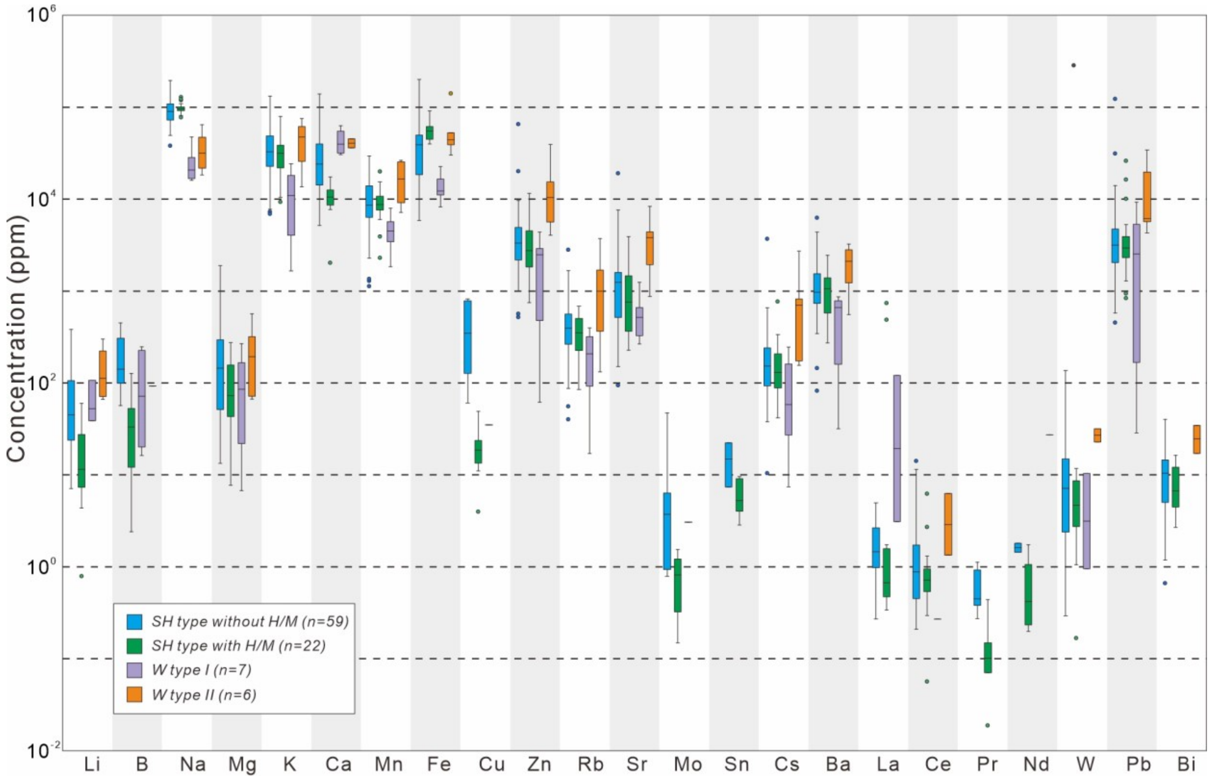

Fig. 4.14 Compositions of different types of fluid inclusions obtained from LA-ICP-MS.

SH-type inclusions are subdivided into SH-type without hematite/magnetite (H/M) and SH-type with H/M, which is easy to distinguish during the analysis. SH-type inclusions are generally rich in Na, K, Ca, Mn, Fe, Zn, Sr, Ba, and Pb. SH-type inclusions without H/M have Na contents ranging from 38122 to 195114 ppm, K contents ranging from 6905 to 131974 ppm, and Ca contents ranging from 5188 to 139643 ppm. Iron concentrations vary greatly, ranging from 5852 to 200339 ppm, with Cu contents of 60–819 ppm. In addition to Fe and Cu, the ore-forming fluids also contain considerable Pb and Zn, ranging from 454–122977 ppm and 520–65531 ppm, respectively. The widespread presence of ameghinite daughter mineral in the inclusions is supported by the B contents of 57–451 ppm for SH-type without H/M. SH-type with H/M is characterized by consistently high Fe contents of 39855–90867 ppm. Compared to SH-type without H/M, B, Ca, and Cu concentrations are lower for SH-type with H/M, ranging from 2–127 ppm, 2026–17435 ppm, and 4–49 ppm, respectively. The difference of B contents in these two subgroups SH-type inclusions is consistent with the change of ameghinite volume percent, where a larger ameghinite crystal is often observed in SH-type inclusions without H/M (Fig. 4.11D–G). The content of other elements in the SH-type with H/M basically falls into the range of the SH-type without H/M (Fig. 4.14).

W-type inclusions are subdivided into W-type I and W-type II according to their Tm_{ice}, W-type I refers to regular inclusions with Tm_{ice}> -21.2 °C, and W-type II are inclusion with Tm_{ice}< -21.2 °C, which implies the possible influence of K, Ca or other solutes. W-type inclusions are characterized by lower Na content, and higher Ca content than the SH-type inclusions (Fig. 4.14).

All W-type inclusions contain Cu lower than the detection limit, except one inclusion with 35 ppm Cu. Except for high Ca, W-type I inclusions contain trace elements up to one order of magnitude lower than SH-type. W-type II, however, contains trace elements comparable to the SH-type inclusions (e.g., K, Ca, Mn, Fe, Zn, Rb, Sr, Ba, and Pb) except for the lower Na concentrations of 15982–64573 ppm.

6. Discussion

6.1 Ca. 1580 Ma magnetite-apatite mineralisation in the northern Gawler Craton

Early magnetite-apatite mineralisation at Cairn Hill experienced upper amphibolite to granulite-facies metamorphism at ca. 1490 Ma, and was subsequently overprinted by later hydrothermal Cu mineralisation at ca. 1460 Ma (Yu et al., 2023; Chapter 3). The magnetite-apatite-hornblende lodes have been deformed into a series of iron lenses of varying size, parallel to the foliation of the gneissic wall rocks (Fig. 4.3). This makes it very challenging to discern the original genesis of Fe-P assemblages; for example, whether they represent chemical anomalies in the stratigraphy or later magmatic-hydrothermal veins. Conventional isotope or mineral thermometers are likely to be reset by high-grade metamorphism, therefore, the use of mineral compositions to infer genesis must also be interpreted with care.

Here the widely used [Al + Mn] versus [Ti + V] diagram (Fig. 4.6) is used to discriminate the origin of magnetite (Nadoll et al., 2014; Knipping et al., 2015). Magnetite from the Fe-P mineralisation stage is mainly located in the skarn and IOCG fields, without IOA or BIF affinity. Compared to sedimentary magnetite, Mag1-M, Mag1-V and Mag2 contain higher concentrations of Al, Mn, Ti and V, which tend to incorporate into magnetite at higher temperatures (Nadoll et al., 2014; Salazar et al., 2020). The Ti and V concentrations of magnetite from Cairn Hill are lower than those of Porphyry, Kiruna or Fe-Ti, V deposits (Fig. 4.6), indicating the magnetite may be precipitated in the hydrothermal system rather than igneous, as natural igneous magnetite is ubiquitously enriched in Ti and V elements (Nadoll et al., 2014; Knipping et al., 2015 and references therein). The prevalent exsolution of Mg-bearing silicate in coarse-grained magnetite may also imply relatively high temperatures of formation (Canil and Lacourse, 2020), which is uncommon in BIF or sedimentary magnetite. This is consistent with the igneous host rocks of the magnetite deposit.

At Cairn Hill, apatite associated with magnetite mineralisation (Type Ia and Ib) is characterized by high chlorine concentrations, with X_{Cl} of 0.22–0.44 and 0.04–0.16, respectively (Fig. 4.9). These halogen contents are very different from sedimentary or authigenic apatite, which is dominated by hydroxyapatite and carbonate fluorapatite (Gunnars et al., 2004; Joosu et al., 2016 and references therein). Chlorine-rich apatite is common in IOA deposits in the Chilean iron belt, magmatic-hydrothermal systems related to magmatic arcs dominated by tholeiitic basaltic rocks, gabbros, and mafic dikes associated with calc-alkaline andesites and basaltic andesite flows (e.g., Palma et al., 2019; La Cruz et al., 2020). At Olympic Dam, hydrothermal apatite is predominately F-apatite, while higher Cl apatite are considered to represent magmatic apatite in mafic rocks (Krneta et al., 2016). In felsic igneous systems, apatite is typically dominated by the end-member phase fluorapatite, while Cl-rich apatite commonly occurs in mafic intrusions (Harlov et al., 2002 and references therein; Piccoli and Candela, 2002; Webster and Piccoli, 2015). The Cl-rich composition of the Cairn Hill primary apatite suggests the magnetite-apatite ore is not a felsic magmatic system or derived from late stage magmatic fluids (e.g. IOA, IOCG, W or Sn systems; Rasmussen and Mortensen, 2013; Palma et al., 2019; Roy-Garand et al., 2022; Zhang et al., 2023). Further research using radiogenic and stable isotope systems is required to further constrain the mechanism for formation of the magnetite ore system.

6.2 Apatite as an indicator mineral for hydrothermal Cu mineralisation

At Cairn Hill, apatite associated with iron mineralisation and copper mineralisation show notable variations under both visible light and BSE imaging (Fig. 4.7). They display unique geochemical compositions that further distinguish these two mineralisation stages (Fig. 4.8–10). Hence apatite is used to fingerprint the physical and compositional characteristics of the fluids forming the Cu mineralisation and hydrothermal alteration by detailed petrography, mineral texture and halogens, and trace element studies. Furthermore, the characterization of apatite from a known Cu system makes apatite a potential indicator accessory mineral for exploring Cu mineralisation in the buried northern Gawler Craton.

Apatite types IIw, IIs, and III are linked to Cu mineralisation, with types IIw and IIs arising from early apatite that underwent different degrees of hydrothermal modification. During the metasomatic processes, the altered apatite is characterized by increasing X_F and depletion of Mn, REE and Na. Substituting Cl-rich apatite with F-rich apatite can indicate the prevalence of higher F/Cl ratios in felsic ore systems, as reported by Piccoli and Candela (2002) and Webster and Piccoli (2015). However, experimental studies have demonstrated that F/Cl ratios cannot be directly tied to Cl content of the fluid phase during replacement reactions as Cl partitioning into apatite varies significantly depending upon T, P and OH- activity (Kusebauch et al., 2015).

Prior studies have reported the removal of Mn from modified apatite through the influence of acidic fluids in IOA and porphyry copper deposits (Bonyadi et al., 2011; Bouzari et al., 2016). However, a comprehensive explanation for this phenomenon is currently absent. In apatite lattice, Mn^{2+} has an ionic radius of 0.90 Å in 7-fold and 1.0 Å in 9-fold coordination, while Mn^{3+} has a smaller ionic radius of 0.62–0.67 Å (Miles et al., 2014 and references therein). Thus, the Mn concentration of apatite was previously regarded as an indicator of oxygen fugacity based on the fact that Mn^{2+} substitutes into apatite more readily than Mn^{3+} (Miles et al., 2014), but Stokes et al. (2019) suggest that Mn is present predominantly as Mn^{2+} over a wide range of oxidation state in natural apatite and not controlled by oxygen fugacity. In hydrothermal systems, the loss of Mn would be necessarily accompanied by its dissolution and transport in the ore-forming fluids, mostly as Mn^{2+} that is more soluble in acidic fluids. We suggest the depletion in apatite Mn content simply reflects the high Mn solubility in fluids, as supported by high Mn concentration in fluid inclusions (Fig. 4.14). Apatite Mn content may be an effective tracer of fluid activity rather than oxygen fugacity changes.

The depletion of LREE in altered apatite is consistent with the widespread monazite inclusions within apatite (Fig. 4.7 and 4.8). Coupled removal of LREE in apatite and formation of secondary monazite has been proposed to occur via coupled dissolution–reprecipitation processes (Torab and Lehmann, 2007; Putnis, 2009; Harlov, 2015 and references therein; Chapter 3). Although, fluids dissolving Cl-rich apatite will be increasingly likely to transport REEs (increased fluid Cl content, Kusebauch et al., 2015), the localised enrichment in LREEs during apatite recrystallisation leads to rapid crystallisation of monazite, presumably in response to fluid LREE saturation. The mineralizing fluids must have some ability to transport LREEs as indicated by the detectable LREE concentrations in fluid inclusions (Fig. 4.14) and high LREE concentrations in the Type III apatite (Fig. 4.10I) that is directly precipitated from hydrothermal fluids. Along with the loss of LREE and formation of secondary monazite, the apatite thorium contents also decrease during recrystallisation (Fig. 4.10F), potentially due to the high thorium mobility in sulfate-bearing aqueous fluids (Nisbet et al., 2019).

While the difference of Mn, REE, and $(La/Yb)_N$ ratios between Type IIw and IIs apatites may be due to various degrees of fluid alteration, the opposite patterns of redox-sensitive elements, i.e., Fe and As in Type IIw and IIs apatites may record the evolution of ore-forming fluids (Fig. 4.10B and C). Both single grain and overall trends record varying degrees of iron enrichment (Fig. 4.8 and 4.10B) in the weakly altered Type IIw apatite and the depletion of As (Fig. 4.10C); however, the strongly altered Type IIs apatite is characterized by depletion of iron and enrichment of As. The opposite trend of these two elements is consistent with a change in fluid oxygen fugacity. Apatite commonly incorporates divalent cations due to the same charge and similar cation sized to Ca^{2+}, including Sr^{2+}, Ba^{2+}, Mg^{2+}, Mn^{2+}, Fe^{2+}, Eu^{2+} and Pb^{2+} (Pan and Fleet, 2002; Piccoli and Candela, 2002; Mao et al., 2016; O'Sullivan et al., 2020). It is conceivable that the recrystallized apatite would incorporate more Fe during the infiltration of Fe^{2+}-rich fluids but be incompatible with trivalent iron once the fluids become more oxidized (Fig. 4.10B). Similar scenario may also apply to arsenic, which predominantly exists as As (V) in most natural As-bearing apatite, but as As (III) in most hydrothermal fluids or As (V)–As (III) in highly oxidized (hematite-anhydrite stable) fluids (Lee et al., 2009; James-Smith et al., 2010; Liu et al., 2017). Therefore, the recrystallization of apatite in relatively reduced fluids would discharge its As due to the reduction of As (V) to As (III), and more As (V) would be introduced to the recrystallized apatite under more oxidized conditions (Fig. 4.10C). The conclusion of elevating fluid oxygen fugacity derived from the geochemical characteristics of altered apatite is consistent with the pattern revealed by fluid inclusions, where the daughter minerals change from siderite to magnetite, to hematite (Fig. 4.11C–I).

In addition, both Type IIs and Type III apatites record higher Lu concentrations (Fig. 4.10D), which may be introduced by the mineralizing fluids. The acquisition of Lu and loss of Hf in the recrystallized apatite will effectively reset its Lu-Hf geochronometer, allowing it to accurately constrain the timing of mineralisation (Chapter 3).

6.3 Genesis of Cu mineralisation evidenced by fluid inclusions

The ore-forming fluids during Cu mineralisation at Cairn Hill are CO_2-rich and hypersaline, evidenced by the presence of coexisting carbonic fluid inclusions and multiple daughter minerals (Fig. 4.11). LA-ICP-MS analyses indicate that the fluid inclusions have high K/Na, Rb/Na, and Cs/Na ratios (Fig. 4.14). These are typical characteristics of magmatic fluids, distinct from the metamorphic fluids, meteoric water, or basinal brines (e.g., Lowenstern, 2001; Ulrich et al., 2001; Rusk et al., 2004; Klemm et al., 2007; Audétat et al., 2008; Williams-Jones et al., 2010). The coexisting CO_2-rich and hypersaline brine inclusion assemblages are commonly formed by fluid immiscibility or phase separation of aqueous brine phase sourced from synchronous intrusions, which is the common case in IOCG systems in Cloncurry and Carajás districts (Williams et al., 2001; Baker et al., 2008; de Melo et al., 2019; Previato et al., 2020; Craveiro et al., 2020), e.g., the ore-forming fluids in Cloncurry IOCG deposits have been suggested to exsolve from the ca. 1550–1490 Ma Williams-Naraku Batholith (Page and Sun, 1998; Baker et al., 2008). Ca. 1460 Ma intrusions have not been discovered within the mine area, but contemporaneous magmatism is not uncommon in the extensively buried northern Gawler Craton, e.g., ca. 1460 Ma A-type granites in drill holes Karkaro 1 and OBD 08 (Morrissey et al., 2019). Hidden intrusions near Cairn Hill may provide magmatic-hydrothermal fluids responsible for the ca. 1460 Ma Cu mineralisation.

The boiling fluid inclusion assemblages may provide an estimation of the capture temperature and pressure without additional correction (Fig. 4.13). Despite the broad decrepitation during heating, the homogenization temperatures of coexisting C-type and SH-type inclusions range from 325 to 470 °C (Fig. 4.12A and C). Similar temperature conditions have been reported for the magnetite alteration in the Olympic Province (Oreskes and Einaudi, 1992; Bastrakov el al., 2007; Davidson et al., 2007) and the magnetite-rich Cu mineralisation in the Cloncurry district (Williams et al., 2001; Baker et al., 2008).

The capture pressures of C-type and SH-type inclusions are estimated independently (Brown and Lamb, 1989; Becker et al., 2008) but consistent from 0.5 to 3 kbar (Fig. 4.13A and B). Here we argue the large range represents pressure fluctuation between lithostatic and hydrostatic pressure, corresponding to a depth of 5 – 10.5 km. The PC-type inclusions yield homogeneous trapping pressure, corresponding to a depth of 4 – 5.5 km, provided that the maximum values represent the minimum estimation of hydrostatic pressure (Fig. 4.13C). Considering the prevalence of PC-type inclusions at the current mining depth, more extensive fluid immiscibility may develop at greater depths. The secondary SN-type and W-type inclusions have lower homogenization temperatures ranging from 130 to 330 °C and lower salinities ranging from 5.4 to 23 wt.% NaCl equiv. (Fig. 4.12), reflecting the gradual cooling and dilution of ore-forming fluids.

Ore-forming fluids at Cairn Hill are rich in B, Na, K (10^4–10^5 ppm), Ca (10^4–10^5 ppm), and Fe (10^4–10^5 ppm) (Fig. 4.14). The solid ability of ore-forming fluids to transport Fe (Hayward and Skirrow, 2010) is consistent with the presence of siderite, magnetite, and hematite in the fluid inclusions (Fig.4.11C–I). Based on the presence or absence of magnetite and hematite, the halite-bearing inclusions are further classified as SH-type without H/M and SH-type with H/M. These two subtypes display an apparent decrease of B, Cu and Mo concentrations from SH-type without H/M to SH-type with H/M inclusions, although that many analyses were below the detection limit (Fig. 4.14 and Table A6). The decrease in copper concentration in the ore-forming fluids, i.e., the precipitation of copper, may be triggered by the interaction of fluids with chemical barrier magnetite via a reaction:

$$2CuCl_2^- + Fe_3O_4 + 4H_2S = 2CuFeS_2 + FeCl_2^0 + 2Cl^- + 4H_2O.$$

The occurrence of siderite in fluid inclusions is usually associated with high CO_2 proportion, and siderite (Hayward and Skirrow, 2010), as well as ameghinite, would decrease or disappear with the appearance of magnetite and hematite, indicating that the iron-bearing phases are controlled by the partial pressure of CO_2 and oxygen fugacity. The potential mechanism may be via the following reactions,

$$Fe_3O_4 + 3CO_2 = 3FeCO_3 + 1/2O_2$$

$$Fe_3O_4 + CO_2 = FeCO_3 + Fe_2O_3.$$

The aforementioned mechanisms suggest that pre-existing magnetite is essential to later Cu mineralisation, during which time earlier magnetite would be modified, mobilized and recrystallized. Therefore, the relic magnetite Mag3 and hydrothermal magnetite Mag4 tend to have lower Al, Mn, Ti and Mg concentrations (Fig. 4.6). This process is also accompanied by the alteration of Ca-bearing minerals, e.g., hornblende and plagioclase, which may account for the higher Ca, Mn and Sr contents of the late fluids (Fig. 4.14).

Our favored model for the Cu mineralisation at Cairn Hill involves the generation of high-temperature, CO_2-rich, oxidized Cu-bearing magmatic fluids that exsolved from hidden intrusions and were channeled to the mineralisation site. As magmatic-hydrothermal fluids ascend, they undergo decompression, fluid immiscibility and concentrating, and interaction with the earlier magnetite lead to the final Cu mineralisation. While we consider that the fluid immiscibility of CO_2 plays a vital role in the Cu mineralisation and controls iron-bearing phases, no difference in pressure was observed between the SH-type inclusions with H/M and SH-type inclusions without H/M (Fig. 4.13A). This indicates the mineralisation was not a single-phase but periodic boiling, making the pressure fluctuate between lithostatic and hydrostatic, and resulting in continued precipitation of chalcopyrite, pyrite and magnetite. The whole system became more oxidized with the continued infiltration of oxidizing ore-forming fluids, which is consistent with the development of hematite-bornite-chalcocite (Fig. 4.4F and 4.5E), more hematite daughter minerals in fluid inclusions (Fig. 4.11G–I), and variations in apatite trace elements (Fig. 4.10B and C).

6.4 Implication for regional Fe-Cu mineralisation in the Gawler Craton

Recent drilling has revealed early, deep magnetite-apatite mineralisation at depth and at the outer margins (e.g., Wirrda Well and Acropolis prospects) of the hematite-dominant Olympic Dam deposit, supporting the genetic models that the earlier magnetite mineralisation develops beneath the hematite-dominant IOCG systems (Ehrig et al., 2012; Apukhtina et al., 2017; Verdugo-Ihl et al., 2020). Cairn Hill, as the largest deposit in the northern Olympic Fe-Cu-Au Province, is of central importance to the concept that the northern Olympic Fe-Cu-Au Province represents deeper crustal levels of the much large hematite-dominated deposits elsewhere in the province.

Early-stage magnetite-apatite hydrothermal mineralisation at Cairn Hill is similar in many respects to the early, deep magnetite-apatite mineralisation in the Olympic Dam district. The mineralisation time of magnetite-apatite-hornblende assemblage is constrained to 1583 ± 30 Ma (Yu et al., 2023), which, despite the large uncertainty, still falls within the conventional IOCG mineralisation window for the Olympic Province (Skirrow et al., 2007; Reid, 2019; Courtney-Davies et al., 2020). Deep magnetite mineralisation at Olympic Dam, Wirrda Well and Acropolis also occurred at roughly the same time (~1590 Ma; Apukhtina et al., 2017; Courtney-Davies et al., 2019). Apatite associated with early magnetite tends to have more chlorapatite component (Krneta et al., 2016, 2017), with that at Cairn Hill having the highest Cl content (Fig. 4.9). In addition, early, deep magnetite-apatite assemblage is generally accompanied by limited Cu mineralisation compared to the hematite-dominant zones (Krneta et al., 2016, 2017; Apukhtina et al., 2017).

Despite these similarities, Cairn Hill presents the following characteristics that distinguish it from the Olympic Dam district. The silicate phase accompanying the magnetite-apatite mineralisation at Cairn Hill is predominantly hornblende (Fig. 4.3), rather than chlorite and sericite which are common in the Olympic Dam district. Unlike Olympic Dam, magnetite at Cairn Hill was not subsequently altered to siderite or hematite (Krneta et al., 2016, 2017; Apukhtina et al., 2017; Courtney-Davies et al., 2019; Verdugo-Ihl et al., 2020). Apatite at Cairn Hill has higher Cl contents (X_{Cl} up to 0.44, Fig. 4.9A) than all apatite reported in the Olympic Dam district, implying a deeper fluid source with less fractionation and devolatilization, while this conclusion is equivocal due to the ca. 1490 Ma reprocessing.

The Gawler Craton and the North Australian Craton have a linked history from the Archean to early Mesoproterozoic (Cawood and Korsch, 2008; Payne et al., 2009), with subsequent rifting between ca. 1.5 – 1.35 Ga (Giles et al., 2004; Betts and Giles, 2006; Morrissey et al., 2019). While the magnetite-apatite-hornblende assemblage at Cairn Hill may represent the deeper crustal expression of the ca. 1590 Ma IOCG system in the Olympic IOCG Province, its Cu mineralisation formed at ca. 1460 Ma, >100 Ma later than the iron mineralisation and separated by a phase of granulite-facies deformation and metamorphism at ca. 1490 Ma (Yu et al., 2023; Chapter 3). It is the first recognition of a copper prospect outside the Olympic IOCG mineralisation window in the northern Gawler Craton, and may be related to the ca. 1590–1490 Ma Cloncurry IOCG deposits in the Mount Isa region (Duncan et al., 2011 and references therein). The carbonic hypersaline fluids in Cloncurry IOCG deposits (Perring et al., 2000; Pollard, 2001; Williams et al., 2001; Baker et al., 2008; Bertelli and Baker, 2010) resemble the fluids responsible for the Cu mineralisation at Cairn Hill. The trace element concentrations in fluid inclusions at Cairn Hill (e.g., K 10^4–10^5 ppm, Ca 10^4–10^5 ppm, Fe 10^4–10^5 ppm, Mn ~10^4 ppm, Ba ~10^3 ppm, Zn 10^3–10^4 ppm, Pb 10^3–10^4 ppm) are also comparable to the PIXE data acquired from the Cloncurry IOCG deposits (e.g., Starra and Lightning Creek; Perring et al., 2000; Williams et al., 2001; Baker et al., 2008). Similarities in mineralisation time and ore-forming fluids between Cairn Hill and Cloncurry IOCG deposits imply that they may share a similar ore genesis in a similar geodynamic context.

The tectonic setting for the ca. 1460 Ma Cu mineralisation and magmatism could be crustal extension related to the breakup of the North Australian Craton (NAC) and South Australian Craton (Morrissey et al., 2019). This regional extension and thinning align with the *PT* evolutionary history of Cairn Hill. Cairn Hill underwent granulite facies metamorphism at ca. 1490 Ma with *PT* conditions of 4.6–5.3 kbar (~15 km) and 740–770°C. Thermochronology data with ages of ca. 1460 Ma (e.g., apatite U-Pb and biotite ^{40}Ar-^{39}Ar) suggest that Cairn Hill had cooled to a temperature of ~300 °C by this time (Jagodzinski and Reid, 2015), and fluid inclusion data from ca. 1460 Ma mineral assemblages in this study indicate a depth of 5–10 km. These data indicate that Cairn Hill has been uplifted by 5–10 km from 1490 to 1460 Ma. During this process, mantle upwelling may provide heat to melt the dehydrated and refractory crust and metals to form new Cu systems. The ca. 1460 Ma Cu mineralisation at Cairn Hill has opened up possibilities for young Cu mineralisation systems in the northern Gawler Craton, with large-scale shear zones active at ca. 1460 Ma potentially representing valuable conduits for magmatism and fluids and may prove to be valuable targets in future exploration.

7. Conclusion

During the Fe-P mineralisation, magnetite exhibits varying concentrations of Al, Mn, Ti, V, and Mg, without IOA or BIF affinity. Apatite associated with magnetite is Cl-rich, implying a hydrothermal magnetite-apatite mineralisation event at around ca. 1583 Ma, probably related to mafic intrusions. During the hydrothermal Cu mineralisation, early apatite experienced a metasomatic process, with increasing F contents and depletion of Mn, REE, Na and Th by the ore-forming fluids. The different behavior of iron and arsenic in various apatite types indicates an elevating fluid oxygen fugacity, which is supported by the variation in solid phases in fluid inclusions. The fluid inclusions provide evidence for a Cu mineralisation model that involves high-temperature, CO_2-rich, oxidized Cu-bearing magmatic fluids that exsolved from hidden intrusions. As the Cu-bearing fluids ascend, they experience multiple stages of decompression, fluid immiscibility, and concentration. Early magnetite acts as a chemical barrier, ultimately leading to the final Cu mineralisation. Early magnetite-apatite-hornblende assemblage at Cairn Hill may represent a deeper counterpart to the deep, early magnetite-apatite at depth and at the outer margins of the Olympic Dam deposit. The ca. 1460 Ma Cu mineralisation may be related to the Cloncurry IOCG deposits, developing in an extensional setting where mantle contributes the necessary melt and metals for the young Cu systems.

Acknowledgments

This project was supported by ARC Linkage Project LP160100578 (JLP and MH), the Mineral Exploration Cooperative Research Centre (MinEX CRC), and the China Scholarship Council. LJM is supported by an ARC DECRA Fellowship DE210101126. K Faure is thanked for his assistance in the field. S Gilbert and B Wade are thanked for their technical support at Adelaide Microscopy. TG Lan is thanked for his technical support at the State Key Laboratory of Ore Deposit Geochemistry, IGCAS.

Data availability

Appendix Tables A1–A6 that accompany this thesis chapter is available on Open Science Framework: https://osf.io/rcm7g/

References

Allan, M. M., Yardley, B. W., Forbes, L. J., Shmulovich, K. I., Banks, D. A., and Shepherd, T. J., 2005, Validation of LA-ICP-MS fluid inclusion analysis with synthetic fluid inclusions: American Mineralogist, v. 90, p. 1767-1775.

Apukhtina, O. B., Kamenetsky, V. S., Ehrig, K., Kamenetsky, M. B., Maas, R., Thompson, J., McPhie, J., Ciobanu, C. L., and Cook, N. J., 2017, Early, deep magnetite-fluorapatite mineralisation at the Olympic Dam Cu-U-Au-Ag deposit, South Australia*: Economic Geology, v. 112, p. 1531-1542.

Audetat, A., Pettke, T., Heinrich, C. A., and Bodnar, R. J., 2008, The Composition of Magmatic-Hydrothermal Fluids in Barren and Mineralized Intrusions: Economic Geology, v. 103, p. 877-908.

Baker, T., Mustard, R., Fu, B., Williams, P. J., Dong, G., Fisher, L., Mark, G., and Ryan, C. G., 2008, Mixed messages in iron oxide–copper–gold systems of the Cloncurry district, Australia: insights from PIXE analysis of halogens and copper in fluid inclusions: Mineralium Deposita, v. 43, p. 599-608.

Barton, M. D., 2014, Iron Oxide(–Cu–Au–REE–P–Ag–U–Co) Systems, Treatise on Geochemistry, p. 515-541.

Bastrakov, E. N., Skirrow, R. G., and Davidson, G. J., 2007, Fluid Evolution and Origins of Iron Oxide Cu-Au Prospects in the Olympic Dam District, Gawler Craton, South Australia: Economic Geology, p. 1415-1440.

Becker, S. P., and Bodnar, R. J., 2008, Synthetic Fluid Inclusions. XVII.1 PVTX Properties of High Salinity H2O-NaCl Solutions (30 wt % NaCl) Application to Fluid Inclusions that Homogenize by Halite Disappearance from Porphyry Copper and Other Hydrothermal Ore Deposits: Economic Geology, v. 103.

Belperio, A., Flint, R., and Freeman, H., 2007, Prominent Hill: A Hematite-Dominated, Iron Oxide Copper-Gold System: Economic Geology, v. 102, p. 1499-1510.

Bertelli, M., and Baker, T., 2010, A fluid inclusion study of the Suicide Ridge Breccia Pipe, Cloncurry district, Australia: Implication for Breccia Genesis and IOCG mineralisation: Precambrian Research, v. 179, p. 69-87.

Betts, P. G., and Giles, D., 2006, The 1800–1100Ma tectonic evolution of Australia: Precambrian Research, v. 144, p. 92-125.

Betts, P. G., Valenta, R. K., and Finlay, J., 2003, Evolution of the Mount Woods Inlier, northern Gawler Craton, Southern Australia: an integrated structural and aeromagnetic analysis: Tectonophysics, v. 366, p. 83-111.

Bodnar, R., 1993, Revised equation and table for determining the freezing point depression of H2O-NaCl solutions: Geochimica et Cosmochimica acta, v. 57, p. 683-684.

Bonyadi, Z., Davidson, G. J., Mehrabi, B., Meffre, S., and Ghazban, F., 2011, Significance of apatite REE depletion and monazite inclusions in the brecciated Se–Chahun iron oxide–apatite deposit, Bafq district, Iran: insights from paragenesis and geochemistry: Chemical Geology, v. 281, p. 253-269.

Bouzari, F., Hart, C. J. R., Bissig, T., and Barker, S., 2016, Hydrothermal Alteration Revealed by Apatite Luminescence and Chemistry: A Potential Indicator Mineral for Exploring Covered Porphyry Copper Deposits*: Economic Geology, v. 111, p. 1397-1410.

Bowden, B., Fraser, G., Davidson, G. J., Meffre, S., Skirrow, R., Bull, S., and Thompson, J., 2017, Age constraints on the hydrothermal history of the Prominent Hill iron oxide copper-gold deposit, South Australia: Mineralium Deposita, v. 52, p. 863-881.

Brown, P. E., 1989, FLINCOR; a microcomputer program for the reduction and investigation of fluid-inclusion data: American Mineralogist, v. 74, p. 1390-1393.

Brown, P. E., and Hagemann, S. G., 1995, MacFlinCor and its application to fluids in Archean lode-gold deposits: Geochimica et Cosmochimica Acta, v. 59, p. 3943-3952.

Brown, P. E., and Lamb, W. M., 1989, PVT properties of fluids in the system H2O±CO2±NaCl: New graphical presentations and implications for fluid inclusion studies: Geochimica et Cosmochimica Acta, v. 53, p. 1209-1221.

Canil, D., and Lacourse, T., 2020, Geothermometry using minor and trace elements in igneous and hydrothermal magnetite: Chemical Geology, v. 541.

Cawood, P. A., and Korsch, R., 2008, Assembling Australia: Proterozoic building of a continent: Precambrian Research, v. 166, p. 1-35.

Clark, J. M., 2014, Defining the style of mineralisation at the Cairn Hill magnetite-sulphide deposit, Mount Woods Inlier, Gawler Craton, South Australia, The University of Adelaide.

Collins, P. L., 1979, Gas hydrates in CO 2-bearing fluid inclusions and the use of freezing data for estimation of salinity: Economic geology, v. 74, p. 1435-1444.

Courtney-Davies, L., Ciobanu, C. L., Tapster, S. R., Cook, N. J., Ehrig, K., Crowley, J. L., Verdugo-Ihl, M. R., Wade, B. P., and Condon, D. J., 2020, Opening the magmatic-hydrothermal window: high-precision U-Pb Geochronology Of The Mesoproterozoic Olympic Dam Cu-U-Au-Ag deposit, South Australia: Economic Geology, v. 115, p. 1855-1870.

Courtney-Davies, L., Ciobanu, C. L., Verdugo-Ihl, M. R., Dmitrijeva, M., Cook, N. J., Ehrig, K., and Wade, B. P., 2019, Hematite geochemistry and geochronology resolve genetic and temporal links among iron-oxide copper gold systems, Olympic Dam district, South Australia: Precambrian Research, v. 335, p. 105480.

Craveiro, G. S., Villas, R. N. N., and Xavier, R. P., 2020, A fluid inclusion and stable isotope (O, H, S and C) study of the Archean IOCG Cristalino deposit, Carajás mineral Province, Brazil: Implications to ore genesis: Ore Geology Reviews, v. 127, p. 103822.

Davidson, G. J., Paterson, H., Meffre, S., and Berry, R. F., 2007, Characteristics and origin of the Oak Dam East breccia-hosted, iron oxide Cu-U-(Au) deposit: Olympic Dam region, Gawler craton, South Australia: Economic Geology, v. 102, p. 1471-1498.

de Melo, G. H. C., Monteiro, L. V. S., Xavier, R. P., Moreto, C. P. N., and Santiago, E., 2019, Tracing Fluid Sources for the Salobo and Igarapé Bahia Deposits: Implications for the Genesis of the Iron Oxide Copper-Gold Deposits in the Carajás Province, Brazil: Economic Geology, v. 114, p. 697-718.

Donovan, J. J., Singer, J. W., and Armstrong, J. T., 2016, A new EPMA method for fast trace element analysis in simple matrices: American Mineralogist, v. 101, p. 1839-1853.

Duncan, R. J., Stein, H. J., Evans, K. A., Hitzman, M. W., Nelson, E. P., and Kirwin, D. J., 2011, A new geochronological framework for mineralisation and alteration in the Selwyn-Mount Dore corridor, Eastern fold belt, Mount Isa inlier, Australia: Genetic implications for iron oxide copper-gold deposits: Economic Geology, v. 106, p. 169-192.

Ehrig, K., McPhie, J., and Kamenetsky, V., 2012, Geology and mineralogical zonation of the Olympic Dam iron oxide Cu-U-Au-Ag deposit, South Australia, *in* Hedenquist, J., Harris, M., and Camus, F., eds., Geology and genesis of major copper deposits and districts of the world: a tribute to Richard H. Sillitoe., Soc of Econ Geol Spec Pub, p. 16: 237–267.

Ferris, G., and Schwarz, M., 2004, Definition of the Tunkillia Suite, western Gawler craton: Minerals and Energy South Australia Journal, v. 34, p. 32-41.

Forbes, C. J., Giles, D., Jourdan, F., Sato, K., Omori, S., and Bunch, M., 2012, Cooling and exhumation history of the northeastern Gawler Craton, South Australia: Precambrian Research, v. 200-203, p. 209-238.

Fraser, G., McAvaney, S., Neumann, N., Szpunar, M., and Reid, A., 2010, Discovery of early Mesoarchean crust in the eastern Gawler Craton, South Australia: Precambrian Research, v. 179, p. 1-21.

Fraser, G., Reid, A., and Stern, R., 2012, Timing of deformation and exhumation across the Karari Shear Zone, north-western Gawler Craton, South Australia: Australian Journal of Earth Sciences, v. 59, p. 547-570.

Fraser, G. L., Skirrow, R. G., Schmidt-Mumm, A., and Holm, O., 2007, Mesoproterozoic gold in the central Gawler craton, South Australia: Geology, alteration, fluids, and timing: Economic Geology, v. 102, p. 1511-1539.

Freeman, H., and Tomkinson, M., 2010, Geological setting of iron oxide related mineralisation in the southern Mount Woods Domain, South Australia, Hydrothermal iron oxide copper-gold & related deposits: A global perspective, 3, p. 171-190.

Giles, D., Betts, P. G., and Lister, G. S., 2004, 1.8–1.5-Ga links between the North and South Australian Cratons and the Early–Middle Proterozoic configuration of Australia: Tectonophysics, v. 380, p. 27-41.

Guillong, M., Meier, D. L., Allan, M. M., Heinrich, C. A., and Yardley, B. W., 2008, Appendix A6: SILLS: A MATLAB-based program for the reduction of laser ablation ICP-MS data of homogeneous materials and inclusions: Mineralogical Association of Canada Short Course, v. 40, p. 328-333.

Gunnars, A., Blomqvist, S., and Martinsson, C., 2004, Inorganic formation of apatite in brackish seawater from the Baltic Sea: an experimental approach: Marine Chemistry, v. 91, p. 15-26.

Hall, J. W., Glorie, S., Reid, A. J., Boone, S. C., Collins, A. S., and Gleadow, A., 2018, An apatite U–Pb thermal history map for the northern Gawler Craton, South Australia: Geoscience Frontiers, v. 9, p. 1293-1308.

Hand, M., Reid, A., and Jagodzinski, L., 2007, Tectonic framework and evolution of the Gawler craton, southern Australia: Economic Geology, v. 102, p. 1377-1395.

Harlov, D. E., 2015, Apatite: A Fingerprint for Metasomatic Processes: Elements, v. 11, p. 171-176.

Harlov, D. E., Förster, H.-J. r., and Nijland, T. G., 2002, Fluid-induced nucleation of (Y+ REE)-phosphate minerals within apatite: Nature and experiment. Part I. Chlorapatite: American Mineralogist, v. 87, p. 245-261.

Hayward, N., and Skirrow, R., 2010, Geodynamic setting and controls on iron oxide Cu-Au (±U) ore in the Gawler Craton, South Australia: Hydrothermal iron oxide copper-gold and related deposits: A global perspective, v. 3, p. 105-131.

Heinrich, C. A., Pettke, T., Halter, W. E., Aigner-Torres, M., Audétat, A., Günther, D., Hattendorf, B., Bleiner, D., Guillong, M., and Horn, I., 2003, Quantitative multi-element analysis of minerals, fluid and melt inclusions by laser-ablation inductively-coupled-plasma mass-spectrometry: Geochimica et Cosmochimica Acta, v. 67, p. 3473-3497.

Hitzman, M. W., Oreskes, N., and Einaudi, M. T., 1992, Geological characteristics and tectonic setting of Proterozoic iron oxide (Cu-U-Au-REE) deposits: Precambrian Research, v. 58, p. 241-287.

Howard, K., Hand, M., Barovich, K., and Belousova, E., 2011a, Provenance of late Paleoproterozoic cover sequences in the central Gawler Craton: exploring stratigraphic correlations in eastern Proterozoic Australia using detrital zircon ages, Hf and Nd isotopic data: Australian Journal of Earth Sciences, v. 58, p. 475-500.

Howard, K. E., Hand, M., Barovich, K. M., Payne, J. L., Cutts, K. A., and Belousova, E. A., 2011b, U–Pb zircon, zircon Hf and whole-rock Sm–Nd isotopic constraints on the evolution of Paleoproterozoic rocks in the northern Gawler Craton: Australian Journal of Earth Sciences, v. 58, p. 615-638.

Hughes, J. M., and Rakovan, J. F., 2015, Structurally robust, chemically diverse: apatite and apatite supergroup minerals: Elements, v. 11, p. 165-170.

Jagodzinski, E., 2005, Compilation of SHRIMP U-Pb geochronological data, Olympic Domain, Gawler Craton, South Australia, 2001-2003, Geoscience Australia, p. 197.

Jagodzinski, E., and Reid, A., 2015, PACE Geochronology: Results of collaborative geochronology projects 2013-2015, Government of South Australia. Department of the Premier and Cabinet. , p. Report Book, 2015/00003.

Jagodzinski, E., Reid, A., Chalmers, N., Swain, G., Frew, R., and Foudoulis, C., 2007, Compilation of SHRIMP U-Pb geochronological data for the Gawler Craton, South Australia, 2007, Report Book 2007/21, South Australian Department of Primary Industries and Resources.

Jagodzinski, E. A., Reid, A. J., Crowley, J. L., Wade, C. E., and Curtis, S., 2023, Precise zircon U-Pb dating of the Mesoproterozoic Gawler large igneous province, South Australia: Results in Geochemistry, v. 10, p. 100020.

James-Smith, J., Cauzid, J., Testemale, D., Liu, W., Hazemann, J.-L., Proux, O., Etschmann, B., Philippot, P., Banks, D., Williams, P., and Brugger, J. l., 2010, Arsenic speciation in fluid inclusions using micro-beam X-ray absorption spectroscopy: American Mineralogist, v. 95, p. 921-932.

Joosu, L., Lepland, A., Kreitsmann, T., Üpraus, K., Roberts, N. M. W., Paiste, P., Martin, A. P., and Kirsimäe, K., 2016, Petrography and the REE-composition of apatite in the Paleoproterozoic Pilgujärvi Sedimentary Formation, Pechenga Greenstone Belt, Russia: Geochimica et Cosmochimica Acta, v. 186, p. 135-153.

Klemm, L. M., Pettke, T., Heinrich, C. A., and Campos, E., 2007, Hydrothermal evolution of the El Teniente deposit, Chile: Porphyry Cu-Mo ore deposition from low-salinity magmatic fluids: Economic Geology, v. 102, p. 1021-1045.

Knipping, J. L., Bilenker, L. D., Simon, A. C., Reich, M., Barra, F., Deditius, A. P., Wälle, M., Heinrich, C. A., Holtz, F., and Munizaga, R., 2015, Trace elements in magnetite from massive iron oxide-apatite deposits indicate a combined formation by igneous and magmatic-hydrothermal processes: Geochimica et Cosmochimica Acta, v. 171, p. 15-38.

Krneta, S., Ciobanu, C. L., Cook, N. J., Ehrig, K., and Kontonikas-Charos, A., 2016, Apatite at Olympic Dam, South Australia: A petrogenetic tool: Lithos, v. 262, p. 470-485.

Krneta, S., Cook, N. J., Ciobanu, C. L., Ehrig, K., and Kontonikas-Charos, A., 2017, The Wirrda Well and Acropolis prospects, Gawler Craton, South Australia: Insights into evolving fluid conditions through apatite chemistry: Journal of Geochemical Exploration, v. 181, p. 276-291.

Kusebauch, C., John, T., Whitehouse, M. J., Klemme, S., and Putnis, A., 2015, Distribution of halogens between fluid and apatite during fluid-mediated replacement processes: Geochimica et Cosmochimica Acta, v. 170, p. 225-246.

La Cruz, N. L., Ovalle, J. T., Simon, A. C., Konecke, B. A., Barra, F., Reich, M., Leisen, M., and Childress, T. M., 2020, The Geochemistry of Magnetite and Apatite from the El Laco Iron Oxide-Apatite Deposit, Chile: Implications for Ore Genesis: Economic Geology, v. 115, p. 1461-1491.

Lan, T.-G., Hu, R.-Z., Bi, X.-W., Mao, G.-J., Wen, B.-J., Liu, L., and Chen, Y.-H., 2018, Metasomatized asthenospheric mantle contributing to the generation of Cu-Mo deposits within an intracontinental setting: a case study of the~ 128 Ma Wangjiazhuang Cu-Mo deposit, eastern North China Craton: Journal of Asian Earth Sciences, v. 160, p. 460-489.

Lan, T., Hu, R., Fan, H., Bi, X., Tang, Y., Zhou, L., Mao, W., and Chen, Y., 2017, In-situ analysis of major and trace elements in fluid inclusion and quartz: LA-ICP-MS method and applications to ore deposits: Acta Petrologica Sinica, v. 33, p. 3239-3262.

Lee, Y. J., Stephens, P. W., Tang, Y., Li, W., Phillips, B. L., Parise, J. B., and Reeder, R. J., 2009, Arsenate substitution in hydroxylapatite: Structural characterization of the Ca5(PxAs1–xO4)3OH solid solution: American Mineralogist, v. 94, p. 666-675.

Liu, W., Mei, Y., Etschmann, B., Brugger, J., Pearce, M., Ryan, C. G., Borg, S., Wykes, J., Kappen, P., Paterson, D., Boesenberg, U., Garrevoet, J., Moorhead, G., and Falkenberg, G., 2017, Arsenic in hydrothermal apatite: Oxidation state, mechanism of uptake, and comparison between experiments and nature: Geochimica et Cosmochimica Acta, v. 196, p. 144-159.

Lowenstern, J. B., 2001, Carbon dioxide in magmas and implications for hydrothermal systems: Mineralium Deposita, v. 36, p. 490-502.

Mao, M., 2016, Apatite Trace Element Compositions A Robust New Tool for Mineral Exploration: Economic Geology, v. 111.

McPhie, J., Ehrig, K. J., Kamenetsky, M. B., Crowley, J. L., and Kamenetsky, V. S., 2020, Geology of the Acropolis prospect, South Australia, constrained by high-precision CA-TIMS ages: Australian Journal of Earth Sciences, v. 67, p. 699-716.

Miles, A. J., Graham, C. M., Hawkesworth, C. J., Gillespie, M. R., Hinton, R. W., and Bromiley, G. D., 2014, Apatite: A new redox proxy for silicic magmas?: Geochimica et Cosmochimica Acta, v. 132, p. 101-119.

Morrissey, L. J., Barovich, K. M., Hand, M., Howard, K. E., and Payne, J. L., 2019, Magmatism and metamorphism at ca. 1.45 Ga in the northern Gawler Craton: The Australian record of rifting within Nuna (Columbia): Geoscience Frontiers, p. 175-194.

Morrissey, L. J., Payne, J. L., Hand, M., Clark, C., and Janicki, M., 2023, One billion years of tectonism at the Paleoproterozoic interface of North and South Australia: Precambrian Research, v. 393, p. 107077.

Nadoll, P., Angerer, T., Mauk, J. L., French, D., and Walshe, J., 2014, The chemistry of hydrothermal magnetite: A review: Ore Geology Reviews, v. 61, p. 1-32.

Nisbet, H., Migdisov, A. A., Williams-Jones, A. E., Xu, H., van Hinsberg, V. J., and Roback, R., 2019, Challenging the thorium-immobility paradigm: Scientific Reports, v. 9, p. 17035.

Norris, A., and Danyushevsky, L., 2018, Towards estimating the complete uncertainty budget of quantified results measured by LA-ICP-MS: Goldschmidt: Boston, MA, USA.

O'Sullivan, G., Chew, D., Kenny, G., Henrichs, I., and Mulligan, D., 2020, The trace element composition of apatite and its application to detrital provenance studies: Earth-Science Reviews, v. 201.

Oreskes, N., and Einaudi, M. T., 1992, Origin of hydrothermal fluids at Olympic Dam Preliminary results from fluid inclusions and stable isotopes: Economic Geology, v. 87, p. 64-90.

Page, R., and Sun, S., 1998, Aspects of geochronology and crustal evolution in the Eastern Fold Belt, Mt Isa Inlier: Australian Journal of Earth Sciences, v. 45, p. 343-361.

Palma, G., Barra, F., Reich, M., Simon, A. C., and Romero, R., 2020, A review of magnetite geochemistry of Chilean Iron Oxide-Apatite (IOA) deposits and its implications for ore-forming processes: Ore Geology Reviews.

Palma, G., Barra, F., Reich, M., Valencia, V., Simon, A. C., Vervoort, J., Leisen, M., and Romero, R., 2019, Halogens, trace element concentrations, and Sr-Nd isotopes in apatite from iron oxide-apatite (IOA) deposits in the Chilean iron belt: Evidence for magmatic and hydrothermal stages of mineralisation: Geochimica et Cosmochimica Acta, v. 246, p. 515-540.

Pan, Y., and Fleet, M. E., 2002, Compositions of the Apatite-Group Minerals: Substitution Mechanisms and Controlling Factors: Reviews in Mineralogy and Geochemistry, v. 48, p. 13-49.

Payne, J. L., Hand, M., Barovich, K. M., Reid, A., and Evans, D. A. D., 2009, Correlations and reconstruction models for the 2500-1500 Ma evolution of the Mawson Continent: Geological Society, London, Special Publications, v. 323, p. 319-355.

Perring, C., Pollard, P., Dong, G., Nunn, A., and Blake, K., 2000, The Lightning Creek sill complex, Cloncurry district, northwest Queensland: A source of fluids for Fe oxide Cu-Au mineralisation and sodic-calcic alteration: Economic Geology, v. 95, p. 1067-1089.

Piccoli, P. M., and Candela, P. A., 2002, Apatite in Igneous Systems: Reviews in Mineralogy and Geochemistry, v. 48, p. 255-292.

Pollard, P. J., 2001, Sodic(–calcic) alteration in Fe-oxide–Cu–Au districts: an origin via unmixing of magmatic H2O-CO2-NaCl: Mineralium Deposita, v. 36, p. 93-100.

Previato, M., Monteiro, L. V. S., Bello, R. M. d. S., and Gonçales, L. C. G., 2020, Evolution of brines and CO2-rich fluids and hydrothermal overprinting in the genesis of the Borrachudo copper deposit, Carajás Province: Ore Geology Reviews, v. 121, p. 103561.

Putnis, A., 2009, Mineral replacement reactions: Reviews of Mineralogy and Geochemistry, v. 70.

Rasmussen, K. L., and Mortensen, J. K., 2013, Magmatic petrogenesis and the evolution of (F:Cl:OH) fluid composition in barren and tungsten skarn-associated plutons using apatite and biotite compositions: Case studies from the northern Canadian Cordillera: Ore Geology Reviews, v. 50, p. 118-142.

Reid, A., 2019, The Olympic Cu-Au Province, Gawler Craton: A Review of the Lithospheric Architecture, Geodynamic Setting, Alteration Systems, Cover Successions and Prospectivity: Minerals, v. 9, p. 371.

Reid, A., and Fabris, A., 2015, Influence of Preexisting Low Metamorphic Grade Sedimentary successions on the distribution of iron oxide copper-gold mineralisation in the olympic Cu-Au province, Gawler Craton: Economic Geology, v. 110, p. 2147-2157.

Reid, A. J., Jagodzinski, E. A., Armit, R. J., Dutch, R. A., Kirkland, C. L., Betts, P. G., and Schaefer, B. F., 2014a, U-Pb and Hf isotopic evidence for Neoarchean and Paleoproterozoic basement in the buried northern Gawler Craton, South Australia: Precambrian Research, v. 250, p. 127-142.

Reid, A. J., Jagodzinski, E. A., Fraser, G. L., and Pawley, M. J., 2014b, SHRIMP U–Pb zircon age constraints on the tectonics of the Neoarchean to early Paleoproterozoic transition within the Mulgathing Complex, Gawler Craton, South Australia: Precambrian Research, v. 250, p. 27-49.

Roedder, E., 1984, Fluid inclusion. Rev. Mineralogy.

Roedder, E., and Bodnar, R., 1980, Geologic pressure determinations from fluid inclusion studies: Annual review of earth and planetary sciences, v. 8, p. 263-301.

Roy-Garand, A., Adlakha, E., Hanley, J., Elongo, V., Lecumberri-Sanchez, P., Falck, H., and Boucher, B., 2022, Timing and sources of skarn mineralisation in the Canadian Tungsten Belt: revisiting the paragenesis, crystal chemistry and geochronology of apatite: Mineralium Deposita, v. 57, p. 1391-1413.

Rusk, B. G., Reed, M. H., Dilles, J. H., Klemm, L. M., and Heinrich, C. A., 2004, Compositions of magmatic hydrothermal fluids determined by LA-ICP-MS of fluid inclusions from the porphyry copper–molybdenum deposit at Butte, MT: Chemical Geology, v. 210, p. 173-199.

Salazar, E., Barra, F., Reich, M., Simon, A., Leisen, M., Palma, G., Romero, R., and Rojo, M., 2020, Trace element geochemistry of magnetite from the Cerro Negro Norte iron oxide−apatite deposit, northern Chile: Mineralium Deposita, v. 55, p. 409-428.

Schlegel, T. U., Wagner, T., Wälle, M., and Heinrich, C. A., 2018, Hematite Breccia-Hosted Iron Oxide Copper-Gold Deposits Require Magmatic Fluid Components Exposed to Atmospheric Oxidation: Evidence from Prominent Hill, Gawler Craton, South Australia: Economic Geology, v. 113, p. 597-644.

Skirrow, R. G., Bastrakov, E. N., Baroncii, K., Fraser, G. L., Creaser, R. A., Fanning, C. M., Raymond, O. L., and Davidson, G. J., 2007, Timing of iron oxide Cu-Au-(U) hydrothermal activity and Nd isotope constraints on metal sources in the Gawler craton, south Australia: Economic Geology, v. 102, p. 1441-1470.

Steele-MacInnis, M., Lecumberri-Sanchez, P., and Bodnar, R. J., 2012, Short note: HokieFlincs_H2O-NaCl: A Microsoft Excel spreadsheet for interpreting microthermometric data from fluid inclusions based on the PVTX properties of H2O-NaCl: Computers & Geosciences, v. 49, p. 334-337.

Sterner, S. M., Hall, D. L., and Bodnar, R. J., 1988, Synthetic fluid inclusions. V. Solubility relations in the system NaCl-KCl-H2O under vapor-saturated conditions: Geochimica et Cosmochimica Acta, v. 52, p. 989-1005.

Stokes, T. N., Bromiley, G. D., Potts, N. J., Saunders, K. E., and Miles, A. J., 2019, The effect of melt composition and oxygen fugacity on manganese partitioning between apatite and silicate melt: Chemical Geology, v. 506, p. 162-174.

Tiddy, C. J., Betts, P. G., Neumann, M. R., Murphy, F. C., Stewart, J., Giles, D., Sawyer, M., Freeman, H., and Jourdan, F., 2020, Interpretation of a ca. 1600–1580 Ma metamorphic core complex in the northern Gawler Craton, Australia: Gondwana Research, v. 85, p. 263-290.

Torab, F. M., and Lehmann, B., 2007, Magnetite-apatite deposits of the Bafq district, Central Iran: apatite geochemistry and monazite geochronology: Mineralogical Magazine, v. 71, p. 347-363.

Ulrich, T., Gunther, D., and Heinrich, C. A., 2001, The evolution of a porphyry Cu-Au deposit, based on LA-ICP-MS analysis of fluid inclusions: Bajo de la Alumbrera, Argentina: Economic Geology and the Bulletin of the Society of Economic Geologists, v. 96, p. 1743-1774.

Verdugo-Ihl, M. R., Ciobanu, C. L., Cook, N. J., Ehrig, K. J., and Courtney-Davies, L., 2020, Defining early stages of IOCG systems: evidence from iron oxides in the outer shell of the Olympic Dam deposit, South Australia: Mineralium Deposita, v. 55, p. 429-452.

Webster, J. D., and Piccoli, P. M., 2015, Magmatic Apatite: A Powerful, Yet Deceptive, Mineral: Elements, v. 11, p. 177-182.

Whitney, D. L., and Evans, B. W., 2010, Abbreviations for names of rock-forming minerals: American Mineralogist, v. 95, p. 185-187.

Williams-Jones, A., Samson, I., Ault, K., Gagnon, J., and Fryer, B., 2010, The genesis of distal zinc skarns: Evidence from the Mochito deposit, Honduras: Economic Geology, v. 105, p. 1411-1440.

Williams, P. J., Barton, M. D., Johnson, D. A., Fontboté, L., De Haller, A., Mark, G., Oliver, N. H., and Marschik, R., 2005, Iron oxide copper-gold deposits: Geology, space-time distribution, and possible modes of origin: Economic Geology, p. 371-405.

Williams, P. J., Dong, G., Ryan, C. G., Pollard, P. J., Rotherham, J. F., Mernagh, T. P., and Chapman, L. H., 2001, Geochemistry of hypersaline fluid inclusions from the Starra (Fe oxide)-Au-Cu deposit, Cloncurry District, Queensland: Economic Geology, v. 96, p. 875-883.

Yu, J., Morrissey, L., Hand, M., Payne, J. L., and YanJing, C., 2023a, The Fe-Cu disconnect: unravelling a composite IOCG deposit in the Olympic Fe-Cu-Au Province, Gawler Craton: Economic Geology, p. in press.

Yu, J., Hand, M., Payne, J. L., Morrissey, L., Simpson, A., Glorie, S. and Chen, Y.J., 2023b, Innovation in apatite geochronology opens new opportunity for copper systems in southern Australia, in preparation.

Zhang, X.-N., Pan, J.-Y., Lehmann, B., Li, J.-X., Yin, S., Ouyang, Y.-P., Wu, B., Fu, J.-L., Zhang, Y., Sun, Y., Wan, J.-J., and Liu, T., 2023, Diagnostic REE patterns of magmatic and hydrothermal apatite in the Zhuxi tungsten skarn deposit, China: Journal of Geochemical Exploration, v. 252, p. 107271.

Chapter 5

A buried gneiss dome in the northern Gawler Craton: The record of early Mesoproterozoic (ca. 1600–1560 Ma) extension in southern Proterozoic Australia

In revision by Journal of Metamorphic Geology

Statement of Authorship

Title of Paper	A buried gneiss dome in the northern Gawler Craton: The record of early Mesoproterozoic extension in southern Proterozoic Australia
Publication Status	☐ Published ☐ Accepted for Publication ☑ Submitted for Publication ☐ Unpublished and Unsubmitted work written in manuscript style
Publication Details	Yu, J., Hand, M., Morrissey, L., Payne, J. 2023. A buried gneiss dome in the northern Gawler Craton: The record of early Mesoproterozoic extension in southern Proterozoic Australia. Journal of Metamorphic Gelogy, in revision

Principal Author

Name of Principal Author (Candidate)	Jie Yu		
Contribution to the Paper	Data collection and modelling Ideas for manuscript Manuscript writing		
Overall percentage (%)	70		
Certification:	This paper reports on original research I conducted during the period of my Higher Degree by Research candidature and is not subject to any obligations or contractual agreements with a third party that would constrain its inclusion in this thesis. I am the primary author of this paper.		
Signature		Date	24 July 2023

Co-Author Contributions

By signing the Statement of Authorship, each author certifies that:

i. the candidate's stated contribution to the publication is accurate (as detailed above);
ii. permission is granted for the candidate in include the publication in the thesis; and
iii. the sum of all co-author contributions is equal to 100% less the candidate's stated contribution.

Name of Co-Author	Martin Hand		
Contribution to the Paper	Manuscript editing Ideas for manuscript		
Signature		Date	24 July 2023

Name of Co-Author	Laura Morrissey		
Contribution to the Paper	Manuscript editing Ideas for manuscript		
Signature		Date	24 July 2023

Name of Co-Author	Justin Payne		
Contribution to the Paper	Manuscript editing Ideas for manuscript		
Signature		Date	24 July 2023

Please cut and paste additional co-author panels here as required.

Abstract

Mabel Creek Ridge, in the northern Gawler Craton, is a granulite-facies domain recording early Mesoproterozoic metamorphism, flanked by less metamorphosed rocks and dissected by crustal-scale divergent structures. The nature of early Mesoproterozoic events is poorly understood due to the lack of basement outcrop. Calculated metamorphic phase diagrams and geochronology are used to decipher the tectonic regime of a potential gneiss dome. Pressure–temperature (*P*–*T*) modelling of metapelites from five drill holes across Mabel Creek Ridge suggests it has experienced conditions of ~6.4–7.4 kbar and 800–850 °C, and the growth of suprasolidus cordierite after garnet indicates subsequent decompression. In situ U–Pb monazite and Lu–Hf garnet geochronology constrain the granulite-facies metamorphism of Mabel Creek Ridge to ca. 1600–1560 Ma. In contrast, drill hole GOMA DH4 located to the north of Mabel Creek Ridge records conditions of 2.2–5.4 kbar and 710–740 °C at ca. 1520Ma, with no evidence for 1600–1560 Ma metamorphism. Our new *P*–*T* pseudosection results and geochronology data from Mabel Creek Ridge and adjacent crust, coupled with the regional seismic and airborne magnetic data, reveal that Mabel Creek Ridge represents a record of early Mesoproterozoic extension in the Gawler Craton, during which thermally perturbed lower crustal rocks were exhumed within a gneiss dome. Early Mesoproterozoic extension took place within a complex geodynamic regime resulting from the interplay between final Nuna convergence along the margin of northeast Australia at ca. 1600 Ma and subduction to the southwest at ca. 1630–1610 Ma.

Keywords: gneiss dome, Gawler Craton, monazite U–Pb, garnet Lu–Hf, extension

1. Introduction

The Gawler Craton in southern Australia is one of the major components of Proterozoic Australia (Fig. 5.1; Daly, 1998; Hand et al., 2007). It has a long-linked history with the North Australian Craton (NAC) from the Archean to early Mesoproterozoic (Cawood and Korsh, 2008; Payne et al., 2009; Howard et al., 2011a) and is critical in deciphering the evolution of Proterozoic Australia within the Nuna supercontinent (Payne et al., 2009; Betts et al., 2016; Morrissey et al., 2019). The proposed time interval of final assembly and breakup of the Nuna supercontinent in the late Paleoproterozoic to early Mesoproterozoic (Giles et al., 2004; Betts and Giles, 2006; Pisarevsky et al., 2014; Aitken et al., 2016; Betts et al., 2016; Pourteau et al., 2018; Morrissey et al., 2019; Volante et al., 2020) corresponds to the timing of a major phase of tectonic activity in the Gawler Craton (Hand et al., 2007; Reid and Hand, 2012). During the interval ca. 1630–1450 Ma, the Gawler Craton records a series of magmatic, metamorphic and mineralization events (Skirrow et al., 2007; Cutts et al., 2011; Morrissey et al., 2013, 2019; Wade et al., 2019; Reid et al., 2020; Bockmann et al., 2022). The most prominent of these events involves voluminous high-temperature felsic magmatism between 1595–1575 Ma (Jagozdinski

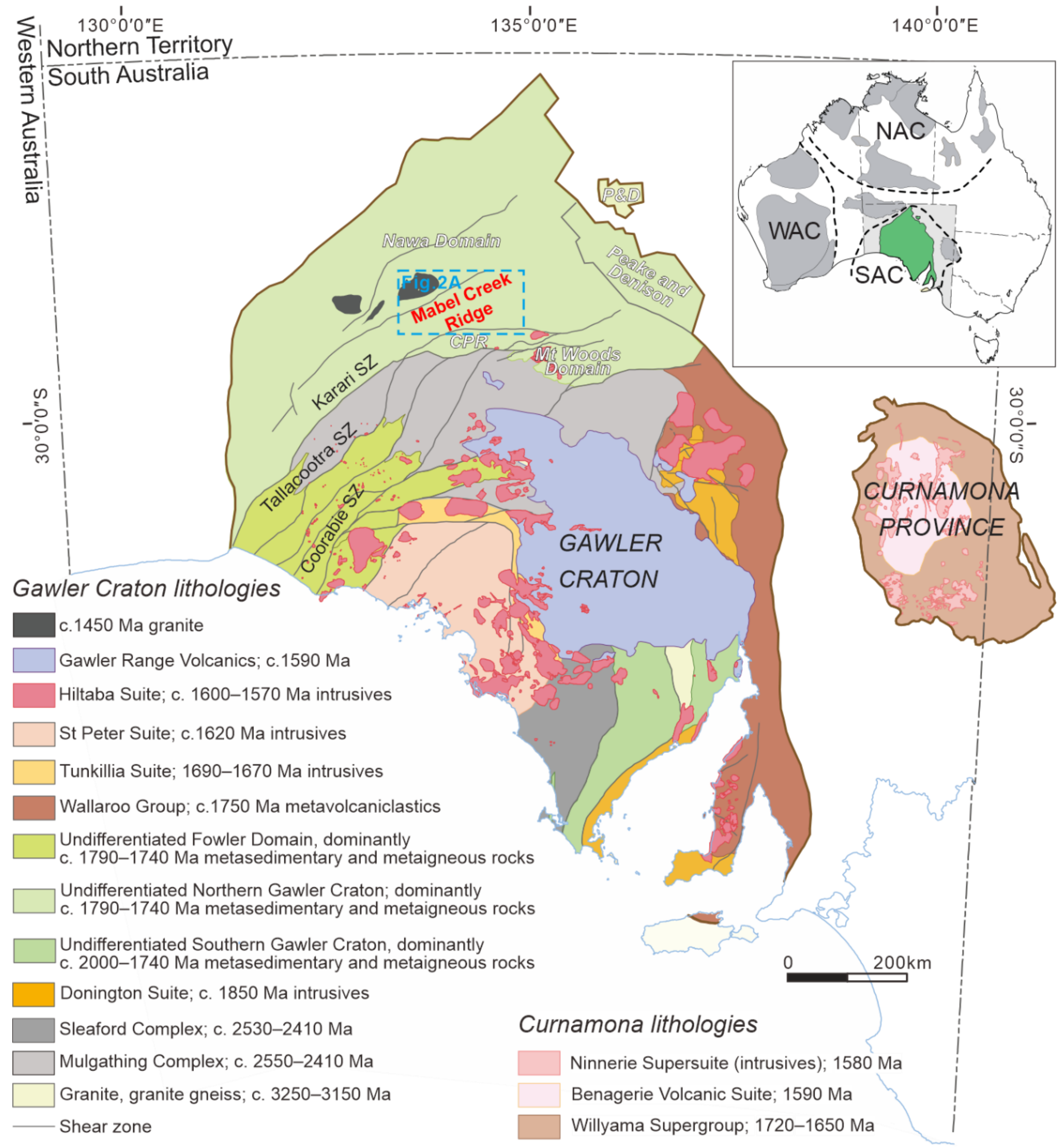

Fig. 5.1. Simplified solid geology map of the Gawler Craton (after Reid et al., 2014b). NAC, North Australian Craton; SAC, South Australian Craton; WAC, West Australian Craton; SZ, shear zone; CPR, Coober Pedy Ridge; P&D, Peake and Denison).

et al., 2023). In part coincident with this magmatism is widespread high-temperature metamorphism in the north, west, and south of the craton (Payne et al., 2008; Cutts et al., 2011; Morrissey et al., 2013; Reid et al., 2019; Tiddy et al., 2020; Bockmann et al., 2022). However, while generalized constraints exist on the age of metamorphism and deformation during the late Paleoproterozoic and early Mesoproterozoic in the Gawler Craton, the nature of these events is poorly understood. This is because extensive regions (> 20,000 km^2) of the southern Australian Proterozoic rock system are unexposed. Consequently, information on the tectonic development of the basement can only be derived from sparse mineral exploration drill holes and

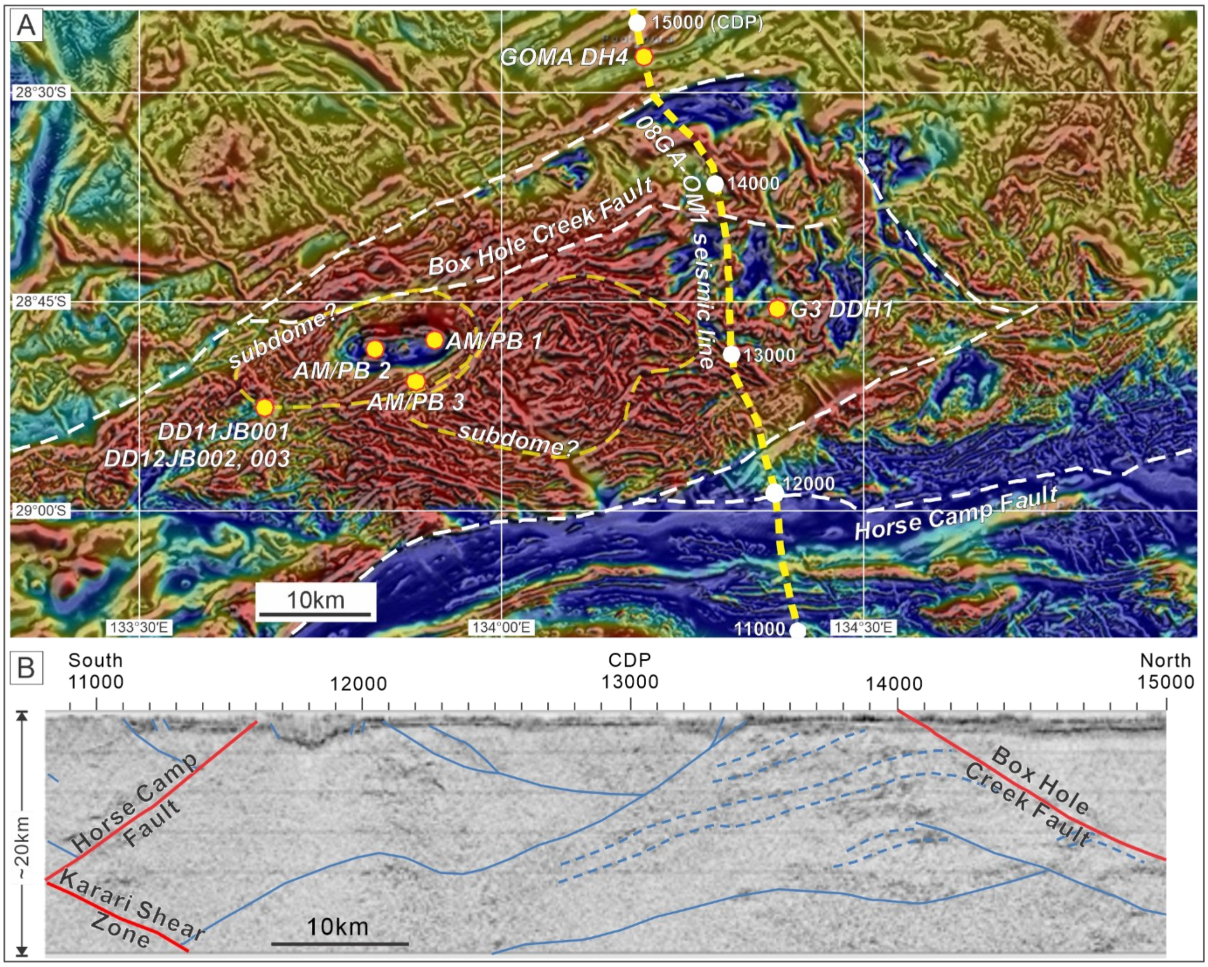

Fig. 5.2. (A) Stacked TMI RTP (Total Magnetic Intensity reduced to pole) and 1VD (first vertical derivative) image of Mabel Creek Ridge, showing major faults and drillhole locations. TMI from South Australian Resources Information Gateway (SARIG; https://map.sarig.sa.gov.au/) (B) 08GA-OM1 deep seismic reflection line from CDP (common depth point) 11000 to CDP 15000, showing the major textures and faults in the Mabel Creek Ridge. Modified from Korsch et al. (2010).

regional geophysical datasets, making it challenging to decipher tectonic regimes associated with metamorphism.

In the central northern Gawler Craton, Mabel Creek Ridge is a buried prominent geophysical domain consisting of granulite-facies rocks (Payne et al., 2008; Cutts et al., 2011; Fig. 5.1 and 5.2A). Seismic reflection data show it is flanked and dissected by crustal-scale divergent structures and contains subhorizontal internal reflectors (Fig. 5.2B; Korsch et al., 2010). Airborne magnetic data shows the internal structure consists of regional-scale circular structural trends, which, combined with the apparent gentle dips of the internal reflectors, suggests that Mabel Creek Ridge has a regional-scale dome-like character. This character, combined with the divergent geometry of the bounding structures, resembles a gneiss dome (Teyssier and Whitney, 2002; Rey et al., 2011). Gneiss domes typically represent the localized rise of lower crustal material into the mid and upper crust during extension (Rey et al., 2009, 2011; Whitney et al., 2015; Korchinski et al., 2018). Similar to metamorphic core complexes, the exhumed material within a gneiss dome is commonly characterized by decompressional thermobarometric evolutions (Teyssier and Whitney, 2002; Whitney et al., 2004; Korchinski et al., 2018; Varga et al., 2022). In contrast, the surrounding crust comprising the upper plate shows lower pressure metamorphism and comparatively modest baric change, or even an absence of metamorphism of the same age as within the gneiss dome (Teyssier and Whitney, 2002; Rey et al., 2011).

In this contribution, we present calculated phase equilibria models and geochronology from six drill holes to constrain the *P–T-time* histories of Mabel Creek Ridge and its immediately adjacent crust. We then suggest the development of a buried gneiss dome in the early Mesoproterozoic. The recognition of a Mesoproterozoic gneiss dome in the northern Gawler Craton provides new insights into the tectonic regime of southern Proterozoic Australia at a time that coincides with the last stages of Nuna amalgamation or the onset of early Nuna fragmentation.

2. Geological setting

2.1 Gawler Craton

The Gawler Craton records a complex geological history from the Archean to the Mesoproterozoic (Fig. 5.1; Hand et al., 2007; Reid and Hand, 2012). The basement of the Gawler Craton comprises Mesoarchean gneisses in the southeastern Gawler Craton (3250–3150 Ma; Fraser et al., 2010) and two belts of 2555–2410 Ma volcanic, sedimentary and magmatic rocks known as the Sleaford Complex in the southern Gawler Craton and the Mulgathing Complex in the central region of the craton (Daly and Fanning, 1993; Reid et al., 2014a). These rock packages were deformed and metamorphosed during the early Paleoproterozoic Sleafordian Orogeny (2470–2410 Ma; Hand et al., 2007; Reid and Hand, 2012; Halpin and Reid, 2016). The ca. 2000 Ma Miltalie Gneiss is interpreted to mark the onset of an extended period of rifting in the Gawler Craton (Payne et al., 2006; Hand et al., 2007). From ca. 2000 to 1730 Ma, a series of volcano-sedimentary and metasedimentary rocks were deposited across the Gawler Craton (Fanning et al., 1988, 2007; Oliver and Fanning, 1997; Payne et al., 2006; Jagodzinski et al., 2007; Howard et al., 2011b; Szpunar et al., 2011).

The craton-wide Kimban Orogeny (ca. 1730–1690 Ma) terminated widespread basin development and sedimentation, with activation of crustal-scale shear zones, granitic magmatism, widespread metamorphism, and localized basin development (Hand et al., 2007; Payne et al., 2008; Dutch et al., 2010; Reid et al., 2019; Morrissey et al., 2023). Following the Kimban Orogeny, the Gawler Craton experienced a series of dominantly magmatic events. The central and western Gawler Craton were intruded by the ca. 1690–1670 Ma Tunkillia Suite (Payne et al., 2010), with localized high- to ultrahigh-temperature metamorphism at ca. 1690–1665 Ma in the western Gawler Craton known as the Ooldean Event (Hand et al., 2007; Cutts et al., 2013). This was followed by the arc-related St Peter Suite in the southern Gawler Craton (ca. 1633–1608 Ma; Swain et al., 2008; Reid et al., 2020) and high-temperature magmas of the Gawler Range Volcanics (1595–1590 Ma) and coeval Hiltaba Suite granites (1595–1570 Ma) (Daly, 1998; Wade et al., 2019; Jagozdinski et al., 2023). The ca. 1633–1608 Ma St Peter Suite experienced east- to northeast-directed shortening during its crystallisation (in current orientation; Stewart and Betts, 2010; Reid et al., 2020). In contrast, the Hiltaba Suite records only a younger phase of extensional deformation, and the bimodal GRV is largely flat-lying and undeformed (Hand et al., 2007). The ca. 1600–1540 Ma Kararan Orogeny was broadly coeval with magmatism and involved deformation and high thermal gradient metamorphism in the northern, western and southeastern Gawler Craton (Daly, 1998; Hand et al., 2007; Payne et al., 2008; Cutts et al., 2011; Forbes et al., 2011; Morrissey et al., 2013; Reid et al., 2019; Tiddy et al., 2020; Bockmann et al., 2022; Morrissey et al., 2023). Ca. 1520 Ma migmatisation is intersected in the northern Gawler Craton (Reid et al., 2014b), and minor magmatism at ca. 1500 Ma has been identified in the southern Gawler Craton (Fanning et al., 2007; Jagodzinski et al., 2007). Localized ca. 1450 Ma A-type magmatism, metamorphism, and shear zone reactivation occur in the northern Gawler Craton (Fraser and Lyons, 2006; Fraser et al., 2012; Morrissey et al., 2019). Neoproterozoic and Phanerozoic sediments overlie much of the stable craton (Preiss, 2000).

2.2 Nawa Domain

The extensively buried northern Gawler Craton is composed of four geophysically defined units located to the north of the Karari Shear Zone: the Nawa Domain, Coober Pedy Ridge, Mount Woods Domain, and the Peake and Denison Domain (Fig. 5.1). Mabel Creek Ridge is located in the southernmost part of the Nawa Domain and is bounded by Box Hole Creek Fault and Horse Camp Fault (Fig. 5.2).

The existing geological constraints in the Mabel Creek region come from a small number of drill holes. The oldest known rock in the region is Neoarchean felsic gneiss (ca. 2520 Ma) intersected in drill hole GOMA DH4 to the north of Mabel Creek Ridge (Fig. 5.2A; Reid et al., 2014b); however, most of the Nawa Domain comprises orthogneiss with crystallisation ages of 1775–1750 Ma and iron-rich metasedimentary rocks with maximum depositional ages of ca. 1740 Ma (Payne et al., 2006; Howard et al., 2011b; Armit et al., 2017). Metamorphic zircon and monazite ages from granulite-facies gneisses suggest the Nawa Domain was widely affected by the ca. 1730–1690 Ma Kimban Orogeny (Payne et al., 2008; Armit et al., 2017). High-temperature reworking during the ca. 1590–1550 Ma Kararan Orogeny affected Mabel Creek Ridge and Cooper Pedy Ridge but is not known from elsewhere in the Nawa Domain (Payne et al., 2008; Cutts et al., 2011). Estimated peak P–T conditions in Mabel Creek Ridge come from a single sample from drill hole AM/PB 1 (Fig. 5.2A) and are interpreted to be 9 kbar and 850 °C at ca. 1600 Ma, followed by near isothermal decompression to ~ 6 kbar by 1580 Ma (Cutts et al., 2011).

Following the Kararan Orogeny, the northern Gawler Craton records a series of apparently localized metamorphic events. Metamorphic zircon in the ca. 2520 Ma Neoarchean felsic gneiss from GOMA DH4 provides evidence for an enigmatic ca. 1520 Ma high-temperature event (Reid et al., 2014b). A-

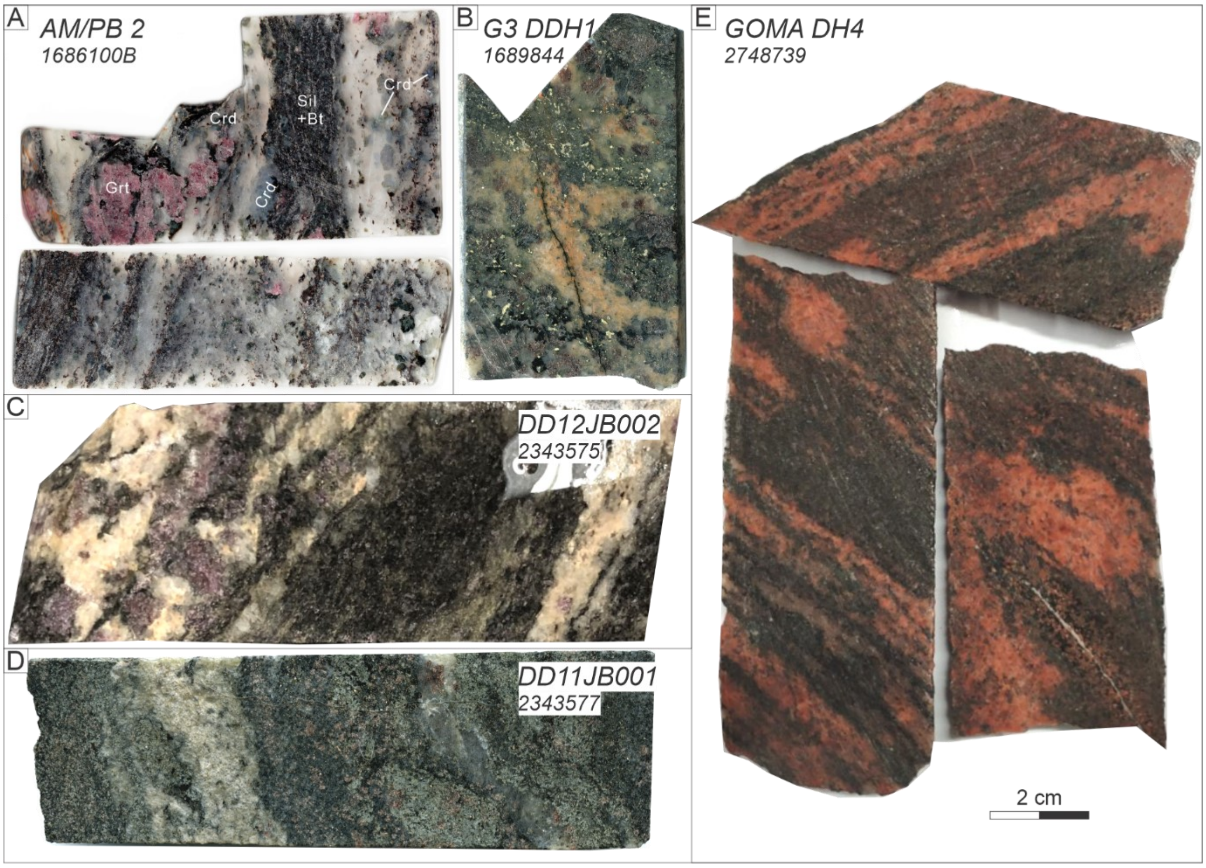

Fig. 5.3. Photographs of representative drill hole lithologies. (A) Drill hole AM/PB 2 (sample 1686100B), biotite–sillimanite-bearing layers interlayered with garnet–cordierite-bearing leucosomes. Cordierite occurs as pale blue grains in leucosomes. (B) Drill hole G3 DDH1 (sample 1689844), cross-cutting leucosomes bounded by garnet–biotite melanosomes. This sample is overprinted by later sulfides. (C) Drill hole DD12JB002 (sample 2343575), garnet-bearing leucosomes interlayered with biotite–sillimanite-bearing layers. (D) Drill hole DD11JB001 (sample 2343577), plagioclase–quartz leucosomes hosted in biotite–cordierite–garnet gneiss. (E) Drill hole GOMA DH4 (sample 2748739), plagioclase–quartz leucosomes surrounded by biotite–orthoamphibole-bearing layers.

type magmatism and coeval granulite-facies metamorphism at ca. 1450 Ma are identified in drill holes in the western Nawa Domain (Morrissey et al., 2019). Biotite $^{40}Ar/^{39}Ar$ thermochronology suggests the northern Gawler Craton cooled through mid-crustal temperatures between 1460–1415 Ma (Reid and Forster, 2021).

3. Sample selection and petrography

There is no outcrop across Mabel Creek Ridge, with the basement covered by 120–210 m of younger sedimentary successions (https://map.sarig.sa.gov.au). The samples chosen for petrographic analysis, phase equilibria modelling, and geochronology cover a large area of Mabel Creek Ridge (Fig. 5.2A and Table 1). Drill holes piercing the basement of Mabel Creek Ridge intersect iron-rich metasedimentary rocks with maximum depositional ages of ca. 1740 Ma (Payne et al., 2006; Armit et al., 2017). Additional samples were selected from drill hole GOMA DH4 which intersects the crust immediately north of Mabel Creek Ridge and is separated from it by the Box Hole Creek Fault. Unfortunately, no drill holes penetrate the basement immediately south of Mabel Creek Ridge, meaning GOMA DH4 is

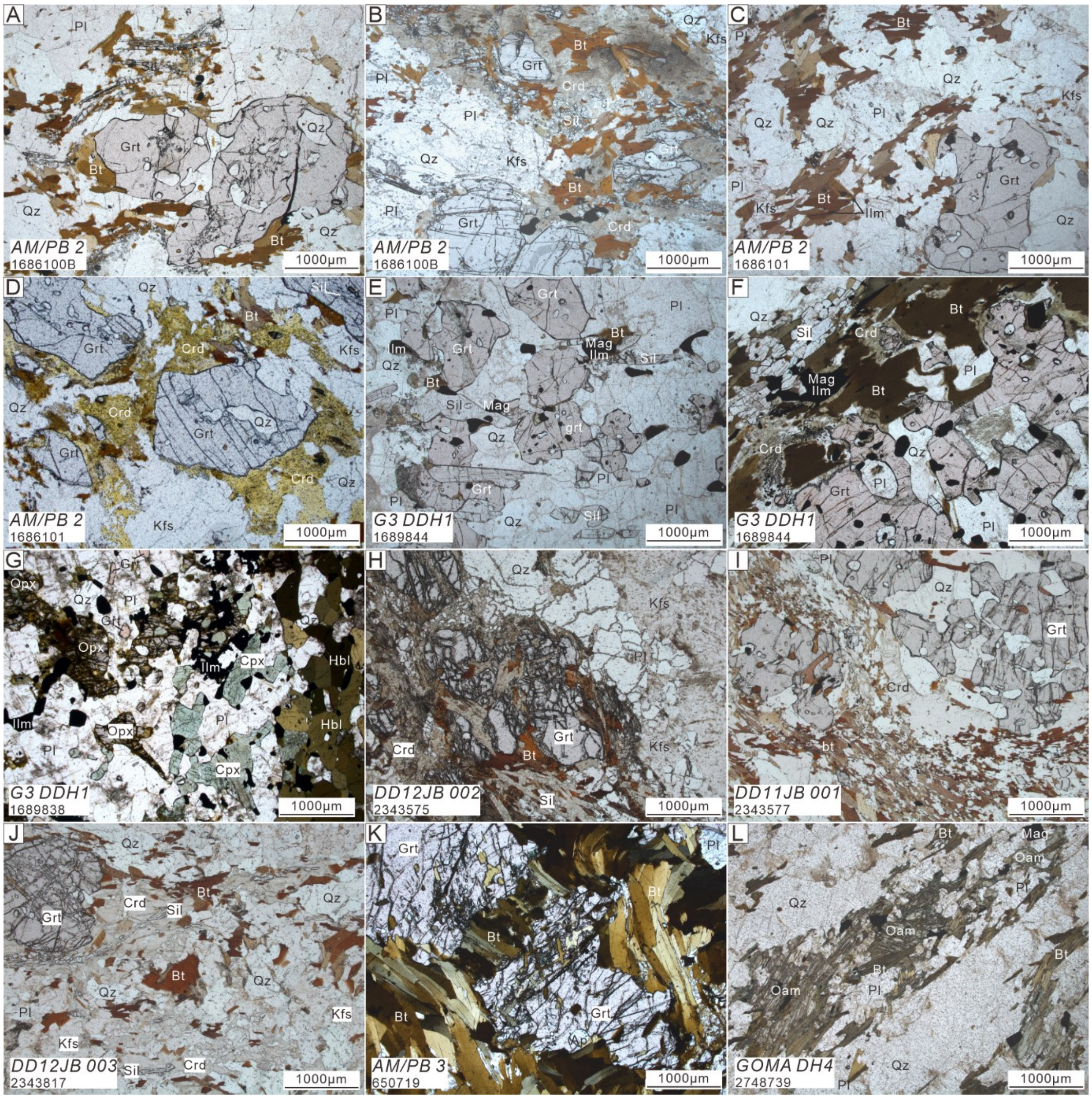

Fig. 5.4. Photomicrographs of representative samples. (A) Sample 1686100B from AM/PB 2: porphyroblastic garnet contains inclusions of biotite, sillimanite, and quartz. The matrix has a strong foliation defined by biotite and sillimanite. (B) Sample 1686100B from AM/PB 2: a domain of pinitized cordierite surrounds garnet, sillimanite, biotite and ilmenite. (C) Sample 1686101 from AM/PB 2: subhedral garnet porphyroblast hosted in matrix of biotite, K-feldspar, plagioclase, quartz, and ilmenite. (D) Sample 1686101 from AM/PB 2: garnet mantled by suprasolidus cordierite in a leucosome (qz + kfs + pl), cordierite is now pinitized. (E) Sample 1689844 from G3 DDH1: biotite-poor domain composed of garnet, quartz, plagioclase, sillimanite, magnetite, ilmenite, and minor fine-grained biotite. The sillimanite is foliated parallel to the gneissic layering in the sample. (F) Sample 1689844 from G3 DDH1: anhedral garnet with embayed margins. The matrix contains a moderate foliation defined by biotite and sillimanite. Cordierite occurs at the margins of garnet. (G) Sample 1689838 from G3 DDH1: boundary of garnet-bearing leucosomes and hornblende-rich melanosomes, garnet grains in leucosome are surrounded by orthopyroxene + plagioclase and clinopyroxene. (H) Sample 2343575 from DD12JB 002: porphyroblastic garnet grains are strongly fractured, and rimmed by cordierite and biotite. Both cordierite and sillimanite have been altered to clay minerals. (I) Sample 2343577 from DD11JB 001: Anhedral coarse-grained garnet is wrapped by a foliation defined by biotite, sillimanite, quartz and cordierite. (J) Sample 2343817 from DD12JB 003: garnet contains inclusions of sillimanite, biotite and quartz, wrapped by a foliation defined by biotite and sillimanite. Cordierite occurs as partial coronas on garnet and surrounds foliation-parallel sillimanite. (K) Sample 650719 from AM/PB 3: garnet contains inclusions of biotite and apatite, and is surrounded by coarse-grained biotite in the matrix. Biotite also occurs along fractures within garnet. (L) Sample 2748739 from GOMA DH4: felsic gneiss with a moderate foliation defined by biotite and orthoamphibole.

the only drill hole that samples crust adjacent to Mabel Creek Ridge.

AM/PB 2

Drill hole AM/PB 2 is located in the central part of the low TMI (Total Magnetic Intensity) response area and has a total depth of 437 m. It intersects metamorphosed banded iron formation beginning at 176 m and metapelitic granulite beginning at 349.4 m. The drill hole is migmatised, containing leucosomes up to 2 cm in width (Fig. 5.3A). Six metapelitic samples were taken from drill hole AM/PB 2 over the interval 410–437 m (Table 1). These samples display similar mineral assemblages but are characterized by the variable development of late cordierite. Detailed petrological descriptions of representative samples 1686100B and 1686101 are provided here, and detailed descriptions of the remaining samples are provided in Appendix 1.

Sample 1686100B (410.05–410.55 m) is migmatitic and comprises biotite, garnet, plagioclase, K-feldspar, sillimanite, quartz, ilmenite and cordierite. It exhibits a strong foliation, defined by biotite, sillimanite and quartzofeldspathic leucosomes (Fig. 5.3A). Porphyroblastic garnet grains are euhedral to subhedral, reaching up to 10 mm in diameter, and surrounded by intergrowths of sillimanite and biotite (Fig. 5.4A). Garnet contains inclusions of rounded quartz and weakly foliated biotite and sillimanite, which have no systematic orientation with respect to the foliation in the matrix. Garnet grains in the biotite-rich domains are finer-grained and more anhedral than those in the leucosome and are typically surrounded by domains of now pinitized cordierite (Fig. 5.4B). The matrix primarily consists of medium- to coarse-grained plagioclase, quartz, K-feldspar, biotite and medium-grained sillimanite. Biotite and sillimanite are 1–2 mm long and 0.1–0.5 mm wide, forming foliation parallel to the gneissic fabrics. Ilmenite mostly occurs as inclusions within biotite or along biotite grain boundaries. Quartz is fine to medium-grained and weakly elongated parallel to the foliation. Leucosomes are dominated by quartz, plagioclase and K-feldspar, and also contain biotite, cordierite, and sillimanite (Fig. 5.3A). Locally, domains of pinitized cordierite along the boundary of the melanosome contain inclusions of garnet, sillimanite, ilmenite and weakly foliated biotite (Fig. 5.4B). The peak mineral assemblage in the sample is interpreted to be biotite + garnet + ilmenite + K-feldspar + plagioclase + quartz + sillimanite + melt, with cordierite forming subsequently at the expense of garnet + sillimanite.

Sample 1686101 (414.6–414.8 m) is a metapelitic granulite with a mineral assemblage consisting of biotite, garnet, plagioclase, K-feldspar, quartz, ilmenite, sillimanite and cordierite. A gneissic fabric is defined by alternating biotite-rich and biotite-poor layers, while biotite in the thin section is weakly foliated and 0.2–1 mm in length (Fig. 5.4C). Garnet porphyroblasts are euhedral to subhedral, up to 6 mm in diameter, and contain inclusions of quartz, biotite, ilmenite, minor sillimanite, and monazite. The matrix of the sample comprises biotite, K-feldspar, plagioclase, quartz, and ilmenite, and does not contain sillimanite. Ilmenite is commonly associated with garnet and biotite. The sample also contains 2–5 mm wide layer-parallel garnet-bearing leucosomes that are made up of quartz, K-feldspar, plagioclase, garnet, cordierite, and minor biotite, indicating the presence of melt. Cordierite comprises 4–5 vol% of the sample and commonly mantles garnet and biotite in the leucosome (Fig. 5.4D). Fine-grained sulfides occur in cross-cutting fractures. The peak assemblage sample 1686101 is interpreted to be biotite + garnet + ilmenite + K-feldspar + plagioclase + quartz + melt with a precursor sillimanite-bearing assemblage. Cordierite is interpreted to post-date garnet.

Table 1 Sample locations, mineral assemblages and summary of geochronology results

Drill hole	Sample	Interval (m)	Mineral assemblage	*P T*	U-Pb monazite age ± 2σ (Ma)	Lu-Hf garnet age ± 2σ (Ma)
AM/PB 2 *133°49'38.36"E* *28°49'11.792"S*	1686100B	410.05–410.55	bt–grt–ilm–kfs–pl–qz–sil–melt–late crd	√	1585 ± 6 1569 ± 3	1596 ± 32
	1686101	414.60–414.80	bt–grt–ilm–kfs–pl–qz–melt–late crd	√		
	1686102	417.80–418.00		√		
	1686103	421.05–421.55	bt–grt–ilm–kfs–pl–qz–sil–melt–late crd	√		
	1686105	428.60–429.10		√		
	1686106	436.85–437.00		√		
G3 DDH1 *134°22'57.195"E* *28°46'23.899"S*	1689844	385.65–385.85	bt–grt–ilm–mag–pl–qz–sill–melt–late crd	√	1586 ± 9 1565 ± 9	1594 ± 32
	1689838	278.4–278.55	amp–cpx–grt–ilm–opx–pl–qtz–melt–mag	√		1561 ± 24
	1689840	342.00–342.25	bt–grt–ilm–kfs–pl–qz–melt	√		1611 ± 26
	1686859	335.75–335.95		√		
	1689834	264.40–264.55	amp–cpx–grt–ilm–opx–pl–qtz–melt–mag			1594 ± 21
	1689842	343.32–343.52	bt–grt–ilm–kfs–pl–qz–melt			1730 ± 42
DD12JB002 *133°40'33.223"E* *28°53'0.673"S*	2343575	234.8–235.18	bt–grt–kfs–pl–qz–sil–melt–late crd	√	1562 ± 7	1571 ± 84
DD11JB001 *133°40'47.083"E* *28°53'19.717"S*	2343577	263.53–264	bt–crd–grt–ilm–pl–qz–melt	√	1718 ± 6 1595 ± 9	1594 ± 75
DD12JB003 *133°42'29.186"E* *28°51'44.796"S*	2343817	274.43–274.7	bt–grt–kfs–pl–qz–sil–melt–late crd	√		1591 ± 28
AM/PB 3 *133°53'1.562"E* *28°51'37.283"S*	650719	234.80–235.50	bt–grt–ilm–mag–pl–qz–ap–mnz		1705 ± 9 1549 ± 7	1595 ± 38
	650713	220.70–221.10	bt–grt–ilm–mag–pl–qz			1598 ± 32
AM/PB 1 *133°54'46.207"E* *28°48'20.6"S*	967234	351.30–351.40	bt–grt–ilm–qtz–rt–sil–melt–late crd*	√	1597 ± 9* 1578 ± 7*	1564 ± 26
GOMA DH4 *134°11'37.944"E* *28°28'7.461"S*	2748739	510.90–511.15	bt–mag–oam–pl–qz–melt	√	1526 ± 9	

*From Cutts et al. (2011)

G3 DDH1

Drill hole G3 DDH 1 is located in eastern Mabel Creek Ridge and has a total depth of 500.5 m, intersecting basement at 207.5 m. The basement rocks include plagioclase-rich igneous rocks, biotite amphibolite, biotite-plagioclase-quartz gneiss and metapelite. Four samples were taken from drill hole G3 DDH1 (Table 1). Detailed petrological descriptions of representative samples 1689844 and 1689838 are provided below, and detailed descriptions of the remaining samples are provided in Appendix 1.

Sample 1689844 (385.65–385.85 m) contains biotite, garnet, plagioclase, sillimanite, quartz, ilmenite, magnetite, and cordierite. It contains a gneissic foliation defined by biotite-poor leucosomes and biotite-rich domains. The biotite-poor leucosomes are primarily composed of garnet, quartz, plagioclase, sillimanite, and minor fine-grained biotite, magnetite and ilmenite (Fig. 5.3B and 5.4E). Anhedral garnet porphyroblasts with inclusions of quartz, ilmenite, magnetite, and sillimanite range in size from 1 to 10 mm. Garnet porphyroblasts are commonly surrounded by plagioclase, sillimanite and quartz. The biotite-rich domains contain garnet, biotite, sillimanite, plagioclase, quartz, cordierite (now pinitised), ilmenite, and magnetite (Fig. 5.4F). Poikiloblastic garnet grains with embayed margins are up to 20 mm in size. They contain inclusions of biotite, sillimanite, quartz, magnetite, and ilmenite. Biotite in these domains is coarse-grained and unfoliated, whereas sillimanite is typically oriented parallel to the gneissic fabric. Cordierite, which is now pinitised, partially mantles garnet, biotite and sillimanite and comprises approximately 5 vol% of the sample (Fig. 5.4F). The peak assemblage is interpreted to be biotite + garnet + ilmenite + magnetite + plagioclase + quartz + sillimanite + melt, with cordierite forming subsequently at the expense of garnet + sillimanite ± biotite.

Sample 1689838 (278.40–278.55 m) is migmatitic, composed of interlayered garnet-bearing leucosomes and hornblende-rich melanosomes. The leucosomes are up to 13 mm wide and contain garnet, orthopyroxene, clinopyroxene, plagioclase, quartz, ilmenite and late magnetite. Garnet grains are anhedral, ranging from 0.1–8 mm, with rare inclusions of biotite and ilmenite. Garnet grains are commonly surrounded by orthopyroxene, clinopyroxene and plagioclase, indicating garnet is replaced by plagioclase or orthopyroxene + plagioclase + clinopyroxene (Fig. 5.4G). Clinopyroxene is locally altered to actinolite. The melanosome is primarily composed of hornblende and plagioclase, with minor clinopyroxene, quartz, ilmenite and magnetite.

DD12JB002, DD11JB001 & DD12JB003

DD12JB002, DD11JB001 & DD12JB003 are adjacent drill holes in western Mabel Creek Ridge, located within 1–4 kilometres of each other. Geophysical imagery does not show evidence for any major structures between drill holes (https://map.sarig.sa.gov.au). They have total depths ranging from 359.5 to 437.5m (Fig. 5.2A). Representative basement lithologies intersected include mafic granulites, metapsammite, metapelite, banded iron formation, and carbonate. Metapelites in these drill holes are all migmatitic (Fig. 5.3C, D). Detailed petrography of representative samples is described below.

Sample 2343575 (234.8–235.18 m) was obtained from drill hole DD12JB002 and contains biotite, garnet, cordierite, sillimanite, K-feldspar, plagioclase, and quartz (Fig. 5.3C and 4H). The sample contains a gneissic foliation defined by alternating ferromagnesian domains and leucosomes. In the ferromagnesian domains, garnet porphyroblasts range from 2–8 mm in size and are highly fractured, with argillaceous material filling the fractures. Garnet contains inclusions of quartz, biotite, and rare sillimanite. The matrix is composed of foliated biotite and bladed domains of sericite (interpreted to have been sillimanite, Fig. 5.4H), K-feldspar, plagioclase and quartz. The fractured garnet grains are enclosed by anhedral domains of fine-grained pinite, which also surrounds biotite and sillimanite. These domains are interpreted to have formerly been cordierite. The leucosomes consist of coarse-grained K-feldspar, quartz, and minor amounts of plagioclase, sillimanite and biotite. The peak mineral assemblage is interpreted to be biotite + garnet + K-feldspar + plagioclase + quartz + sillimanite + melt, with subsequent growth of cordierite. The extensive alteration means it is difficult to determine the modal proportions of minerals in this sample.

Sample 2343577 (263.53–264 m) from drill hole DD11JB001 contains biotite, cordierite, garnet, plagioclase, quartz and ilmenite (Fig. 5.3D and 4I). It has a strong foliation defined by biotite and elongate garnet porphyroblasts (2–8 mm in length). Garnet porphyroblasts are anhedral and contain inclusions of foliation-parallel biotite, quartz and ilmenite. The matrix is strongly foliated and composed of biotite, cordierite, plagioclase, quartz and ilmenite. Cordierite occurs together with biotite in the matrix and also as partial to full coronas on embayed garnet (Fig. 5.4I). The peak mineral assemblage is interpreted to be biotite + cordierite + garnet + ilmenite + plagioclase + quartz and melt, with a post-peak increase in the abundance of cordierite at the expense of garnet.

Sample 2343817 (274.43–274.7 m) from DD12JB003 has a similar mineral assemblage to sample 2343575, with a foliation defined by biotite, sillimanite and elongate domains of partially pinitised cordierite (Fig. 5.4J). The matrix is composed of biotite, cordierite, K-feldspar, plagioclase, quartz and sillimanite. Garnet poikiloblasts are 1–5 mm and contain inclusions of sillimanite, biotite and quartz. Biotite and sillimanite inclusions in garnet have no systematic orientation with respect to the foliation in the matrix. Garnet grains are partially surrounded by large domains of cordierite. Domains of cordierite also surround foliation-parallel biotite and sillimanite (Fig. 5.4J). The peak mineral assemblage is interpreted to be biotite + cordierite + garnet + K-feldspar + plagioclase + quartz + sillimanite and melt, with a subsequent post-peak increase in the abundance of cordierite at the expense of garnet and sillimanite.

AM/PB 3

The AM/PB 3 drill hole intersects the basement at a depth of 187.25 m, with a total depth of 287 m. The basement comprises steeply-dipping, interlayered magnetite-rich and magnetite-poor metasedimentary rocks with a maximum depositional age of ca. 1740 Ma (Payne et al., 2006). The magnetite-poor rocks consist of interlayered coarse-grained biotite + garnet + plagioclase + quartz assemblages, and biotite + garnet + hornblende + plagioclase + quartz assemblages where garnet has been partially replaced by orthopyroxene and plagioclase (Payne et al., 2008). Sample 650719 (234.80–235.50 m) is sampled from the biotite + garnet + plagioclase + quartz domain and contains a primary assemblage of biotite + garnet + ilmenite + magnetite + plagioclase + quartz, with abundant apatite and monazite (Fig. 5.4K). The garnet poikiloblasts contain inclusions of quartz, apatite, and biotite. The primary assemblage has been overprinted by narrow shear zones that formed at a high angle to the primary fabrics. The shear fabric assemblage is dominated by biotite (Fig. 5.4K), which encloses and infills the fractured garnet. Monazite and apatite occur in close proximity throughout the biotite-rich shear fabrics and are coarse-grained (commonly 100–500 µm in diameter but may be up to 1.5 mm).

GOMA DH4

Drill hole GOMA DH4 is located on the deep crustal seismic reflection section (08GA-OM1) (Fig. 5.2A). It is the closest drill hole (6 km) to Mabel Creek Ridge that intersects the basement. It has a total depth of 517 m and intersects 462 m of Neoproterozoic and Phanerozoic cover above basement, which comprises ~ 20 m of medium-grained granite and ~40 m of migmatitic felsic gneiss with leucocratic patches. Previously, Reid et al. (2014b) sampled a felsic gneiss from a depth of 510.4–510.6 m, and this felsic gneiss was interpreted to have a crystallisation age of 2526 ± 7 Ma with inherited zircons of ca. 3170–2680 Ma. Metamorphic zircon from the same sample yielded a U–Pb age of ca. 1520 Ma.

Sample 2748739 is sampled from a similar depth of 510.90–511.15 m. It is a coarse-grained felsic gneiss (Fig. 5.3E) with a mineral assemblage of biotite + magnetite + orthoamphibole + plagioclase + quartz with minor late chlorite and sulfides. Orthoamphibole is 0.5–1.5 mm in length and plagioclase is 0.5–2 mm in diameter. It displays a well-developed foliation defined by interlayered biotite–orthoamphibole-rich domains and leucosomes. The biotite–orthoamphibole-rich domains are primarily composed of biotite, orthoamphibole and plagioclase (Fig. 5.4L). Magnetite typically occurs alongside biotite and orthoamphibole. Some of the orthoamphibole has undergone partial alteration, forming green biotite or chlorite. The leucosomes are composed of plagioclase, quartz and minor biotite, and the presence of leucosomes indicates this sample has experienced partial melting (Reid et al., 2014b). Accessory minerals, such as apatite, monazite, and zircon, are present in both biotite–orthoamphibole-rich domains and leucosomes. The interpreted peak mineral assemblage is interpreted to be biotite + magnetite + orthoamphibole + plagioclase + quartz + melt.

Table 2 Bulk-Rock geochemistry used in phase equilibria modelling (wt. %).

Drill hole	Sample No.	SiO_2	Al_2O_3	CaO	Fe_2O_3	K_2O	MgO	Na_2O	P_2O_5	TiO_2	MnO	LOI	Total
AM/PB2	1686100B	66.3	15.6	1.5	8.0	2.6	3.7	1.5	0.1	0.5	0.1	1.5	101.4
	1686101	70.2	12.0	1.2	8.3	2.4	3.7	1.1	0.1	0.4	0.2	1.6	101.1
	1686102	71.2	11.9	1.3	8.2	2.1	3.2	1.2	0.1	0.3	0.1	0.9	100.4
	1686103	71.0	12.3	1.3	7.1	2.7	3.3	1.2	0.1	0.4	0.1	1.0	100.5
	1686105	71.8	12.4	1.4	6.2	2.5	3.2	1.5	0.1	0.4	0.1	1.3	100.9
	1686106	71.6	12.0	1.5	7.3	1.9	3.2	1.4	0.1	0.5	0.1	0.8	100.4
G3 DDH1	1689844	52.6	19.6	3.6	15.3	1.1	4.0	1.9	0.5	1.2	0.2	1.2	101.3
	1689838	51.6	12.2	7.5	17.7	1.0	3.4	2.1	0.7	3.3	0.3	1.7	101.5
	1689840	55.4	18.1	2.7	11.7	4.4	4.3	2.1	0.2	1.0	0.2	1.2	101.2
	1689859	55.7	18.6	3.0	10.5	3.5	4.4	2.8	0.1	1.3	0.1	1.9	101.8
DD12JB002	2343575	69.1	14.7	0.2	5.8	3.7	3.3	0.7	0.0	0.4	0.1	1.9	99.7
DD11JB001	2343577	62.5	13.0	0.7	12.0	2.2	6.9	0.8	0.1	1.3	0.1	0.0	99.6
DD12JB003	2343817	67.3	15.7	0.7	5.5	3.9	3.0	1.9	0.0	0.4	0.1	1.3	99.7
GOMA DH4	2748739	63.3	14.6	3.2	10.0	1.2	2.3	4.6	0.3	0.5	0.1	2.0	102.0

4. Analytical methods

4.1 Mineral equilibria forward modeling

P–T modelling was undertaken using GeoPS (Xiang and Connelly, 2021), a mineral equilibria forward modelling tool based on Gibbs energy minimization. It is similar to widely used forward modelling tools such as PerpleX, Theriak-Domino, and THERMOCALC in that it allows computation of the physicochemical properties of the stable minerals in a specified system, typically defined by the effective bulk composition of metamorphic assemblage (Xiang and Connelly, 2021 and references therein).

Bulk compositions for *P–T* modelling were determined by Bureau Veritas, Perth. Samples were powdered, oven dried (105 °C) and cast using 12:22 flux with 4% Li-nitrate to form a glass bead before being analysed by X-ray fluorescence spectrometry. The bulk-rock geochemistry is summarized in Table 2. All the modelled samples are homogenous at the sample scale. Despite later low temperature retrogression of cordierite, the whole rock compositions are considered to be representative of the effective bulk composition at the time of final melt crystallisation. Microprobe analyses were obtained using a Cameca SXFive electron microprobe at Adelaide Microscopy, The University of Adelaide, with a beam current of 20 nA and an accelerating voltage of 15 kV (Morrissey et al., 2016). The complete dataset of mineral chemistry analyses can be found in Appendix Table 1.

P–T modelling of metapelitic granulites from drill holes AM/PB 2, G3 DDH1, DD12JB002, DD11JB001 and DD12JB003 was carried out using the internally consistent dataset, HP62, of Holland and Powell (2011), and activity–composition (*a–x*) models re-parameterized for metapelites in the system MnNCKFMASHTO (MnO–Na_2O–CaO–K_2O–FeO–MgO–Al_2O_3–SiO_2–H_2O–TiO_2–Fe_2O_3)

(Powell et al., 2014; White et al., 2014a, b). Drill hole GOMA DH4 contains orthoamphibole, which cannot be modelled using the most recent *a–x* models and the HP62 dataset. It was therefore modelled using the previous dataset, HP04, of Holland and Powell (1998, updated 2004), in the system NCKFMASHTO ($MnO–Na_2O–CaO–K_2O–FeO–MgO–Al_2O_3–SiO_2–H_2O–TiO_2–Fe_2O_3$). Activity–composition models used were: Bio(WPH) and Gt(WPH) (White et al., 2007), Fsp(C1) (Holland and Powell, 2003), hCrd (Holland and Powell, 1998), Ilm(W) (White et al., 2000), melt(HP) (White et al., 2001), Mica(CHA) (Coggon and Holland, 2002; Auzanneau et al., 2010), oAmph(DP) (Diener et al., 2011), Opx(HP) (Powell and Holland, 1999) and Sp(WPC) (White et al., 2002). The H_2O contents for each sample were determined using the modal proportion of hydrous minerals, whereas the oxidation state was determined based on the proportion of Fe^{3+}-bearing minerals. The sensitivity of the modelled peak conditions to variations in H_2O content and oxidation state was assessed using $T–M_{H2O}$ sections $T–M_{O}$, respectively, presented in Appendix Fig. 1. Minor variations in H_2O content and oxidation state do not significantly change the interpreted peak conditions.

4.2 Monazite U–Pb geochronology and trace elements

Five samples from Mabel Creek Ridge (drill holes AM/PB 2, G3 DDH1, DD12JB002, DD11JB001 and AM/PB 3) and one sample from drill hole GOMA DH4 were selected for monazite geochronology (Fig. 5.2A). Monazite grains were identified in thin section using optical petrography. Back-scattered electron (BSE) images were collected using a FEI Quanta 600 scanning electron microscope (SEM) at Adelaide Microscopy, University of Adelaide, to reveal any compositional zoning and identify sites for laser analyses.

LA-ICP-MS monazite U–Pb and trace element data were collected on an Agilent 8900 ICP-MS coupled with a RESOlution 193 nm excimer laser ablation system, following the method of Payne et al. (2008). The ablation of monazite was performed with a spot size of 13 µm, a frequency of 5 Hz, and a laser energy of 4–5 J/cm^2. The total acquisition time for each analysis was 60 s, including 30 s of background measurement, followed by 30 s of laser ablation. Common lead was not corrected for in the age calculations due to unresolvable interference of ^{204}Hg on the ^{204}Pb isotope peak. Mass ^{204}Pb was monitored to compensate for this, and analyses were omitted if appreciable common lead was observed.

Mass bias, elemental fractionation, and instrument drift were corrected using the monazite standard MAdel (TIMS normalization data: $^{207}Pb/^{206}Pb$ age = 492.01 ± 0.77 Ma, $^{206}Pb/^{238}U$ age = 517.9 ± 2.6 Ma and $^{207}Pb/^{235}U$ age = 513.13 ± 0.20 Ma; updated from Payne et al., 2008 with additional TIMS analyses). Data accuracy was monitored by analyses of in-house monazite standard 222 (SHRIMP $^{206}Pb/^{238}U$ age 450.2 ± 3.4 Ma; Maidment, 2005) and Ambat ($^{206}Pb/^{238}U$ age ca. 520 Ma). Standards were analyzed every 12–15 unknown analyses. Throughout the course of this study standard 222 yielded a $^{206}Pb/^{238}U$ weighted mean age of 451.8 ± 1.7 Ma (n = 41, MSWD = 2, prob. = 0) and

Ambat yielded a $^{206}Pb/^{238}U$ weighted mean age of 524.8 ± 1.9 Ma (n = 22, MSWD = 0.69, prob. = 0.85). These values are within the expected external uncertainty of the LA-ICP-MS method of 1–2 % (Horstwood et al., 2016). Trace elements were processed using the glass NIST SRM 610. All monazite analyses were assumed to contain 20 wt. % Ce, then the sum of the oxides was normalized to 100% to account for the varying amounts of Ce in natural monazite.

Age calculation and trace element content of monazite were reduced using Iolite version 3.1 (Paton et al., 2011). U–Pb data were plotted using Isoplot 4.15 (Ludwig, 2012). Uncertainties on weighted average ages are quoted using 2σ and 95 % confidence.

4.3 Garnet Lu–Hf geochronology

Selected garnet-bearing samples from Mabel Creek Ridge were used for *in-situ* Lu–Hf dating. LA-ICP-MS Lu–Hf analyses were conducted at Adelaide Microscopy at the University of Adelaide. The analysis process mainly followed the method of Simpson et al. (2021) and is briefly summarised here. The Lu–Hf analyses were conducted using a RESOlution 193 nm excimer laser ablation system with an S155 sample chamber (Laurin Technic) coupled to an Agilent 8900 ICP-MS/MS. A squid mixing device (Laurin Technic) was used to smooth the pulses of the laser. NH_3 was used as the reaction gas, supplied as a mixture of 10 % NH_3 in 90 % He. Laser spot diameters of 60–120 μm were used to increase the sensitivity on Hf. Similarly, high laser repetition rates of 10 Hz were used to increase sensitivity. The following isotopes (mass shifts included in brackets) were measured: ^{24}Mg, ^{27}Al, ^{43}Ca, $^{(47+66)}Ti$, ^{55}Mn, ^{57}Fe, ^{88}Sr, $^{(89+83)}Y$, $^{(90+83)}Zr$, ^{172}Yb, ^{175}Lu, $^{(175+82)}Lu$, $^{(176+82)}Hf$, $^{(178+82)}Hf$. ^{175}Lu was monitored as a proxy for ^{176}Lu, and ^{178}Hf was monitored as a proxy for ^{177}Hf. Calculation of ^{176}Lu and ^{177}Hf was performed assuming stable present-day $^{176}Lu/^{175}Lu$ and $^{177}Hf/^{178}Hf$ ratios. Details of this correction can be found in Simpson et al. (2022).

LADR (Norris and Danyushevsky, 2018) was used to calculate background-subtracted ratios and correct instrument mass bias and drift for Lu–Hf ratios. NIST 610 glass was used as the primary reference material for Lu–Hf analysis (analysed every 20–40 unknowns), using $^{176}Lu/^{177}Hf$ and $^{176}Hf/^{177}Hf$ composition of 0.1379 ± 0.005 and 0.282111 ± 0.000009, respectively, as determined by ID-MC-ICP-MS (Nebel et al., 2009). Högsbo garnet (1029 ± 1.7 Ma; Romer and Smeds, 1996) are used to correct the matrix-induced fractionation. In-house reference Black Point garnet (corrected Lu–Hf age: 1745 Ma) was monitored for accuracy checks. Throughout the course of this study, standard Black Point garnet yielded inverse isochron ages ranging from 1741 ± 21 Ma to 1746 ± 30 Ma. IsoplotR was used to calculate the inverse isochron ages (Vermeesch, 2018). The ^{176}Lu decay constant of 0.00001867 ± 0.00000008 Myr^{-1} (Söderlund et al., 2004) was used for all age calculations.

5. Results

5.1 Mineral equilibria forward modeling

Calculated P–T pseudosections for all samples are summarised in Fig. 5.5, with complete pseudosections given in Fig. 5.6 and Appendix Fig. 2. All the modelled samples are

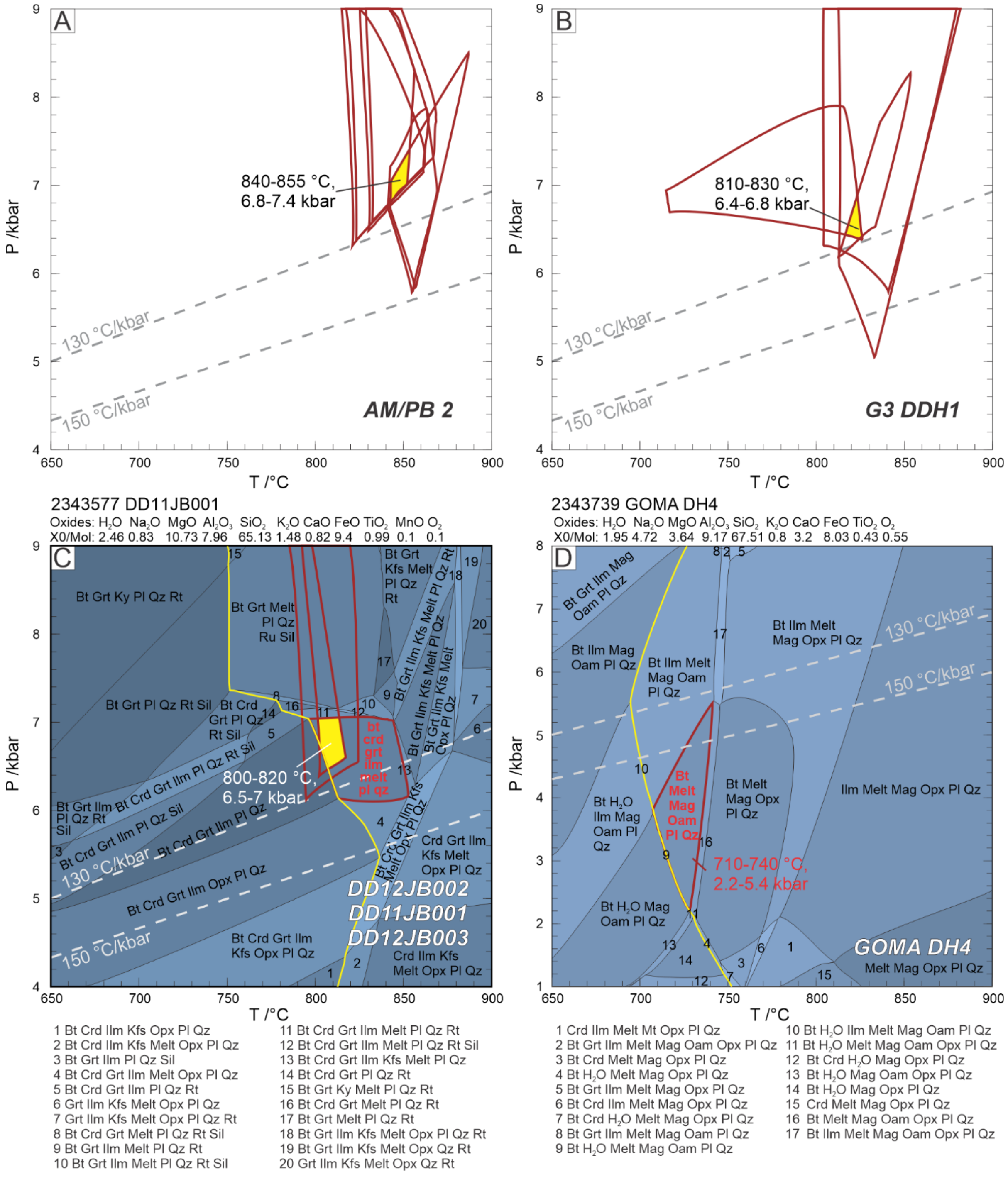

Fig. 5.5. Interpreted peak P–T fields for samples from drill hole (A) AM/PB 2, (B) G3 DDH1, (C) DD11JB001 and DD12JB002, 003, and (D) GOMA DH4. The fields highlighted in yellow are the interpreted peak conditions. The dashed lines are apparent thermal gradients. Complete P–T diagrams for each sample are available in Fig. 5.6 and Appendix Fig. 2.

migmatitic (Fig. 5.3), and therefore melt is interpreted to have formed part of the peak mineral assemblage in each sample. As the rocks have lost melt, we have not attempted to quantitatively model the prograde evolution of the rock.

AM/PB 2

Sample 1686100B has an interpreted peak assemblage of biotite + garnet + ilmenite + K-

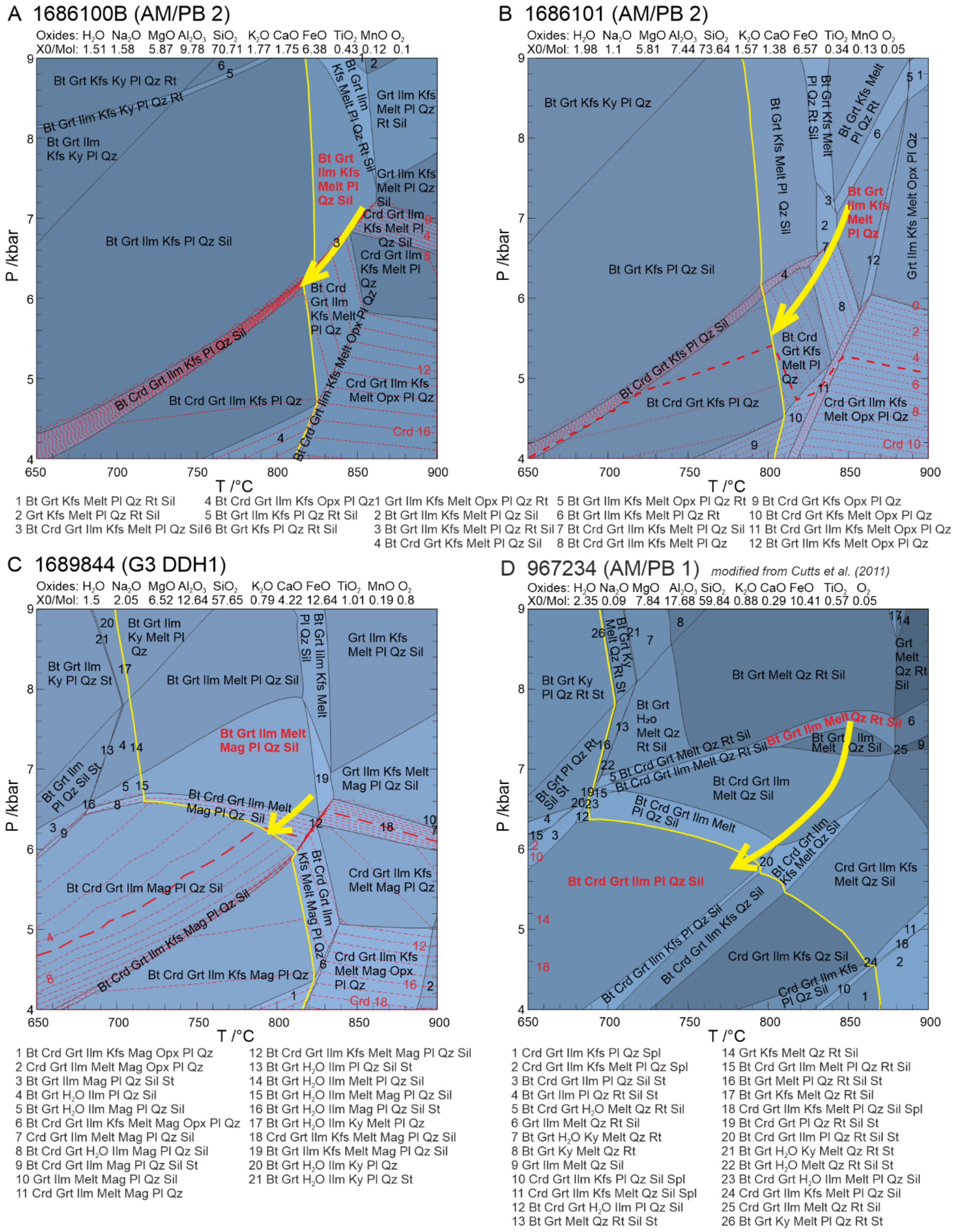

Fig. 5.6. Calculated P–T pseudosections for samples (A) 1686100 B from AM/PB 2, (B) 1686101 from AM/PB 2, (C) 1689844 from G3 DDH1, and (D) 967234 from AM/PB 1. The yellow arrows indicate the interpreted P–T path. The solidus is outlined in yellow. The bulk composition in mol % is given above each pseudosection. Samples in this study are contoured for the modal proportion of cordierite.

feldspar + plagioclase + quartz + sillimanite + melt. Sillimanite and biotite inclusions in garnet imply garnet formed at the expense of sillimanite and biotite. The peak mineral assemblage is calculated to be stable in the range of 6.2–9 kbar and 820–860 °C (Fig. 5.5A and 5.6A). The presence of cordierite in the leucosomes (Fig. 5.3A) and the persistence of sillimanite suggest a down-*P* evolution from peak conditions through the biotite + cordierite + garnet + ilmenite + K-feldspar + plagioclase + quartz + sillimanite + melt field (Fig. 5.6A).

To better constrain the *P*–*T* conditions, five additional samples are selected for phase equilibria modelling from drill hole AM/PB 2 (Table 1, Fig. 5.5A and Appendix Fig. 2) in the interval 410.05 to 437.0 m. Samples 1686103, 1686105 and 1686106 have the same peak mineral assemblages as 1686100B, including biotite + garnet + ilmenite + K-feldspar + plagioclase + quartz + sillimanite with melt. Sillimanite modes in these three samples decrease to varying degrees during retrograde metamorphism, and retrograde cordierite occurs within leucosomes and overprints garnet. Samples 1686101 and 1686102 do not contain sillimanite and have a peak mineral assemblage of biotite + garnet + ilmenite + K-feldspar + plagioclase + quartz + melt. Cordierite replaces garnet in leucosomes, which are dominated by K-feldspar + plagioclase + quartz (Fig. 5.4D). This suggests cordierite develops at suprasolidus conditions. The modelled peak assemblage fields from all samples from AM/PB 2 overlap in the range of 6.8–7.4 kbar and 840–855 °C (Fig. 5.5A).

The formation of late cordierite after garnet is variably developed between samples but implies the rocks underwent post-peak decompression. In sample 1686101, where retrograde cordierite is the most developed (Fig. 5.4D), the estimated cordierite mode is 4–5 vol. %. This corresponds to pressures of ~ 5.5 kbar, suggesting decompression of over 1 kbar from peak pressures (Fig. 5.5A, 5.6B).

G3 DDH1

The interpreted peak assemblage in sample 1689844 is biotite + garnet + ilmenite + magnetite + plagioclase + quartz + sillimanite with melt. The peak mineral assemblage is modelled to be stable over a wide range of *P*–*T* conditions (6.4–7.7 kbar and 710–830 °C, Fig. 5.5B, 5.6C). Late cordierite (now altered) forms between the edges of embayed garnet and sillimanite (Fig. 5.4F), indicating the development of cordierite at the expense of garnet and sillimanite. Coarse-grained, weakly oriented biotite adjacent to the cordierite domains may support suprasolidus growth of cordierite as melt began to crystalise. In an attempt to better constrain the *P*–*T* conditions, three additional samples (1689840, 1689859 and 1689838) were also modelled from the same drill hole (Table 1 and Appendix Fig. 2).

Sample 1689840 and sample 1689859 have the same peak mineral assemblage of biotite + garnet + ilmenite + K-feldspar + plagioclase + quartz with melt, while 1689840 preserves minor sillimanite inclusions in garnet porphyroblasts. Sample 1689838 has a peak assemblage of clinopyroxene + garnet + hornblende + ilmenite + orthopyroxene + plagioclase + quartz + melt with subsequent replacement of garnet by orthopyroxene + clinopyroxene + plagioclase (Fig. 5.4G). Collectively, the modelled stability fields of all samples from drill hole G3 DDH1 overlap at *P*–*T* conditions of 6.4–6.8 kbar, 810–830 °C (Fig. 5.5B). Late development of cordierite (in samples 1689840, 1689844, and

1689859) and orthopyroxene + clinopyroxene + plagioclase in sample 1689838 implies a post-peak pressure decrease similar to AM/PB 2.

In sample 1689844, the estimated retrograde cordierite mode is 5 vol. %, suggesting decompression of at least 0.5 kbar after the peak *P*–*T* conditions (Fig. 5.6C).

DD12JB002, DD11JB001 & DD12JB003

Three samples (2343575, 2343577, and 2343817) from three adjacent drill holes have similar mineral assemblages. Samples 2343575 and 2343817 have the same mineral assemblage of biotite + garnet + K-feldspar + plagioclase + quartz + sillimanite with melt, and they are stable at similar *P*–*T* conditions, >6.2 kbar and ~810 °C. The subsequent development of cordierite after garnet and the presence of sillimanite constrain a retrograde path along the field of biotite–cordierite–garnet–K-feldspar–plagioclase–quartz–sillimanite (Appendix Fig. 2). Sample 2343577 from DD11JB001 has a peak mineral assemblage of biotite + cordierite + garnet + ilmenite + plagioclase + quartz + melt, and is stable at *P*–*T* conditions of 6–7 kbar and 800–850 °C. The three samples overlap at narrow *P*–*T* conditions of 6.5–7 kbar and 800–820 °C (Fig. 5.5C).

GOMA DH4

Sample 2748739 has a mineral assemblage of biotite + magnetite + orthoamphibole + plagioclase + quartz + melt. In the modelled pseudosection, the absence of ilmenite and orthopyroxene constrain the mineral assemblage to be stable at conditions of 2.2–5.4 kbar and 710–740 °C (Fig. 5.5D). The same assemblage containing small amounts of ilmenite is stable at similar temperatures but over a larger pressure interval. This sample does not contain mineral reaction microstructures that could constrain the retrograde history.

5.2 Monazite U–Pb geochronology and trace element geochemistry

Representative photomicrographs and BSE images of analyzed monazite are provided in Fig. 5.7. All monazite U–Pb geochronological, trace element data and location are listed in Appendix Table 2 and plotted in Fig. 5.8. Yttrium vs. age and thorium vs. age plots are provided in Fig. 5.9 to better display the trace elements pattern. Only analyses within 2σ uncertainty of concordia are used for weighted average age calculations; discordant analyses are shown as dashed ellipses where they fall within the field of view. The concordia plots are colour-scaled for yttrium for each sample. Uncertainties calculated on weighted mean ages are 2σ and use the propagated uncertainties from Iolite, which in some cases gives uncertainties below the 1–2 % expected external uncertainty of the LA-ICP-MS method (Horstwood et al., 2016). We have therefore also provided a 1% uncertainty on each age in brackets.

AM/PB 2

Monazite grains in sample 1686100B are included in biotite, plagioclase, and quartz, or located in the intergrowths of sillimanite and biotite (Fig. 5.7A). No monazite was observed included in garnet. Monazite grains are 50–100 µm in diameter and less commonly up to 250 µm. Rare grains contain biotite inclusions and a dark

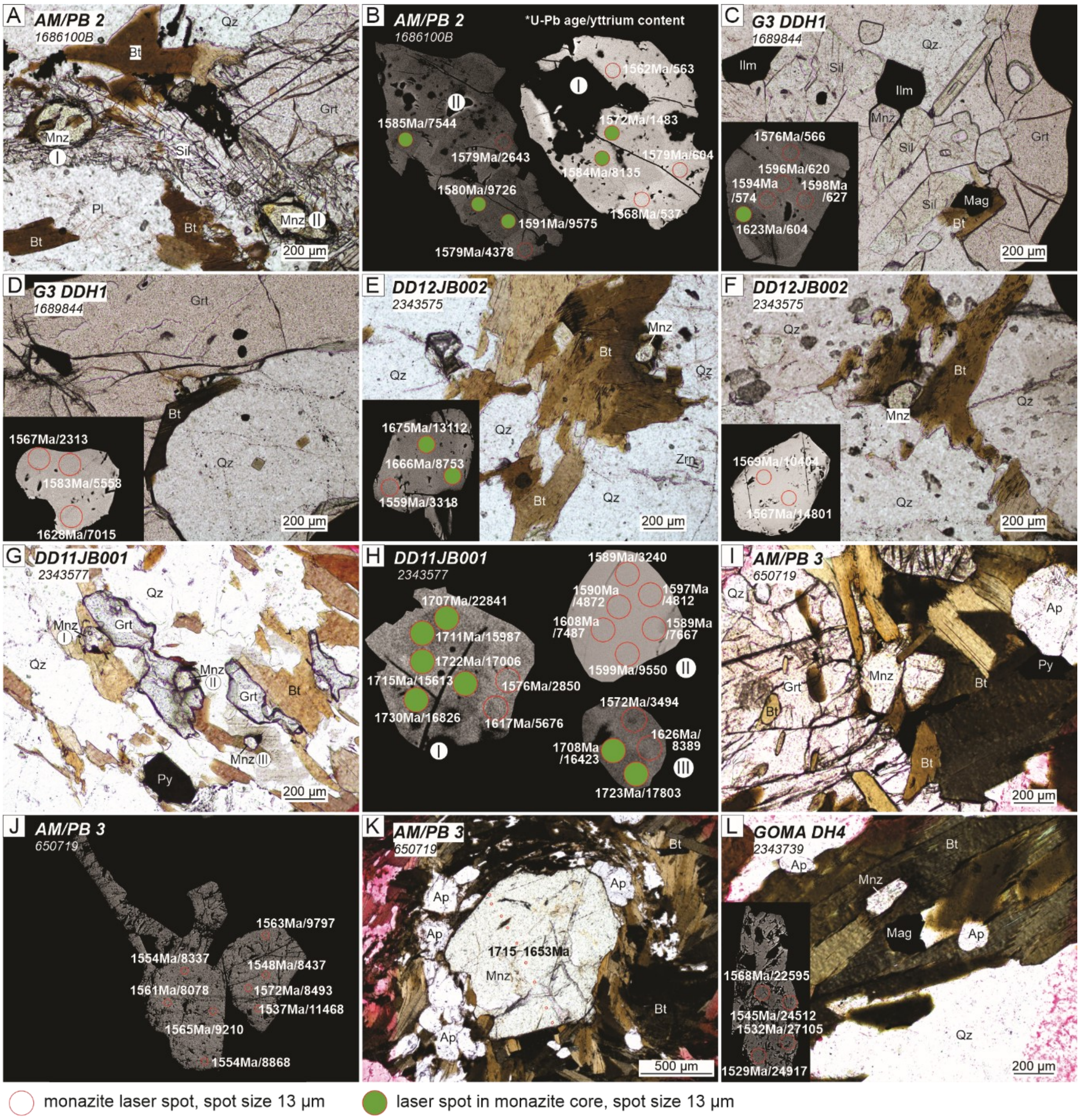

Fig. 5.7. Representative monazite photomicrographs and BSE images of monazite grains from samples (A and B) 1686100B, AM/PB 2, (C and D) 1689844, G3 DDH1, (E and F) 2343575, DD12JB002, (G and H) 2343577, DD11JB001, (I–K) 650719, AM/PB 3 and (L) 2343739, GOMA DH4. The ages shown on the BSE images are $^{207}Pb/^{206}Pb$ ages, and yttrium concentration in ppm is also given.

core in BSE images (Fig. 5.7B), but most are unzoned. Twenty-eight monazite grains were dated *in situ*. In single monazite grain, the dark cores have higher yttrium + HREE (heavy rare earth element) and lower Th concentrations and typically yield older ages (Fig. 5.7B and Appendix Table 2). Ten analyses with yttrium concentrations > 2100 ppm yielded a weighted mean $^{207}Pb/^{206}Pb$ age of 1585 ± 6 (±16) Ma (n = 10, MSWD = 0.65, prob. = 0.76, Fig. 5.8A and 5.9A). Thirty-two analyses with yttrium concentrations < 1600 ppm yielded a weighted mean $^{207}Pb/^{206}Pb$ age of 1569 ± 3 (±16) Ma (n = 30/32, MSWD = 1.19, prob. = 0.22).

G3 DDH1

Analyzed monazite grains in sample 1689844 are 50–100 μm in diameter and are

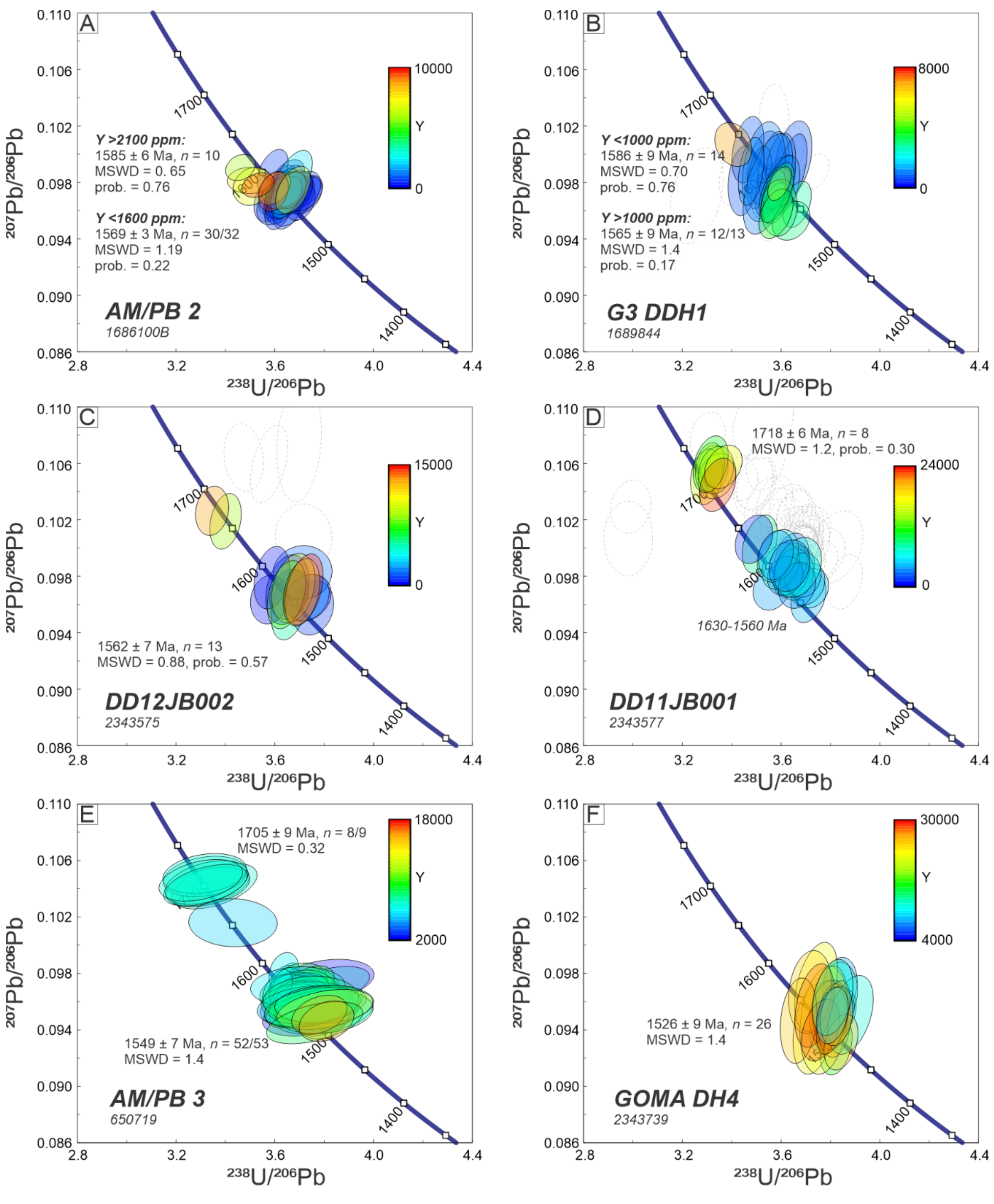

Fig. 5.8. Tera-Wasserburg concordia plots of monazite. The plots are colour-scaled by yttrium concentrations (ppm). Scales vary between samples to best depict trends in the data. Error ellipses are 2σ. Discordant analyses are shown as dashed ellipses where they fall within the field of view. (A) sample 1686100B from AM/PB 2. (B) sample 1689844 from G3 DDH1. (C) sample 2343575 from DD12JB002. (D) sample 2343577 from DD11JB001. (E) sample 650719 from AM/PB 3. (F) sample 2343739 from GOMA DH4.

included in plagioclase, biotite and quartz, or located along grain boundaries of biotite, garnet, plagioclase and sillimanite. Four grains contain a dark core in BSE images, but the majority are unzoned (Fig. 5.7C and D). Thirty-four analyses were collected from 13 grains *in situ*, with seven analyses excluded on the basis of discordance. The remaining analyses yield $^{207}Pb/^{206}Pb$ dates between 1628–1540 Ma but do not define a single statistically valid age population. Fourteen analyses with yttrium concentrations < 1000 ppm yielded a weighted mean $^{207}Pb/^{206}Pb$ age of 1586 ± 9 (±16) Ma (*n* = 14, MSWD = 0.70, prob. = 0.76, Fig. 5.8B). Thirteen analyses with yttrium concentrations > 1000 ppm yielded a weighted mean $^{207}Pb/^{206}Pb$ age of 1565 ± 9 (±16) Ma (*n* = 12/13, MSWD = 1.4, prob. = 0.17). There is a general increase in Y + HREE and a decrease in Th concentrations with younger ages (Fig. 5.9B and Appendix Table 2).

DD12JB002

Monazite grains in sample 2343575 are 20–200 µm in diameter, weakly to unzoned in BSE images, and are included in quartz and biotite, or located along grain boundaries of biotite and quartz in the matrix (Fig. 5.7E and F). Nineteen analyses were collected *in situ* from 11 monazite grains, with four analyses excluded on the basis of discordance. Two analyses from a single grain yield older dates of 1666 ± 19 Ma and 1675 ± 18 Ma, but the same grain also yields a young date of 1559 ± 21 Ma (Fig. 5.7E). The concordant analyses in the younger population yield a statistically valid weighted mean $^{207}Pb/^{206}Pb$ age of 1562 ± 7 (±16) Ma (*n* = 13, MSWD = 0.88, prob. = 0.57; Fig. 5.8C). This young population comprises two groups with distinctly different Y + HREE concentrations, but there is no relationship between trace element chemistry and age that could be used to refine this population further (Fig. 5.9C).

DD11JB001

Monazite grains in sample 2343577 are 20–150 µm in diameter, and are typically included in quartz and biotite, partially occluded by garnet or biotite or located along grain boundaries (Fig. 5.7G and H). Most grains are unzoned in BSE images, while some grains display clear zonation. Seventy-one analyses were collected from 27 monazite grains *in situ*, 44 of which were excluded on the basis of discordance because of a combination of Pb loss and common Pb. The remaining 27 analyses define two age groups on a Tera-Wasserburg plot (Fig. 5.8D). The oldest group has higher Y + HREE contents and yields a weighted mean $^{207}Pb/^{206}Pb$ age of 1718 ± 6 (± 17) Ma (*n* = 8, MSWD = 1.2, prob. = 0.30). Monazite grains that yield old dates may also yield young dates, and grains yielding older dates do not come from a specific microstructural location (Fig. 5.7H). Monazite grains partially occluded by garnet yield all young dates. The 19 analyses making up the younger population range from 1630–1560 Ma and do not define a single age population. Within the younger population, analyses with higher Th and Ca contents are generally older but these groups also do not define statistically valid ages (Appendix Table 2).

AM/PB 3

Monazite grains in sample 650719 are typically 50–100 µm in diameter, and are located in the biotite shear fabrics or along the boundaries of fractured garnet (Fig. 5.7I and J). One monazite grain is up to 1200 µm, surrounded by apatite and secondary biotite (Fig. 5.7K). Most grains are unzoned in BSE images, but some grains have thin bright rims. Sixty-three spots were analysed *in situ* from 22 monazite grains in sample 650719.

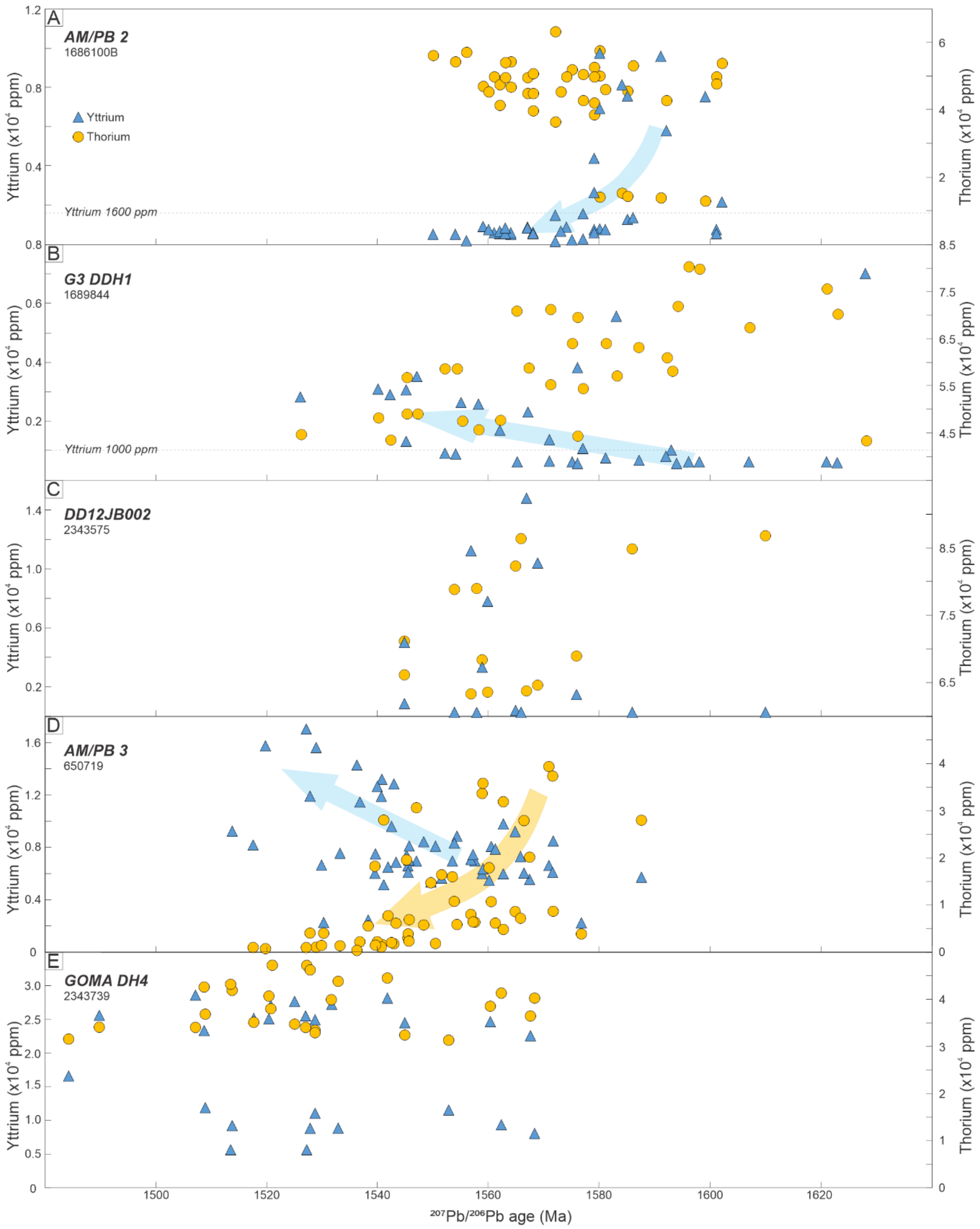

Fig. 5.9. Plots of yttrium and thorium vs. ^{207}Pb/^{206}Pb age for monazite from samples (A) 1686100B from AM/PB 2. (B) 1689844 from G3 DDH1 and (C) 2343575 from DD12JB002. (D) 650719 from AM/PB 3. (E) 2343739 from GOMA DH4.

One analyses were excluded on the basis of discordance. Two age populations are defined by the remaining 62 analyses (Fig. 5.8E). Nine analyses from the 1200 µm monazite grain yield ^{207}Pb/^{206}Pb dates between 1715–1653 Ma, and form an old population with a weighted mean ^{207}Pb/^{206}Pb age of 1705 ± 9 (± 17) Ma (n = 8, MSWD = 0.32). A younger population comes from smaller monazite grains and yields dates between 1588–1518 Ma, with a weighted mean

$^{207}Pb/^{206}Pb$ age of 1549 ± 7 (± 15) Ma (n = 52/53, MSWD = 1.4). Analyses within the younger population show increasing Y + HREE and decreasing Th concentrations with younger ages (Fig. 5.9D and Appendix Table 2).

GOMA DH4

Monazite grains in sample 2748739 typically occur as inclusions in quartz, biotite, and feldspar, and some grow along grain boundaries of apatite, biotite and quartz. Monazites are typically unzoned in BSE images and commonly display a pitted surface (Fig. 5.7L). Thirty-one spots were dated *in situ* from 15 monazite grains, with five analyses excluded on the basis of discordance. The remaining analyses display various Y+REE concentrations, albeit there is no age difference between them. All 26 analyses yield a weighted mean $^{207}Pb/^{206}Pb$ age of 1526 ± 9 (± 15) Ma (MSWD = 1.4, Fig. 5.8F and 5.9E).

5.3 Garnet Lu–Hf geochronology

In-situ Lu–Hf analyses were collected from garnet samples from drill holes AM/PB 2, G3 DDH1, DD12JB002, DD11JB001, DD12JB003, AM/PB 3 and AM/PB 1 (Table 1), with the aim of constraining the age of garnet growth relative to monazite. All results are listed in Appendix Table 3.

AM/PB 2

Ten garnet grains were analyzed from sample 1686100B, ranging from 1.7–8.7 mm in diameter. During the analysis, spots from both cores and rims were analyzed to cover areas with different Lu concentrations. One hundred and thirteen analyses yield an initial $^{177}Hf/^{176}Hf$ ratio of 3.55 ± 0.01 and an inverse isochron age of 1596 ± 32 Ma (2σ; MSWD = 0.95, p(χ^2) = 0.63; Fig. 5.10A).

G3 DDH1

Analyses from 11 garnet grains in sample 1689844 have low Lu concentrations and yield an imprecise inverse isochron age of 1594 ± 52 Ma (n=161, MSWD = 0.82, p(χ^2) = 0.95; Fig. 5.10B). Fifty-four analyses from 10 garnets in sample 1689838 (278.40–278.55 m) yield an inverse isochron age of 1561 ± 24 Ma (MSWD = 0.79, p(χ^2) = 0.86; Fig. 5.10C). Forty-nine analyses from four garnet grains in sample 1689840 (342.0–342.25 m) define an inverse isochron with an age of 1611 ± 26 Ma (MSWD = 0.46, p(χ^2) = 1; Fig. 5.10D). Fifty-nine analyses from 19 anhedral garnets in sample 1689834 (264.40–264.55 m) yield an inverse isochron age of 1594 ± 21 Ma (MSWD = 0.57, p(χ^2) = 1; Fig. 5.10E).

Two garnet porphyroblasts with diameters of 4 and 8 mm were analyzed for sample 1689842 (343.32–343.52 m) and yielded an inverse isochron age of 1730 ± 42 Ma (n = 50, MSWD = 0.63, p(χ^2) = 0.98; Fig. 5.10F).

DD12JB002, DD11JB001 & DD12JB003

Analyses from samples 2343575 (DD12JB002) and 2343577 (DD11JB001) have overall low Lu/Hf ratios and consequently have large uncertainties. Fifty-four analyses from nine garnet grains in sample 2343575 yield an inverse isochron age of 1571 ± 84 Ma (MSWD = 1.2, p(χ^2) = 0.2; Fig. 5.10G), and 53 analyses from eight garnet grains in sample 2343577 yield an inverse isochron age of 1594 ± 75 Ma (MSWD = 0.9, p(χ^2) = 0.67; Fig. 5.10H).

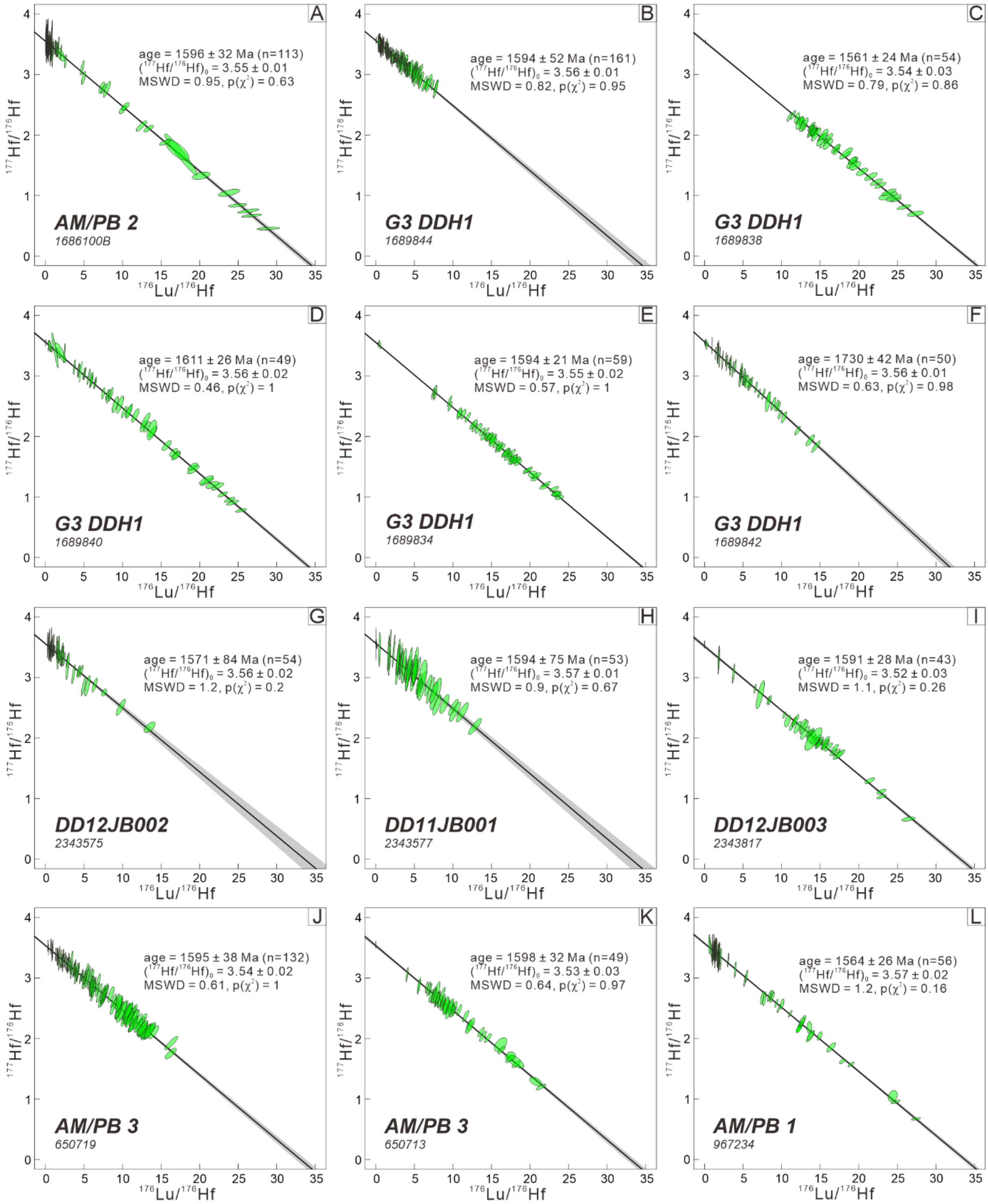

Fig. 5.10. Garnet Lu–Hf geochronology data of samples (A) 1686100B from AM/PB 2. (B) 1689844 from G3 DDH1. (C) 1689838 from G3 DDH1. (D) 1689840 from G3 DDH1. (E) 1689834 from G3 DDH1. (F) 1689842 from G3 DDH1. (G) 2343575 from DD12JB002. (H) 2343577 from DD11JB001. (I) 2343817 from DD12JB003. (J) 650719 from AM/PB 3. (K) 650713 from AM/PB 3. (L) 967234 from AM/PB 1.

Eight garnet grains were analyzed from sample 2343817 in drill hole DD12JB003. Garnet porphyroblasts range in size from 3–5 mm. Laser spots preferentially targeted the garnet cores to obtain higher Lu/Hf ratios and improve precision. An initial $^{177}Hf/^{176}Hf$ ratio of 3.55 ± 0.05 is used to anchor the inverse isochron and all analyses yield an age of 1591 ± 28 Ma (n=43, MSWD = 1.1, p(χ^2) = 0.26; Fig. 5.10I).

AM/PB 3

Thirteen garnet grains were analyzed from sample 650719, ranging from 1.4–6.1 mm in diameter. During the analysis, garnet adjacent to apatite was handled separately to observe the possible Lu–Hf diffusion between garnet and apatite. No difference was observed between garnet cores and rims or garnet adjacent to apatite. All analyses yield an inverse isochron age of 1595 ± 38 Ma (n = 132; MSWD = 0.61, p(χ^2) = 1; Fig. 5.10J). Nine garnet grains were analyzed from sample 650713. Garnet grains are 1–4 mm in diameter, and all analyses yield an inverse isochron age of 1598 ± 32 Ma (n=49, MSWD = 0.64, p(χ^2) = 0.97; Fig. 5.10K).

AM/PB 1

Two garnet grains were dated from sample 967234 from Cutts et al. (2011). Fifty-six spots yield an inverse isochron age of 1564 ± 26 Ma (MSWD = 1.2, p(χ^2) = 0.16; Fig. 5.10L).

6. Discussion

Due to the lack of basement outcrop in the northern Gawler Craton, previous inferences about its tectonic character are based almost entirely on limited datasets, e.g., drill hole-derived data and regional geophysical data (Payne et al., 2006, 2008; Korsch et al., 2010; Cutts et al., 2011, 2013; Reid et al., 2014b; Morrissey et al., 2019). In outcropping terranes, the presence of contractional or extensional structures is easy to detect via kinematic indicators and stratigraphic relationships and provides strong constraints on the tectonic regime. In contrast, determining the tectonic regime in basement terranes that do not crop out is challenging because kinematics are commonly difficult to infer solely from geophysical data and drill holes do not necessarily target key structures. Consequently, conclusions regarding tectonics are general rather than specific compared to outcrop-derived analysis. Nonetheless, in the case of Mabel Creek Ridge, the integration of geochronology (e.g., monazite U–Pb and garnet Lu–Hf), P–T pseudosection modelling, and regional structural style can illuminate the tectonic character of a largely blind orogenic system.

6.1 *P–T* character and evolution of Mabel Creek Ridge and adjacent crust

The results of the P–T modelling from metapelites from across Mabel Creek Ridge suggest the rocks experienced conditions of around 6.4–7.4 kbar at temperatures between 800–850 °C (Fig. 5.5A–C). These are slightly lower than the peak pressure of ~ 9kbar determined by Cutts et al. (2011) from drill hole AM/PB 1. However, Cutts et al. (2011) used a different thermodynamic dataset and activity-composition models. A P–T pseudosection calculated using the bulk composition of Cutts et al. (2011) and the updated HP62 thermodynamic dataset yields peak P–T conditions of 7.2–7.7 kbar and 780–870 °C, 1–1.5 kbar lower in pressure and overlapping with the estimates in this study (Fig. 5.6D). Therefore, the apparent differences in pressure may simply reflect differences in thermodynamic datasets, as opposed to sampling a different part of the thermobarometric evolution.

Most of the studied samples from Mabel Creek Ridge, as well as the sample from Cutts et al. (2011), show the post-peak formation of cordierite at the expense of garnet. Cordierite forms partial coronas on garnet and replaces sillimanite and biotite (Fig. 5.4B, D, F, H and J). The formation of cordierite after garnet in biotite-sillimanite-bearing rocks generally suggests a *P–T* evolution toward higher *T/P* ratios. In most cases where cordierite forms as coronas on garnet, the increasing *T/P* ratios are primarily a function of decompression rather than temperature increase (e.g., Clarke and Powell, 1991; Tomkins et al., 2005; Korhonen et al., 2010). The retrograde paths associated with the formation of post-peak cordierite in Mabel Creek Ridge are not particularly well constrained, as it is difficult to determine the accurate modes of cordierite because cordierite is mostly now replaced by low-temperature clay minerals. Some samples retain clear evidence of cordierite occurring within leucosomes and overprinting garnet, e.g., 1686101 and 1689844 (Fig. 5.4B, D and F), suggesting that these rocks may have experienced decompression of 0.5–1 kbar after peak metamorphism (Fig. 5.6). Overall, drill holes in the central Mabel Creek Ridge (e.g., AM/PB 1 and 2, this study and Cutts et al., 2011) record higher peak metamorphic conditions and more decompression compared to drill holes around the margin (Fig. 5.6).

Unfortunately, the availability of drill holes that penetrate the basement in the regions surrounding Mabel Creek Ridge is limited. The closest drill hole to Mabel Creek Ridge that intersects the surrounding basement crust is GOMA DH4, which is located 6 km north of Mabel Creek Ridge (Fig. 5.2A). In the deep crustal seismic reflection section (08GA-OM1), GOMA DH4 is separated from Mabel Creek Ridge by a crustal-scale north-dipping structure, the Box Hole Creek Fault (Fig. 5.2B), that places Mabel Creek Ridge in the relative footwall position. Mineral assemblages in samples from GOMA DH4 are stable over a relatively large *P–T* range of 2.2–5.4 kbar and 710–740 ºC. In addition, the presence of orthoamphibole in drill hole GOMA DH4 necessitates the use of a different thermodynamic dataset and *a–x* models, preventing a direct comparison with the modelled *P–T* conditions of Mabel Creek Ridge. However, if GOMA DH4 had reached the peak conditions of Mabel Creek Ridge (6.4–7.4 kbar, 800–850 °C), the peak mineral assemblage would be ilmenite + magnetite + orthopyroxene + plagioclase + quartz + melt ± biotite. Therefore, it is evident the crust penetrated by GOMA DH4 records lower pressures and temperatures compared to the structurally underlying Mabel Creek Ridge.

6.2 Age constraints on metamorphism in Mabel Creek Ridge and its surrounds

The oldest monazite U–Pb ages preserved within Mabel Creek Ridge are ca. 1700 Ma in age from drill holes DD12JB002, DD11JB001, AM/PB 3, and AM/PB 1 (Fig. 5.8C–E; Payne et al., 2008; Cutts et al., 2011). The ca. 1700 Ma monazites come from a small number of grains in samples that dominantly contain Mesoproterozoic monazite. The ca. 1700 Ma monazite have relatively high yttrium concentrations, suggesting their crystallisation prior to the growth of early Mesoproterozoic garnet, which appears consistent with the ca. 1600–1560 Ma garnet Lu–Hf age data from the same samples (Fig. 5.10, below). One sample from drill hole G3 DDH1 yielded a 1730 ± 42 Ma garnet Lu–Hf age, whereas garnet from the same lithology one metre away in the drill hole gives an age of 1611 ± 26 Ma. This suggests the presence of relict ca. 1730–1700 Ma garnet in rocks that were pervasively recrystalised during the Mesoproterozoic. The ca. 1730–1700 Ma monazite and garnet ages correspond to the Kimban Orogeny, which variably affected most of the Gawler Craton (Hand et al., 2007; Payne et al., 2008; Morrissey et al., 2023).

The majority of the monazite from the Mabel Creek Ridge records dates between 1600–1560 Ma (Fig. 5.8A–D; this study and Cutts et al., 2011). Monazites from drill holes DD11JB001 and DD12JB002 contain a range of trace element concentrations but do not show a clear relationship between composition and age. Determining a relationship between monazite age and composition in these samples may be complicated by the presence of variably recrystallised Kimban-aged domains within individual grains (Fig. 5.7G and H). However, samples 1686100B and 1689844 from drill holes AM/PB 2 and G3 DDH1 contain only Mesoproterozoic monazite and do show coherent patterns between Y concentrations and age (Fig. 5.8A and B; 5.9A and B). In drill hole AM/PB 2, monazite cores with higher Y concentrations (> 2100 ppm) yield a $^{207}Pb/^{206}Pb$ weighted mean age of 1585 ± 6 (±16) Ma, whereas the bulk of the monazite analyses in this sample have lower Y contents (<1600 ppm) and yield a younger $^{207}Pb/^{206}Pb$ weighted mean age of 1569 ± 3 (±16) Ma, albeit within 1% uncertainty. The higher Y + HREE contents of the older population may reflect monazite growth prior to the majority of garnet in sample 1686100B, while the lower Y + HREE contents of the younger population suggest it crystallised after garnet growth. In contrast, low Y monazite in drill hole G3 DDH1 yields a $^{207}Pb/^{206}Pb$ weighted mean age of 1586 ± 9 (±16) Ma, whereas monazite analyses with higher Y contents yield a $^{207}Pb/^{206}Pb$ weighted mean age of 1565 ± 9 (± 16) Ma. Garnet in sample 1689844 is skeletal and is surrounded by cordierite and coarse-grained biotite, suggesting that the younger, high Y monazite may have formed as garnet was breaking down whereas the older garnet may have grown in an environment where garnet was stable or increasing in mode. Hence, if changing Y contents in monazite relate to the formation or breakdown of garnet (e.g. Morrissey et al., 2022), the contrasting trends between samples suggest apparently different monazite growth histories relative to garnet from drill holes AM/PB 2 and G3 DDH1. This may be a function of their different bulk compositions. Although compositional information is not available, two age populations of 1597 ± 9 Ma and 1578 ± 7 Ma have also been previously obtained from drill hole AM/PB 1 for monazites in garnet and in the matrix, respectively (Fig. 5.2; Cutts et al., 2011).

As highlighted above, monazite petrochronology can be challenging to interpret in granulite-facies rocks, particularly if those rocks have experienced a protracted high-temperature history, as is the case in Mabel Creek Ridge. The mineral assemblages in the Mabel Creek drill

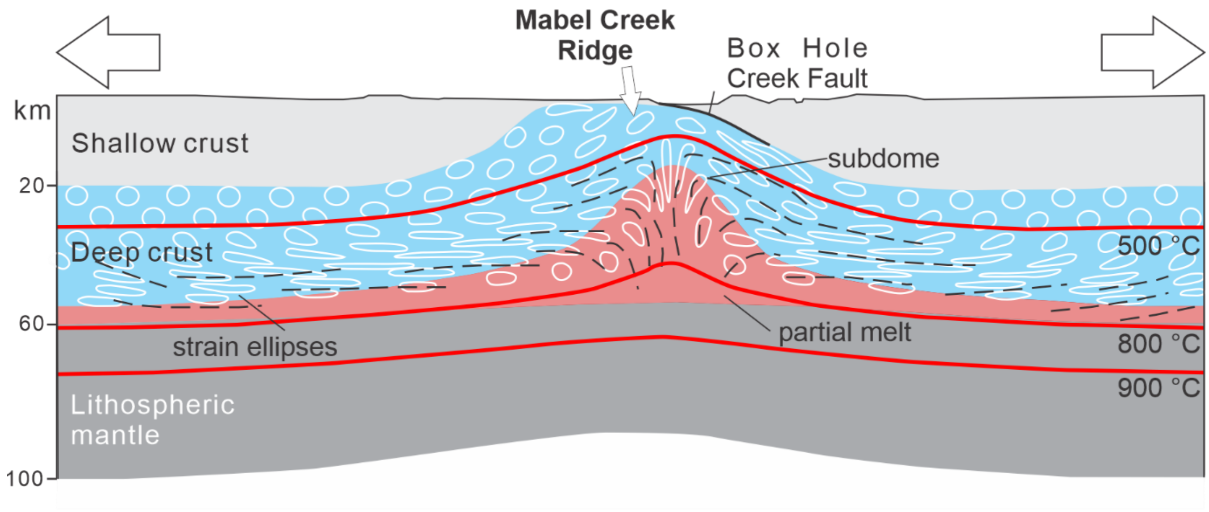

Fig. 5.11. Sketch of Mabel Creek Ridge showing crustal geometry and strain patterns in the deep crust, modified from numerical modelling of typical gneiss dome in Korchinski et al. (2018).

holes all display evidence for extensive anatexis, expressed most commonly by the presence of garnet- and sometimes cordierite-bearing quartzo-feldspathic leucosomes (Fig. 5.3A–J). In anatectic rocks, the stability of monazite can be sensitive to the presence of melt, provided the bulk rock P and LREE contents are insufficient to saturate both the solid and anatectic components of the rock (Kelsey et al., 2008; Yakymchuk and Brown, 2014). As a result, monazite ages in migmatites are typically interpreted to reflect post-peak cooling and melt crystallisation (Kelsey et al., 2008; Spear and Pyle, 2010; Yakymchuk and Brown, 2014). If this is the case, the bulk of the monazite ages in these samples should reflect the development of post-peak mineral assemblage (e.g., cordierite) as the rocks experienced decompression, cooling and crystallisation. The older monazite populations are likely to provide a minimum age for prograde to peak metamorphism, due to the potential for minor age resetting during continued metamorphism.

In an attempt to directly date garnet growth and the prograde to peak history of the rock prior to decompression and melt crystallisation, *in-situ* garnet Lu–Hf data was collected from 12 samples. With the exception of sample 1689842, all samples range in age from ca. 1610–1560 Ma. The majority of the precise garnet ages yield isochron ages of 1600–1590 Ma, which is slightly older but within uncertainty of the older monazite age populations. This suggests garnet growth in Mabel Creek Ridge predominantly occurred between 1600–1585 Ma. Two samples from drill holes G3 DDH1 and AM/PB 1 yield ages of 1561 ± 24 Ma and 1564 ± 26 Ma, respectively. Although these younger ages are within the uncertainty of the older ages, the analyses typically come from areas adjacent to the garnet rim and from garnets that show petrographic evidence for resorption (Fig. 5.4G). These ages are also consistent with the younger high-Y monazite age population of 1565 ± 9 Ma in G3 DDH1, which may reflect garnet breakdown (Fig. 5.9B; Table 1). Therefore, though the large uncertainties mean assigning significance to these younger garnet Lu-Hf ages is speculative, they may reflect the timing of garnet resorption during decompression. Taken together, the garnet Lu–Hf and monazite U–Pb age data from the Mabel Creek Ridge appear to document an interval of high-temperature conditions spanning ca. 1600–1560 Ma.

In addition to the bulk of the monazite age data from the Mabel Creek Ridge, sample 650719 from drill hole AM/PB 3 contains a distinct monazite population that gives an age of 1549 ± 7 (± 15) Ma (Fig. 5.8E), whereas it yields a garnet Lu–Hf inverse isochron age of 1595 ± 38 Ma. These younger monazites are located in the biotite shear fabrics overprinting the granulite-facies metamorphism or located along the boundaries of fractured garnet. Similar monazite U-Pb age of 1555 ± 11 Ma has been obtained from the same drill hole (Payne et al., 2008). The origin of these young monazites is not clear but conceivably reflects fluid-driven dissolution and precipitation of pre-existing monazite coeval with garnet breakdown, as indicated by the increasing yttrium concentration and low thorium concentration in younger monazite (Fig. 5.9D).

In contrast to the drill holes in Mabel Creek Ridge, samples from drill hole GOMA DH4 immediately to the north contain no evidence of metamorphism in the interval ca. 1600–1560 Ma (Fig. 5.8F). Reid et al. (2014b) obtained an age of 1521 ± 9 Ma for interpreted metamorphic zircon from a felsic gneiss and c. 1520 Ma for a leucocratic vein in GOMA DH4. In the present study, monazite was analyzed from the same interval in the drill hole and gave a similar age of 1526 ± 9 Ma. While the sample from GOMA DH4 lacks a record of ca. 1600–1560 Ma metamorphism, it seems to have experienced a thermal event that in part coincides in age with the young ca. 1550 Ma metamorphism in Mabel Creek Ridge, recorded by the yttrium-rich monazite in drill hole AM/PB 3 (Fig. 5.8E and 9D). Alternatively, the ca. 1520 Ma metamorphism may be related to the newly identified c. 1500–1480 Ma high-grade metamorphism along the Karari Shear Zone in the northern Gawler Craton (Fig. 5.1; Morrissey et al., 2023; Yu et al., 2023).

6.3 A case for Early Mesoproterozoic extension in the Southern Proterozoic Australia

Mabel Creek Ridge is transected by a crustal-scale seismic reflection line that is approximately perpendicular to the strike of the major structures that bound the Mabel Creek Ridge (Fig. 5.2; Korsch et al., 2010), providing information about the 3D geometry of the structures. The seismic reflection data shows that Mabel Creek Ridge is bound by structures that dip outward from the region composed of granulite-facies rocks intersected in the drill holes used in this study (Fig. 5.2B). On the northern side of Mabel Creek Ridge, hanging wall crust is intersected by GOMA DH4. The structures on the southern side of the Mabel Creek Ridge are interpreted to be truncated structures associated with the Karari Shear system (Fig. 5.1 and 2B), which is a craton-scale structure that was active to at least ca. 1450 Ma (Fraser and Lyons, 2006; Fraser et al., 2012), but also more recently where it controls Neoproterozoic-Phanerozoic depocentres.

Within the granulites in the northern part of Mabel Creek Ridge, the seismic data is characterized by gently dipping (in two dimensions) reflectors, suggesting the tectonic layering is regionally flat-lying (Fig. 5.2B). Regional airborne magnetic data shows that in plane view, the regional structure fabrics define a broadly E-W elongate elliptical pattern (Fig. 5.2A). In combination, the seismic and magnetic data coupled with the metamorphic character suggest the Mabel Creek Ridge is a crustal-scale dome-like culmination composed of granulite-facies rocks. Garnet-bearing assemblages that formed at around 1600–1585 Ma have been overprinted by cordierite-bearing assemblages that formed between ca. 1580–1560 Ma, suggesting the rocks within the Mabel Creek Ridge underwent high-temperature exhumation in the earliest Mesoproterozoic (Fig. 5.6). In contrast, the crust comprising the hanging wall intersected by GOMA DH4 shows no evidence for ca. 1600–1560 Ma metamorphism but instead records ca. 1520 Ma metamorphism (Fig. 5.8F and 9E). Conceivably the record of ca. 1600–1560 Ma metamorphism has been obliterated by metamorphism at around 1520 Ma. However, the metamorphic temperatures conditions recorded in GOMA DH4 appear lower than those within the Mabel Creek Ridge (Fig. 5.5), suggesting that even if ca. 1600–1560 Ma-aged metamorphism had affected the crust penetrated by GOMA DH4, it would be less intense than within the Mabel Creek Ridge.

While it is difficult to be confident as the entire system is covered by younger sedimentary units, there are several potential ways the structural and metamorphic data could be explained. One possibility is the rocks intersected in GOMA DH4 are a cover sequence deposited on the Mabel Creek Ridge basement between ca. 1560–1520 Ma, with the structure between them, i.e., Box Hole Creek Fault, being a growth fault. The rocks in GOMA DH4 are mostly migmatitic felsic gneiss composed of leucocratic bands of plagioclase ± quartz interlayered at the centimeter scale with biotite ± hornblende ± orthoamphibole. In addition to ca. 1520 Ma metamorphic zircon, the felsic gneiss contains zircon with a range of dates between c. 3200–2600 Ma and a dominant population at ca. 2500 Ma, which were interpreted by Reid et al. (2014b) to be the age of the magmatic protolith. However, it is also possible that the ca. 2500 Ma zircons could be detrital grains derived from a restricted source region, allowing for the possibility GOMA DH4 intersected a cover sequence.

A second possibility for the presence of ca. 1600–1560 Ma granulites in the Mabel Creek and the absence of equivalent metamorphism in the hanging wall is the exhumation of the footwall with respect to the hanging wall. Systems comprising an exhumed high-grade metamorphic footwall and a less metamorphosed or unmetamorphosed hanging wall typify extensional regimes, most characteristically expressed by the development of metamorphic core complexes (e.g., Armstrong, 1982; Coney et al., 1984; Davis et al., 2002; Whitney et al., 2015) or gneiss domes (e.g., Teyssier and Whitney, 2002; Yin, 2004; Rey et al., 2011). Among published numerical modelling studies on the formation of gneiss domes, a common feature of these models is lowest viscosity flow within hot lower crust occurs toward regions of mid and upper-crustal extension (e.g., Rey et al., 2011, 2017; Korchinski et al., 2018). This mechanism can create crustal-scale structures that are characterized by domal foliation patterns in high-grade metamorphic rocks, and *P–T* paths from many gneiss domes record a pressure drop equivalent to over 10–20 km of crustal exhumation at high temperatures (Whitney et al., 2004; Korchinski et al., 2018). In our samples, the growth of cordierite coronas at the expense of garnet and sillimanite is consistent with decompression at high temperatures as the footwall (Mabel Creek Ridge) is exhumed, whereas the hanging wall (GOMA DH4) was at shallower levels and does not record this event. The inward flow of the hot lower crust may result in the viscous collision below the zone of upper crustal extension, leading to the formation of gneiss domes that contain internal sub-domes (Fig. 5.11; Rey et al., 2011, 2017; Korchinski et al., 2018; Varga et al., 2022). Although speculative because of the obscuring cover, the magnetic trend lines in the Mabel Creek Ridge appear to delineate two ovoid structural domains that bear a resemblance to outcrop-generated structural maps of gneiss domes containing internal sub-domes (Fig. 5.2A).

In the Gawler Craton, the interval ca. 1600–1560 Ma encompasses a period of craton-scale mantle-driven magmatism that generated voluminous high-temperature felsic magmas (Wade et al., 2019, Jagzodinski et al., 2023). One consequence of this thermal regime is the lower crust would have almost certainly been hot, as evidenced by the incorporation of crust into the felsic magmas (Stewart and Foden, 2003; Chapman et al., 2019; Wade et al., 2019). In addition, the migmatitic nature of the Mabel Creek Ridge granulites suggests they would have been characterized by melt-weakened rheology that would have facilitated flow (Rey et al., 2011; Varga et al., 2022), as shown by Fig. 5.11, a typical example of the formation of a gneiss dome based on numerical models (Korchinski et al., 2018). We tentatively suggest the Mabel Creek Ridge is a record of Early Mesoproterozoic extension in the Gawler Craton during which thermally perturbed lower crustal rocks were exhumed within a broad approximately east-west elongate dome-like culmination reminiscent of a gneiss dome (Teyssier and Whitney, 2002; Yin, 2004; Rey et al., 2011).

Due to the uncertainties in the paleogeography of Gawler Craton, the drivers for early Mesoproterozoic extension are unclear. However, there is a general consensus the southern Australia Palaeo-Mesoproterozoic rock system was formerly continuous with the North Australian Craton (Cawood and Korsh, 2008; Payne et al., 2009; Betts et al., 2016; Morrissey et al., 2023). Within this configuration, the proto-cratonic crust of the northern Gawler Craton is envisaged to have been sandwiched between two subduction systems (Fig. 5.12). To the NE, convergence is interpreted to have led to the amalgamation of Paleoproterozoic Australia and Laurentia at around 1600 Ma (Pourteau et al., 2018), resulting in contractional deformation in NE Australia and conceivably in the Curnamona Province (Pourteau et al., 2018; Volante et al.,

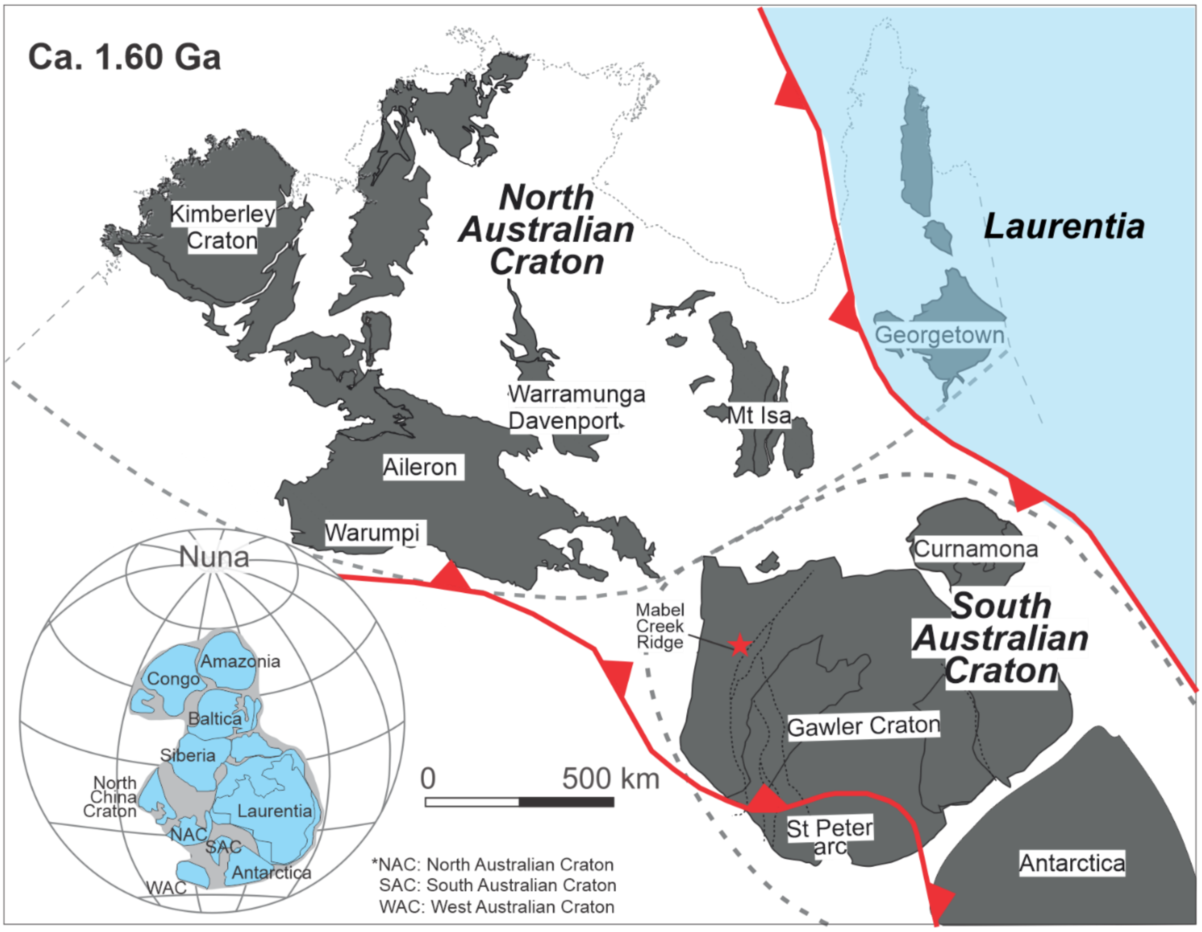

Fig. 5.12. The reconstructed paleogeography of North Australian Craton (NAC) and South Australian Craton (SAC) at ca. 1.60 Ga. Modified after Kirscher et al. (2019) and Morrissey et al. (2019).

2020; De Vries Van Leeuwen et al., 2022) which now forms the eastern part of the South Australian Craton. To the SW, St Peter Suite arc magmatism is well documented in the interval 1633–1608 Ma (Swain et al., 2008; Reid et al., 2020). Within this geodynamically complex setting, plume-driven magmatism resulted in the generation of voluminous felsic melts within the Gawler Craton-Curnamona Province system over the interval 1595–1570 Ma (Allen et al., 2008; Betts et al., 2009; Pankhurst et al., 2011; Wade et al., 2012; Jagozdinski et al., 2023). Plausibly the thermally perturbed nature of the lower crust would have made it conducive to flow and migration toward areas of extension that may have arisen due to changes in the dynamics along the active margins of southern and northern Australia.

7. Conclusions

(1) *P–T* modelling of metapelites from across Mabel Creek Ridge suggests peak conditions of ~6.4–7.4 kbar and 800–850 °C. Post-peak suprasolidus cordierite growth after garnet indicates subsequent decompression. In contrast, the drill hole located immediately north of Mabel Creek Ridge records lower-grade metamorphism.

(2) Mabel Creek Ridge preserves relic Kimban monazite and garnet (ca. 1730–1700 Ma), while the bulk of garnet Lu–

Hf and monazite U–Pb age data appear to document an interval of high-temperature conditions spanning ca. 1600–1560 Ma. Drill hole GOMA DH4 contains no evidence of contemporaneous metamorphism but yields a monazite U–Pb age of ca. 1520 Ma.

(3) The seismic and airborne magnetic data, coupled with the metamorphic character, suggest that Mabel Creek Ridge is composed of granulite-facies rocks in the footwall flanked by the less metamorphosed hanging wall. Therefore, it is a record of Early Mesoproterozoic extension in the Gawler Craton, during which thermally perturbed lower crustal rocks were exhumed within a gneiss dome.

Acknowledgments

This project was supported by ARC Linkage Project LP160100578 (JLP and MH), the Mineral Exploration Cooperative Research Centre (MinEX CRC), and the China Scholarship Council. LJM is supported by an ARC DECRA Fellowship DE210101126. S. Gilbert and B. Wade are thanked for their technical support at Adelaide Microscopy. A. Simpson and S. Glorie are thanked for their help in processing the Lu–Hf geochronology.

References

Aitken, A. R. A., Betts, P. G., Young, D. A., Blankenship, D. D., Roberts, J. L., & Siegert, M. J. (2016). The Australo-Antarctic Columbia to Gondwana transition. *Gondwana Research, 29*(1), 136-152. doi:https://doi.org/10.1016/j.gr.2014.10.019

Allen, S. R., McPhie, J., Ferris, G., & Simpson, C. (2008). Evolution and architecture of a large felsic Igneous Province in western Laurentia: The 1.6 Ga Gawler Range Volcanics, South Australia. *Journal of Volcanology and Geothermal Research, 172*(1-2), 132-147. doi:10.1016/j.jvolgeores.2005.09.027

Anczkiewicz, R., Szczepański, J., Mazur, S., Storey, C., Crowley, Q., Villa, I. M., . . . Jeffries, T. E. (2007). Lu–Hf geochronology and trace element distribution in garnet: Implications for uplift and exhumation of ultra-high pressure granulites in the Sudetes, SW Poland. *Lithos, 95*(3), 363-380. doi:https://doi.org/10.1016/j.lithos.2006.09.001

Armit, R., Betts, P. G., Schaefer, B. F., Yi, K., Kim, Y., Dutch, R. A., . . . Ailleres, L. (2017). Late Palaeoproterozoic evolution of the buried northern Gawler Craton. *Precambrian Research, 291*, 178-201. doi:10.1016/j.precamres.2017.01.023

Armstrong, R. L. (1982). Cordilleran metamorphic core complexes-from Arizona to southern Canada. *Annual review of earth planetary sciences, 10*, 129.

Auzanneau, E., Schmidt, M. W., Vielzeuf, D., & D Connolly, J. A. (2010). Titanium in phengite: a geobarometer for high temperature eclogites. *Contributions to Mineralogy and Petrology, 159*(1), 1-24. doi:10.1007/s00410-009-0412-7

Betts, P. G., Armit, R. J., Stewart, J., Aitken, A. R. A., Ailleres, L., Donchak, P., . . . Murphy, J. B. (2016). Australia and Nuna. In *Supercontinent Cycles Through Earth History* (Vol. 424, pp. 0): Geological Society of London.

Betts, P. G., & Giles, D. (2006). The 1800–1100Ma tectonic evolution of Australia. *Precambrian Research, 144*(1), 92-125. doi:https://doi.org/10.1016/j.precamres.2005.11.006

Betts, P. G., Giles, D., Foden, J., Schaefer, B. F., Mark, G., Pankhurst, M. J., . . . Hills, Q. (2009). Mesoproterozoic plume-modified orogenesis in eastern Precambrian Australia. *Tectonics, 28*(3), TC3006. doi:10.1029/2008tc002325

Bloch, E., & Ganguly, J. (2015). 176Lu–176Hf geochronology of garnet II: numerical simulations of the development of garnet–whole-rock 176Lu–176Hf isochrons and a new method for constraining the thermal history of metamorphic rocks. *Contributions* *to Mineralogy and Petrology, 169*(2), 14. doi:10.1007/s00410-015-1115-x

Bloch, E. M., Jollands, M. C., Devoir, A., Bouvier, A. S., Ibañez-Mejia, M., & Baumgartner, L. P. (2020). Multispecies Diffusion of Yttrium, Rare Earth Elements and Hafnium in Garnet. *Journal of Petrology, 61*(7), egaa055. doi:10.1093/petrology/egaa055

Bockmann, M. J., Hand, M., Morrissey, L. J., Payne, J. L., Hasterok, D., Teale, G., & Conor, C. (2022). Punctuated geochronology within a sustained high-temperature thermal regime in the southeastern Gawler Craton. *Lithos, 430*, 106860.

Cawood, P. A., & Korsch, R. (2008). Assembling Australia: Proterozoic building of a continent. *Precambrian Research, 166*(1-4), 1-35.

Chapman, N. D., Ferguson, M., Meffre, S. J., Stepanov, A., Maas, R., & Ehrig, K. J. (2019). Pb-isotopic constraints on the source of A-type Suites: Insights from the Hiltaba Suite - Gawler Range Volcanics Magmatic Event, Gawler Craton, South Australia. *Lithos, 346-347*, 105156. doi:https://doi.org/10.1016/j.lithos.2019.105156

Clarke, G. L., & Powell, R. (1991). Decompressional coronas and symplectites in granulites of the Musgrave Complex, central Australia. *Journal of Metamorphic Geology, 9*(4), 441-450. doi:https://doi.org/10.1111/j.1525-1314.1991.tb00538.x

Coggon, R., & Holland, T. J. B. (2002). Mixing properties of phengitic micas and revised garnet-phengite thermobarometers. *Journal of Metamorphic Geology, 20*(7), 683-696. doi:https://doi.org/10.1046/j.1525-1314.2002.00395.x

Coney, P. J., & Harms, T. A. (1984). Cordilleran metamorphic core complexes: Cenozoic extensional relics of Mesozoic compression. *Geology, 12*(9), 550-554. doi:10.1130/0091-7613(1984)12<550:CMCCCE>2.0.CO;2

Cutts, K., Hand, M., & Kelsey, D. E. (2011). Evidence for early Mesoproterozoic (ca. 1590Ma) ultrahigh-temperature metamorphism in southern Australia. *Lithos, 124*(1-2), 1-16. doi:10.1016/j.lithos.2010.10.014

Cutts, K. A., Kelsey, D. E., & Hand, M. (2013). Evidence for late Paleoproterozoic (ca 1690–1665Ma) high- to ultrahigh-temperature metamorphism in southern Australia: Implications for Proterozoic supercontinent models. *Gondwana Research, 23*(2), 617-640. doi:10.1016/j.gr.2012.04.009

Daly, S. (1998). Tectonic evolution and exploration potential of the Gawler Craton, South Australia. *AGSO J. Aust. Geol. Geophys., 17*, 145-168.

Daly, S., & Fanning, C. (1993). *Archaean*. Retrieved from

Davis, G. A., Darby, B. J., Yadong, Z., & Spell, T. L. (2002). Geometric and temporal evolution of an extensional detachment fault, Hohhot metamorphic core complex, Inner Mongolia, China. *Geology, 30*(11), 1003-1006. doi:10.1130/0091-7613(2002)030<1003:GATEOA>2.0.CO;2

De Vries Van Leeuwen, A. T., Morrissey, L. J., Raimondo, T., & Hand, M. (2022). Prolonged high thermal gradient metamorphism in the Curnamona Province, south-central Australia, during the latter stages of Nuna assembly. *Precambrian Research, 378*, 106775. doi:https://doi.org/10.1016/j.precamres.2022.106775

Diener, J. F. A., & Powell, R. (2011). Revised activity–composition models for clinopyroxene and amphibole. *Journal of Metamorphic Geology, 30*(2), 131-142. doi:https://doi.org/10.1111/j.1525-1314.2011.00959.x

Dutch, R., Hand, M., & Kelsey, D. (2010). Unravelling the tectonothermal evolution of reworked Archean granulite facies metapelites using in situ geochronology: an example from the Gawler Craton, Australia. *Journal of Metamorphic Geology, 28*(3), 293-316.

Fanning, C., Flint, R., Parker, A., Ludwig, K., & Blissett, A. (1988). Refined Proterozoic evolution of the Gawler craton, South Australia, through U-Pb zircon geochronology. *Precambrian Research, 40*, 363-386.

Fanning, C., Reid, A., & Teale, G. (2007). A geochronological framework for the Gawler Craton, South Australia. *South Australia Geological Survey Bulletin, 55*(258).

Fisher, C. M., & Vervoort, J. D. (2018). Using the magmatic record to constrain the growth of continental crust—The Eoarchean zircon Hf record of Greenland. *Earth and Planetary Science Letters, 488*, 79-91.

doi:https://doi.org/10.1016/j.epsl.2018.01.031

Forbes, C. J., Giles, D., Hand, M., Betts, P. G., Suzuki, K., Chalmers, N., & Dutch, R. (2011). Using P–T paths to interpret the tectonothermal setting of prograde metamorphism: An example from the northeastern Gawler Craton, South Australia. *Precambrian Research, 185*(1-2), 65-85. doi:10.1016/j.precamres.2010.12.002

Fraser, G., McAvaney, S., Neumann, N., Szpunar, M., & Reid, A. (2010). Discovery of early Mesoarchean crust in the eastern Gawler Craton, South Australia. *Precambrian Research, 179*(1-4), 1-21. doi:10.1016/j.precamres.2010.02.008

Fraser, G., Reid, A., & Stern, R. (2012). Timing of deformation and exhumation across the Karari Shear Zone, north-western Gawler Craton, South Australia. *Australian Journal of Earth Sciences, 59*(4), 547-570. doi:10.1080/08120099.2012.678586

Fraser, G. L., & Lyons, P. (2006). Timing of Mesoproterozoic tectonic activity in the northwestern Gawler Craton constrained by 40Ar/39Ar geochronology. *Precambrian Research, 151*(3-4), 160-184. doi:10.1016/j.precamres.2006.08.007

Giles, D., Betts, P. G., & Lister, G. S. (2004). 1.8–1.5-Ga links between the North and South Australian Cratons and the Early–Middle Proterozoic configuration of Australia. *Tectonophysics, 380*(1), 27-41. doi:https://doi.org/10.1016/j.tecto.2003.11.010

Halpin, J. A., & Reid, A. J. (2016). Earliest Paleoproterozoic high-grade metamorphism and orogenesis in the Gawler Craton, South Australia: The southern cousin in the Rae family? *Precambrian Research, 276*, 123-144. doi:https://doi.org/10.1016/j.precamres.2016.02.001

Hand, M., Reid, A., & Jagodzinski, L. (2007). Tectonic framework and evolution of the Gawler craton, southern Australia. *Economic Geology, 102*(8), 1377-1395. doi:DOI 10.2113/gsecongeo.102.8.1377

Holland, T., & Powell, R. (2003). Activity–composition relations for phases in petrological calculations: an asymmetric multicomponent formulation. *Contributions to Mineralogy and Petrology, 145*(4), 492-501. doi:10.1007/s00410-003-0464-z

Holland, T. J. B., & Powell, R. (1998). An internally consistent thermodynamic data set for phases of petrological interest. *Journal of Metamorphic Geology, 16*(3), 309-343. doi:https://doi.org/10.1111/j.1525-1314.1998.00140.x

Holland, T. J. B., & Powell, R. (2011). An improved and extended internally consistent thermodynamic dataset for phases of petrological interest, involving a new equation of state for solids. *Journal of Metamorphic Geology, 29*(3), 333-383. doi:https://doi.org/10.1111/j.1525-1314.2010.00923.x

Horstwood, M. S. A., Košler, J., Gehrels, G., Jackson, S. E., McLean, N. M., Paton, C., . . . Schoene, B. (2016). Community-Derived Standards for LA-ICP-MS U-(Th-)Pb Geochronology – Uncertainty Propagation, Age Interpretation and Data Reporting. *Geostandards and Geoanalytical Research, 40*(3), 311-332. doi:https://doi.org/10.1111/j.1751-908X.2016.00379.x

Howard, K., Hand, M., Barovich, K., & Belousova, E. (2011). Provenance of late Paleoproterozoic cover sequences in the central Gawler Craton: exploring stratigraphic correlations in eastern Proterozoic Australia using detrital zircon ages, Hf and Nd isotopic data. *Australian Journal of Earth Sciences, 58*(5), 475-500.

Howard, K. E., Hand, M., Barovich, K. M., Payne, J. L., Cutts, K. A., & Belousova, E. A. (2011). U–Pb zircon, zircon Hf and whole-rock Sm–Nd isotopic constraints on the evolution of Paleoproterozoic rocks in the northern Gawler Craton. *Australian Journal of Earth Sciences, 58*(6), 615-638. doi:10.1080/08120099.2011.594905

Jagodzinski, E., Reid, A., Chalmers, N., Swain, G., Frew, R., & Foudoulis, C. (2007). *Compilation of SHRIMP U-Pb geochronological data for the Gawler Craton, South Australia, 2007*. Retrieved from

Jagodzinski, E. A., Reid, A. J., Crowley, J. L., Wade, C. E., & Curtis, S. (2023). Precise zircon U-Pb dating of the Mesoproterozoic Gawler large igneous province, South Australia. *Results in Geochemistry, 10*, 100020. doi:https://doi.org/10.1016/j.ringeo.2022.100020

Janots, E., Engi, M., Berger, A., Allaz, J., Schwarz, J. O., & Spandler, C. (2008). Prograde metamorphic sequence of REE minerals in pelitic rocks of the Central Alps: implications for allanite–monazite–xenotime phase relations from 250 to 610 °C. *Journal of Metamorphic Geology, 26*(5), 509-526. doi:https://doi.org/10.1111/j.1525-1314.2008.00774.x

Kelly, E. D., Carlson, W. D., & Connelly, J. N. (2011). Implications of garnet resorption for the Lu–Hf garnet geochronometer: an example from the contact aureole of the Makhavinekh Lake Pluton, Labrador. *Journal of Metamorphic Geology, 29*(8), 901-916. doi:https://doi.org/10.1111/j.1525-1314.2011.00946.x

Kelsey, D. E., Clark, C., & Hand, M. (2008). Thermobarometric modelling of zircon and monazite growth in melt-bearing systems: examples using model metapelitic and metapsammitic granulites. *Journal of Metamorphic Geology, 26*(2), 199-212. doi:https://doi.org/10.1111/j.1525-1314.2007.00757.x

Kirscher, U., Liu, Y., Li, Z. X., Mitchell, R. N., Pisarevsky, S. A., Denyszyn, S. W., & Nordsvan, A. (2019). Paleomagnetism of the Hart Dolerite (Kimberley, Western Australia) – A two-stage assembly of the supercontinent Nuna? *Precambrian Research, 329*, 170-181. doi:https://doi.org/10.1016/j.precamres.2018.12.026

Kohn, M. J., & Malloy, M. A. (2004). Formation of monazite via prograde metamorphic reactions among common silicates: implications for age determinations. *Geochimica et Cosmochimica Acta, 68*(1), 101-113. doi:https://doi.org/10.1016/S0016-7037(03)00258-8

Korchinski, M., Rey, P. F., Mondy, L., Teyssier, C., & Whitney, D. L. (2018). Numerical investigation of deep-crust behavior under lithospheric extension. *Tectonophysics, 726*, 137-146. doi:https://doi.org/10.1016/j.tecto.2017.12.029

Korhonen, F. J., Saito, S., Brown, M., & Siddoway, C. S. (2010). Modeling multiple melt loss events in the evolution of an active continental margin. *Lithos, 116*(3), 230-248. doi:https://doi.org/10.1016/j.lithos.2009.09.004

Korsch, R., Blewett, R., Giles, D., Reid, A., Neumann, N., Fraser, G., . . . Kennett, B. (2010). *Geological interpretation of the deep seismic reflection and magnetotelluric line 08GA-OM1: Gawler craton-officer basin-musgrave province-Amadeus basin (GOMA), south Australia and northern territory.* Paper presented at the GOMA (Gawler Craton-Officer Basin-Musgrave Province-Amadeus Basin) Seismic and MT Workshop.

Ludwig, K. (2012). Isoplot 4.15: a geochronological toolkit for Microsoft Excel. In: Berkeley Geochronological Center.

Maidment, D. W. (2005). *Palaeozoic high-grade metamorphism within the Centralian Superbasin, Harts Range region, central Australia.* (PhD), Australian National University,

Morrissey, L., Hand, M., Wade, B., & Szpunar, M. (2013). Early Mesoproterozoic metamorphism in the Barossa Complex, South Australia: links with the eastern margin of Proterozoic Australia. *Australian Journal of Earth Sciences, 60*(8), 769-795.

Morrissey, L. J., Hand, M., Lane, K., Kelsey, D. E., & Dutch, R. A. (2016). Upgrading iron-ore deposits by melt loss during granulite facies metamorphism. Ore Geology Reviews, 74, 101-121. https://doi.org/https://doi.org/10.1016/j.oregeorev.2015.11.012

Morrissey, L. J., Barovich, K. M., Hand, M., Howard, K. E., & Payne, J. L. (2019). Magmatism and metamorphism at ca. 1.45 Ga in the northern Gawler Craton: The Australian record of rifting within Nuna (Columbia). *Geoscience Frontiers*, 175-194. doi:10.1016/j.gsf.2018.07.006

Morrissey, L. J., Card, C. D., & Reid, A. J. (2022). Pressure–temperature–time constraints on metamorphism in the southeastern Taltson Domain, Saskatchewan, Canada. Precambrian Research, 373, 106643. https://doi.org/https://doi.org/10.1016/j.precamres.2022.106643

Morrissey, L. J., Payne, J., Hand, M., Clark, C., & Janicki, M. (2023). One billion years of tectonism at the Paleoproterozoic interface of North and South Australia. *Precambrian Research*, under review.

Nebel, O., Morel, M. L., & Vroon, P. Z. (2009). Isotope dilution determinations of Lu, Hf, Zr, Ta and W, and Hf isotope compositions of NIST SRM 610 and 612 glass wafers.

Geostandards and Geoanalytical Research, 33(4), 487-499.

Norris, A., & Danyushevsky, L. (2018). Towards estimating the complete uncertainty budget of quantified results measured by LA-ICP-MS. *Goldschmidt: Boston, MA, USA*.

Oliver, R., & Fanning, C. (1997). *Australia and Antarctica: precise correlation of Palaeoproterozoic terrains*. Retrieved from Siena:

Pankhurst, M. J., Schaefer, B. F., Betts, P. G., Phillips, N., & Hand, M. (2011). A Mesoproterozoic continental flood rhyolite province, the Gawler Ranges, Australia: the end member example of the Large Igneous Province clan. *Solid Earth, 2*(1), 25-33. doi:10.5194/se-2-25-2011

Paton, C., Hellstrom, J., Paul, B., Woodhead, J., & Hergt, J. (2011). Iolite: Freeware for the visualisation and processing of mass spectrometric data. *Journal of Analytical Atomic Spectrometry, 26*(12), 2508-2518.

Payne, J. L., Barovich, K. M., & Hand, M. (2006). Provenance of metasedimentary rocks in the northern Gawler Craton, Australia: Implications for Palaeoproterozoic reconstructions. *Precambrian Research, 148*(3-4), 275-291. doi:10.1016/j.precamres.2006.05.002

Payne, J. L., Ferris, G., Barovich, K. M., & Hand, M. (2010). Pitfalls of classifying ancient magmatic suites with tectonic discrimination diagrams: An example from the Paleoproterozoic Tunkillia Suite, southern Australia. *Precambrian Research, 177*(3-4), 227-240.

Payne, J. L., Hand, M., Barovich, K. M., Reid, A., & Evans, D. A. D. (2009). Correlations and reconstruction models for the 2500-1500 Ma evolution of the Mawson Continent. *Geological Society, London, Special Publications, 323*(1), 319-355. doi:10.1144/sp323.16

Payne, J. L., Hand, M., Barovich, K. M., & Wade, B. P. (2008). Temporal constraints on the timing of high-grade metamorphism in the northern Gawler Craton: implications for assembly of the Australian Proterozoic. *Australian Journal of Earth Sciences, 55*(5), 623-640. doi:10.1080/08120090801982595

Pisarevsky, S. A., Elming, S.-Å., Pesonen, L. J., & Li, Z.-X. (2014). Mesoproterozoic paleogeography: Supercontinent and beyond. *Precambrian Research, 244*, 207-225. doi:https://doi.org/10.1016/j.precamres.2013.05.014

Pourteau, A., Smit, M. A., Li, Z.-X., Collins, W. J., Nordsvan, A. R., Volante, S., & Li, J. (2018). 1.6 Ga crustal thickening along the final Nuna suture. *Geology, 46*(11), 959-962.

Powell, R., & Holland, T. (1999). Relating formulations of the thermodynamics of mineral solid solutions; activity modeling of pyroxenes, amphiboles, and micas. *American Mineralogist, 84*(1-2), 1-14. doi:10.2138/am-1999-1-201

Powell, R., White, R. W., Green, E. C. R., Holland, T. J. B., & Diener, J. F. A. (2014). On parameterizing thermodynamic descriptions of minerals for petrological calculations. *Journal of Metamorphic Geology, 32*(3), 245-260. doi:https://doi.org/10.1111/jmg.12070

Preiss, W. (2000). The Adelaide Geosyncline of South Australia and its significance in Neoproterozoic continental reconstruction. *Precambrian Research, 100*(1-3), 21-63.

Reid, A., & Forster, M. (2021). Mesoproterozoic thermal evolution of the northern Gawler Craton from 40Ar/39Ar geochronology. *Precambrian Research, 358*, 106180.

Reid, A., Pawley, M., Wade, C., Jagodzinski, E., Dutch, R., & Armstrong, R. (2020). Resolving tectonic settings of ancient magmatic suites using structural, geochemical and isotopic constraints: the example of the St Peter Suite, southern Australia. *Australian Journal of Earth Sciences, 67*(1), 31-58.

Reid, A. J., Halpin, J. A., & Dutch, R. A. (2019). Timing and style of high-temperature metamorphism across the Western Gawler Craton during the Paleo- to Mesoproterozoic. *Australian Journal of Earth Sciences, 66*(8), 1085-1111. doi:10.1080/08120099.2019.1602565

Reid, A. J., & Hand, M. (2012). Mesoarchean to Mesoproterozoic evolution of the southern Gawler Craton, South Australia. *Episodes, 35*(1), 216-225.

Reid, A. J., Jagodzinski, E. A., Armit, R. J., Dutch, R. A., Kirkland, C. L., Betts, P. G., & Schaefer, B. F. (2014). U-Pb and Hf isotopic evidence for Neoarchean and Paleoproterozoic basement in the buried northern Gawler Craton, South Australia. *Precambrian Research, 250*, 127-142. doi:10.1016/j.precamres.2014.05.019

Reid, A. J., Jagodzinski, E. A., Fraser, G. L., & Pawley, M. J. (2014). SHRIMP U–Pb zircon age constraints on the tectonics of the Neoarchean to early Paleoproterozoic transition within the Mulgathing Complex, Gawler Craton, South Australia. *Precambrian Research, 250*, 27-49. doi:https://doi.org/10.1016/j.precamres.2014.05.013

Rey, P. F., Mondy, L., Duclaux, G., Teyssier, C., Whitney, D. L., Bocher, M., & Prigent, C. (2017). The origin of contractional structures in extensional gneiss domes. *Geology, 45*(3), 263-266. doi:10.1130/g38595.1

Rey, P. F., Teyssier, C., Kruckenberg, S. C., & Whitney, D. L. (2011). Viscous collision in channel explains double domes in metamorphic core complexes. *Geology, 39*(4), 387-390. doi:10.1130/g31587.1

Rey, P. F., Teyssier, C., & Whitney, D. L. (2009). Extension rates, crustal melting, and core complex dynamics. *Geology, 37*(5), 391-394. doi:10.1130/g25460a.1

Romer, R. L., & Smeds, S.-A. (1996). U-Pb columbite ages of pegmatites from Sveconorwegian terranes in southwestern Sweden. *Precambrian Research, 76*(1), 15-30. doi:https://doi.org/10.1016/0301-9268(95)00023-2

Scherer, E. E., Cameron, K. L., & Blichert-Toft, J. (2000). Lu–Hf garnet geochronology: closure temperature relative to the Sm–Nd system and the effects of trace mineral inclusions. *Geochimica et Cosmochimica Acta, 64*(19), 3413-3432. doi:https://doi.org/10.1016/S0016-7037(00)00440-3

Simpson, A., Gilbert, S., Tamblyn, R., Hand, M., Spandler, C., Gillespie, J., . . . Glorie, S. (2021). In-situ Lu Hf geochronology of garnet, apatite and xenotime by LA ICP MS/MS. *Chemical Geology, 577*. doi:10.1016/j.chemgeo.2021.120299

Simpson, A., Glorie, S., Hand, M., Spandler, C., Gilbert, S., & Cave, B. (2022). In situ Lu–Hf geochronology of calcite. *Geochronology, 4*(1), 353-372. doi:10.5194/gchron-4-353-2022

Skirrow, R. G., Bastrakov, E. N., Baroncii, K., Fraser, G. L., Creaser, R. A., Fanning, C. M., . . . Davidson, G. J. (2007). Timing of iron oxide Cu-Au-(U) hydrothermal activity and Nd isotope constraints on metal sources in the Gawler craton, south Australia. *Economic Geology, 102*(8), 1441-1470. doi:DOI 10.2113/gsecongeo.102.8.1441

Söderlund, U., Patchett, P. J., Vervoort, J. D., & Isachsen, C. E. (2004). The 176Lu decay constant determined by Lu–Hf and U–Pb isotope systematics of Precambrian mafic intrusions. *Earth and Planetary Science Letters, 219*(3-4), 311-324.

Spear, F. S. (2010). Monazite–allanite phase relations in metapelites. *Chemical Geology, 279*(1), 55-62. doi:https://doi.org/10.1016/j.chemgeo.2010.10.004

Spear, F. S., & Pyle, J. M. (2010). Theoretical modeling of monazite growth in a low-Ca metapelite. *Journal of Metamorphic Geology, 273*(1-2), 111-119.

Spencer, C. J., Kirkland, C. L., Roberts, N. M. W., Evans, N. J., & Liebmann, J. (2020). Strategies towards robust interpretations of in situ zircon Lu–Hf isotope analyses. *Geoscience Frontiers, 11*(3), 843-853. doi:https://doi.org/10.1016/j.gsf.2019.09.004

Stewart, K., & Foden, J. (2003). Mesoproterozoic granites of South Australia. *South Australia Department of Primary Industries and Resources, Report Book, 2003*, 15.

Swain, G., Barovich, K., Hand, M., Ferris, G., & Schwarz, M. (2008). Petrogenesis of the St Peter Suite, southern Australia: Arc magmatism and Proterozoic crustal growth of the South Australian Craton. *Precambrian Research, 166*(1-4), 283-296. doi:10.1016/j.precamres.2007.07.028

Szpunar, M., Hand, M., Barovich, K., Jagodzinski, E., & Belousova, E. (2011). Isotopic and geochemical constraints on the Paleoproterozoic Hutchison Group, southern Australia: Implications for Paleoproterozoic continental reconstructions. *Precambrian Research, 187*(1-2), 99-126.

Tamblyn, R., Hand, M., Simpson, A., Gilbert, S., Wade, B., & Glorie, S. (2022). In situ laser ablation Lu–Hf geochronology of garnet across the Western Gneiss Region: campaign-style dating of metamorphism. *Journal of the Geological Society, 179*(4), jgs2021-2094. doi:10.1144/jgs2021-094

Teyssier, C., & Whitney, D. L. (2002). Gneiss domes and orogeny. *Geology, 30*(12), 1139-1142. doi:10.1130/0091-7613(2002)030<1139:Gdao>2.0.Co;2

Tiddy, C. J., Betts, P. G., Neumann, M. R., Murphy, F. C., Stewart, J., Giles, D., . . .

Jourdan, F. (2020). Interpretation of a ca. 1600–1580 Ma metamorphic core complex in the northern Gawler Craton, Australia. *Gondwana Research, 85*, 263-290. doi:10.1016/j.gr.2020.04.008

Tomkins, H., Williams, I., & Ellis, D. (2005). In situ U–Pb dating of zircon formed from retrograde garnet breakdown during decompression in Rogaland, SW Norway. *Journal of Metamorphic Geology, 23*(4), 201-215.

Varga, J., Raimondo, T., Hand, M., Curtis, S., & Daczko, N. (2022). Hydration, melt production and rheological weakening within an intracontinental gneiss dome. *Lithos, 432-433*, 106872. doi:https://doi.org/10.1016/j.lithos.2022.106872

Vermeesch, P. (2018). IsoplotR: A free and open toolbox for geochronology. *Geoscience Frontiers, 9*(5), 1479-1493.

Volante, S., Pourteau, A., Collins, W. J., Blereau, E., Li, Z.-X., Smit, M., . . . Günter, C. (2020). Multiple P–T–d–t paths reveal the evolution of the final Nuna assembly in northeast Australia. *Journal of Metamorphic Geology, 38*(6), 593-627. doi:https://doi.org/10.1111/jmg.12532

Wade, B. P., Barovich, K. M., Hand, M., Scrimgeour, I. R., & Close, D. F. (2006). Evidence for Early Mesoproterozoic Arc Magmatism in the Musgrave Block, Central Australia: Implications for Proterozoic Crustal Growth and Tectonic Reconstructions of Australia. *The Journal of Geology, 114*(1), 43-63. doi:10.1086/498099

Wade, B. P., Kelsey, D. E., Hand, M., & Barovich, K. M. (2008). The Musgrave Province: Stitching north, west and south Australia. *Precambrian Research, 166*(1), 370-386. doi:https://doi.org/10.1016/j.precamres.2007.05.007

Wade, C. E., Payne, J. L., Barovich, K. M., & Reid, A. J. (2019). Heterogeneity of the sub-continental lithospheric mantle and 'non-juvenile' mantle additions to a Proterozoic silicic large igneous province. *Lithos, 340-341*, 87-107. doi:10.1016/j.lithos.2019.05.005

Wade, C. E., Reid, A. J., Wingate, M. T. D., Jagodzinski, E. A., & Barovich, K. (2012). Geochemistry and geochronology of the c. 1585Ma Benagerie Volcanic Suite, southern Australia: Relationship to the Gawler Range Volcanics and implications for the petrogenesis of a Mesoproterozoic silicic large igneous province. *Precambrian Research, 206-207*, 17-35. doi:https://doi.org/10.1016/j.precamres.2012.02.020

White, Powell, Holland, & Worley. (2000). The effect of TiO2 and Fe2O3 on metapelitic assemblages at greenschist and amphibolite facies conditions: mineral equilibria calculations in the system K2O–FeO–MgO–Al2O3–SiO2–H2O–TiO2–Fe2O3. Journal of Metamorphic Geology, 18(5), 497-511. https://doi.org/https://doi.org/10.1046/j.1525-1314.2000.00269.x

White, R. W., Powell, R., & Clarke, G. L. (2002). The interpretation of reaction textures in Fe-rich metapelitic granulites of the Musgrave Block, central Australia: constraints from mineral equilibria calculations in the system K2O–FeO–MgO–Al2O3–SiO2–H2O–TiO2–Fe2O3. *Journal of Metamorphic Geology, 20*(1), 41-55. doi:https://doi.org/10.1046/j.0263-4929.2001.00349.x

White, R. W., Powell, R., & Holland, T. J. B. (2001). Calculation of partial melting equilibria in the system Na2O–CaO–K2O–FeO–MgO–Al2O3–SiO2–H2O (NCKFMASH). *Journal of Metamorphic Geology, 19*(2), 139-153. doi:https://doi.org/10.1046/j.0263-4929.2000.00303.x

White, R. W., Powell, R., & Holland, T. J. B. (2007). Progress relating to calculation of partial melting equilibria for metapelites. *Journal of Metamorphic Geology, 25*(5), 511-527. doi:https://doi.org/10.1111/j.1525-1314.2007.00711.x

White, R. W., Powell, R., Holland, T. J. B., Johnson, T. E., & Green, E. C. R. (2014). New mineral activity–composition relations for thermodynamic calculations in metapelitic systems. *Journal of Metamorphic Geology, 32*(3), 261-286. doi:https://doi.org/10.1111/jmg.12071

White, R. W., Powell, R., & Johnson, T. E. (2014). The effect of Mn on mineral stability in metapelites revisited: new a–x relations for manganese-bearing minerals. *Journal of Metamorphic Geology, 32*(8), 809-828. doi:https://doi.org/10.1111/jmg.12095

Whitney, D. L., & Evans, B. W. (2010). Abbreviations for names of rock-forming minerals. *American Mineralogist, 95*(1), 185-187. doi:10.2138/am.2010.3371

Whitney, D. L., Roger, F., Teyssier, C., Rey, P. F., & Respaut, J. P. (2015). Syn-collapse eclogite metamorphism and exhumation of deep crust in a migmatite dome: The P–T–t record of the youngest Variscan eclogite (Montagne Noire, French Massif Central). *Earth and Planetary Science Letters, 430*, 224-234. doi:https://doi.org/10.1016/j.epsl.2015.08.026

Whitney, D. L., Teyssier, C., & Vanderhaeghe, O. (2004). Gneiss domes and crustal flow. In *Gneiss domes in orogeny* (Vol. 380, pp. 15).

Xiang, H., & Connolly, J. A. D. (2021). GeoPS: An interactive visual computing tool for thermodynamic modelling of phase equilibria. *Journal of Metamorphic Geology, 40*(2), 243-255. doi:https://doi.org/10.1111/jmg.12626

Yakymchuk, C., & Brown, M. (2014). Behaviour of zircon and monazite during crustal melting. *Journal of the Geological Society, 171*(4), 465-479. doi:10.1144/jgs2013-115

Yin, A. (2004). Gneiss domes and gneiss dome systems. *Geological Society of America Special Papers, 380*, 1-14.

Supplementary material

Appendix Tables A1–A3 that accompany this thesis chapter is available on Open Science Framework: https://osf.io/rcm7g/

Appendix 1. Petrology for additional samples from Mabel Creek Ridge.

AM/PB 2

Sample 1686102 (417.8–418 m), has similar petrographic features to sample 1686101, described in the main text. The sample is not strongly foliated at the thin section scale. It comprises biotite + garnet + plagioclase + K-feldspar + quartz + ilmenite and cordierite. Garnet porphyroblasts are commonly euhedral to subhedral, ranging from 2 to 12 mm. They contain inclusions of quartz, ilmenite, minor biotite and monazite. No sillimanite is observed in the matrix or within garnet porphyroblasts. Minor cordierite is observed adjacent to garnet. The peak assemblage in the samples is interpreted to have been biotite + garnet + ilmenite + quartz + K-feldspar + plagioclase + melt, with cordierite forming subsequently. This sample contains narrow cross-cutting sulfide veins.

Sample 1686103 (421.05–421.55 m) shares many petrographic characteristics with sample 1686100B but contains less sillimanite. The sample is weakly foliated. The mineral assemblage in this sample comprises biotite + garnet + ilmenite + K-feldspar + plagioclase + quartz + minor sillimanite. Garnet porphyroblasts range from 1 to 6 mm in size, and contain mineral inclusions of quartz, ilmenite, biotite and monazite. Minor cordierite forms as partial coronas on garnet and sillimanite. The peak mineral assemblage is interpreted to be biotite + garnet + ilmenite + K-feldspar + plagioclase + quartz + sillimanite, with subsequent disappearance of sillimanite and growth of cordierite. The sample contains minor sulfide veins.

Samples 1686105 (428.6–429.1 m) and 1686106 (436.85–437.0 m) have the same mineral assemblage as sample 1686100B, and contain biotite + garnet + ilmenite + K-feldspar + plagioclase + quartz + sillimanite + cordierite. They display a gneissic foliation defined by elongate sillimanite and biotite and quartzofeldspathic leucosomes. Euhedral garnet porphyroblasts range from 1 to 8 mm in diameter, and contain inclusions of sillimanite, quartz, biotite and ilmenite. Minor cordierite occurs at the margins of garnet and surrounds sillimanite. Both samples have interpreted peak mineral assemblages of biotite + garnet + ilmenite + K-feldspar + plagioclase + quartz + sillimanite + melt, with subsequent growth of minor cordierite.

AMPB 3

Sample 650713 (220.7–221.1 m) shares a similar mineral assemblage to sample 650719, but with less apatite. It contains garnet + biotite + plagioclase + quartz + ilmenite + magnetite + minor apatite and monazite. The garnet poikiloblasts are anhedral, ranging 1–4 mm and contain inclusions of quartz, apatite, and biotite.

G3 DDH1

Sample 1689840 (342.0–342.25 m) contains biotite, garnet, K-feldspar, plagioclase, quartz, ilmenite, minor sillimanite and cordierite. The sample is migmatitic and exhibits a 1–2.5 cm wide leucosome in the thin section. The leucosome is mainly composed of garnet, quartz, plagioclase, and minor K-feldspar. The garnet in the leucosome contains rare quartz inclusions. The melanosome domains contain biotite + garnet + K-feldspar + plagioclase + quartz + ilmenite. Garnet porphyroblasts in the melanosome contain abundant inclusions of quartz, biotite, and sillimanite. Garnet grains are fractured, with the fractures filled by biotite or cordierite. Sillimanite does not occur in the matrix. The sample has an interpreted peak mineral assemblage of biotite + garnet + ilmenite + K-feldspar + plagioclase + quartz + melt.

Sample 1689859 (335.75–335.95 m) has similar petrographic features to sample 1689840, described above. It contains biotite, garnet, ilmenite, K-feldspar, plagioclase and quartz. Euhedral garnet porphyroblasts are up to 15 mm in size and contain inclusions of biotite, quartz and ilmenite. The thin section contains a 1 cm wide leucosome, consisting of garnet, quartz, plagioclase, K-feldspar and biotite. Some biotite and plagioclase grains are now altered to clay minerals. The sample has an interpreted peak mineral assemblage of biotite + garnet + ilmenite + K-feldspar + plagioclase + quartz + melt.

Sample 1689842 (343.32–343.52 m) has a mineral assemblage of garnet, biotite, plagioclase, K-feldspar, quartz and ilmenite, similar to samples 1689840 and 1689859. Sample 1689834 (264.40–264.55 m) shares the same mineral assemblage as sample 1689838 (278.40–278.55 m).

Appendix Figure 1. *T–M$_{H2O}$* and *T–M$_O$* modeling for samples from Mabel Creek Ridge and drill hole GOMA DH4.

AM/PB 2 P=6.9 kbar

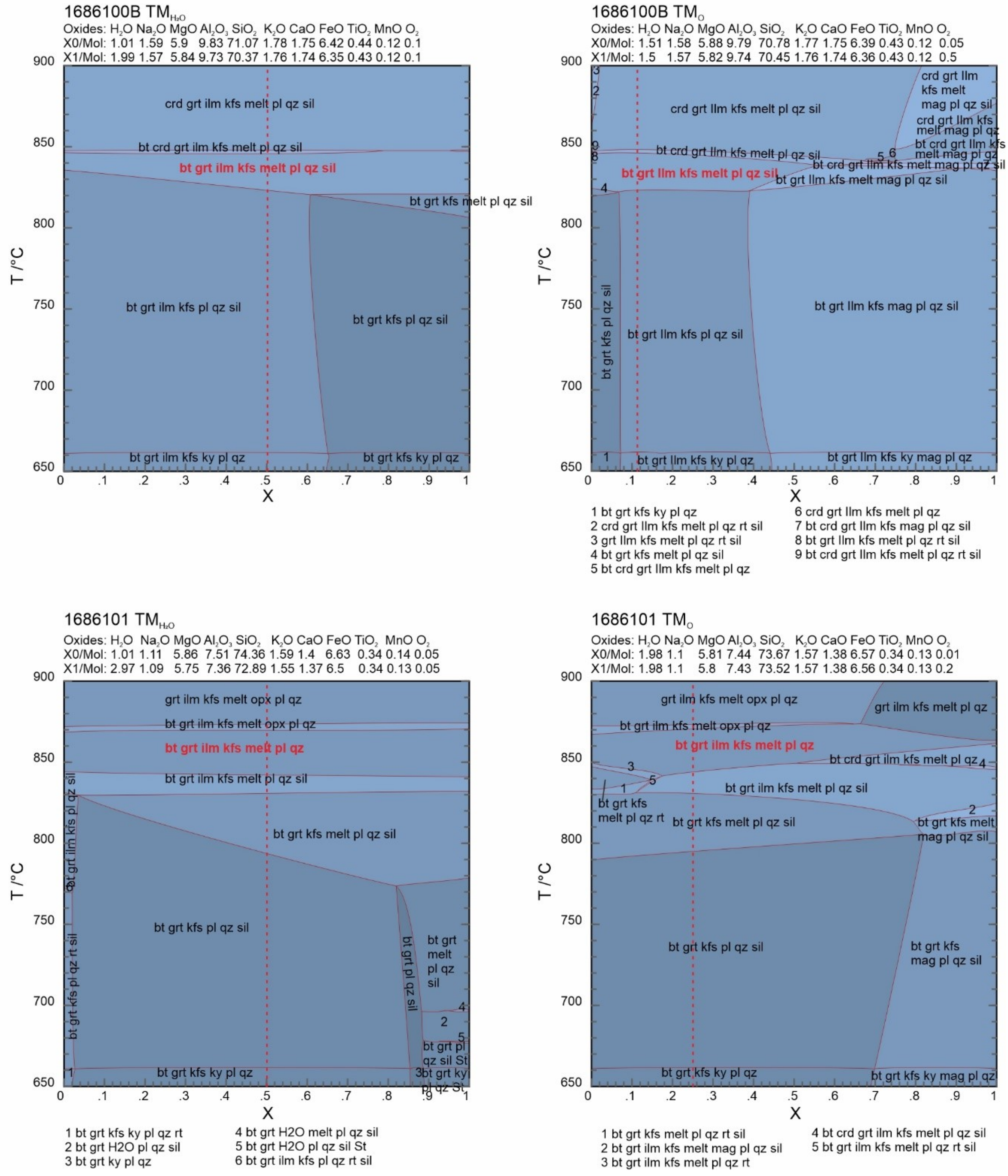

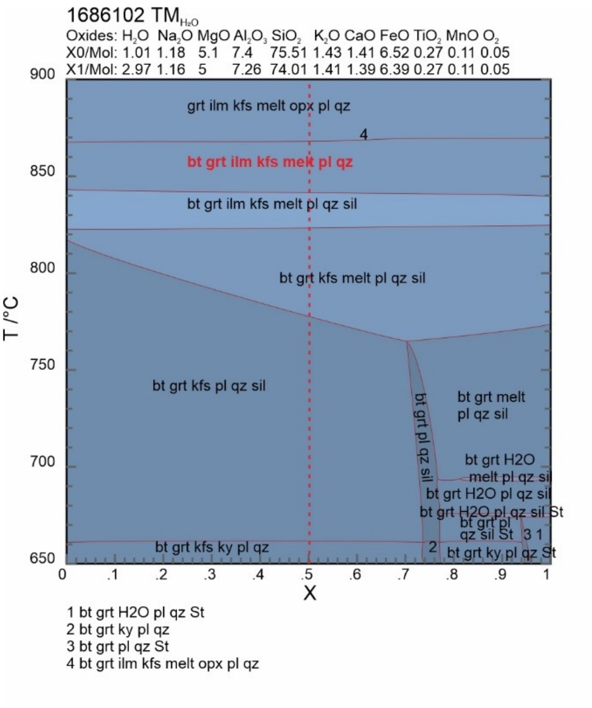
1686102 TM$_{H_2O}$
Oxides: H_2O Na_2O MgO Al_2O_3 SiO_2 K_2O CaO FeO TiO_2 MnO O_2
X0/Mol: 1.01 1.18 5.1 7.4 75.51 1.43 1.41 6.52 0.27 0.11 0.05
X1/Mol: 2.97 1.16 5 7.26 74.01 1.41 1.39 6.39 0.27 0.11 0.05
grt ilm kfs melt opx pl qz
bt grt ilm kfs melt pl qz
bt grt ilm kfs melt pl qz sil
bt grt kfs melt pl qz sil
bt grt kfs pl qz sil
bt grt melt pl qz sil
bt grt pl qz sil
bt grt H2O melt pl qz sil
bt grt H2O pl qz sil
bt grt H2O pl qz sil St
bt grt pl qz sil St
bt grt kfs ky pl qz
bt grt ky pl qz St
T /°C
X
1 bt grt H2O pl qz St
2 bt grt ky pl qz
3 bt grt pl qz St
4 bt grt ilm kfs melt opx pl qz

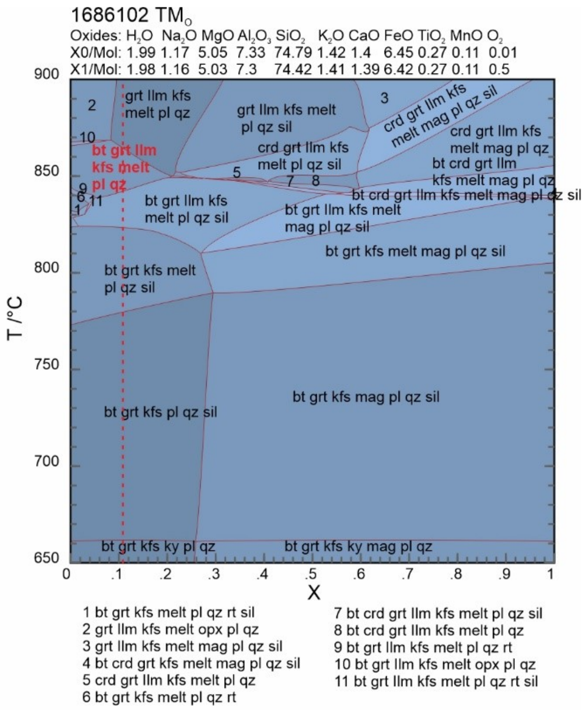
1686102 TM$_O$
Oxides: H_2O Na_2O MgO Al_2O_3 SiO_2 K_2O CaO FeO TiO_2 MnO O_2
X0/Mol: 1.99 1.17 5.05 7.33 74.79 1.42 1.4 6.45 0.27 0.11 0.01
X1/Mol: 1.98 1.16 5.03 7.3 74.42 1.41 1.39 6.42 0.27 0.11 0.5
grt Ilm kfs melt pl qz
grt Ilm kfs melt pl qz sil
crd grt Ilm kfs melt mag pl qz sil
crd grt Ilm kfs melt mag pl qz
crd grt Ilm kfs melt pl qz sil
bt crd grt Ilm kfs melt mag pl qz
bt grt Ilm kfs melt pl qz
bt crd grt Ilm kfs melt mag pl qz sil
bt grt Ilm kfs melt pl qz sil
bt grt Ilm kfs melt mag pl qz sil
bt grt kfs melt mag pl qz sil
bt grt kfs melt pl qz sil
bt grt kfs pl qz sil
bt grt kfs mag pl qz sil
bt grt kfs ky pl qz
bt grt kfs ky mag pl qz
T /°C
X
1 bt grt kfs melt pl qz rt sil
2 grt Ilm kfs melt opx pl qz
3 grt Ilm kfs melt mag pl qz sil
4 bt crd grt kfs melt mag pl qz sil
5 crd grt Ilm kfs melt pl qz
6 bt grt kfs melt pl qz rt
7 bt crd grt Ilm kfs melt pl qz sil
8 bt crd grt Ilm kfs melt pl qz
9 bt grt Ilm kfs melt pl qz rt
10 bt grt Ilm kfs melt opx pl qz
11 bt grt Ilm kfs melt pl qz rt sil

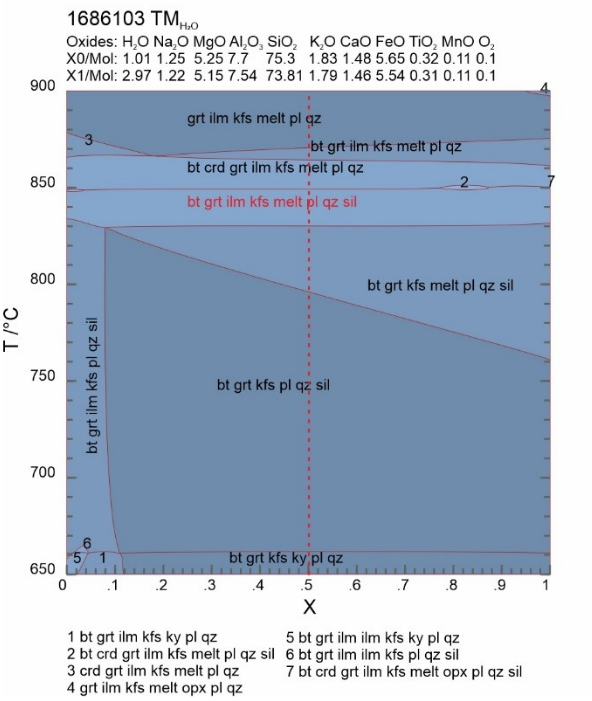
1686103 TM$_{H_2O}$
Oxides: H_2O Na_2O MgO Al_2O_3 SiO_2 K_2O CaO FeO TiO_2 MnO O_2
X0/Mol: 1.01 1.25 5.25 7.7 75.3 1.83 1.48 5.65 0.32 0.11 0.1
X1/Mol: 2.97 1.22 5.15 7.54 73.81 1.79 1.46 5.54 0.31 0.11 0.1
grt ilm kfs melt pl qz
bt grt ilm kfs melt pl qz
bt crd grt ilm kfs melt pl qz
bt grt ilm kfs melt pl qz sil
bt grt kfs melt pl qz sil
bt grt kfs pl qz sil
bt grt ilm kfs pl qz sil
bt grt kfs ky pl qz
T /°C
X
1 bt grt ilm kfs ky pl qz
2 bt crd grt ilm kfs melt pl qz sil
3 crd grt ilm kfs melt pl qz
4 grt ilm kfs melt opx pl qz
5 bt grt ilm ilm kfs ky pl qz
6 bt grt ilm ilm kfs pl qz sil
7 bt crd grt ilm kfs melt opx pl qz sil

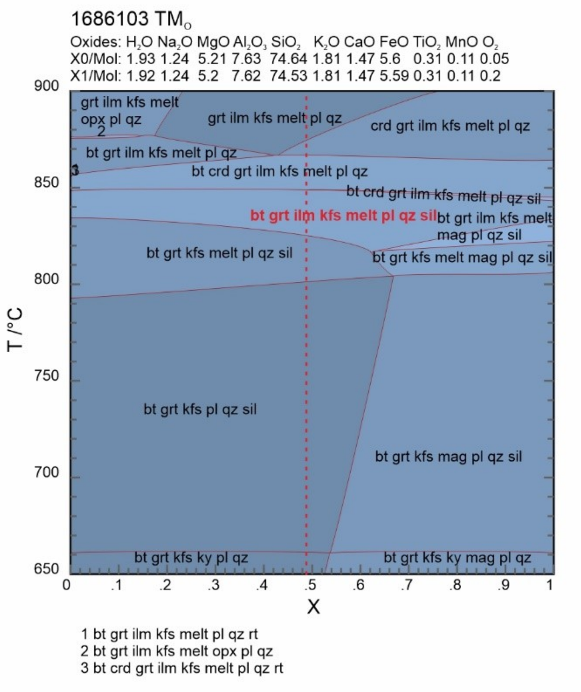
1686103 TM$_O$
Oxides: H_2O Na_2O MgO Al_2O_3 SiO_2 K_2O CaO FeO TiO_2 MnO O_2
X0/Mol: 1.93 1.24 5.21 7.63 74.64 1.81 1.47 5.6 0.31 0.11 0.05
X1/Mol: 1.92 1.24 5.2 7.62 74.53 1.81 1.47 5.59 0.31 0.11 0.2
grt ilm kfs melt opx pl qz
grt ilm kfs melt pl qz
crd grt ilm kfs melt pl qz
bt grt ilm kfs melt pl qz
bt crd grt ilm kfs melt pl qz
bt crd grt ilm kfs melt pl qz sil
bt grt ilm kfs melt pl qz sil
bt grt ilm kfs melt mag pl qz sil
bt grt kfs melt pl qz sil
bt grt kfs melt mag pl qz sil
bt grt kfs pl qz sil
bt grt kfs mag pl qz sil
bt grt kfs ky pl qz
bt grt kfs ky mag pl qz
T /°C
X
1 bt grt ilm kfs melt pl qz rt
2 bt grt ilm kfs melt opx pl qz
3 bt crd grt ilm kfs melt pl qz rt

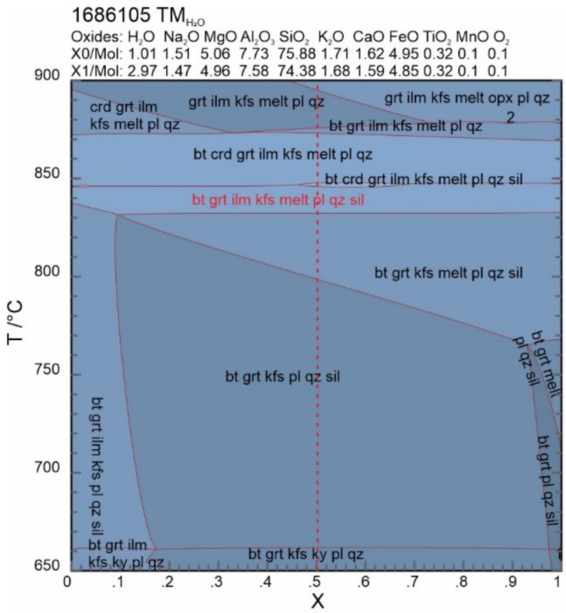

1 bt grt ky pl qz
2 bt grt ilm kfs melt opx pl qz

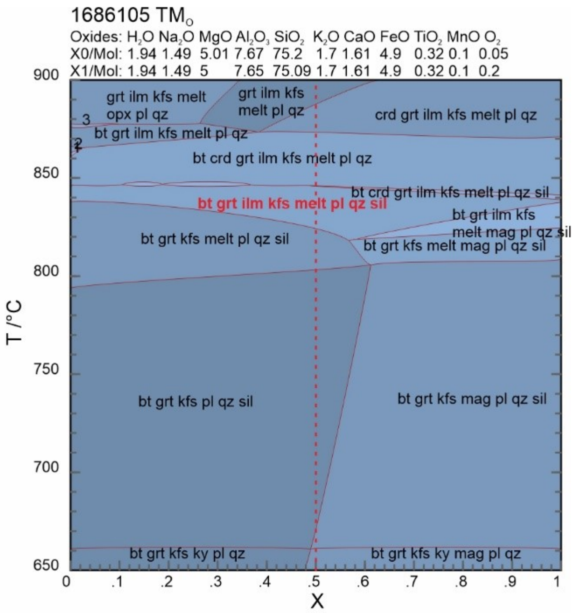

1 bt crd grt ilm kfs melt pl qz rt
2 bt grt ilm kfs melt pl qz rt
3 bt grt ilm kfs melt opx pl qz

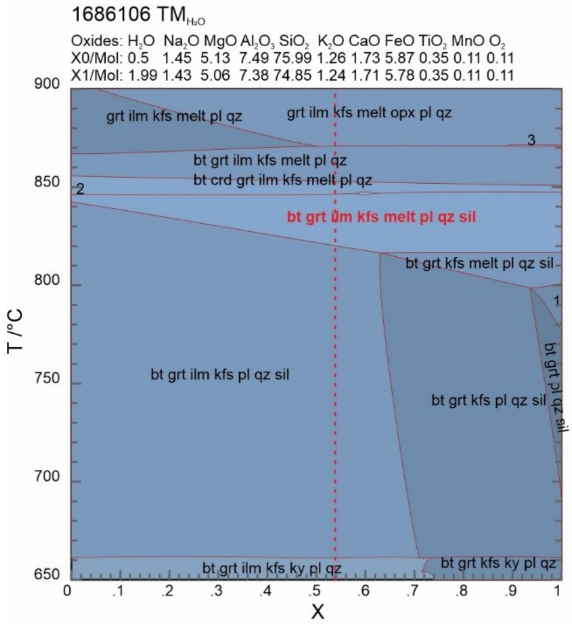

1 bt grt melt pl qz sil
2 bt crd grt ilm kfs melt pl qz sil
3 bt grt ilm kfs melt opx pl qz

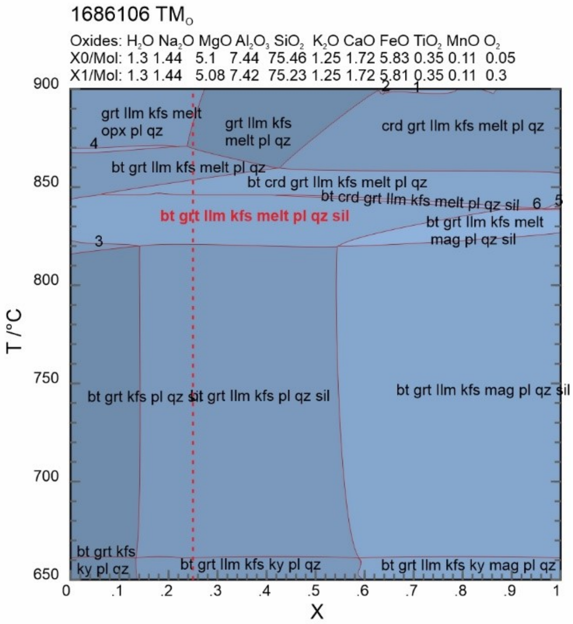

1 crd grt Ilm kfs melt pl qz sil
2 grt Ilm kfs melt pl qz sil
3 bt grt kfs melt pl qz sil
4 bt grt Ilm kfs melt opx pl qz
5 bt crd grt Ilm kfs melt mag pl qz
6 bt crd grt Ilm kfs melt mag pl qz sil

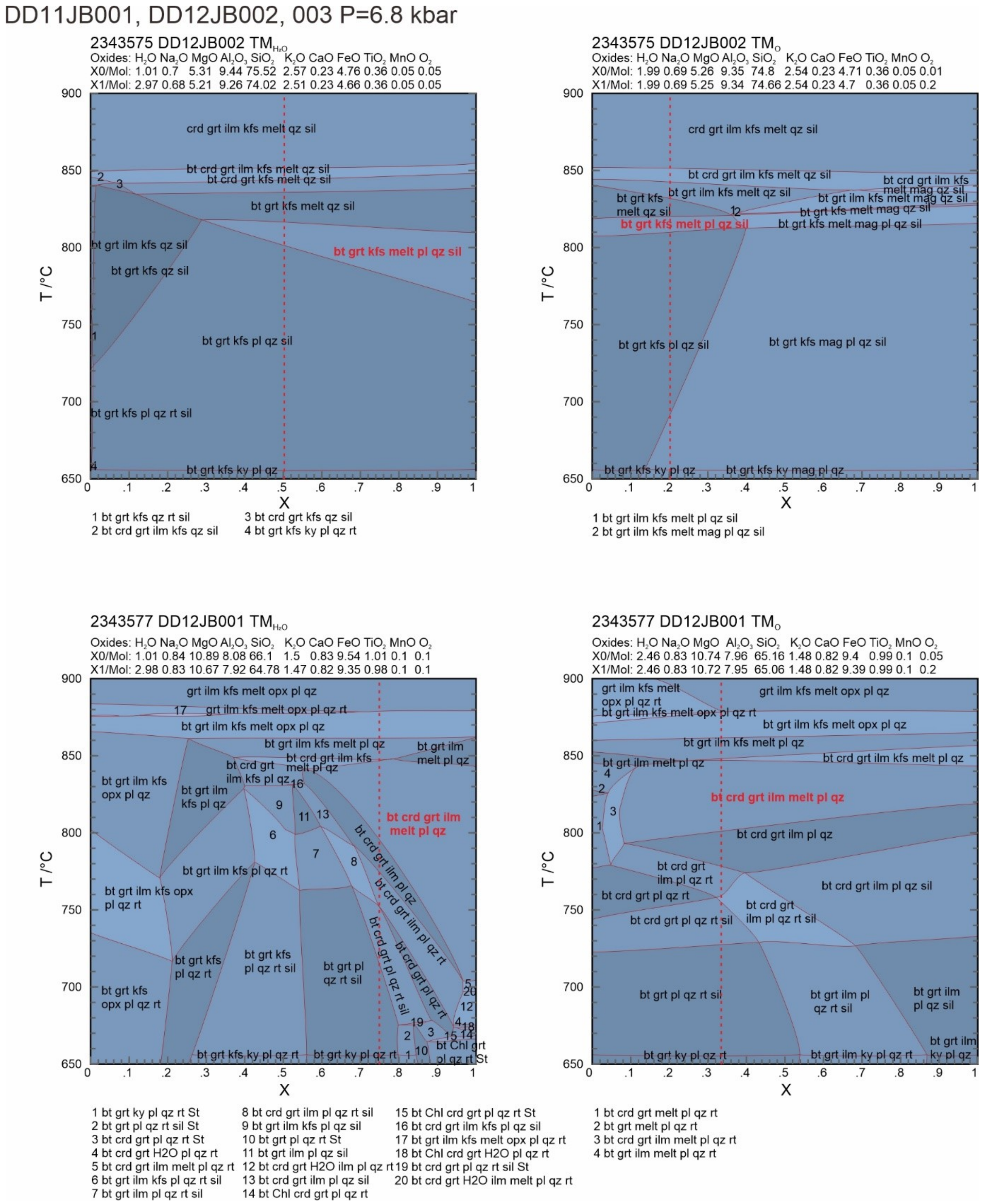
DD11JB001, DD12JB002, 003 P=6.8 kbar
2343575 DD12JB002 TMH₂O
Oxides: H2O Na2O MgO Al2O3 SiO2 K2O CaO FeO TiO2 MnO O2
X0/Mol: 1.01 0.7 5.31 9.44 75.52 2.57 0.23 4.76 0.36 0.05 0.05
X1/Mol: 2.97 0.68 5.21 9.26 74.02 2.51 0.23 4.66 0.36 0.05 0.05
crd grt ilm kfs melt qz sil
bt crd grt ilm kfs melt qz sil
bt crd grt kfs melt qz sil
bt grt kfs melt qz sil
bt grt ilm kfs qz sil
bt grt kfs melt pl qz sil
bt grt kfs qz sil
bt grt kfs pl qz sil
bt grt kfs pl qz rt sil
bt grt kfs ky pl qz
T °C
X
1 bt grt kfs qz rt sil
2 bt crd grt ilm kfs qz sil
3 bt crd grt kfs qz sil
4 bt grt kfs ky pl qz rt
2343575 DD12JB002 TMO
Oxides: H2O Na2O MgO Al2O3 SiO2 K2O CaO FeO TiO2 MnO O2
X0/Mol: 1.99 0.69 5.26 9.35 74.8 2.54 0.23 4.71 0.36 0.05 0.01
X1/Mol: 1.99 0.69 5.25 9.34 74.66 2.54 0.23 4.7 0.36 0.05 0.2
crd grt ilm kfs melt qz sil
bt crd grt ilm kfs melt qz sil
bt crd grt ilm kfs melt mag qz sil
bt grt kfs melt qz sil
bt grt ilm kfs melt qz sil
bt grt ilm kfs melt mag qz sil
bt grt kfs melt mag qz sil
bt grt kfs melt pl qz sil
bt grt kfs melt mag pl qz sil
bt grt kfs pl qz sil
bt grt kfs mag pl qz sil
bt grt kfs ky pl qz
bt grt kfs ky mag pl qz
1 bt grt ilm kfs melt pl qz sil
2 bt grt ilm kfs melt mag pl qz sil
2343577 DD12JB001 TMH₂O
Oxides: H2O Na2O MgO Al2O3 SiO2 K2O CaO FeO TiO2 MnO O2
X0/Mol: 1.01 0.84 10.89 8.08 66.1 1.5 0.83 9.54 1.01 0.1 0.1
X1/Mol: 2.98 0.83 10.67 7.92 64.78 1.47 0.82 9.35 0.98 0.1 0.1
grt ilm kfs melt opx pl qz
grt ilm kfs melt opx pl qz rt
bt grt ilm kfs melt opx pl qz
bt grt ilm kfs melt pl qz
bt crd grt ilm kfs melt pl qz
bt grt ilm melt pl qz
bt crd grt ilm kfs pl qz
bt grt ilm kfs opx pl qz
bt grt ilm kfs pl qz
bt crd grt ilm melt pl qz
bt grt ilm kfs pl qz rt
bt crd grt ilm pl qz
bt crd grt ilm pl qz rt
bt grt ilm kfs opx pl qz rt
bt grt kfs pl qz rt
bt grt kfs pl qz rt sil
bt grt pl qz rt sil
bt crd grt pl qz rt sil
bt crd grt pl qz rt
bt grt kfs opx pl qz rt
bt Chl grt pl qz rt St
bt grt kfs ky pl qz rt
bt grt ky pl qz rt
1 bt grt ky pl qz rt St
2 bt grt pl qz rt sil St
3 bt crd grt pl qz rt St
4 bt crd grt H2O pl qz rt
5 bt crd grt ilm melt pl qz rt
6 bt grt ilm kfs pl qz rt sil
7 bt grt ilm pl qz rt sil
8 bt crd grt ilm pl qz rt sil
9 bt grt ilm kfs pl qz sil
10 bt grt pl qz rt St
11 bt grt ilm pl qz sil
12 bt crd grt H2O ilm pl qz rt
13 bt crd grt ilm pl qz sil
14 bt Chl crd grt pl qz rt
15 bt Chl crd grt pl qz rt St
16 bt crd grt ilm kfs pl qz sil
17 bt grt ilm kfs melt opx pl qz rt
18 bt Chl crd grt H2O pl qz rt
19 bt crd grt pl qz rt sil St
20 bt crd grt H2O ilm melt pl qz rt
2343577 DD12JB001 TMO
Oxides: H2O Na2O MgO Al2O3 SiO2 K2O CaO FeO TiO2 MnO O2
X0/Mol: 2.46 0.83 10.74 7.96 65.16 1.48 0.82 9.4 0.99 0.1 0.05
X1/Mol: 2.46 0.83 10.72 7.95 65.06 1.48 0.82 9.39 0.99 0.1 0.2
grt ilm kfs melt opx pl qz rt
grt ilm kfs melt opx pl qz
bt grt ilm kfs melt opx pl qz rt
bt grt ilm kfs melt opx pl qz
bt grt ilm kfs melt pl qz
bt grt ilm melt pl qz
bt crd grt ilm kfs melt pl qz
bt crd grt ilm melt pl qz
bt crd grt ilm pl qz
bt crd grt ilm pl qz rt
bt crd grt pl qz rt
bt crd grt ilm pl qz sil
bt crd grt pl qz rt sil
bt crd grt ilm pl qz rt sil
bt grt pl qz rt sil
bt grt ilm pl qz rt sil
bt grt ilm pl qz sil
bt grt ky pl qz rt
bt grt ilm ky pl qz rt
bt grt ilm ky pl qz
1 bt crd grt melt pl qz rt
2 bt grt melt pl qz rt
3 bt crd grt ilm melt pl qz rt
4 bt grt ilm melt pl qz rt

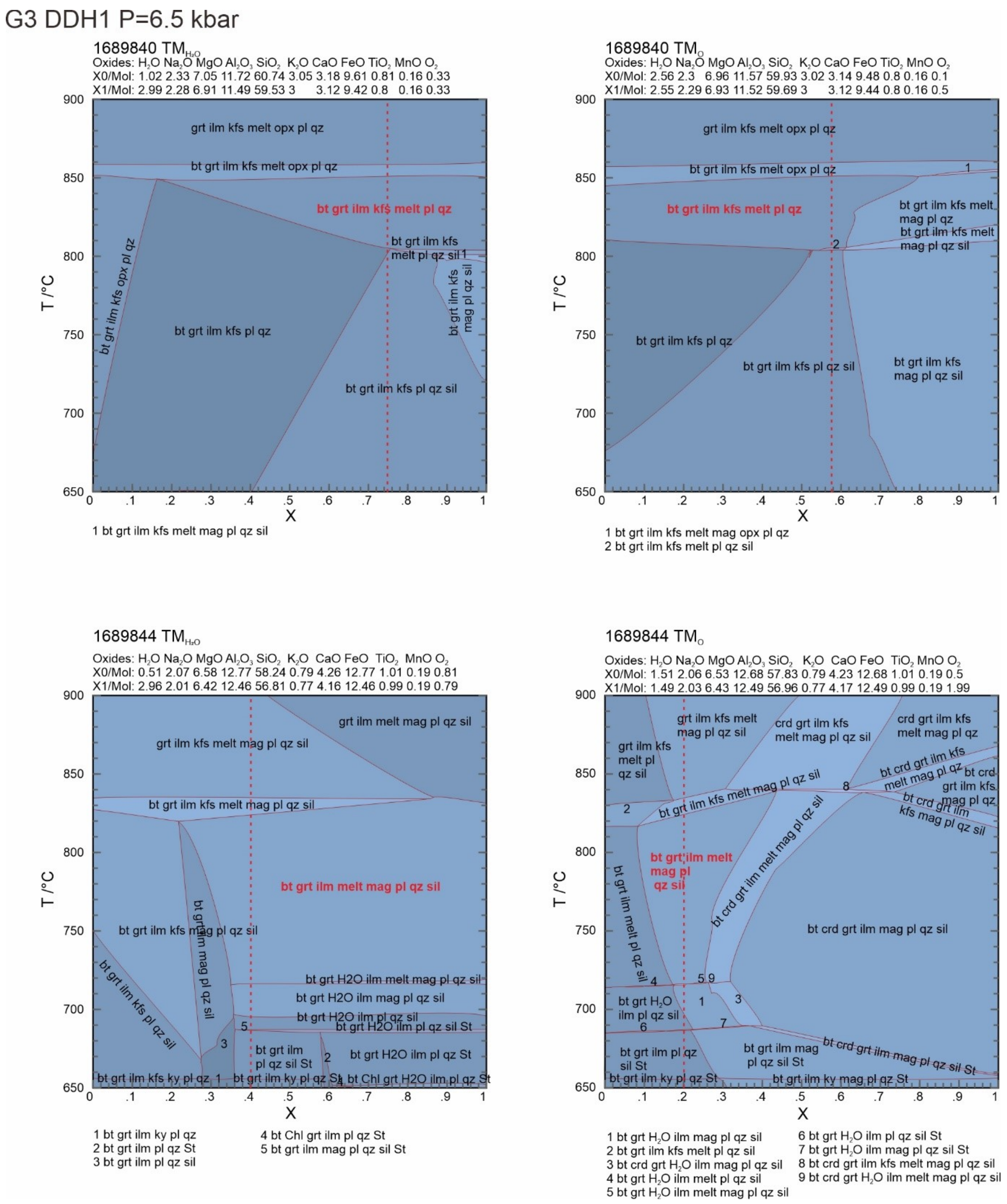
G3 DDH1 P=6.5 kbar
1689840 TM_{H_2O}
Oxides: H_2O Na_2O MgO Al_2O_3 SiO_2 K_2O CaO FeO TiO_2 MnO O_2
X0/Mol: 1.02 2.33 7.05 11.72 60.74 3.05 3.18 9.61 0.81 0.16 0.33
X1/Mol: 2.99 2.28 6.91 11.49 59.53 3 3.12 9.42 0.8 0.16 0.33
grt ilm kfs melt opx pl qz
bt grt ilm kfs melt opx pl qz
bt grt ilm kfs melt pl qz
bt grt ilm kfs melt pl qz sil
bt grt ilm kfs opx pl qz
bt grt ilm kfs pl qz
bt grt ilm kfs mag pl qz sil
bt grt ilm kfs pl qz sil
T /°C
X
1 bt grt ilm kfs melt mag pl qz sil
1689840 TM_O
Oxides: H_2O Na_2O MgO Al_2O_3 SiO_2 K_2O CaO FeO TiO_2 MnO O_2
X0/Mol: 2.56 2.3 6.96 11.57 59.93 3.02 3.14 9.48 0.8 0.16 0.1
X1/Mol: 2.55 2.29 6.93 11.52 59.69 3 3.12 9.44 0.8 0.16 0.5
grt ilm kfs melt opx pl qz
bt grt ilm kfs melt opx pl qz
bt grt ilm kfs melt pl qz
bt grt ilm kfs melt mag pl qz
bt grt ilm kfs melt mag pl qz sil
bt grt ilm kfs pl qz
bt grt ilm kfs pl qz sil
bt grt ilm kfs mag pl qz sil
1 bt grt ilm kfs melt mag opx pl qz
2 bt grt ilm kfs melt pl qz sil
1689844 TM_{H_2O}
Oxides: H_2O Na_2O MgO Al_2O_3 SiO_2 K_2O CaO FeO TiO_2 MnO O_2
X0/Mol: 0.51 2.07 6.58 12.77 58.24 0.79 4.26 12.77 1.01 0.19 0.81
X1/Mol: 2.96 2.01 6.42 12.46 56.81 0.77 4.16 12.46 0.99 0.19 0.79
grt ilm melt mag pl qz sil
grt ilm kfs melt mag pl qz sil
bt grt ilm kfs melt mag pl qz sil
bt grt ilm melt mag pl qz sil
bt grt ilm kfs mag pl qz sil
bt grt ilm mag pl qz sil
bt grt ilm kfs pl qz sil
bt grt H2O ilm melt mag pl qz sil
bt grt H2O ilm mag pl qz sil
bt grt H2O ilm pl qz sil
bt grt H2O ilm pl qz sil St
bt grt ilm pl qz sil St
bt grt H2O ilm pl qz St
bt grt ilm kfs ky pl qz
bt grt ilm ky pl qz St
bt Chl grt H2O ilm pl qz St
1 bt grt ilm ky pl qz
2 bt grt ilm pl qz St
3 bt grt ilm pl qz sil
4 bt Chl grt ilm pl qz St
5 bt grt ilm mag pl qz sil St
1689844 TM_O
Oxides: H_2O Na_2O MgO Al_2O_3 SiO_2 K_2O CaO FeO TiO_2 MnO O_2
X0/Mol: 1.51 2.06 6.53 12.68 57.83 0.79 4.23 12.68 1.01 0.19 0.5
X1/Mol: 1.49 2.03 6.43 12.49 56.96 0.77 4.17 12.49 0.99 0.19 1.99
grt ilm kfs melt mag pl qz sil
crd grt ilm kfs melt mag pl qz sil
crd grt ilm kfs melt mag pl qz
grt ilm kfs melt pl qz sil
bt crd grt ilm kfs melt mag pl qz
bt crd grt ilm kfs mag pl qz
bt crd grt ilm kfs mag pl qz sil
bt grt ilm kfs melt mag pl qz sil
bt grt ilm melt mag pl qz sil
bt crd grt ilm melt mag pl qz sil
bt grt ilm melt pl qz sil
bt crd grt ilm mag pl qz sil
bt grt H_2O ilm pl qz sil
bt grt ilm pl qz sil St
bt grt ilm mag pl qz sil St
bt crd grt ilm mag pl qz sil St
bt grt ilm ky pl qz St
bt grt ilm ky mag pl qz St
1 bt grt H_2O ilm mag pl qz sil
2 bt grt ilm kfs melt pl qz sil
3 bt crd grt H_2O ilm mag pl qz sil
4 bt grt H_2O ilm melt pl qz sil
5 bt grt H_2O ilm melt mag pl qz sil
6 bt grt H_2O ilm pl qz sil St
7 bt grt H_2O ilm mag pl qz sil St
8 bt crd grt ilm kfs melt mag pl qz sil
9 bt crd grt H_2O ilm melt mag pl qz sil

G3 DDH1 P=6.5 kbar

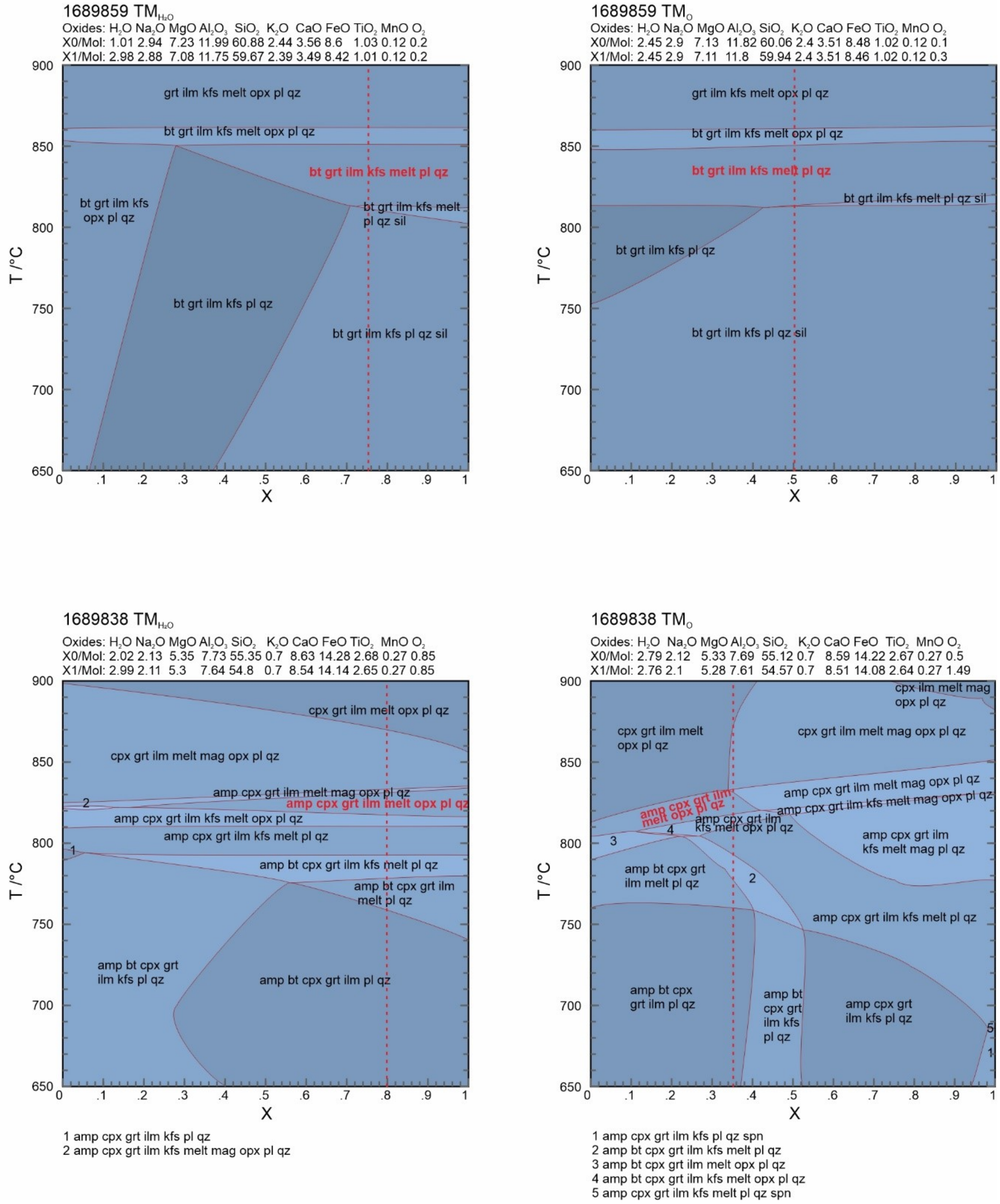

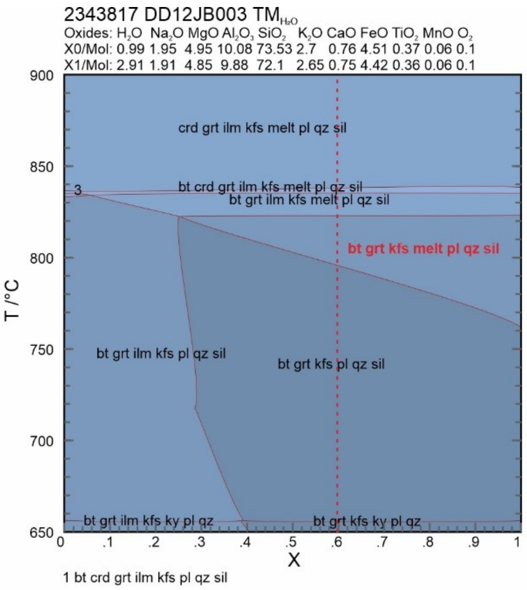

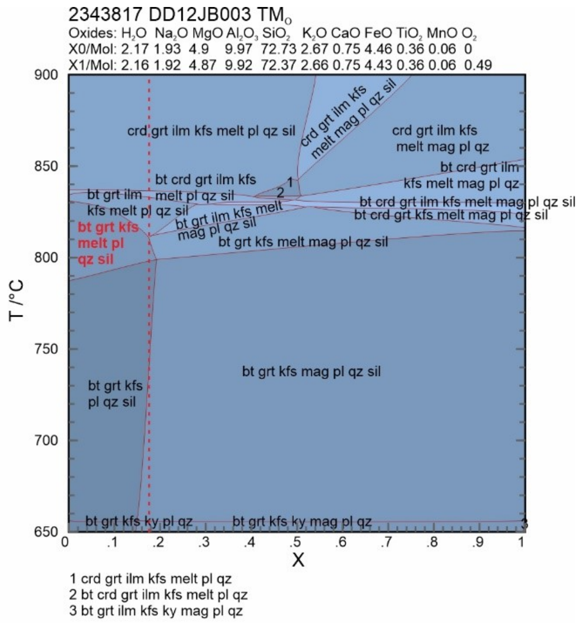

GOMA DH4 P=4 kbar

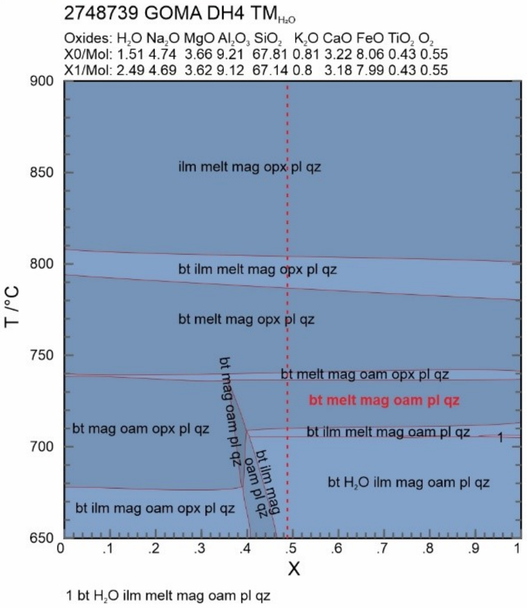

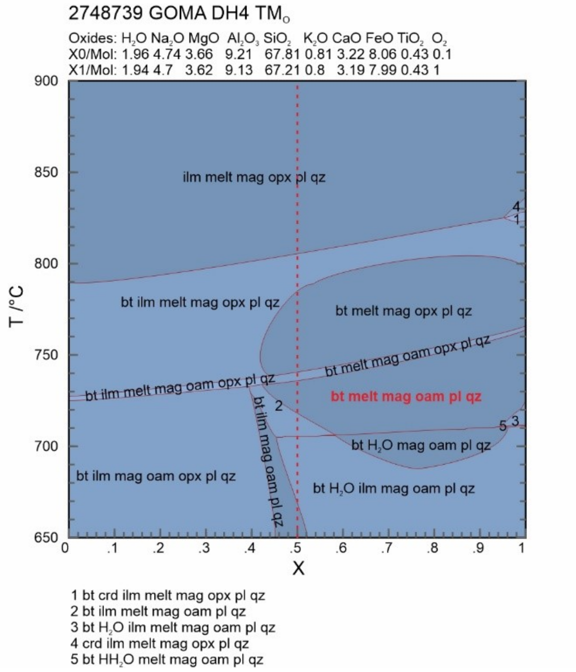

Appendix Figure 2. ***P–T*** **pseudosection modeling for additional samples from Mabel Creek Ridge.**

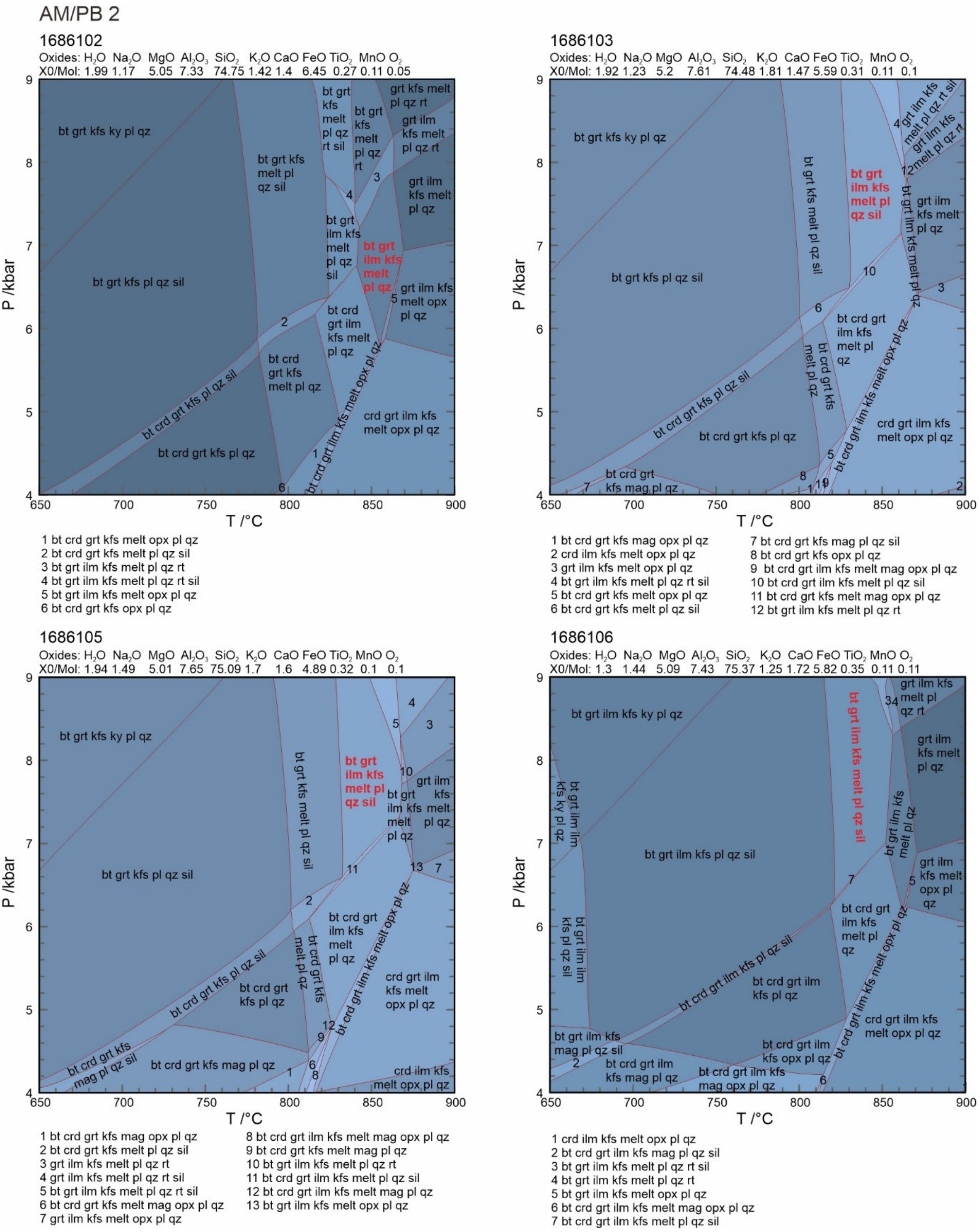

G3 DDH1

1689840

Oxides: H_2O Na_2O MgO Al_2O_3 SiO_2 K_2O CaO FeO TiO_2 MnO O_2
X0/Mol: 2.55 2.29 6.94 11.54 59.8 3.01 3.13 9.46 0.8 0.16 0.33

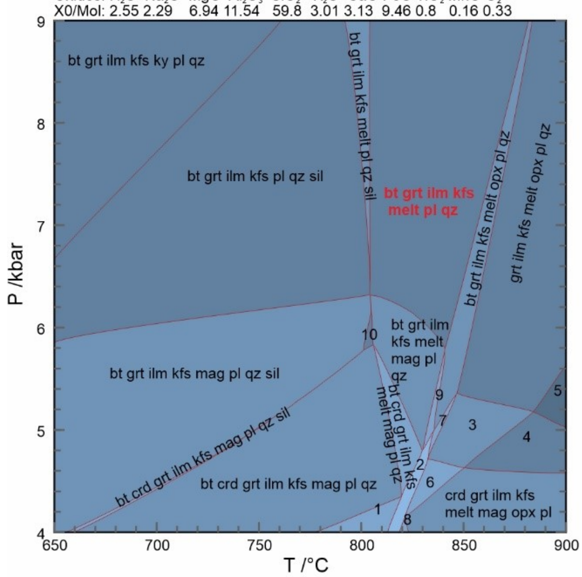

1 bt crd grt ilm kfs mag opx pl qz
2 bt crd grt ilm kfs melt mag opx pl qz
3 crd grt ilm kfs melt opx pl qz
4 crd grt ilm kfs melt opx pl
5 grt ilm kfs melt opx pl
6 crd grt ilm kfs melt mag opx pl qz
7 bt crd grt ilm kfs melt opx pl qz
8 bt crd grt ilm kfs melt mag opx pl
9 bt grt ilm kfs melt mag opx pl qz
10 bt grt ilm kfs mag pl qz

1689859

Oxides: H_2O Na_2O MgO Al_2O_3 SiO_2 K_2O CaO FeO TiO_2 MnO O_2
X0/Mol: 2.45 2.9 7.12 11.81 60 2.4 3.51 8.47 1.02 0.12 0.2

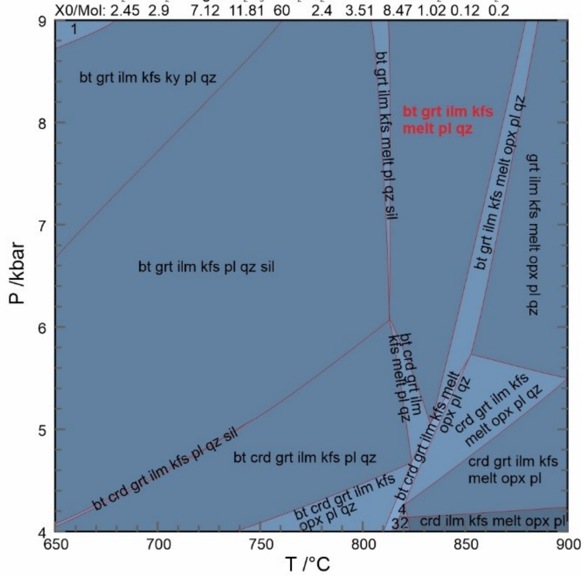

1 bt grt ilm kfs ky pl qz rt
2 bt crd ilm kfs melt opx pl
3 bt crd ilm kfs melt opx pl qz
4 bt crd grt ilm kfs melt opx pl

1689838

Oxides: H_2O Na_2O MgO Al_2O_3 SiO_2 K_2O CaO FeO TiO_2 MnO O_2
X0/Mol: 2.78 2.11 5.31 7.66 54.92 0.7 8.56 14.17 2.66 0.27 0.85

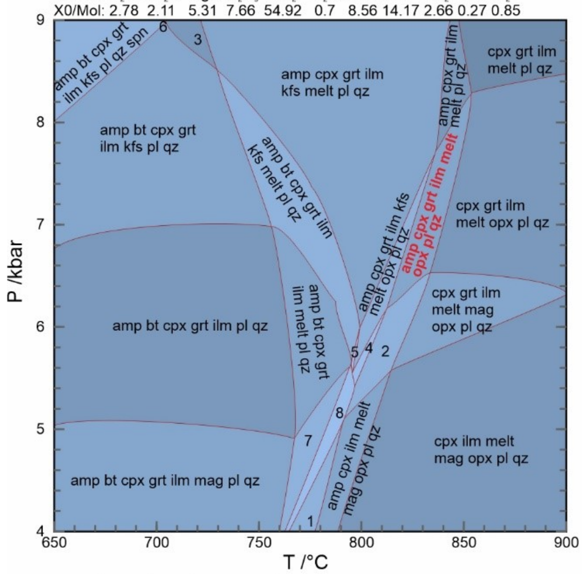

1 amp bt cpx ilm melt mag opx pl qz
2 amp cpx grt ilm melt mag opx pl qz
3 amp cpx grt ilm kfs pl qz
4 amp cpx grt ilm kfs melt mag opx pl qz
5 amp bt cpx grt ilm kfs melt opx pl qz
6 amp cpx grt ilm kfs pl qz spn
7 amp bt cpx grt ilm melt mag pl qz
8 amp bt cpx grt ilm melt mag opx pl qz

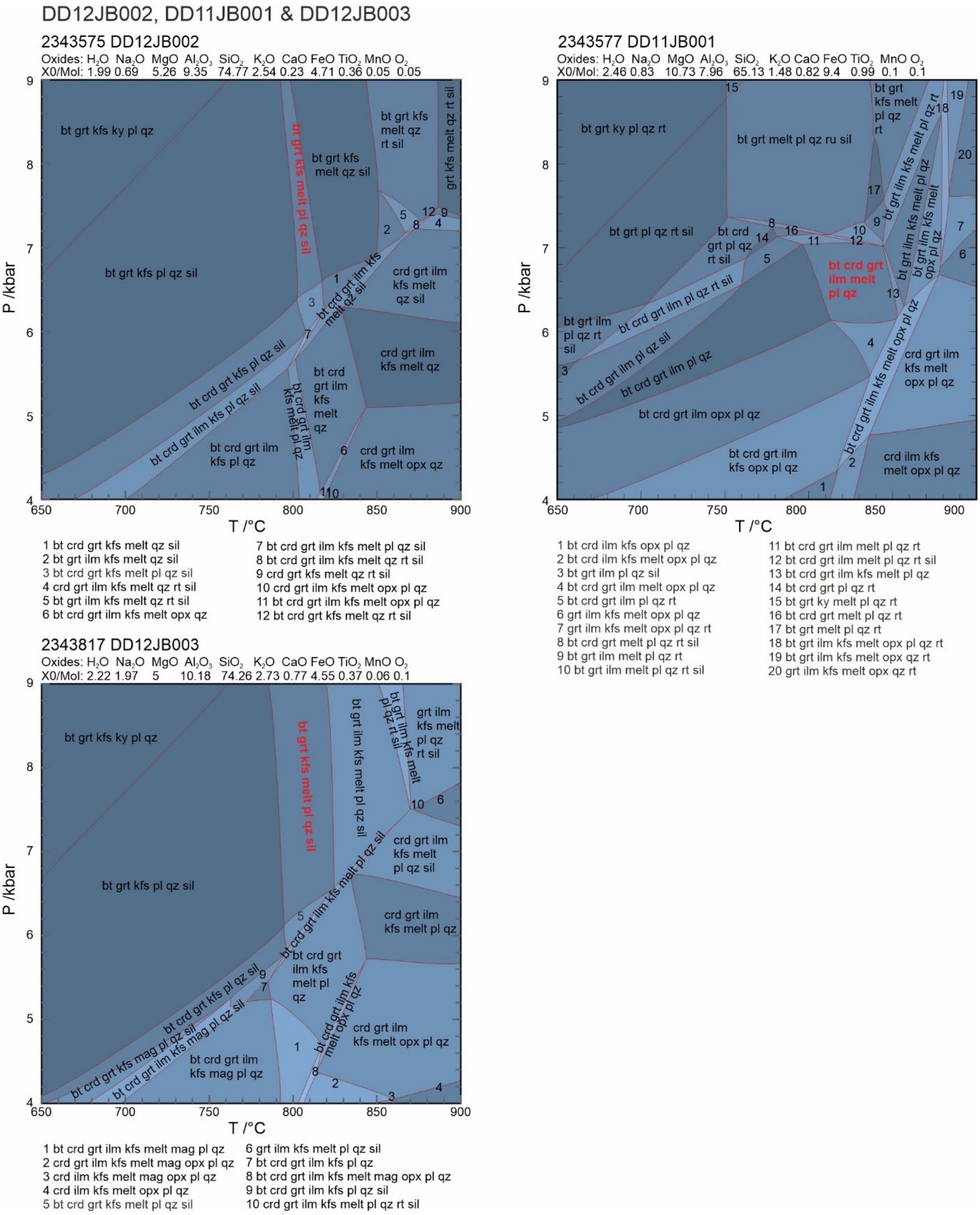
DD12JB002, DD11JB001 & DD12JB003
2343575 DD12JB002
Oxides: H2O Na2O MgO Al2O3 SiO2 K2O CaO FeO TiO2 MnO O2
X0/Mol: 1.99 0.69 5.26 9.35 74.77 2.54 0.23 4.71 0.36 0.05 0.05
bt grt kfs ky pl qz
bt grt kfs pl qz sil
bt grt kfs melt pl qz sil
bt grt kfs melt qz sil
bt grt kfs melt qz rt sil
grt kfs melt qz rt sil
crd grt ilm kfs melt qz sil
crd grt ilm kfs melt qz
bt crd grt ilm kfs melt qz
bt crd grt kfs pl qz sil
bt crd grt ilm kfs pl qz sil
bt crd grt ilm kfs pl qz
crd grt ilm kfs melt opx qz
P /kbar
T /°C
1 bt crd grt kfs melt qz sil
2 bt grt ilm kfs melt qz sil
3 bt crd grt kfs melt pl qz sil
4 crd grt ilm kfs melt qz rt sil
5 bt grt ilm kfs melt qz rt sil
6 bt crd grt ilm kfs melt opx qz
7 bt crd grt ilm kfs melt pl qz sil
8 bt crd grt ilm kfs melt qz rt sil
9 crd grt kfs melt qz rt sil
10 crd grt ilm kfs melt opx pl qz
11 bt crd grt ilm kfs melt opx pl qz
12 bt crd grt kfs melt qz rt sil
2343577 DD11JB001
Oxides: H2O Na2O MgO Al2O3 SiO2 K2O CaO FeO TiO2 MnO O2
X0/Mol: 2.46 0.83 10.73 7.96 65.13 1.48 0.82 9.4 0.99 0.1 0.1
bt grt ky pl qz rt
bt grt melt pl qz ru sil
bt grt kfs melt pl qz rt
bt grt pl qz rt sil
bt crd grt pl qz rt sil
bt crd grt ilm melt pl qz
bt grt ilm pl qz rt sil
bt crd grt ilm pl qz rt sil
bt crd grt ilm pl qz sil
bt crd grt ilm pl qz
bt crd grt ilm opx pl qz
bt crd grt ilm kfs opx pl qz
crd grt ilm kfs melt opx pl qz
crd ilm kfs melt opx pl qz
P /kbar
T /°C
1 bt crd ilm kfs opx pl qz
2 bt crd ilm kfs melt opx pl qz
3 bt grt ilm pl qz sil
4 bt crd grt ilm melt opx pl qz
5 bt crd grt ilm pl qz rt
6 grt ilm kfs melt opx pl qz
7 grt ilm kfs melt opx pl qz rt
8 bt crd grt melt pl qz rt sil
9 bt grt ilm melt pl qz rt
10 bt grt ilm melt pl qz rt sil
11 bt crd grt ilm melt pl qz rt
12 bt crd grt ilm melt pl qz rt sil
13 bt crd grt ilm kfs melt pl qz
14 bt crd grt pl qz rt
15 bt grt ky melt pl qz rt
16 bt crd grt melt pl qz rt
17 bt grt melt pl qz rt
18 bt grt ilm kfs melt opx pl qz rt
19 bt grt ilm kfs melt opx qz rt
20 grt ilm kfs melt opx qz rt
2343817 DD12JB003
Oxides: H2O Na2O MgO Al2O3 SiO2 K2O CaO FeO TiO2 MnO O2
X0/Mol: 2.22 1.97 5 10.18 74.26 2.73 0.77 4.55 0.37 0.06 0.1
bt grt kfs ky pl qz
bt grt kfs pl qz sil
bt grt kfs melt pl qz sil
bt grt ilm kfs melt pl qz sil
grt ilm kfs melt pl qz rt sil
crd grt ilm kfs melt pl qz sil
crd grt ilm kfs melt pl qz
bt crd grt ilm kfs melt pl qz
crd grt ilm kfs melt opx pl qz
bt crd grt ilm kfs mag pl qz
P /kbar
T /°C
1 bt crd grt ilm kfs melt mag pl qz
2 crd grt ilm kfs melt mag opx pl qz
3 crd ilm kfs melt mag opx pl qz
4 crd ilm kfs melt opx pl qz
5 bt crd grt kfs melt pl qz sil
6 grt ilm kfs melt pl qz sil
7 bt crd grt ilm kfs pl qz
8 bt crd grt ilm kfs melt mag opx pl qz
9 bt crd grt ilm kfs pl qz sil
10 crd grt ilm kfs melt pl qz rt sil

Chapter 6

Summary and Conclusions

The primary aim of this thesis was to improve the current understanding of IOCG mineralisation in the northern Gawler Craton. This thesis explores the currently exposed crustal level, metamorphic history, tectonic evolution and ore genesis of the northern Gawler Craton at both the deposit and regional scale. The following discussion highlights the key outcomes of this study, presenting a concise summary of the current state of knowledge on these topics.

1. Crustal level and thermal history of the northern Olympic Cu-Au Province

The northern Olympic Cu-Au Province includes a series of magnetite-dominated deposits/prospects associated with Cu-Au mineralisation. In contrast to the Olympic Domain south of Southern Overthrust, these magnetite-dominated deposits/prospects in the northern Olympic Cu-Au Province are hosted in rocks that experienced multiple phases of high temperature metamorphism and deformation during the Kimban and Kararan Orogenies (Payne et al., 2008; Freeman and Tomkinson, 2010; Morrissey et al. 2023) and again at ca. 1490 Ma (Chapter 2). Prior to this thesis, there was no geochronologic constraints on the protoliths, metamorphic and magmatic history of these deposits, limiting our understanding of the IOCG mineralisation in the northern Olympic Cu-Au Province.

In this thesis, host rocks to the Cairn Hill mineral deposit system yield zircon U-Pb ages from ca. 1830–1725 Ma, with a major peak at ca. 1740 and a minor peak at ca. 1800 Ma. They are interpreted to represent interlayered igneous and metasedimentary gneisses, similar to the Skylark Metasediments preserved in the southern and western Mount Woods Domain (Chalmers, 2007; Jagodzinski et al., 2007; Morrissey et al., 2023). The Skylark Metasediments were deposited after ca. 1750 Ma and comprise metapelitic and metapsammitic lithologies, minor banded iron formation, and calc-silicate. They host the magnetite-dominated IOCG prospects in the southern Mount Woods Domain, e.g., Manxman and Joe's Dam (Freeman and Tomkinson, 2010). At Peculiar Knob, iron-oxides contain zircons with ages of ca. 1741 Ma (Keyser et al., 2019), indicating their host rocks may also be Skylark Metasediments.

Gneissic host rocks at Cairn Hill record metamorphism at ca. 1580 Ma. The *P–T* conditions associated with the ca. 1580 Ma event are difficult to estimate due to the superposition of the later ca. 1490 Ma metamorphism. The metamorphic conditions at 1580 Ma are conservatively estimated to be upper amphibolite facies based on the formation of the hornblende selvages to magnetite mineralisation, the growth of monazite, and the crystallization of zircon in hornblende. In the southern Mount Woods Domain, amphibolite facies conditions are also recorded in sillimanite-bearing metasedimentary rocks that yield a metamorphic zircon age of 1595 ± 10 Ma (Jagodzinski et al., 2007).

After intrusion of the ca. 1515 Ma granitic dykes, Cairn Hill records a second phase of high temperature tectonism at ca. 1490 Ma. This involved granulite facies metamorphism and deformation along the Cairn Hill shear zone (4.6–

5.3 kbar and 740–770 °C). Metamorphism at comparable conditions (2.2–5.4 kbar and 710–740 ºC) has been identified in drill hole GOMA DH4 immediately north of Mabel Creek Ridge, with monazite U-Pb age of 1526 ± 9 Ma and metamorphic zircon U-Pb age of 1521 ± 9 Ma (Chapter 5 and Reid et al., 2014). Similar monazite U-Pb ages of 1500–1480 Ma have also been obtained from drill hole SR2 in the northernmost Mount Woods Domain (Morrissey et al., 2023), pointing to widespread ca. 1520–1490 Ma thermal reworking. Records of these ca. 1490 Ma events are commonly located close to the crustal-scale Karari Shear Zone and its splays and have not been reported elsewhere in the Gawler Craton. The tectonic setting and importance of the ca. 1490 Ma event remain unclear and may record the early stage and high temperature history of the reactivation of lithospheric-scale shear zones (Fraser and Lyons, 2006; Fraser et al., 2012).

Across the Mount Woods Domain, apatite U-Pb ages and biotite ^{40}Ar-^{39}Ar ages range from ca. 1560 to 1400 Ma (Forbes et al., 2012; Fraser et al., 2012; Hall et al., 2018; Tiddy et al., 2020), and in-situ Rb-Sr biotite ages range between ca. 1480–1390 Ma, with the majority around ca. 1450 Ma (Morrissey et al., 2023). This suggests the Mount Woods Domain cooled through ca. 450 ºC at ca. 1450 Ma. This cooling history is consistent with the ca. 1490–1460 Ma thermochronology data at Cairn Hill (Jagodzinski and Reid, 2015; Chapter 3).

2. New Cu mineralisation creates a composite IOCG deposit

Previous fluid inclusion studies in the Olympic Cu-Au Province reveal the temperatures of mineralisation were < 500 °C for the magnetite stage and < 400 °C for the hematite-copper stage (Oreskes and Einaudi, 1992; Bastrakov et al., 2007; Davidson et al., 2007; Schlegel et al., 2018). The deeper crustal level suggested by the ca. 1580 Ma amphibolite facies metamorphic mineral assemblages makes Cairn Hill likely to have been above the temperature window of IOCG mineralisation seen elsewhere in the Olympic IOCG Province. Therefore, if any IOCG-mineralisation did form in this region at 1580 Ma it is likely to have been at a higher crustal level that was subsequently eroded. This possibility may also be present in the southern Mount Woods Domain, where the magnetite-dominated IOCG prospects are hosted in amphibolite facies rocks (Freeman and Tomkinson, 2010). Currently, there are no geochronology or thermobarometric constraints on these prospects, and the host rocks could have been metamorphosed either during the Kimban Orogeny (1730–1690 Ma) or the intrusion of the White Hill Gabbro at ca. 1580 Ma (Freeman and Tomkinson, 2010; Morrissey et al. 2023). Future work is needed to determine the metamorphic history of the southern Mount Woods Domain, especially for the host rocks of Manxman and Joe’s Dam, which would enhance our understanding of the crustal level and IOCG mineralisation potential for the northern Olympic IOCG Province.

Lithospheric-scale geophysical imaging reveals metasomatic alteration connecting the upper mantle to the giant Olympic Dam deposit in the upper crust (Heinson et al., 2006, 2018; Skirrow et al., 2018). The magnetite-dominated Cu-Au mineralisation in the deeply exhumed mid-crustal northern Olympic Cu-Au Province may represent the roots of the world-class hematite-dominated Olympic Dam and the associated large IOCG mineralizing systems. Therefore, it is important to precisely constrain the mineralisation age in order to test this hypothesis. Magnetite at Cairn Hill is paragenetically associated with hornblende and apatite. Zircon separated from hornblende selvages developed at the margins of magnetite-apatite mineralisation yield a U-Pb age of 1583 ± 30 Ma, constraining the magnetite mineralisation to no later than 1583 Ma (Chapter 2), broadly coeval with IOCG mineralisation in the southern Olympic Cu-Au Province (Bowden et al., 2017; Cherry et al., 2018; Courtney-Davies et al., 2020; McPhie et al., 2020).

While magnetite-hornblende-apatite mineralisation and crosscutting 1515 Ma granitic dykes have been metamorphosed and deformed by the ca. 1490 Ma event, the Cu-bearing sulfide–quartz veins show no signs of ductile deformation or metamorphism. Instead they form hydrothermal infill of open space fractures in magnetite and apatite. This means the Cu mineralisation must post-date the ca. 1490 Ma high-grade event and therefore form at least 100 Myr after the magnetite mineralisation. The spatial but not temporal association between magnetite and Cu has created a composite IOCG deposit signature in the northern Olympic Cu-Au province, as opposed to a cogenetic IOCG system.

Detailed petrography reveals two generations of apatite at Cairn Hill, which yield systematically different in situ apatite Lu-Hf ages. Apatite syngenetic with magnetite is clear, relatively inclusion free, and yields in-situ Lu-Hf ages of ca. 1490 Ma, consistent with the resetting of its Lu-Hf as a result of ca. 1490 Ma granulite facies metamorphism (Chapter 2). During the infiltration of Cu-bearing fluids, clear apatite was altered to pink apatite, with the removal of LREE and the development of hydrothermal monazite. Cu-related apatite yields Lu-Hf ages of ca. 1460 Ma, consistent with ca. 1460 Ma U-Pb ages from hydrothermal monazite. The Lu-Hf data demonstrate the utility of the in-situ apatite Lu-Hf method for directly recording the timing of hydrothermal fluid activity and mineralisation. The data indicate the ca. 1460 Ma Cu mineralisation in the deeply exhumed northern Olympic Cu-Au Province is not an expression of the deep roots of the 1590 Ma Olympic Dam and the associated IOCG deposits.

3. Ore genesis of Fe and Cu in the composite IOCG system

The composite IOCG system at Cairn Hill comprises a 1583 ± 30 Ma magnetite-apatite assemblage overprinted by Cu mineralisation at ca. 1460 Ma. Petrological and geochemical analyses of magnetite, apatite, and fluid inclusions have helped to elucidate the genesis of iron and copper mineralisation.

Magnetite in the early Fe-P mineralisation exhibits varying concentrations of Al, Mn, Ti, V, and Mg, distinct from IOA or BIF deposits. Apatite associated with magnetite in coarse veins is Cl-rich, with gradually increasing F contents in the fine veins. Geochemical compositions of magnetite and apatite, together with their petrology, support a hydrothermal magnetite-apatite mineralisation event at around ca. 1583 Ma. This is the same age as granitic intrusions in the area (Jagodzinski and Reid, 2015), and therefore the magnetite mineralisation may have been driven by magmatic fluids interacting with country rocks. Early magnetite-apatite-hornblende assemblage at Cairn Hill may represent a deeper counterpart to the deep, early magnetite-apatite at depth and at the outer margins of the Olympic Dam deposit (Ehrig et al., 2012; Apukhtina et al., 2017; Verdugo-Ihl et al., 2020). Whether this is also the case for magnetite-dominated prospects e.g., Manxman and Joe's Dam (Freeman and Tomkinson, 2010) in the southern Mount Woods Domain requires further study to determine.

During the hydrothermal Cu mineralisation at ca. 1460 Ma, existing apatite experienced metasomatic alteration by the ore-forming fluids, with increased F contents and depletion of Mn, REE, Na, and Th. In addition, the different behaviors of redox-sensitive elements e.g., iron and arsenic, in different hydrothermal apatite types indicate an elevated fluid oxygen fugacity. This is further supported by the variation in solid phases in fluid inclusions where the daughter minerals change from siderite to magnetite, to hematite. The ore-forming fluids responsible for Cu mineralisation are high-temperature, CO_2-rich and hypersaline, evidenced by the presence of coexisting carbonic fluid inclusions and multiple daughter minerals. Their petrography and geochemistry indicate the ore-forming fluids may have exsolved from ca. 1460 Ma intrusions, and the intrusions may be similar to ca. 1460 Ma magmatism in the northern Nawa Domain (Morrissey et al., 2019) and Peake and Denison Domain (Bockmann et al., 2023). As the Cu-bearing fluids ascended, they experienced decompression, fluid immiscibility, and concentration. The early magnetite may act as a redox barrier, ultimately leading to the final precipitation of Cu.

The carbonic hypersaline fluids responsible for the Cu mineralisation at Cairn Hill resemble the ore-forming fluids in Cloncurry IOCG deposits (Perring et al., 2000; Pollard, 2001; Williams et al., 2001; Baker et al., 2008; Bertelli and Baker, 2010). The trace element concentrations of fluid inclusions at Cairn Hill are also comparable to thoseacquired by PIXE from the Cloncurry IOCG deposits (e.g., Starra and Lightning Creek; Perring et al., 2000; Williams et al., 2001; Baker et al., 2008). Similarities in mineralisation time and ore-forming fluids between Cairn Hill and Cloncurry IOCG deposits imply that they may share a similar ore genesis in a similar geodynamic context.

4. Tectonic setting of the northern Gawler Craton in the Mesoproterozoic

Mabel Creek Ridge, in the northern Gawler Craton, is a granulite-facies domain with seismic reflection data showing it is flanked by crustal-scale divergent structures and contains subhorizontal internal reflectors. Airborne magnetic data show the internal structure consists of regional-scale circular structural trends, suggesting that Mabel Creek Ridge has a regional-scale dome-like character. Previous studies have revealed ca. 1600–1560 Ma granulite-facies metamorphism and decompressive *P*–*T* path in rocks from Mabel Creek Ridge (Payne et al., 2008; Cutts et al., 2011). However, these constraints came from limited drill holes. In this thesis, pressure–temperature modeling was carried out for samples from across the Mabel Creek Ridge. The results indicate Mabel Creek Ridge has experienced conditions of ~6.4–7.4 kbar and 800–850 °C. Post-peak suprasolidus cordierite growth after garnet indicates near-isothermal decompression of 0.5–1 kbar above the solidus. In contrast, the drill hole located immediately north of Mabel Creek Ridge, i.e., GOMA DH4, records lower-grade metamorphism (2.2–5.4 kbar and 710–740 °C).

In-situ monazite U-Pb and garnet Lu-Hf geochronology reveal that Mabel Creek Ridge preserves minor relics of Kimban monazite and garnet, consistent with the conclusions from Payne et al. (2008) and Cutts et al. (2011). The bulk of garnet and monazite age data appear to document an interval of high-temperature conditions spanning ca. 1600–1560 Ma. In contrast, drill hole GOMA DH4 records no evidence for 1600–1560 Ma metamorphism but metamorphism at ca. 1520 Ma (this theis and Reid et al., 2014).

Our new *P*–*T* pseudosection results and geochronology data from Mabel Creek Ridge and adjacent crust, coupled with the regional seismic and airborne magnetic data, reveal that Mabel Creek Ridge represents a record of Early Mesoproterozoic extension in the Gawler Craton, during which thermally perturbed lower crustal rocks were exhumed within a gneiss dome. The Gawler Craton is envisaged to have been sandwiched between two subduction systems during the early Mesoproterozoic. Within this geodynamically complex setting, plume-driven magmatism resulted in the generation of voluminous felsic melts within the Gawler Craton-Curnamona Province system over the interval 1595–1570 Ma (Allen et al., 2008; Pankhurst et al., 2011; Wade et al., 2012; Jagozdinski et al., 2023). Plausibly the thermally perturbed nature of the lower crust would have made it conducive to flow and migration toward areas of extension that may have arisen due to changes in the dynamics of the evolving St Peter arc system.

The hypothesized extensional system appears to have been overprinted by regional metamorphism around ca. 1520 Ma. This suggestion is based on the similarity between the ages of metamorphism in the hanging wall recorded in GOMA DH4 and the youngest age of monazite growth in the Mabel Creek Ridge footwall. The general similarity in the ages suggests the footwall and hanging wall blocks

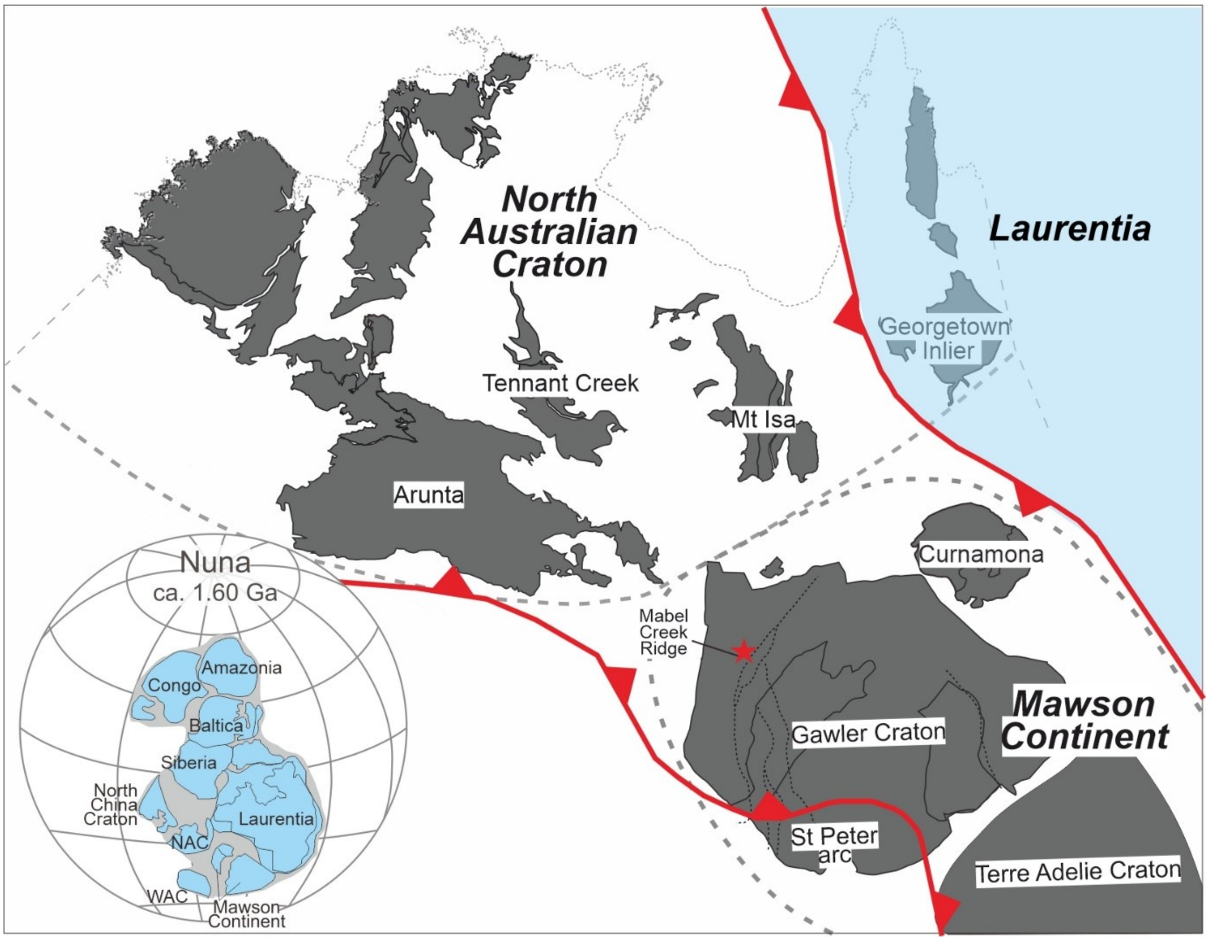

Fig. 6.1 The reconstructed paleogeography of North Australian Craton (NAC) and South Australian Craton (SAC) at ca. 1.60 Ga. Modified after Kirscher et al. (2019) and Morrissey et al. (2019).

shared a common thermal history at ca. 1520 Ma, implying they may have been at approximately the same crustal level by that time, and exhumed to mid-crustal level after 1460 Ma (Hall et al., 2018; Reid and Forster, 2021).

The ca. 1500–1450 Ma time interval may be another important tectonic event for the northern Gawler Craton (Morrissey et al., 2019; Reid and Forster, 2021). The Gawler Craton has a prolonged linked history to the North Australian Craton from the Archean to early Mesoproterozoic (Fig. 6.1; Cawood and Korsch, 2008; Payne et al., 2009), with subsequent rifting between 1.5 Ga and 1.35 Ga (Giles et al., 2004; Betts and Giles, 2006; Aitken et al., 2016; Morrissey et al., 2019; Reid and Forster, 2021). The northern Gawler Craton is thus a key region that connects the world-class Olympic IOCG province (Hand et al., 2007; Skirrow et al., 2007; Reid and Fabris, 2015) in the Gawler Craton and the Cloncurry IOCG district in the North Australian Craton (Bockmann et al., 2023). The Cloncurry IOCG district in the Mount Isa region, North Australian Craton has IOCG deposits with ages of ~1590 Ma to ~1490 Ma (Duncan et al., 2011). The younger phase of mineralisation ranging from ~1515 Ma to ~1490 Ma is interpreted to be related to the intrusion of A-type Williams-Naraku batholith (Betts et al., 2007; Baker et al., 2008; Duncan et al., 2011). The newly identified ca. 1460 Ma Cu mineralisation in the northern Gawler Craton coincides with ca.

1460 Ma A-type magmatism which interpreted to be related to the breakup of the Nuna supercontinent and fragmentation of Mesoproterozoic Australia (Morrissey et al., 2019). Magmatism and alteration around ca. 1460 Ma have been recently identified in the Peake and Denison Domain in the northeastern Gawler Craton, and these hydrothermal systems have been used to link the Gawler Craton and Mount Isa Province (Bockmann et al., 2023). Simultaneously with the A-type magmatism, lithospheric-scale shear zones in the Gawler Craton, including the Karari, Tallacootra, Coorabie, and Kalinjala Shear Zones were reactivated, yielding $^{40}Ar/^{39}Ar$ and monazite ages of 1470 – 1450 Ma (Foster and Ehlers, 1998; Swain et al., 2005; Fraser and Lyons, 2006; Fraser et al., 2012). The Cairn Hill crustal volume would have been largely anhydrous by 1460 Ma due to multiple high-T metamorphism at ca. 1580 and 1490 Ma, the ca. 1460 Ma Cu mineralisation may be a continuum of Cloncurry IOCG mineralisation into the northern Gawler Craton, where mantle upwelling provides heat to melt the dehydrated and refractory crust, and metals to form the Cu deposits (e.g., Lee et al., 2012). Lithospheric-scale shear zones that were active at this time (Fraser et al., 2012) are logical pathways for Cu introduction into the crust.

References

Aitken, A. R. A., Betts, P. G., Young, D. A., Blankenship, D. D., Roberts, J. L., and Siegert, M. J., 2016, The Australo-Antarctic Columbia to Gondwana transition: Gondwana Research, v. 29, p. 136-152.

Allen, S. R., McPhie, J., Ferris, G., and Simpson, C., 2008, Evolution and architecture of a large felsic Igneous Province in western Laurentia: The 1.6 Ga Gawler Range Volcanics, South Australia: Journal of Volcanology and Geothermal Research, v. 172, p. 132-147.

Apukhtina, O. B., Kamenetsky, V. S., Ehrig, K., Kamenetsky, M. B., Maas, R., Thompson, J., McPhie, J., Ciobanu, C. L., and Cook, N. J., 2017, Early, deep magnetite-fluorapatite mineralisation at the Olympic Dam Cu-U-Au-Ag deposit, South Australia*: Economic Geology, v. 112, p. 1531-1542.

Baker, T., Mustard, R., Fu, B., Williams, P. J., Dong, G., Fisher, L., Mark, G., and Ryan, C. G., 2008, Mixed messages in iron oxide–copper–gold systems of the Cloncurry district, Australia: insights from PIXE analysis of halogens and copper in fluid inclusions: Mineralium Deposita, v. 43, p. 599-608.

Bastrakov, E. N., Skirrow, R. G., and Davidson, G. J., 2007, Fluid Evolution and Origins of Iron Oxide Cu-Au Prospects in the Olympic Dam District, Gawler Craton, South Australia: Economic Geology, p. 1415-1440.

Bertelli, M., and Baker, T., 2010, A fluid inclusion study of the Suicide Ridge breccia pipe, Cloncurry district, Australia: Implication for breccia genesis and IOCG mineralisation: Precambrian Research, v. 179, p. 69-87.

Betts, P. G., and Giles, D., 2006, The 1800–1100Ma tectonic evolution of Australia: Precambrian Research, v. 144, p. 92-125.

Betts, P. G., Giles, D., Schaefer, B. F., and Mark, G., 2007, 1600–1500 Ma hotspot track in eastern Australia: implications for Mesoproterozoic continental reconstructions: Terra Nova, v. 19, p. 496-501.

Bockmann, M. J., Payne, J. L., Hand, M., Morrissey, L. J., and Belperio, A. P., 2023, Linking the Gawler Craton and Mount Isa Province through hydrothermal systems in the Peake and Denison Domain, northeastern Gawler Craton: Geoscience Frontiers, p. 101596.

Bowden, B., Fraser, G., Davidson, G. J., Meffre, S., Skirrow, R., Bull, S., and Thompson, J., 2017, Age constraints on the hydrothermal history of the Prominent Hill iron oxide copper-gold deposit, South Australia: Mineralium Deposita, v. 52, p. 863-881.

Cawood, P. A., and Korsch, R., 2008, Assembling Australia: Proterozoic building of a continent: Precambrian Research, v. 166, p. 1-35.

Chalmers, N., 2007, The Mount Woods Domain: a geological review and discussion on mineralisation potential, Report Book 2007/7: South Australia.

Cherry, A. R., Ehrig, K., Kamenetsky, V. S., McPhie, J., Crowley, J. L., and Kamenetsky, M. B., 2018, Precise geochronological constraints on the origin, setting and incorporation of ca. 1.59 Ga surficial facies into the Olympic Dam Breccia Complex, South Australia: Precambrian Research, v. 315, p. 162-178.

Courtney-Davies, L., Ciobanu, C. L., Tapster, S. R., Cook, N. J., Ehrig, K., Crowley, J. L., Verdugo-Ihl, M. R., Wade, B. P., and Condon, D. J., 2020, Opening the magmatic-hydrothermal window: high-precision U-Pb Geochronology Of The Mesoproterozoic Olympic Dam Cu-U-Au-Ag deposit, South Australia: Economic Geology, v. 115, p. 1855-1870.

Cutts, K., Hand, M., and Kelsey, D. E., 2011, Evidence for early Mesoproterozoic (ca. 1590Ma) ultrahigh-temperature metamorphism in southern Australia: Lithos, v. 124, p. 1-16.

Davidson, G. J., Paterson, H., Meffre, S., and Berry, R. F., 2007, Characteristics and origin of the Oak Dam East breccia-hosted, iron oxide Cu-U-(Au) deposit: Olympic Dam region, Gawler craton, South Australia: Economic Geology, v. 102, p. 1471-1498.

Duncan, R. J., Stein, H. J., Evans, K. A., Hitzman, M. W., Nelson, E. P., and Kirwin, D. J., 2011, A new geochronological framework for mineralisation and alteration in the Selwyn-Mount Dore corridor, Eastern fold belt, Mount Isa inlier, Australia: Genetic implications for iron oxide copper-gold deposits: Economic Geology, v. 106, p. 169-192.

Ehrig, K., McPhie, J., and Kamenetsky, V., 2012, Geology and mineralogical zonation of the Olympic Dam iron oxide Cu-U-Au-Ag deposit, South Australia, *in* Hedenquist, J., Harris, M., and Camus, F., eds., Geology and genesis of major copper deposits and districts of the world: a tribute to Richard H. Sillitoe., Soc of Econ Geol Spec Pub, p. 16: 237–267.

Forbes, C. J., Giles, D., Jourdan, F., Sato, K., Omori, S., and Bunch, M., 2012, Cooling and exhumation history of the northeastern Gawler Craton, South Australia: Precambrian Research, v. 200-203, p. 209-238.

Foster, D. A., and Ehlers, K., 1998, 40Ar-39Ar thermochronology of the southern Gawler Craton, Australia: Implications for Mesoproterozoic and Neoproterozoic tectonics of East Gondwana and Rodinia: Journal of Geophysical Research, v. 103, p. 10177-10193.

Fraser, G., Reid, A., and Stern, R., 2012, Timing of deformation and exhumation across the Karari Shear Zone, north-western Gawler Craton, South Australia: Australian Journal of Earth Sciences, v. 59, p. 547-570.

Fraser, G. L., and Lyons, P., 2006, Timing of Mesoproterozoic tectonic activity in the northwestern Gawler Craton constrained by 40Ar/39Ar geochronology: Precambrian Research, v. 151, p. 160-184.

Freeman, H., and Tomkinson, M., 2010, Geological setting of iron oxide related mineralisation in the southern Mount Woods Domain, South Australia, Hydrothermal iron oxide copper-gold & related deposits: A global perspective, 3, p. 171-190.

Giles, D., Betts, P. G., and Lister, G. S., 2004, 1.8–1.5-Ga links between the North and South Australian Cratons and the Early–Middle Proterozoic configuration of Australia: Tectonophysics, v. 380, p. 27-41.

Hall, J. W., Glorie, S., Reid, A. J., Boone, S. C., Collins, A. S., and Gleadow, A., 2018, An apatite U–Pb thermal history map for the northern Gawler Craton, South Australia: Geoscience Frontiers, v. 9, p. 1293-1308.

Hand, M., Reid, A., and Jagodzinski, L., 2007, Tectonic framework and evolution of the Gawler craton, southern Australia: Economic Geology, v. 102, p. 1377-1395.

Jagodzinski, E., and Reid, A., 2015, PACE Geochronology: Results of collaborative geochronology projects 2013-2015, Government of South Australia. Department of the Premier and Cabinet. , p. Report Book, 2015/00003.

Jagodzinski, E., Reid, A., Chalmers, N., Swain, G., Frew, R., and Foudoulis, C., 2007, Compilation of SHRIMP U-Pb geochronological data for the Gawler Craton, South Australia, 2007, Report Book 2007/21, South Australian Department of Primary Industries and Resources.

Jagodzinski, E. A., Reid, A. J., Crowley, J. L., Wade, C. E., and Curtis, S., 2023, Precise zircon U-Pb dating of the Mesoproterozoic Gawler large igneous province, South Australia: Results in Geochemistry, v. 10, p. 100020.

Keyser, Ciobanu, Cook, Feltus, Johnson, Slattery, Wade, and Ehrig, 2019, Mineralogy of Zirconium in Iron-Oxides: A Micron- to Nanoscale Study of Hematite Ore from Peculiar Knob, South Australia: Minerals, v. 9.

McPhie, J., Ehrig, K. J., Kamenetsky, M. B., Crowley, J. L., and Kamenetsky, V. S., 2020, Geology of the Acropolis prospect, South Australia, constrained by high-precision CA-TIMS ages: Australian Journal of Earth Sciences, v. 67, p. 699-716.

Morrissey, L. J., Barovich, K. M., Hand, M., Howard, K. E., and Payne, J. L., 2019, Magmatism and metamorphism at ca. 1.45 Ga in the northern Gawler Craton: The Australian record of rifting within Nuna (Columbia): Geoscience Frontiers, p. 175-194.

Morrissey, L. J., Payne, J., Hand, M., Clark, C., and Janicki, M., 2023, One billion years of tectonism at the Paleoproterozoic interface of North and South Australia: Precambrian Research, p. under review.

Oreskes, N., and Einaudi, M. T., 1992, Origin of hydrothermal fluids at Olympic Dam Preliminary results from fluid inclusions and stable isotopes: Economic Geology, v. 87, p. 64-90.

Pankhurst, M. J., Schaefer, B. F., Betts, P. G., Phillips, N., and Hand, M., 2011, A Mesoproterozoic continental flood rhyolite province, the Gawler Ranges, Australia: the end member example of the Large Igneous Province clan: Solid Earth, v. 2, p. 25-33.

Payne, J. L., Hand, M., Barovich, K. M., Reid, A., and Evans, D. A. D., 2009, Correlations and reconstruction models for the 2500-1500 Ma evolution of the Mawson Continent: Geological Society, London, Special Publications, v. 323, p. 319-355.

Payne, J. L., Hand, M., Barovich, K. M., and Wade, B. P., 2008, Temporal constraints on the timing of high-grade metamorphism in the northern Gawler Craton: implications for assembly of the Australian Proterozoic: Australian Journal of Earth Sciences, v. 55, p. 623-640.

Perring, C., Pollard, P., Dong, G., Nunn, A., and Blake, K., 2000, The Lightning Creek sill complex, Cloncurry district, northwest Queensland: A source of fluids for Fe oxide Cu-Au mineralisation and sodic-calcic alteration: Economic Geology, v. 95, p. 1067-1089.

Pollard, P. J., 2001, Sodic(–calcic) alteration in Fe-oxide–Cu–Au districts: an origin via unmixing of magmatic H2O-CO2-NaCl: Mineralium Deposita, v. 36, p. 93-100.

Reid, A., and Fabris, A., 2015, Influence of Preexisting Low Metamorphic Grade Sedimentary successions on the distribution of iron oxide copper-gold mineralisation in the olympic Cu-Au province, Gawler Craton: Economic Geology, v. 110, p. 2147-2157.

Reid, A., and Forster, M., 2021, Mesoproterozoic thermal evolution of the northern Gawler Craton from 40Ar/39Ar geochronology: Precambrian Research, v. 358, p. 106180.

Reid, A. J., Jagodzinski, E. A., Armit, R. J., Dutch, R. A., Kirkland, C. L., Betts, P. G., and Schaefer, B. F., 2014, U-Pb and Hf isotopic evidence for Neoarchean and Paleoproterozoic basement in the buried northern Gawler Craton, South Australia: Precambrian Research, v. 250, p. 127-142.

Schlegel, T. U., Wagner, T., Wälle, M., and Heinrich, C. A., 2018, Hematite Breccia-Hosted Iron Oxide Copper-Gold Deposits Require Magmatic Fluid Components Exposed to Atmospheric Oxidation: Evidence from Prominent Hill, Gawler Craton, South Australia: Economic Geology, v. 113, p. 597-644.

Skirrow, R. G., Bastrakov, E. N., Baroncii, K., Fraser, G. L., Creaser, R. A., Fanning, C. M., Raymond, O. L., and Davidson, G. J., 2007, Timing of iron oxide Cu-Au-(U) hydrothermal activity and Nd isotope constraints on metal sources in the Gawler craton, south Australia: Economic Geology, v. 102, p. 1441-1470.

Swain, G., Hand, M., Teasdale, J., Rutherford, L., and Clark, C., 2005, Age constraints on terrane-scale shear zones in the Gawler Craton, southern Australia: Precambrian Research, v. 139, p. 164-180.

Tiddy, C. J., Betts, P. G., Neumann, M. R., Murphy, F. C., Stewart, J., Giles, D., Sawyer, M., Freeman, H., and Jourdan, F., 2020, Interpretation of a ca. 1600–1580 Ma metamorphic core complex in the northern Gawler Craton, Australia: Gondwana Research, v. 85, p. 263-290.

Verdugo-Ihl, M. R., Ciobanu, C. L., Cook, N. J., Ehrig, K. J., and Courtney-Davies, L., 2020, Defining early stages of IOCG systems: evidence from iron oxides in the outer shell of the Olympic Dam deposit, South Australia: Mineralium Deposita, v. 55, p. 429-452.

Wade, C. E., Reid, A. J., Wingate, M. T. D., Jagodzinski, E. A., and Barovich, K., 2012, Geochemistry and geochronology of the c. 1585Ma Benagerie Volcanic Suite, southern Australia: Relationship to the Gawler Range Volcanics and implications for the petrogenesis of a Mesoproterozoic silicic large igneous province: Precambrian Research, v. 206-207, p. 17-35.

Williams, P. J., Dong, G., Ryan, C. G., Pollard, P. J., Rotherham, J. F., Mernagh, T. P., and Chapman, L. H., 2001, Geochemistry of hypersaline fluid inclusions from the Starra (Fe oxide)-Au-Cu deposit, Cloncurry District, Queensland: Economic Geology, v. 96, p. 875-883.